FULL WAVEFORM ACOUSTIC LOGS IN RADIALLY LAYERED BOREHOLES

by

Kenneth M. Tubman

B.S., University of Massachusetts

(1978)

SUBMITTED TO THE DEPARTMENT OF
EARTH, ATMOSPHERIC, AND PLANETARY SCIENCES
IN PARTIAL FULFILLMENT OF THE
REQUIREMENTS FOR THE DEGREE OF
DOCTOR OF PHILOSOPHY

at the

August 9, 1984

Signature of Author .....
Department of Earth, Atmospheric, and Planetary Sciences
August 1984

Certified by .....
M. Nafi Toksoz
Thesis Advisor

Accepted by .....
Theodore R. Madden
Chairman
Departmental Committee on Graduate Students

Full Waveform Acoustic Logs in Radially Layered Boreholes

by

Kenneth M. Tubman

submitted to the Department of Earth, Atmospheric, and Planetary Sciences
on August 9, 1984 in partial fulfillment of the requirements for the
Degree of Doctor of Philosophy in Geophysics

Abstract

A general formulation is presented for the dispersion and propagation of elastic waves in a fluid-filled cylinder surrounded by an arbitrary number of solid or fluid annuli. A Thomson-Haskell type propagator matrix method is used to relate displacements and stresses across the layers. Synthetic microseismograms containing all body and guided wave arrivals are calculated with the method of discrete wavenumber integration. Attenuation is incorporated into the calculations through a transformation of the layer velocities to complex parameters.

A major classification of radial layers that are investigated are those corresponding to cased borehole geometries. Layers of steel and cement are inserted into the borehole. Fluid layers are mixed with the layers of steel, cement, and formation in order to model the situation of poor bonding.

It is found that in the well bonded situation the formation body waves are relatively unaffected by the presence of the casing. The velocities and attenuation of the formation body waves can be determined in cased boreholes just as in open hole situations. It is possible for the steel and cement layers to make it more difficult than in an open hole. The amplitudes of the formation body waves depend upon the relationship of the velocities of the formation and the cement. The guided waves are dominated by the steel and cement layers in most cases. The cement layer prevents the formation from having a strong influence on the guided waves. If the cement layer is thin or non-existent, the formation can have a larger effect on the character of the guided waves.

If there is a fluid layer between the steel and the cement the steel is free to ring. The first arrival in this situation is from the casing. Even with an extremely thin fluid layer, or microannulus, the first arrival is from the steel. The amplitude and duration of the pipe signal depends on the thickness of the fluid layer. While the first arrival is from the casing, the

formation body wave energy is present. The character of the waveform will vary as the formation parameters vary. If the duration of the steel arrival is small it is possible to distinguish the formation P-wave arrival.

The situation is more complex if the fluid layer is between the cement and the formation. Here, the steel is well bonded to the cement but the cement is not bonded to the formation. In this case the thickness of the fluid and cement layers become important in determining the nature of the first arrival. If there is a large amount of cement bonded to the steel, the cement can damp out the ringing of the pipe. A large amount of cement can damp out the casing arrival to the point where it is barely observable. This makes it possible to distinguish the formation arrivals.

If there is less cement bonded to the steel, the cement is not able to damp out the steel ringing. In this case the cement rings along with the steel and the first arrival is from the combination of the steel and the cement. The velocity of this wave depends on the velocities and thicknesses of the steel and cement layers.

Open hole geometries including radial layers due to the drilling process are also investigated. Additional layers in the model are those of an invaded zone, a damaged zone, or a mud cake. The presence of these layers does not necessarily affect the ability to determine the formation velocities with long spaced tools. Velocities observed are those of the virgin formation unless the source-receiver separation is particularly short or the depth of alteration is large.

While the determination of formation velocities is not significantly affected, the character of the microseismograms can be changed by the presence of an altered layer. A low velocity damaged zone or mud cake can produce a large change in the amplitude of the formation P-wave arrival. Focusing of energy due to the velocity gradient can increase the amplitudes by as much as a factor of two. An invaded zone with velocities raised above those of the original formation can reduce the observed amplitudes of the formation P-wave.

Thesis Advisor: M. Nafi Toksöz
Title: Professor of Geophysics

Acknowledgements

I would like to thank my advisor Nafi Toksöz for his advice and guidance throughout this endeavor. His scientific insight and commitment continue to amaze me. I need to thank him not only for his help in completing this work, but also for help in selecting what has proved to be a fascinating and timely topic. I had some other foolish ideas, but when I heard "layered boreholes" for the third time, the path was clear.

Arthur Cheng was of great assistance in my learning about borehole Geophysics. He was always there (well, almost always) when I needed to discuss a new idea or an old mistake. He also gave many hours of good competition on the tennis court and hockey rink and many lectures on what I do wrong in each sport. In addition, the collection under his desk provided an indirect technique for monitoring the number of different athletic shoes that are on the market at any given moment. Without Arthur's expertise in fine cuisine I might never have tried alligator sausage.

The people who have taught me the most, both about science and about life, are my fellow students. Steve Taylor (who still stinks) took me by the hand and taught me about surface waves and inverse theory. We had many profitable discussions (at least they were for me) at 3 AM when the rates were cheap (but Multics was painfully slow). Mark Willis helped me in my quest to understand guided normal pseudo-reflected conical modes and supplied valued friendship (and good data via Mobil). He also

kept a close watch on Pulte (who was the fool who offered him all those steak dinners?)

Rob Stewart, Tim Keho, John Nabelek, and Fico Pardo, taught me many things about science and various other topics. (I still wish Fico would use a phone to talk to people in Peru. And what can be said about Tim? I think the last time he smiled was the day he tasted that famous cherry pie — twice.) John Bullitt and Mike Mellen both added a great deal of time to the completion of this thesis. Thanks a lot guys. Stephen Cole gave me much assistance with the work on intermediate fluid layers and his fierce competition on the tennis court helped keep me going. Jay Pulli provided for many good conversations about life and lots of bad advice about investing. Qiming Wang (along with Cao) taught me about Chinese culture and how to be a capitalist. Stephen Gildea tolerated thousands of questions, and Jane Maloof gave me the opportunity to do the same. (It's too bad she never believed my answers.) Gilles Garcia provided me with late night reminders of the things I will miss after being away from academia for a year or so. (I'm still not sure I believe him.) Gilles is also responsible for the figures in chapter 1. Dan Burns found all (I hope) of my typing errors. Colleen Barton continually reminded me that my terminal is able to display CAPITAL LETTERS!!!!! Cengiz Esmersoy, Mike Prange, and Wafik Beydoun, along with Frederic Mathieu, and the rest of the French contingent all provided useful discussions. (Is it true that ERL is to be renamed Laboratoire des Resources Terrestres?)

Roger Turpening (whose "fast" Green car couldn't pass my Honda), Al Taylor, Sue Turbak, Kelly Worrall, and Naida Buckingham all made life at ERL more enjoyable. Sara Brydges gave me lots of advice on how to cope. She really keeps ERL going. I am continually astounded as to how (and why) she does it.

Special thanks go to the consortium representatives who all tried to keep me in touch with the real world. Gopa De was always quick to complain that things are too easy with synthetics. (I hope she notices the lack of lines marking the not-so-obvious arrivals.) Joe Zemanek was responsible for my first trip to the real world. John Minear provided helpful discussions and data. He also served on my thesis committee.

Lastly, and most importantly, I would like to thank Ellen for putting up with all this nonsense with few complaints, (well maybe just a little more than a few). I'll bet she never dreamed she would move to Texas and live down the street from some cows. Michael and Randi both helped keep life interesting.

This work was supported by the Full Waveform Acoustic Logging Consortium at M.I.T. and a Phillips Petroleum Fellowship.

Table of Contents

Abstract 2

Acknowledgements 4

Chapter 1. Introduction

1.1 Overview 9

1.2 Summary of Other Work 12

1.3 Discussion of Present Model 15

Figures 18

Chapter 2. Theoretical Development

2.1 Introduction 22

2.2 Dispersion Relation 24

2.3 Calculation of Synthetic Microseismograms 33

2.4 Calculation of Displacements 37

Figures 39

Chapter 3. Well Bonded Cased Boreholes

3.1 Introduction 42

3.2 General Effects of Waveform Character 44

3.3 Effects on Arrival Times 47

3.4 Effects on Amplitudes 54

3.5 Summary 57

Tables 59

Figures 63

Chapter 4. Poorly Bonded Cased Boreholes

4.1 Introduction 103

4.2 No Steel-Cement Bond, Good Cement-Formation Bond 106

4.3 Good Steel-Cement Bond, No Cement-Formation Bond 114

4.4 Summary 119

Tables 121

Figures 125

Chapter 5. Open Boreholes With Radial Layering

5.1 Introduction 171

5.2 Invaded Zone 173

5.3 Damaged Zone 179

5.4 Mud Cake Layer 182

5.5 Summary 184

Tables 187

Figures 192

Chapter 6. Discussion and Conclusions 225

References 232

Appendix A Boundary Calculations 236

Appendix B Numerical Considerations 247

Chapter 1

Introduction

1.1 Overview

The problem of seismic wave propagation in boreholes has been of interest in resource exploration for many years. Marcel Schlumberger recognized the importance of determining the formation velocities in 1935 with the patent for the acoustic logging tool. Acoustic logging affords a relatively inexpensive technique for measuring formation parameters with good depth resolution. Acoustic logs have now become a routine measurement in most boreholes. Magnolia Oil developed the first continuous velocity logging tool in the early 1950's. Since then acoustic logging has progressed from the simple measurement of the time of first break to the digital recording and analysis of the complete wave train. The once common source-receiver separation of 1.5 meters (5 feet), originally determined by the limited strength of the first sources, has been replaced by tools with a large number of sources and receivers at various spacings. Elf Aquitane has developed a tool with 5 sources and 12 receivers (Arditty et al., 1981). This provides 48 unique source-receiver spacings up to a maximum of 13 meters.

Recently, borehole problems are gaining new importance in global geophysical studies as well as in exploration Geophysics (Kerr, 1984). Borehole Geophysics is being used in investigations of crustal structure, including near the outer continental shelf where standard Geophysical techniques are difficult to employ (e.g. Ocean Drilling Project). Drilling allows observation of formations and conditions that are not present at the surface. The kola hole in the Soviet Union currently has provided measurements at depths of up to 12 km. A special meeting was recently held to discuss the applications of logging to continental crustal studies (International Symposium on Observation of the Continental Crust Through Drilling, Tarrytown, New York, May 1984).

A great deal of effort is being put into extracting more information from the full waveform. The shear as well as the compressional wave velocities can be determined in fast formations. In slow formations there is no formation shear arrival or pseudo-Rayleigh wave. Techniques have recently been developed to acquire indirect measures of the shear velocity through use of the Stoneley wave (Cheng and Toksöz, 1983; Chen and Willen, 1984; Liu, 1984).

Aside from more accurate velocity determinations, the greater number of source-receiver combinations allows for the examination of spatial decay for attenuation measurements. This allows the determination of Q values for the formations of interest (Staal and Robinson, 1977; Lebreton

et al., 1978; Cheng et al., 1981,1982; Willis, 1983).

The new data collection and analysis procedures are greatly improving the ability to gain information about the formation being investigated. They are hindered though, by an incomplete understanding of the nature of the wave propagation in borehole environments. This demonstrates the importance of forward modeling in borehole investigations. Although inversion of data for formation properties is the ultimate goal, we must first have a basic understanding of the processes involved in the collection of that data an the factors affecting the recorded signals.

Generally the borehole has been modeled as a simple fluid filled cylinder (see Figure 1.1). This model has provided a great deal of insight and understanding into the wave propagation problems encountered White (1983). The actual borehole environment is much more complex, though. The process of drilling can damage the formation in the immediate vicinity of the borehole. This results in a zone of fractured and altered formation. The borehole mud filtrate seeps into the formation to various degrees, depending upon the porosity and permeability (see Figure 1.2). The fluid replaces the in situ pore fluids and can change the properties of formation in this region. A residue from the borehole fluid forms a layer along the fluid-formation boundary referred to as a mud cake. Steel and cement layers are also present when the borehole is cased (Figure 1.3). If the bonding is not perfect, there are fluid layers intermixed with the steel and

cement layers.

It is the effects of these radial layers and zones that are investigated in this thesis. Chapter 2 presents the theoretical development for the determination of the dispersion relations and the synthetic microseismograms. Cased hole geometries are examined in Chapters 3 and 4. Well bonded cased boreholes are modeled in Chapter 3. Additional fluid layers are placed between the steel and the cement or between the cement and the formation as models for poorly bonded casing. These models are presented in Chapter 4. Chapter 5 presents the results of modeling damaged zones, invaded zones and mud cake layers. Chapter 6 gives a brief summary of the conclusions and findings from the modeling presented in the other chapters.

1.2 Summary of Other Work

Wave propagation in the simple case of a fluid cylinder surrounded by an infinite formation has been studied by a number of authors. Biot (1952) investigated dispersion characteristics of waves traveling in empty and fluid filled boreholes. He identified the wave types observed in the borehole and gave theoretical descriptions of their behavior. Rosenbaum (1974) generated synthetic microseismograms and used Biot's (1956) theory of propagation in porous media to investigate the ability of sonic logs to measure porosity and permeability. He concluded that the the Stoneley wave can be sensitive to permeability if the source and receivers are close

to the interface and if the fluid flow across the interface (borehole wall) is unrestricted. Roever et al., (1974) studied wave propagation in boreholes in terms of modal theory and a ray-type expansion. The ray expansions were used to study the amplitude decay of the P and S body waves. The effects of having the source and receiver off axis were also examined. One significant effect that was observed was constructive interference if the source and receiver are both on the same side of the axis and destructive interference if they are on opposite sides. Curves are given for amplitude of the body waves as a function of radial positions of the source and receiver. Ray expansion studies of the amplitude decay of the P and S body waves led to the conclusion that the P wave amplitude decays as $1/z\log^2 z$ and the S wave amplitude decays as $1/z^2$. Winbow (1980) and Zhang and Cheng (1984) found the P wave geometric decay to be $1/z$ with the shear decay being $1/z^2$. This is in agreement with the conclusions of White and Tongtaow (1981). The P wave decay was found to be strongly dependent on frequency and Poisson's ratio. The Poisson's ratio also affects the P wave amplitude but not the S wave amplitude or decay rate. Peterson (1974) examined the single frequency point source solution of the wave equation. A discussion is given on the location of the poles in the $\omega-k$ plane and the path of integration accompanies modal dispersion curves. Tsang and Rader (1979) give the form for the pressure response in a fluid filled borehole. Microseismograms are generated with the real axis integration technique but the waveforms shown are limited to the early

part of the signal with the body wave arrivals.

Soft formations, (with the formation shear velocity less the borehole fluid velocity) have been the object of much study. In this situation the determination of shear wave velocities is difficult because there is no pseudo-Rayleigh wave. Cheng et al., (1982) found that if the formation is soft the Stoneley wave is more highly dispersive and the velocity is influenced strongly by the formation shear velocity This allows the use of the Stoneley wave as an indirect method for obtaining the formation shear velocity (Cheng et al., 1983; Chen and Willen, 1984; Liu, 1984).

A number of investigations have gone beyond the simple fluid filled cylinder model. Cheng and Toksöz (1981), while presenting microseismograms for the simple case, also discuss dispersion curves with an elastic tool present in the center of the borehole. They concluded that one effect of the presence of the tool is to decrease the thickness of the fluid annulus between the tool and the formation. This is important in determining the character of the microseismograms because the thickness of the fluid layer influences the excitation of the guided wave modes. White and Zechman (1968) modeled the effects of a rigid tool at the center of the borehole. They present dispersion curves but numerical problems limited the models for which synthetic microseismograms could be generated. An attempt was made to model other than a simple homogeneous isotropic formation by using a viscoelastic solid.

White and Tongtaow (1981) developed similar formulations with transversely isotropic medium rather than the isotropic formulations of the previous papers. Their model allows the specification of elastic constants more than just the velocities and densities.

1.3 Discussion of Present Model

Another complexity that can be added to the simple fluid filled borehole model is radial layering. This is the approach that is taken in this thesis. The improvement of the present model over the simple borehole model mentioned above is the radial layering. The infinite homogeneous formation can be replaced by any number of cylindrical annuli. In addition to allowing solid layers surrounding the borehole as other investigators have done, fluid layers can be included as well. This is invaluable in the study of cased borehole situations. It allows the modeling to go beyond the assumption of perfect bonding. The ability to specify Q factors for each layer is another feature of the model used here. The inclusion of attenuation is important in determining realistic relative amplitudes for waves controlled by different layers (Tubman et al., 1982). Most other studies have not accounted for other than geometric decay of the wave amplitudes.

Some other investigations have examined individual aspects of similar models (Cheng et al., 1981; Schoenberg et al., 1981; Tubman et al., 1983; Chan and Tsang, 1983; Chang and Everhart, 1983; Tubman et al., 1984a,b;

Baker, 1984). These investigations are discussed further where they are relevant to the work done in this study.

In this thesis the modeling technique developed is applied to a variety of different geometries. A systematic and comprehensive study is done of cased hole geometries (both well bonded and poorly bonded) as well as open hole geometries. The emphasis is on understanding the effects of these geometries and additional layer parameters on wave propagation in borehole environments.

Comparisons of the theoretical results with field data are made wherever possible. Unfortunately, there is only a limited amount of available data where the nature of the radial layering in the borehole environment is known. Cased borehole geometries provide a good situation for having some information on the details of the geometry. Full waveform logging data has not generally been recorded is such situations though, because of an incomplete understanding of the effects of the casing on the recorded waveforms. In order to facilitate comparisons with the data, all modeling has been done with distances in terms of feet and inches.

The geometry of the model consists of coaxial annuli surrounding a central fluid cylinder. The outermost annulus is infinite in extent. A Thomson-Haskell type propagator matrix is used to derive the dispersion relations and the impulse response of the medium. The discrete wavenumber integration technique is used to numerically evaluate the

integrals for the calculation of synthetic microseismograms. The treatment is general so the number of layers is arbitrary. Fluid layers are allowed to be located in any position (with the exception of the infinite formation layer). An important feature influencing the character of the microseismograms is the addition of intrinsic attenuation. In the cased hole geometries, the Q factors of the various layers can differ by an order of magnitude or more.

The advances of the radially layered model over the fluid filled borehole model and the addition of intermediate fluid layers have proved valuable in understanding many of the phenomena observed in field data. Cased hole geometries, invaded zones, damaged zones, and other similar complexities cannot be understood with the more simple model.

Figure Captions

Figure. 1.1. Open borehole geometry. This is simple model used in many studies to represent the borehole environment.

Figure. 1.2. Borehole geometry including an invaded zone and a layer of mud cake. After the drilling process, the mud filtrate spreads into the formation creating a zone of altered formation properties. The mud cake is composed of the mud precipitate that is not able to flow into the formation.

Figure. 1.3. Geometry of the cased borehole. There are layers of steel and cement in addition to the infinite formation and the central fluid cylinder. This is the well bonded geometry. The steel and the cement layers are inserted into the borehole so the fluid layer is thinner here than in the open borehole. In the poor bonding situation there is an additional fluid layer between the steel and the cement or between the cement and the formation.

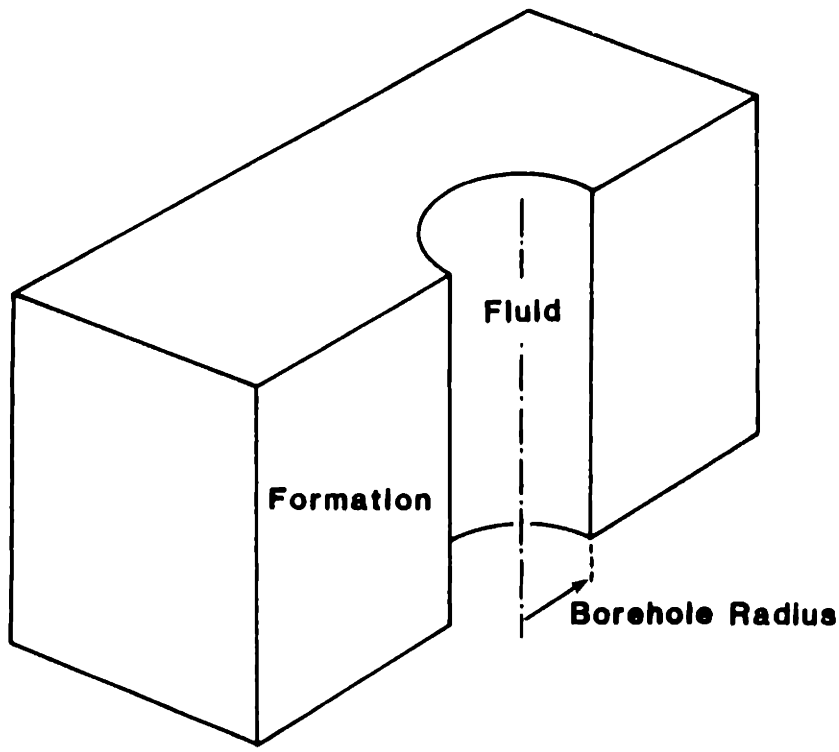

FIG. 1.1

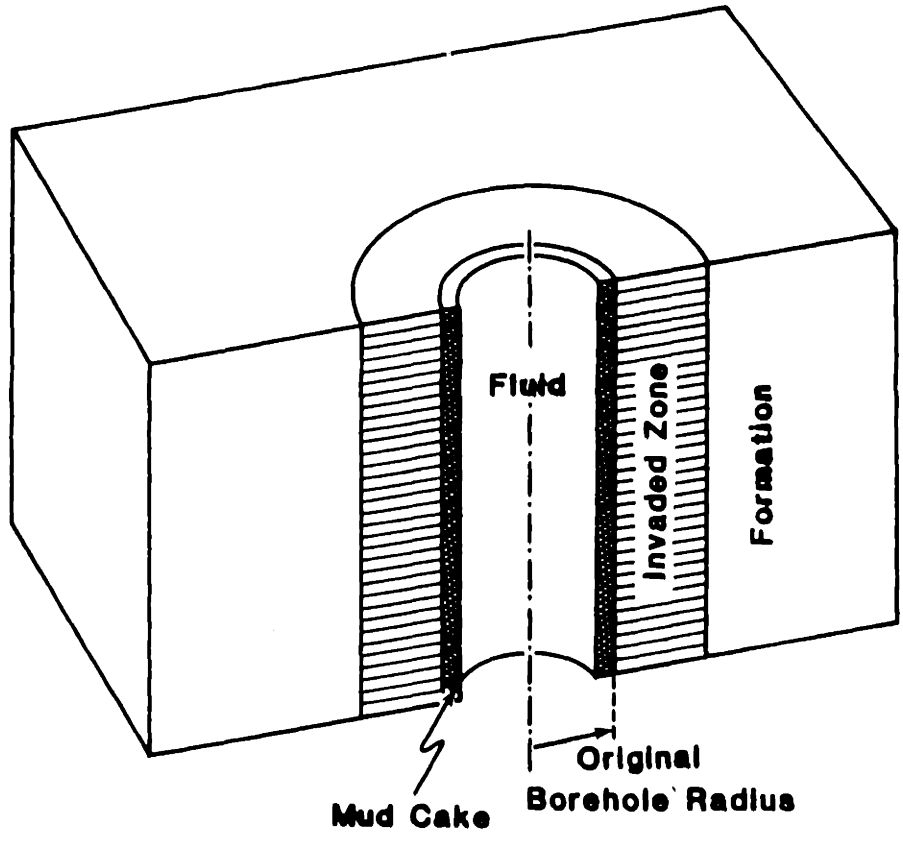
Fluid
Invaded Zone
Formation
Original
Borehole Radius
Mud Cake

FIG. 1.2

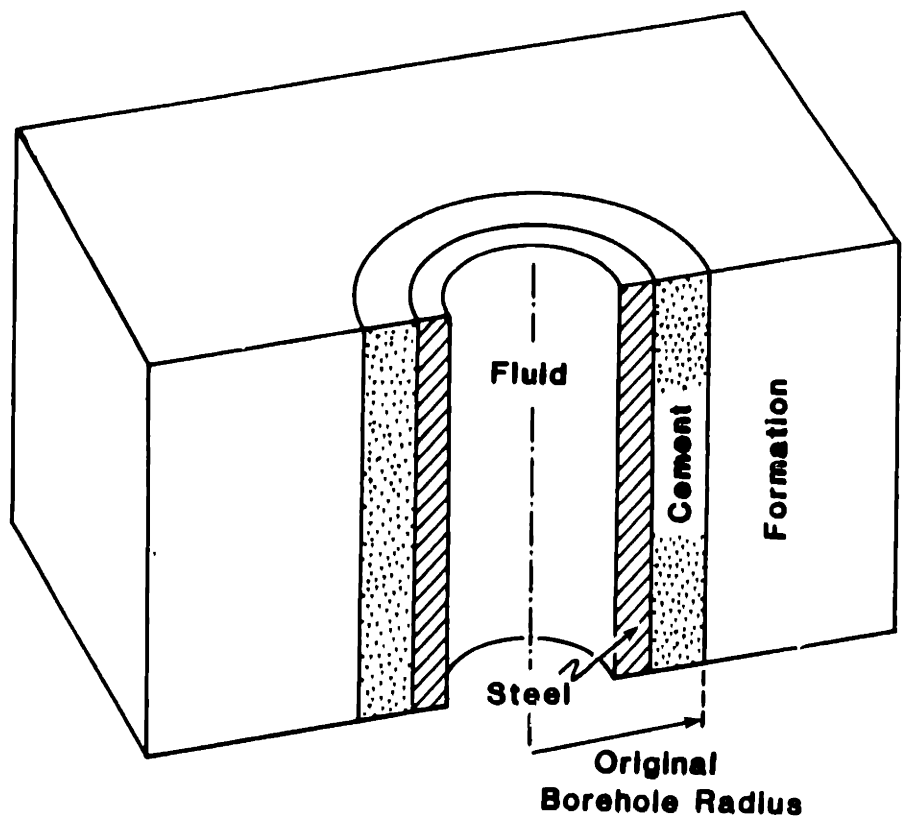

FIG. 1.3

Chapter 2

Theoretical Development

2.1 Introduction

Propagator matrix techniques have frequently been applied to elastic wave problems in global seismology with the flat earth approximation. The situation encountered here is that of radial layers in cylindrical geometries. Rather than a stack of flat layers the problem consists of coaxial annuli. A general formulation is presented for the dispersion characteristics of elastic waves in a fluid-filled cylinder surrounded by an arbitrary number of annuli. The outermost annulus is infinite in extent. There can be any number of intermediate fluid layers in any location. The only restrictions on the model are that the central cylinder is fluid and the infinite outer layer is solid.

A formulation is presented for the calculation of the impulse response for these radially layered geometries. A Thomson-Haskell (Thomson, 1950; Haskell 1953) type propagator matrix is used to relate the displacements and stresses across the layers. The presence of intermediate fluid layers is handled by manual checking at each boundary to see if the next layer is fluid or solid. Expressions are used for each type of interface, (e.g. solid-

fluid, fluid-solid) which match the boundary conditions explicitly. This yields improve speed in the calculation of the frequency-wavenumber information.

The microseismograms generated are complete waveform. They contain all body and guided wave arrivals. The technique used for the calculation of the time series is discrete wavenumber integration (Bouchon and Aki, 1977; Bouchon, 1980). The frequency and wavenumber integrals are discretized and a small imaginary component is added to the frequency in order to move the singularities off the real wavenumber axis.

The pressure response information is calculated and collected for each frequency and wavenumber. The ω and k integrals are then performed via Fast Fourier Transforms. The use of two dimensional Fourier Transforms allows the calculation of microseismograms for multiple source-receiver separations and also yields greatly improved numerical results (over other integration schemes). In addition, the source spectrum, as well as the source-receiver separation, can be specified after the majority of the calculations are completed.

Intrinsic attenuation is included in the calculations through a transformation of the layer velocities to complex parameters (Aki and Richards, 1980). An imaginary part of the velocities is determined to produce spatial decay corresponding to the desired Q value. Q_α and Q_β, the P and S wave quality factors, are specified separately for each layer.

The assumption is that of constant Q, i.e. Q is independent of frequency. The constant Q assumption requires that the velocities be dispersive in order to maintain causality (Futterman, 1962).

2.2 Dispersion Relation

The geometry of the model consists of an arbitrary number of coaxial annuli surrounding a fluid cylinder. The n^{th} annulus has an inner radius of r_{n-1} and an outer radius of r_n (Figure 2.1). The outermost layer is infinite in extent.

Assuming axial symmetry, the wave equations for a given layer n are:

$$\frac{\partial^2 \varphi_n}{\partial r^2} + \frac{1}{r}\frac{\partial \varphi_n}{\partial r} + \frac{\partial^2 \varphi_n}{\partial z^2} = \frac{1}{\alpha_n^2}\frac{\partial^2 \varphi_n}{\partial t^2} \tag{2.1a}$$

and

$$\frac{\partial^2 \psi_n}{\partial r^2} + \frac{1}{r}\frac{\partial \psi_n}{\partial r} - \frac{\psi_n}{r^2} + \frac{\partial^2 \psi_n}{\partial z^2} = \frac{1}{\beta_n^2}\frac{\partial^2 \psi_n}{\partial t^2} \tag{2.1b}$$

α_n and β_n are the compressional and shear wave velocities, respectively. φ_n is the scalar potential and ψ_n is the azimuthal component of the vector potential, the only non-zero component of the vector potential because of the axial symmetry.

The general solutions to these equations for source and receiver on the $r=0$ axis are:

$$\varphi_n = \left[A_n K_0(l_n r) + A'_n I_0(l_n r)\right] e^{ik(z-ct)} \tag{2.2a}$$

and

$$\psi_n = \left[B_n K_1(m_n r) + B'_n I_1(m_n r)\right] e^{ik(z-ct)} \tag{2.2b}$$

where I_i and K_i are the i^{th} order modified Bessel functions of the first and second kind, c is the phase velocity, z the source-receiver separation, and k the axial component of the wave number. A_n, A'_n, B_n, and B'_n are constants corresponding to the outgoing (A_n and B_n) and incoming (A'_n and B'_n) waves, and l_n and m_n are the radial components of the P and S wave numbers. l_n and m_n are given by:

$$l_n^2 = k^2\left(1 - \frac{c^2}{\alpha_n^2}\right) \tag{2.3a}$$

and

$$m_n^2 = k^2\left(1 - \frac{c^2}{\beta_n^2}\right) \tag{2.3b}$$

The radial and axial displacements, u_n and v_n, are given by:

$$u_n = \frac{\partial \varphi_n}{\partial r} - \frac{\partial \psi_n}{\partial z} \tag{2.4a}$$

$$v_n = \frac{\partial \varphi_n}{\partial z} + \frac{\partial\left[r\,\psi_n\right]}{r\,\partial r} \tag{2.4b}$$

The normal and tangential stresses, σ_n and τ_n are given by:

$$\sigma_n = \rho_n \left(\frac{\nu_n}{1-\nu_n} \right) \frac{\partial^2 \varphi_n}{\partial t^2} + 2\mu_n \left(\frac{\partial^2 \varphi_n}{\partial r^2} - \frac{\partial^2 \psi_n}{\partial r \, \partial z} \right) \tag{2.4c}$$

$$\tau_n = \rho_n \frac{\partial^2 \psi_n}{\partial t^2} + 2\mu_n \left(\frac{\partial^2 \varphi_n}{\partial r \, \partial z} - \frac{\partial^2 \psi_n}{\partial z^2} \right) \tag{2.4d}$$

where ρ_n, ν_n, and μ_n are the density, Poisson's ratio, and shear modulus for layer n.

We define the displacement-stress vector for layer n, $\mathbf{u}_n$ as:

$$\mathbf{u}_n = \begin{pmatrix} u_n \\ -iv_n \\ \sigma_n \\ -i\tau_n \end{pmatrix} \tag{2.5}$$

Substituting the forms for φ_n and ψ_n from equation (2.2) into equations (2.4a-d) yields more explicit relationships between the displacements and stresses, and the potentials. By equating terms for each constant, the expressions can be combined into the form:

$$\mathbf{u}_n(r) = \mathbf{D}_n(r)\mathbf{a}_n \tag{2.6}$$

where

$$\mathbf{a}_n = \begin{pmatrix} A_n \\ A'_n \\ iB_n \\ iB'_n \end{pmatrix}$$

and the elements of the **D** matrix are:

$$\mathbf{D}_{n_{11}}(r) = -l_n K_1(l_n r)$$

$$\mathbf{D}_{n_{12}}(r) = l_n I_1(l_n r)$$

$$\mathbf{D}_{n_{13}}(r) = -kK_1(m_n r)$$

$$\mathbf{D}_{n_{14}}(r) = -kI_1(m_n r)$$

$$\mathbf{D}_{n_{21}}(r) = kK_0(l_n r)$$

$$\mathbf{D}_{n_{22}}(r) = kI_0(l_n r)$$

$$\mathbf{D}_{n_{23}}(r) = m_n K_0(m_n r)$$

$$\mathbf{D}_{n_{24}}(r) = -m_n I_0(m_n r)$$

$$\mathbf{D}_{n_{31}}(r) = \rho_n k^2(2\beta_n^2 - c^2)K_0(l_n r) + 2\rho_n \beta_n^2 \frac{l_n}{r} K_1(l_n r)$$

$$\mathbf{D}_{n_{32}}(r) = \rho_n k^2(2\beta_n^2 - c^2)I_0(l_n r) - 2\rho_n \beta_n^2 \frac{l_n}{r} I_1(l_n r)$$

$$\mathbf{D}_{n_{33}}(r) = 2\rho_n \beta_n^2 k m_n \left[K_0(m_n r) + \frac{1}{m_n r} K_1(m_n r)\right]$$

$$\mathbf{D}_{n_{34}}(r) = -2\rho_n \beta_n^2 k m_n \left[I_0(m_n r) - \frac{1}{m_n r} I_1(m_n r)\right]$$

$$\mathbf{D}_{n_{41}}(r) = -2\rho_n \beta_n^2 k l_n K_1(l_n r)$$

$$\mathbf{D}_{n_{42}}(r) = 2\rho_n \beta_n^2 k l_n I_1(l_n r)$$

$$\mathbf{D}_{n_{43}}(r) = -\rho_n k^2 (2\beta_n^2 - c^2) K_1(m_n r)$$

$$\mathbf{D}_{n_{44}}(r) = -\rho_n k^2 (2\beta_n^2 - c^2) I_1(m_n r)$$

We now have expressions for displacements and stresses of layer n in terms of the potentials for that layer. It is necessary to relate the displacements and stresses in all the layers from the infinite outer annulus to the central fluid cylinder. For simplicity, we first assume that all the layers are solids (except, of course, for the central cylinder).

The n^{th} layer has an outer radius of r_n and an inner radius of r_{n-1}, so, using equation (2.6) at the outer radius

$$\mathbf{u}_n(r_n) = \mathbf{D}_n(r_n)\mathbf{a}_n \tag{2.7a}$$

and at the inner radius

$$\mathbf{u}_n(r_{n-1}) = \mathbf{D}_n(r_{n-1})\mathbf{a}_n \tag{2.7b}$$

or

$$\mathbf{a}_n = \mathbf{D}_n^{-1}(r_{n-1})\mathbf{u}_n(r_{n-1}) \tag{2.7c}$$

The displacement-stress vector $\mathbf{u}_n(r)$ can then be related across the layer by combining equations (2.7a) and (2.7c)

$$\mathbf{u}_n(r_n) = \mathbf{D}_n(r_n)\mathbf{D}_n^{-1}(r_{n-1})\mathbf{u}_n(r_{n-1}) \tag{2.8a}$$

This can be written as

$$\mathbf{u}_n(r_n) = \mathbf{E}_n(r_n, r_{n-1})\mathbf{u}_n(r_{n-1}) \tag{2.8b}$$

For the infinite, outermost layer, N, equation (2.7b) gives

$$\mathbf{u}_N(r_{N-1}) = \mathbf{D}_N(r_{N-1})\mathbf{a}_N$$

Since displacements and stresses are continuous across the solid layer boundaries:

$$\mathbf{u}_N(r_{N-1}) = \mathbf{E}_{N-1}(r_{N-1}, r_{N-2})\mathbf{E}_{N-2}(r_{N-2}, r_{N-3}) \cdots \mathbf{E}_2(r_2, r_1)\mathbf{u}_2(r_1)$$

or, defining a matrix **G**

$$\mathbf{G}\mathbf{a}_N = \mathbf{u}_2(r_1) \tag{2.9}$$

where

$$\mathbf{G} = \mathbf{E}_2^{-1}(r_2, r_1) \cdots \mathbf{E}_{N-1}^{-1}(r_{N-1}, r_{N-2})\mathbf{D}_N(r_{N-1})$$

The matrix **G** gives the relationship between the potentials in the outer layer and the displacements and stressed at the first boundary. The particular radiation and boundary conditions are applied to complete this relationship.

In the outermost layer, the radiation condition requires that there are no incoming waves, so $A'_N = B'_N = 0$ and

$$\mathbf{a}_N = \begin{pmatrix} A_N \\ 0 \\ iB_N \\ 0 \end{pmatrix}$$

The requirement that the displacement and stress remain finite at $r = 0$ eliminates the K_0 and K_1 terms of the solutions in the central fluid cylinder ($A_1 = B_1 = 0$); and in a fluid, there is no vector potential so $B_1' = 0$. The displacement and stresses in the central fluid layer (at the outer radius of this layer, r_1) can thus be written as

$$\mathbf{u}_1(r_1) = \begin{bmatrix} u_1(r_1) \\ v_1(r_1) \\ \sigma_1(r_1) \\ \tau_1(r_1) \end{bmatrix} = \begin{bmatrix} D_{12}A'_1 \\ D_{22}A'_1 \\ D_{32}A'_1 \\ 0 \end{bmatrix} = \begin{bmatrix} l_1 I_1(l_1 r_1) \\ k I_1(l_n r) \\ -\rho_1 k^2 c^2 I_0(l_1 r_1) \\ 0 \end{bmatrix} A'_1 \qquad (2.10)$$

At $r = r_1$, the interface between the central fluid and the solid annulus, the radial displacement and stress are continuous; the axial displacement is discontinuous, and the tangential stress vanishes. Equating $\mathbf{u}_2(r_1)$ to $\mathbf{u}_1(r_1)$ and imposing these boundary conditions by using the proper terms of equations (2.9) and (2.10) and rearranging yields:

$$\begin{bmatrix} l_1 I_1(l_1 r_1) & -\mathbf{G}_{11} & -\mathbf{G}_{13} \\ -\rho_1 k^2 c^2 I_0(l_1 r_1) & -\mathbf{G}_{31} & -\mathbf{G}_{33} \\ 0 & \mathbf{G}_{41} & \mathbf{G}_{43} \end{bmatrix} \begin{bmatrix} A'_1 \\ A_N \\ iB_N \end{bmatrix} = 0 \qquad (2.11)$$

This is the period equation for waves traveling in a borehole with solid radial layers. Dispersion relations are obtained by finding values of k and c for which this relation holds true. The rows corresponding to the the axial displacements are not included in the above equation because they are discontinuous and can not be equated across the fluid-solid boundary.

In the presence of intermediate fluid layers the same formulation is used between the infinite formation and the outermost fluid layer that is used when all the layers are solid. Equation (2.9) cannot be extended to relate the displacement-stress vector across all the layers because not all components of the displacement-stress vector are continuous at a solid-fluid boundary. At the outermost fluid layer, the boundary conditions change and so the displacements and stresses can not be related across the boundaries in the same manner as before. The normal displacement, u, and normal stress, σ, are continuous. The tangential stress, τ, vanishes at the boundary. The tangential displacement, v, is discontinuous because the solid and fluid are free to slip along the interface.

The G matrix we have now can relate the displacement-stress vector inward only until the outermost fluid layer (layer f) (see Figure 2.2). At that point the axial displacement is no longer continuous. We now have

$$\mathbf{G}\mathbf{a}_N = \mathbf{u}_{f+1}(r_f) \tag{2.12}$$

where r_f is the outer radius of layer f and $\mathbf{u}_{f+1}$ is the displacement-stress vector in layer $f+1$.

Inside layer f, each boundary is handled individually to allow for general geometries. Details of these calculations are given in the appendix. Starting at the center and working out to layer f, the constants for each layer n, ($\mathbf{a}_n$), are written in terms of $\mathbf{a}_1$ (which is just A'_1). Each

layer may be either solid or fluid. This requires checking at each boundary to check the type (solid or fluid) of the next layer. The type of boundary determines which components of the displacement-stress vector are continuous. This process yields the displacements and stresses in layer f in terms of those in the central fluid layer. They are then matched to those in the next layer out (layer $f+1$). This completes the relationship from the infinite layer to the central cylinder.

The displacements and stresses have been related from the central fluid cylinder to the outermost fluid layer, (layer f). Application of the above results yields A_f and A'_f in terms of A'_1. These are then used in equation (2.12) to complete the relation of the displacements and stresses from the central fluid cylinder to the outer, infinite formation.

The same radiation conditions exist in the central fluid and the outer formation as in the case of all solid layers. A similar procedure yields a new form for equation (2.11):

$$\begin{bmatrix} u_f(r_f) & -G_{11} & -G_{13} \\ \sigma_f(r_f) & -G_{31} & -G_{33} \\ 0 & G_{41} & G_{43} \end{bmatrix} \begin{bmatrix} A'_1 \\ A_N \\ iB_N \end{bmatrix} = 0 \qquad (2.13)$$

This is a more general relation than the one previously obtained. When all the layers are solid, $f=1$ and this yields equation (2.11) again.

2.3 Calculation of Synthetic Microseismograms

In the calculation of synthetic microseismograms, the pressure response, P, inside the borehole is desired. In the time domain it is given by (Tsang and Rader, 1979; Cheng et al., 1982):

$$P(r,z,t) = \int_{-\infty}^{\infty} X(\omega) e^{-i\omega t} d\omega \int_{-\infty}^{\infty} A'_1 I_0(l_1 r) e^{ikz} dk \qquad (2.14)$$

$P(r,z,t)$ is the pressure response, z the source-receiver separation, t time, and $X(\omega)$ the source spectrum. A'_1 is the only non-zero constant associated with the potentials in the fluid layer. To determine A'_1, a boundary condition is imposed at the borehole wall, r_1 . The specific condition is an expression for a $K_0(l_1 r)$ source in the frequency-wavenumber domain. This represents a point isotropic source on the borehole axis. This $K_0(l_1 r)$ source is analogous to the $H_0^{(1)}(l_1 r)$ type of source used by Tsang and Rader (1979). The source terms transform the dispersion relation into an inhomogeneous set of equations. Following the development above for the dispersion relations and then solving for A'_1 yields:

$$A'_1 = \frac{l_1 K_1(l_1 r_1) F_1 - \rho_1 k^2 c^2 K_0(l_1 r_1) F_2}{l_1 I_1(l_1 r_1) F_1 + \rho_1 k^2 c^2 I_0(l_1 r_1) F_2} \qquad (2.15)$$

where

$$F_1 = G_{33} G_{41} - G_{31} G_{43}$$

and

$$F_2 = G_{13}G_{14} - G_{11}G_{34}$$

This is the specific form for the case of all solid annuli. The constant terms associated with the F_i's will vary depending upon the exact geometry. The direct excitation resulting from the $K_0(l_1 r)$ source is added to the response function to give the total pressure field.

The actual calculation of the double integration is performed via the use of Fast Fourier Transforms. This provides efficient and accurate evaluation of the integrals. One implication of the discretization in time and space is the possibility for temporal and spatial wraparound. The integration interval Δk is equivalent to an infinite distribution of imaginary sources along the z-axis separated by a distance $L = \frac{2\pi}{\Delta k}$. Δk and $\Delta\omega$ must be chosen in order to avoid spatial and temporal wraparound. Δk must be chosen so that L is large enough that the first arrival from an imaginary source is much later than the last arrival from the true source (Bouchon and Aki, 1977; Bouchon, 1980).

When determining the ω and k information that will be used in the integration, it is necessary to move the singularities off the real-k axis. This is accomplished by adding a small imaginary component ω_i to the frequency ω (White and Zechman, 1968; Bouchon and Aki, 1977). This moves the singularities off the axis a distance $\frac{\omega_i}{v}$ (Tsang and Rader, 1979). One side effect of the move off the axis is the introduction of attenuation.

Because the distance from the axis that the poles are moved is inversely related to the velocity, the later arrivals are attenuated more than the early arrivals. This causes the tail of the time series to decay more rapidly and aids in the prevention of spatial wraparound. The time domain waveform is multiplied by $e^{\omega_i t}$ in order to remove the effects of this artificial attenuation. It is desirable to have ω_i small to avoid having any numerical noise increased substantially by the exponential multiplication.

Other numerical considerations are also important. A significant portion of the calculation is the determination of the Bessel functions. These are calculated accurately and quickly with a variety of methods. I_0 and I_1 are found using recurrence relations (Abramowitz and Stegun, 1964). Either ascending series or asymptotic series representations are used to calculate K_0, depending on the argument. For improved speed, K_1 is derived by using the other three functions in the Wronskian. Waveforms and $w-k$ information generated with the software developed for this study were repeatedly checked for numerical stability and accuracy. For simple geometries, comparisons were made with results obtained with the method of Cheng and Toksöz (1981). Further details of numerical considerations are given in Appendix B.

Up to this point, all calculations have assumed that the medium is totally elastic, i.e., that there is no amplitude loss except for geometrical factors. Intrinsic attenuation can have a significant effect on the

waveforms, especially in this situation where different layers are involved. Each layer can have different quality factors, Q. In a cased hole the Q value of the steel casing can be orders of magnitude larger than that of the other layers.

Attenuation is incorporated into the calculations through a transformation of the layer velocities to complex parameters. Imaginary components of velocity are determined from the desired Q_n values and are added to the elastic velocities. It is these imaginary parts of the velocities that introduce an exponential spatial decay into the waveform. Given a wave traveling in the z direction:

$$U(z,t) = U_0 e^{i(kz-\omega t)}$$

it is desired to add spatial decay so that

$$U(z,t) = U_0 e^{-\alpha z} e^{i(kz-\omega t)}$$

Defining the attenuation coefficient $\alpha = \frac{\omega}{2cQ}$ the necessary transformation is:

$$\frac{1}{c} \rightarrow \frac{1}{c_0}\left(1+\frac{i}{2Q}\right).$$

In this manner a different Q value can be assigned for compressional (Q_{α_n}) and shear (Q_{β_n}) waves in each layer. Q is assumed to be constant (Futterman, 1962), i.e., attenuation is proportional to frequency. In the present form, this wave does not satisfy causality (Aki and Richards, 1980).

To maintain causality with the constant Q assumption, the real part of the layer velocities must be modified by introducing velocity dispersion (Azimi et al., 1968; Kjartansson, 1979).

$$c \rightarrow c_0\left(1+\frac{1}{\pi Q}\log\left(\frac{\omega}{\omega_{ref}}\right)\right).$$

The phase velocities are then dependent on frequency and are equal to the elastic velocities only at some reference frequency ω_{ref}. The total transformation for the complex velocities is:

$$c_n(\omega) = c_n(\omega_{ref})\left[1+\frac{1}{\pi Q_n}\log\left(\frac{\omega}{\omega_{ref}}\right)-\frac{i}{2Q_n}\right] \qquad (2.16)$$

where $c_n(\omega)$ is the complex velocity, $c_n(\omega_{ref})$ the phase velocity at the reference frequency, and Q_n the specified quality factor (Aki and Richards, 1980). The compressional and shear velocities for each layer are modified with equation (2.16) using either α_n or β_n for $c_n(\omega_{ref})$ along with the appropriate Q_{α_n} or Q_{β_n}.

2.4 Calculation of Displacements

Displacements u_n and v_n, and stresses σ_n and τ_n can be calculated by determining the constants A_n, A'_n, B_n, and B'_n. These constants determine the potentials (equation 2.2) which are substituted into the definitions of displacements and stresses in cylindrical coordinates (equations 2.4).

The period equation (equation 2.13) is a relationship with three equations and three unknowns: A'_1, A_N, and B_N. One of these constants, A'_1, has already been determined (equation 2.15). Using this information in equation (2.13), we can solve for the other two constants A_N, and B_N. In this manner, the constants for all remaining layers can also be determined. The essence of the technique used above to find the period equation is just finding a relationship between the displacements and stresses and the potentials in all the layers. This same relationship can be used to find the constants since the displacements and stresses are related by equation (2.6). In calculating displacements and stresses, the exponential factor $e^{ik(z-ct)}$ is not needed. It is the maximum value that is of interest.

Figure Captions

Figure 2.1. Geometry of the model. Layer n has an outer radius of r_n and an inner radius of r_{n-1}.

Figure 2.2. Geometry including intermediate fluid layers. The outermost fluid layer is layer f. There can be any number of fluid locations in any location. The only restrictions are that the outermost layer (the infinite formation) is solid, and the central cylinder (the borehole itself) is fluid.

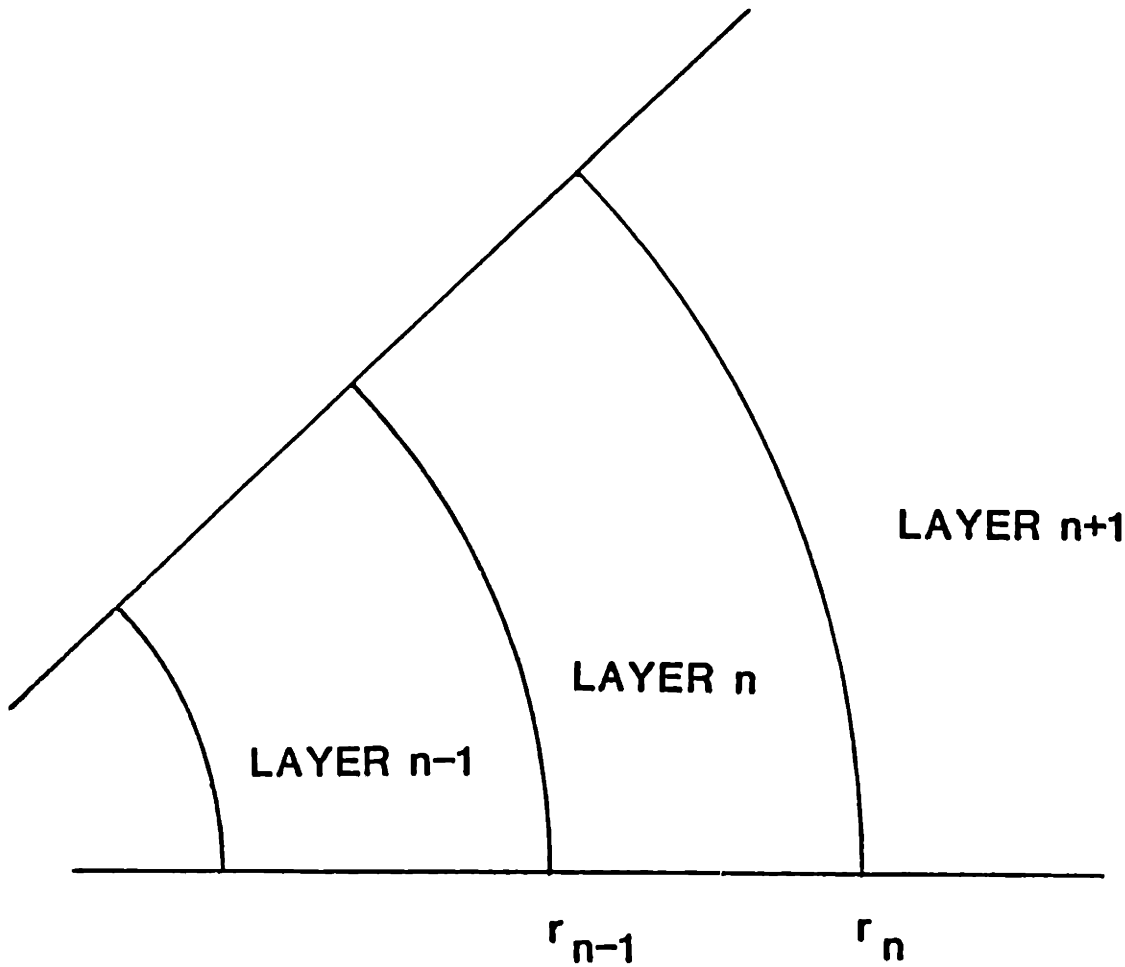

FIG. 2.1

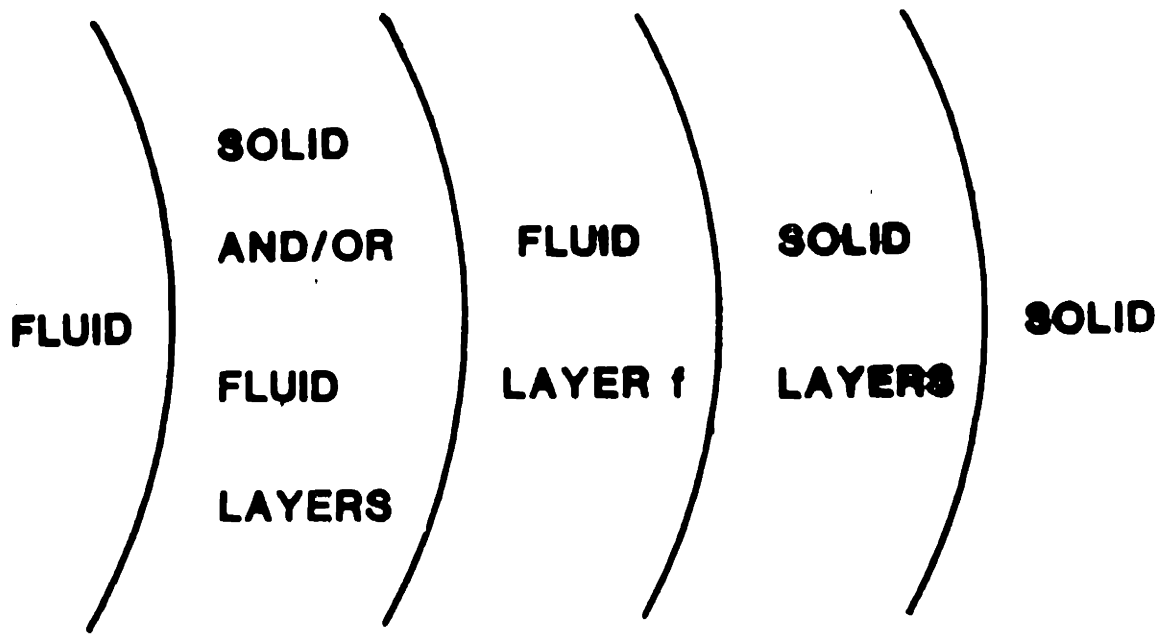
FLUID
SOLID
AND/OR
FLUID
LAYERS
FLUID
LAYER 1
SOLID
LAYERS
SOLID

FIG. 2.2

Chapter 3

Well Bonded Cased Boreholes

3.1 Introduction

Casing is set into a borehole after the logging and formation analysis has been completed. The borehole environment can change during the time that the hole is not cased. Formations can cave in causing irregularities in the wall or even closing off the hole. The casing also seals the borehole wall, preventing possible communication between different stratigraphic layers. It is desirable to set the casing as soon as possible to avoid these problems. Aside from cement evaluation purposes, little effort has been made to study acoustic logs in the presence of casing. Acoustic logs are not run routinely in cased holes. The ability to do so would allow the casing to be set before these logs are run. It would also be useful for examining sections of existing holes that already have casing in place.

The effects of adding a casing to the borehole environment are studied in this chapter. The geometry of a cased hole consists of layers of steel and cement in addition to the infinite formation and the central fluid cylinder (see Figure 3.1). All boundaries are treated as welded contacts therefore the assumption is that of perfect cement bonding. This would

seem to be unrealistic, but the data indicates that this is often a reasonable assumption. The models are limited to four layers (fluid, steel, cement, and formation) to avoid the extra complications of invaded or damaged zones. Adding these additional layers would complicate the models so that it is not possible to understand the effects of the casing only.

Generally only one parameter of the casing, cement, or formation is modified with each model in an attempt to isolate the effects of that particular parameter. Some model parameters are held constant throughout. The parameters of the central fluid layer are not investigated here and so are not changed. Other layers are given standard values and different models are perturbations away from that standard.

The source function is basically the same as that given by Tsang and Rader (1979). The center frequency used here is 13 kHz except where specified otherwise. The Tsang and Rader source has a problem with unreasonably large amplitudes at very low frequencies. A bandpass filter is used to limit the frequency content between approximately 5 kHz and 18 kHz. This eliminates the problems at low frequency but it introduces another problem of slightly non-causal arrivals. These arrivals manifest themselves as a ringing at the beginning of the first arrivals. They give the P-wave packet an emergent rather than an impulsive appearance. This problem is not seen in all models. It is rarely seen in the well bonded

models of this chapter, but it is prominent with unbonded casing (the next chapter). It is never a limitation on the analysis.

The borehole radius is 4 inches in most models. This is the radius that is the result of the drilling, not the outer radius of the fluid cylinder. The steel casing and the cement are treated as being inserted into a hole of this size so the fluid layer has a radius that is less than 4 inches. The thickness of the steel tube is 0.4 inches except where stated otherwise.

3.2 General Effects Of Casing On Waveform Character

The presence of a casing in a borehole can have a large influence on recorded waveforms. Figure 3.2 shows a synthetic microseismogram for the case of a simple formation in an open hole. The microseismogram that results when a casing (steel and cement) is inserted into the same hole is shown in Figure 3.3. Cheng and Toksöz (1981) showed that the frequency range over which the pseudo-Rayleigh wave modes are excited depends on the radius of the fluid layer. A smaller radius shifts dispersion curves to higher frequencies. This effect is clearly seen in Figure 3.4. Part of the fluid layer of the open hole geometry has been replaced by steel and cement layers in the cased hole. The pseudo-Rayleigh waves require higher frequencies to be excited because of the thinner fluid layer. The source function remains constant, however, so the pseudo-Rayleigh waves are excited to a lesser extent than when there was a thicker layer of fluid. The result is that the waveform for the cased hole has a lower apparent

frequency content as the Stoneley wave becomes more dominant, and the pseudo-Rayleigh wave contribution decreases. A microseismogram generated for the case of a simple formation in a hole with the same diameter as the steel tube displays the same shift in frequency content (see Figure 3.5).

The amplitude of the body waves are observed to be less in the cased hole versus the open hole situation while the guided waves have larger amplitudes. There is a smaller contrast between the cement and the formation (in the cased hole) than between the fluid and the formation (in the open hole). This decrease in velocity contrast results in less energy in the P-wave. Figures 3.2 and 3.3 demonstrate this point. The guided wave amplitudes can increase as the waveguide becomes more efficient. (The outside of the borehole changes from some formation to very fast and rigid steel.) The degree of this effect depends on the nature of the formation. In a slow formation there will be a large change in the amplitude while in a fast formation the change will be minimal. Figure 3.6 shows data recorded in a section where the tool passes from an open hole section into casing. The source-receiver separation is 4.57 m (15 ft). A large decrease in the P-wave amplitude and increase in the Stoneley amplitude is observed as the tool crosses into the cased section. The formation in this section of the well is slow (P-wave velocity of approximately 2.29 km/s (7.5 ft/ms) so it is possible that the cement has velocities close to those of the formation. This causes much less energy to be contained in the P-wave packet. While

there was only an intermittent Stoneley wave presence in the open hole, there is a consistent, well defined Stoneley wave in the cased portion of the section. This can also be seen in Figure 3.7. The presence of the casing improves the efficiency of the waveguide considerably. Figures 3.7a and 3.7b are data recorded in an open borehole at offsets of 4.57 m (15 ft) and 6.1 m (20 ft). The formation is an unconsolidate sandstone similar to that in Figure 3.6. Data from the same section of the well with the casing in place is shown in Figures 3.7c and 3.7d. Figures 3.8a and 3.8b show the amplitude of the spectrum for a synthetic model of a "slow" formation in an open hole and a cased hole. In the open hole (Figure 3.8a) the Stoneley wave is small. The P-wave is the arrival with the largest amplitude. The casing (Figure 3.8b) results in greatly increased Stoneley wave amplitudes. The decrease in the P-wave amplitude discussed above is also clear.

In some situations the presence of a casing can make the waveform far more complex than in the corresponding open hole. The formation used in the calculation of the synthetic microseismograms in Figure 3.9 has velocities comparable to those of the steel. The result is a considerable amount of ringing in the waveform. This ringing obscures the formation shear arrivals. The shear arrival can be identified as a slight phase shift can be seen in the ringing portion of the microseismograms. This identification would be extremely difficult, if not impossible in actual data. The steel and formation are fast layers on either side of the slow cement layer. It is interesting to note that, for the ringing portion of the time

series, the thickness of the cement layer is one quarter of the dominant wavelength. The particular source frequency and geometry chosen here appear to cause some sort of resonance effect in this layer. The ringing can be changed by using a different source function (Figure 3.9b). This type of resonance can explain some observed P-wave arrivals that have longer durations in a cased hole versus the corresponding arrivals in an open hole (Willis, 1984, personal communication).

3.3 Effects on Arrival Times

Figure 3.10 shows the first arrivals for the same formation in both an open hole and a cased hole. The P-wave arrivals are somewhat earlier in the cased hole geometry relative to the open hole geometry. The faster velocity steel and cement have replaced the slow fluid for a portion of the wave path. The section of the wave path through the steel and cement is mostly radial so the resulting time difference is independent of source-receiver separation, and the moveout between two receivers at different distances is unaffected.

To confirm that the formation arrivals were picked correctly and were not being confused with some casing arrival, a number of examples were calculated using the same casing but with different formations. In each case, the arrivals were determined to be those from the formation.

Phase velocities were determined by calculating the moveout between corresponding arrivals for the same formation at many offsets. Figures 3.11 and 3.12 give two examples. Open hole and cased hole microseismograms are shown for offsets ranging from 3.05 m (10 ft) to 4.57 m (15 ft) at .15 m (.5 ft) intervals. Arrivals are easily traced from one offset to the next allowing for good velocity calculations. Amplitude and time scales were enlarged as needed for higher resolution.

Figure 3.13 shows the synthetic microseismogram for a formation that is similar to that in Figure 3.12 but has a different compressional wave velocity. The two waveforms are almost identical except for the P-wave arrival time. This arrival, for the case shown in Figure 3.12, is slightly later since the velocity has been lowered from 4.88 km/s (16 ft/ms) to 4 km/s (13.12 ft/ms). The amplitude of the P-wave packet is also different but this is a result of the change in Poisson's ratio. The P-wave velocity was lowered while the S-wave velocity was held constant so the Poisson's ratio of the formation has decreased. This same variation of the amplitude of the P-wave packet with Possion's ratio has been demonstrated in open holes as well (Cheng and Toksöz, 1981; Zhang and Cheng, 1984).

Similar results are obtained by holding the compressional velocity constant while the shear velocity is varied. The formation used to generate the microseismogram of Figure 3.14 has the same P velocity but lower S velocity than that used for Figure 3.10. Except for amplitude differences

resulting from the different Poisson's ratio, the P-wave arrivals overlay. The shear wave arrival is delayed by the expected amount with the lower velocity confirming that the arrival is being correctly identified. In this particular case the pseudo-Rayleigh wave amplitude is significantly reduced. The small contrast between the cement and formation shear velocities shifts the pseudo-Rayleigh cutoff to higher frequencies (see Figure 3.15).

The variation in the P-wave velocities can be seen in the frequency-wavenumber domain also (Figure 3.16). As the formation velocities change, there is an obvious change in the locations of the corresponding peaks.

A much slower formation was used in the calculation of Figure 3.17. The casing in Figure 3.17 has the same parameters as the previous examples, but the compressional wave velocity is now low and the shear wave velocity of the formation is lower than the fluid velocity. While still obvious, the P-wave arrival with this slow formation is small. The contrast between the cement velocity and the formation velocity is slight, so the body waves are not efficiently refracted along the interface. Since the shear velocity in the formation is lower than that in the cement, no shear energy is refracted along the boundary and no pseudo-Rayleigh wave is generated

Field data displays the same ability to observe the formation arrivals in the presence of casing. Figure 3.7 shows data recorded in a slow

formation with and without a casing. The P-wave arrivals track very well in the two cases. Figure 3.18 gives Δt logs of the same sections. The logs were determined by picking the first arrival for the two source-receiver separations of 4.57 m (15 ft) and 6.1 m (20 ft) and calculating the moveout. A depth correction of 2.74 m (9 ft) was made on the cased hole log in order to improve the depth correlation. This helps considerably at the upper depths but some differences in the depth scale become obvious in the lower portion of the log. The agreement between the open hole and the cased hole sections is very good. This confirms that it is the formation arrival that is being observed in the cased hole.

Figures 3.17 and 3.19 demonstrate that, while the effects of the casing on the body wave arrival times are generally small, the effects on the guided waves are significant. The two sets of microseismograms (Figures 3.17 and 3.19) were both calculated with the same slow formation parameters. Figure 3.17 includes the same casing as the previous figures. The Stoneley wave arrives much earlier in the presence of the casing (Figure 3.17) than in the open hole (Figure 3.19). This can bee seen also in the data shown in Figure 3.7. If the cement has lower velocities than the formation (as could be the case in a hard formation) the Stoneley wave velocity can be less in the cased hole. This is clear in the dispersion curves in Figure 3.4. The wave train is also more dispersive in the cased hole. This result was expected from the nature of the dispersion curves (Cheng et al., 1981, Schoenberg et al., 1981). It is apparent that the steel and the

cement must have a strong influence on the Stoneley waves to cause this decrease in the arrival time.

A comparison of Figures 3.12 and 3.17 shows that the casing has in fact, the dominant effect on the Stoneley waves. The formation parameters are very different for the two models but the Stoneley wave arrival times are quite similar. Figures 3.13 and 3.14 were calculated using formations that are intermediate in velocity to those in Figures 3.12 and 3.17. Here again it appears that the Stoneley wave arrival time appears to be almost independent of formation velocities. The phase velocity dispersion curves for the models of Figures 3.12, 3.14, and 3.17 are given in Figure 3.15. There is little change in the Stoneley wave velocity with different formation velocities. At higher frequencies, the pseudo-Rayleigh velocities are also very similar. Near the cutoff frequencies for the various modes though, there is a substantial difference in the pseudo-Rayleigh velocities and the shapes of the curves for different formations. This explains the ability to determine the shear velocity of the formation despite the presence of the casing. The shear arrival is of extremely small amplitude and so it is usually taken to be just the first part of the pseudo-Rayleigh wave packet.

The formation parameters have increasing importance as the thickness of the cement layer decreases, but the casing remains a factor in the guided wave behavior. Figure 3.20 compares the dispersion curves for an open hole with those for the cases where there is no cement and 4.45

cm (1.75 inches) of cement between the steel and the formation. In the absence of cement, the curves are close to those of the open hole. Note that the the pseudo-Rayleigh curves are shifted in frequency because of the differing thickness of the fluid layer. The effect of the thickness of the cement layer can be seen in the time series also. Figure 3.21 shows microseismograms for a model with the same formation and steel parameters as in Figure 3.17. There is no cement layer between the steel and the formation though. Clearly the Stoneley wave velocity is less with no cement than with the 4.45 cm (1.75 inch) layer. The lack of cement allows the formation greater influence on the wave. Since the formation has velocities that are less than those in the cement, the Stoneley wave is slower as the formation has more contribution to its behavior.

The data shown in Figure 3.22 is an example of a situation where the formation exerts a large influence on the Stoneley wave due to a lack of cement between the steel and the formation. This data was recorded in MIT's Burch well in Michigan. A pipe had been inserted but not cemented in the hole. The upper portion of the record displays the characteristics of a free pipe geometry (see chapter 4 of this thesis). At depths beginning at approximately 550 m (1780 ft) the Stoneley wave arrives much later and has a much lower frequency content. An attempt was later made to remove this section of the pipe from the borehole. At this time, it was learned that the formation at this depth is a low velocity shale which had swollen out into the hole and was pressed against the pipe. The formation

is the Bell shale. The geometry that resulted in the observed nature of the data was one in which the steel was effectively bonded to the formation without cement. It is the the cement that limits the formation influence on the Stoneley wave.

Although the Stoneley wave was relatively insensitive to changes in the formation parameters the arrival times can be affected by changing the steel or cement velocities. In Figure 3.23, the cement velocities are increased about forty-five percent above those in Figure 3.12. Here, the Stoneley wave arrivals are noticeably earlier, but the increase in velocity is not on the order of the increase in cement velocity. Similar results are obtained by lowering the steel velocities. The steel and cement velocities both contribute significantly to the Stoneley wave velocity. Increasing the thickness of the steel casing also causes the guided waves to arrive earlier. The layer of steel in Figure 3.24 is doubled relative to the model used for Figure 3.12 to a thickness of 0.8 inches. The hole diameter and inner diameter of the steel remain the same so there is less cement. The thicker layer of steel results in more influence on the Stoneley wave. Steel has replaced some of the cement.

The steel and the cement have only a small effect on the body wave arrival times. Formation velocities can be determined in a well-bonded cased hole with a variety of steel and cement parameters. On the whole, the cemented casing appears to have the predominant influence on the

guided wave portion of the microseismogram. The Stoneley and pseudo-Rayleigh waves are influenced by the combination of the steel casing and the cement, while the formation has a smaller effect depending on the thicknesses of the casing and the cement.

3.4 Effects on Amplitudes

The microseismograms in Figures 3.17 and 3.19 exhibit a reduction in body wave amplitudes in the presence of a casing relative to the open hole. This is true for all formations, although the amount of reduction depends on the formation and cement parameters. The amplitude change is highest when the formation velocities are low. The data shown in Figure 3.6 is from a slow formation. Here there is an obvious reduction in the amplitude of the P-wave as the tool passes from the open hole into the casing.

It is not just a slow formation that yields small formation arrivals. This is a phenomenon that can be seen in other situations also. A fast cement will also result in smaller than expected body wave arrivals. The relationship between the cement and the formation velocities is the important factor. Figure 3.23 shows waveforms that are obtained by taking the model used for Figure 3.12 and increasing the cement velocities. The cement velocities and the formation velocities in this case are close, resulting in a considerable reduction in the body wave amplitudes. The pseudo-Rayleigh wave amplitudes are greatly reduced as well. The cutoff frequencies for these modes are shifted to higher frequencies so they

cannot contribute significantly to the time series. This is a similar effect to that in the case where the hole size is decreased. Figure 3.25 has the same cement but formation velocities that are just below those of the cement. In the presence of noise, it would be difficult to identify the compressional or shear wave arrivals. Attempts to increase the gain so that the P arrivals could be distinguished would result in Stoneley arrivals that were clipped.

Increasing the velocity of the cement has the opposite effect on the Stoneley waves. Their amplitudes increase as the steel and the cement velocities increase. Higher velocities in these layers make the borehole more rigid causing it to be a more efficient waveguide.

The efficiency of the waveguide is also improved by increasing the thickness of the layer of steel. The Stoneley wave amplitudes are significantly higher with a thicker steel casing (Figure 3.24) than with the thinner casing (Figure 3.12).

Q values for the different layers can, as expected, have a large effect on the waveform. The formation Q factors maintain their influence on the body wave arrivals even in the presence of a casing. A comparison of Figures 3.26 and 3.3 makes this apparent. The models for the two figures differ only in the formation Q values. Those used in Figure 3.26 are double the values used in Figure 3.3. The body waves increase in amplitude with the higher Q values. The amount of increase in the cased hole is similar to the increase in amplitudes in an open hole. The casing therefore does not

appear to diminish the influence of the formation Q values on the amplitudes of the body wave arrivals. The guided waves, on the other hand, do not increase in amplitude as much in the cased hole as in the open hole. The casing obscures the effects of the formation Q values on these arrivals. This effect is to be expected since the guided wave attenuation is a linear combination of the body wave attenuations of the different layers (Anderson and Archambeau, 1964; Cheng et al., 1982).

In Figure 3.27 the Q values for the cement have been raised by a factor of two. This is the only change in the model parameters from those in Figure 3.3. Not surprisingly, there is no obvious change in the amplitudes of the body wave arrivals. The portion of the body wave path through the cement is not sufficient to cause any significant decrease in the amount of attenuation. The guided waves are affected however. The pseudo-Rayleigh wave and the Stoneley wave amplitudes are both increased. The low frequency Stoneley wave amplitudes are increased the most, about ten percent.

A change in the Q values for the steel casing also affects the guided wave amplitudes, although this effect is much smaller than for a corresponding change in the cement values. The Q values for the steel are an order of magnitude higher than any of the other Q values in the model. Consequently, the steel has an effectively infinite Q as compared with the other layers. No reasonable change in the steel Q value would change this

relationship, so no noticeable effect on the waveform results from modifications to the steel Q value.

3.5 Summary

The addition of a cemented casing to a borehole can have a dramatic effect on the observed acoustic waveforms. One obvious effect is an apparent lowering of the frequency content of the guided wave portion of the time series. This is a result of the decrease in the thickness of the fluid layer. The change in fluid layer thickness shifts the pseudo-Rayleigh dispersion curves to higher frequencies. A higher frequency source would be required for the same excitation.

The formation body wave arrivals are generally clear and relatively unaffected by the presence of the casing. Both the P-wave and S-wave arrival times are observed to change as the formation compressional and shear velocities are varied individually and simultaneously. In some situations the existence of the steel and the cement can make velocity determination more difficult than in an open hole. The amplitudes of the formation arrivals are greatly reduced if the velocities of the cement are comparable to or larger than the formation velocities. The waves refracted along the casing are generally too small to be observed.

The interface waves, the Stoneley and pseudo-Rayleigh waves, are most significantly affected by the casing. They respond to the combined effects

of the steel, the cement, and the formation.

The steel has a greater influence on the waveforms with increasing thickness but any reasonable change in steel velocity or Q values does not have significant effects.

The cement thickness, velocities, and Q values are all significant contributors to the observed waveform. The velocities and and amplitudes of the guided waves are strongly affected by the cement velocities and attenuation. A thick layer of cement can insulate the guided waves from the formation. The influence of the formation on these waves increases as the thickness of the cement layer decreases.

Figure	thickness cm (inches)	V_p km/s (ft/ms)	V_s km/s (ft/ms)	ρ gm/cm^3	Q_α	Q_β
2,4a,8a,10a 11,19,20a	10.16 (4.00)	1.68 (5.50)	–	1.2	20.	–
21,20b	9.14 (3.60)	1.68 (5.50)	–	1.2	20	–
all others	4.7 (1.85)	1.68 (5.50)	–	1.2	20.	–

Table 3.1. Borehole fluid parameters for theoretical models.

Figure	thickness cm (inches)	V_p km/s (ft/ms)	V_s km/s (ft/ms)	ρ gm/cm^3	Q_α	Q_β
24	2.03 (0.80)	6.1 (20.0)	3.35 (11.00)	7.5	1000.	1000.
3,4b,8b,9 10b,12-17, 20b,c,21, 23,25-27	1.02 (0.40)	6.1 (20.0)	3.35 (11.00)	7.5	1000.	1000.

Table 3.2. Steel parameters for theoretical models.

Figure	thickness cm (inches)	V_p km/s (ft/ms)	V_s km/s (ft/ms)	ρ gm/cm^3	Q_α	Q_β
23,25	4.44 (1.75)	4.11 (13.5)	2.53 (8.30)	1.92	40.	30.
24	3.43 (1.35)	2.82 (9.26)	1.73 (5.67)	1.92	40.	30.
27	4.44 (1.75)	2.82 (9.26)	1.73 (5.67)	1.92	80.	60.
3,4b,8b,9, 10b,12-17, 20c,26	4.44 (1.75)	2.82 (9.26)	1.73 (5.67)	1.92	40.	30.

Table 3.3. Cement parameters for theoretical models.

Figure	thickness cm (inches)	V_p km/s (ft/ms)	V_s km/s (ft/ms)	ρ gm/cm^3	Q_α	Q_β
9	∞	5.94 (19.50)	3.2 (10.5)	2.16	60.	60.
13,16b	∞	4.0 (13.12)	2.6 (8.53)	2.16	60.	60.
8,16d,17, 19,21	∞	2.9 (9.5)	1.52 (5.00)	2.0	100.	50.
7	∞	4.0 (13.12)	2.13 (7.00)	2.16	60.	60.
26	∞	4.88 (16.00)	2.6 (8.53)	2.16	120.	120.
2-5,10-12, 15,16a,20, 23,24,27	∞	4.88 (16.00)	2.6 (8.53)	2.16	60.	60.

Table 3.4. Formation parameters for theoretical models.

Figure Captions

Figure 3.1. Specific layers in the well bonded case hole model. Layers of steel and cement are inserted within the borehole. The radius of the fluid layer is less than in the open borehole situation.

Figure 3.2. Open hole microseismogram. The source-receiver separation is 3.05 m (10 ft.). The amplitude is normalized by an arbitrary factor which is consistent for all single microseismogram figures.

Figure 3.3. Cased hole microseismogram for the same formation as in Figure 3.2.

Figure 3.4. Phase velocity dispersion curves for a) the open hole and b) cased hole geometries. Two Pseudo-Rayleigh modes are shown along with the Stoneley mode for each case. The phase velocities are normalized to the fluid velocity.

Figure 3.5. Open hole microseismogram for the formation of Figure 3.2 with the hole diameter equal to the inner diameter of the casing used in Figure 3.3. The central fluid layer has the same radius as in the cased hole.

Figure 3.6. Data recorded as the tool passes from an open hole hole into a cased section (above 100 ft). The source-receiver separation is 4.57 m (15 ft) and there is one trace every foot.

Figure 3.7. Data recorded in an open hole (3.7a and 3.7b) and the same section after casing is set in place (3.7c and 3.7d). 4.57 m (15 ft) and 6.1 m (20 ft) offsets are shown for each case. The trace spacing is 1 ft. The formation is slow so there is no pseudo-Rayleigh wave present.

Figure 3.8 Magnitude of the synthetic ω–k information for a soft formation in a) an open hole and b) a cased hole.

Figure 3.9 Microseismograms for offsets ranging from 3.05 m (10 ft) to 4.57 m (15 ft) at .15 m (0.5 ft) increments. The formation is has velocities comparable to those of the steel. The source functions are: a) the same as the previous figures. This is an example of how certain combinations of layer thicknesses and source function can result in a waveform that is difficult to interpret. b) a source center frequency of 20 kHz with no filter applied. The shear wave is more obvious with this different source function.

Figure 3.10 P-wave packet for a) open hole and b) cased hole geometries. The P-wave arrival time is slightly earlier in the presence of the casing.

Figure 3.11 Multiple offset microseismograms for the case of a fluid filled cylinder in a homogeneous formation. The vertical scale is the same for all multiple offset figures except where noted otherwise.

Figure 3.12 Multiple offset microseismograms for the same formation as Figure 3.11 in a cased hole.

Figure 3.13 Microseismograms for a formation with a lower P-wave velocity than that Figure 3.12. The S-wave velocity is the same.

Figure 3.14 Microseismograms for a formation with a lower S-wave velocity than that in Figure 3.13. The P-wave velocity is the same.

Figure 3.15 Phase velocity dispersion curves for 3 different formations behind the same casing. Formations are those of a) Figure 3.12 b) Figure 3.14 and c) Figure 3.17. For clarity, only the first pseudo-Rayleigh mode is shown. Note that since one of the formations is slow, there are no unattenuated pseudo-Rayleigh modes for this formation. The phase velocities are normalize to the fluid velocity.

Figure 3.16 Log-power of the synthetic ω–k information for the models of a) Figure 3.12, b) Figure 3.13 c) Figure 3.14 and d) Figure 3.17.

Figure 3.17 Microseismograms for a slow formation in a cased hole.

Figure 3.18 Δt log calculated from the data in Figure 3.7. This is a plot of slowness vs depth.

Figure 3.19 Microseismograms for a slow formation in an open hole. The formation is the same as that in Figure 3.17.

Figure 3.20 Phase velocity dispersion curves for a) open hole b) steel with no cement and c) steel with 4.44 cm (1.75 inches) of cement. Again, only one pseudo-Rayleigh mode is shown. The phase velocities are

normalize to the fluid velocity.

Figure 3.21 Microseismograms for a slow formation with a layer of steel but no cement.

Figure 3.22 Data recorded with the EVA tool in MIT's Burch well. The top of the Bell shale is at approximately 1800 ft. For about 30 m (100 ft) this formation is swollen against the pipe.

Figure 3.23 Microseismograms for a model with higher cement velocities than in Figure 3.12. The higher cement velocities result in smaller formation body wave arrivals and higher cutoff frequencies for the pseudo-Rayleigh waves.

Figure 3.24 Microseismograms for a model with the thickness of the steel doubled to 1.02 cm (0.4 inches) relative to that in Figure 3.12. The hole size is the same so there is less cement than in the previous examples.

Figure 3.25 Microseismograms for model of Figure 3.14 with fast cement velocities. The cement velocities are now higher than those of the formation.

Figure 3.26 Microseismogram for a model that is the same as in Figure 3.3 with the formation Q values doubled.

Figure 3.26 Microseismogram for a model that is the same as in Figure 3.3 with the cement Q values doubled.

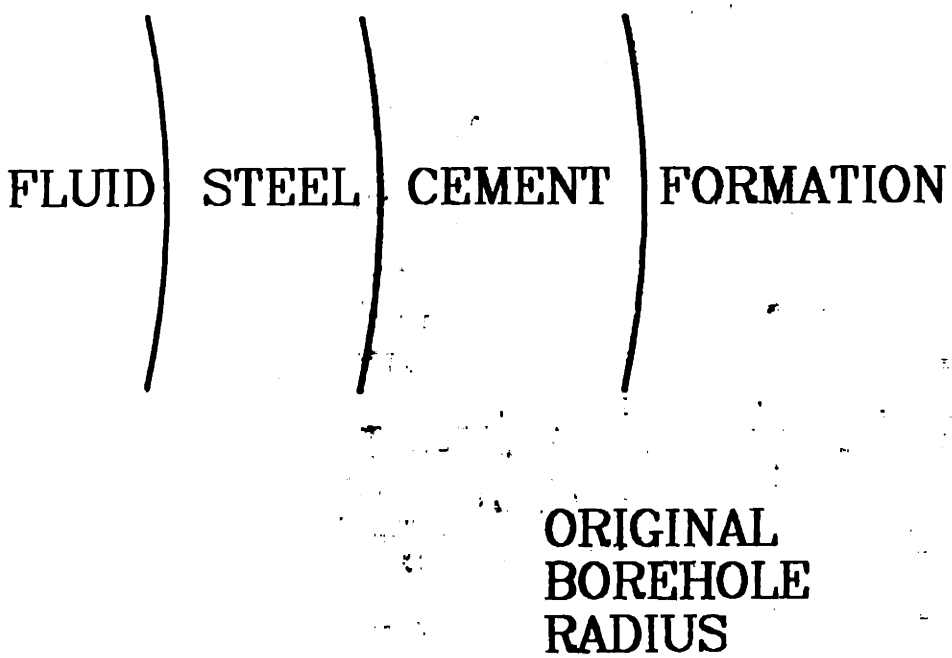

FIG. 3.1

H (FT)	VP (FT/MS)	VS (FT/MS)	RHO (GM/CC)	QP	QS
0.333333	5.5000	0.	1.2000	20.00	0.
0.	16.0000	8.5300	2.1600	60.00	60.00

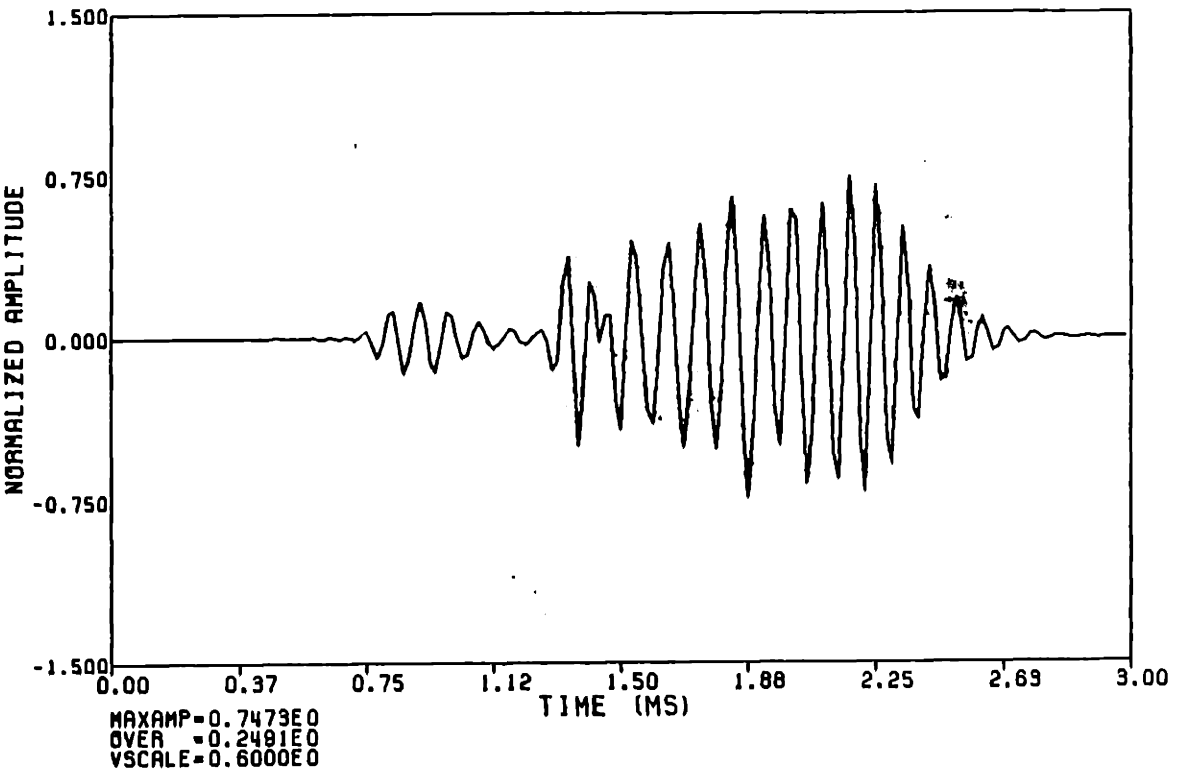

FIG. 3.2

R (FT)	VP (FT/MS)	VS (FT/MS)	RHO (GM/CC)	QP	QS
0.154167	5.5000	0.	1.2000	20.00	0.
0.187500	20.0000	11.0000	7.5000	1000.00	1000.00
0.333333	9.2590	5.6700	1.9200	40.00	30.00
0.	16.0000	8.5900	2.1600	60.00	60.00

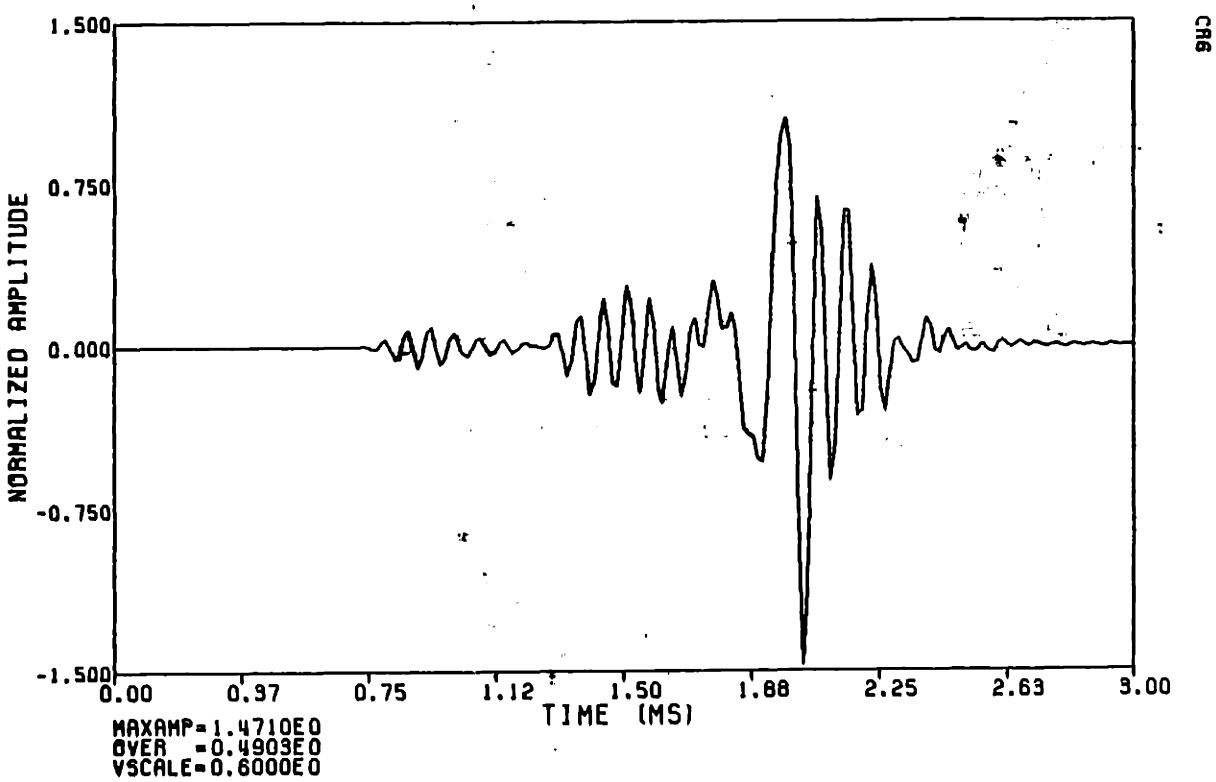

FIG. 3.3

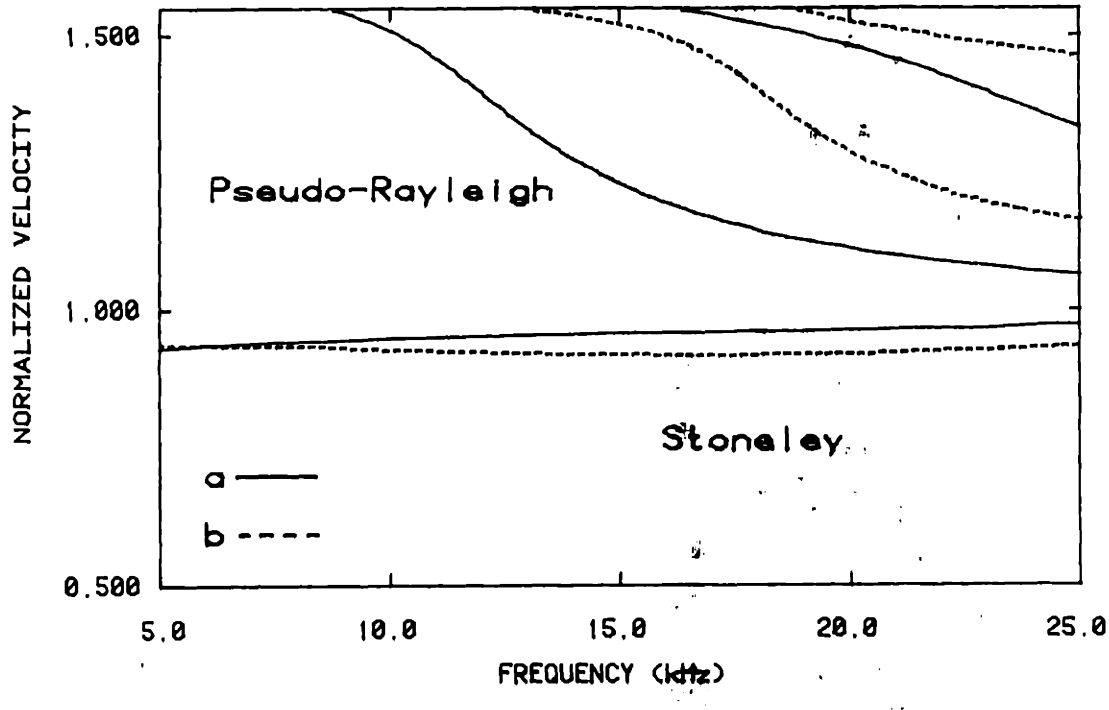
1.500
1.000
0.500
NORMALIZED VELOCITY
Pseudo-Rayleigh
Stoneley
a
b
5.0
10.0
15.0
20.0
25.0
FREQUENCY (kHz)

FIG. 3.4

R (FT)	VP (FT/MS)	VS (FT/MS)	RHO (GM/CC)	QP	QS
0.154167	5.5000	0.	1.2000	20.00	0.
0.	16.0000	8.5300	2.1600	60.00	60.00

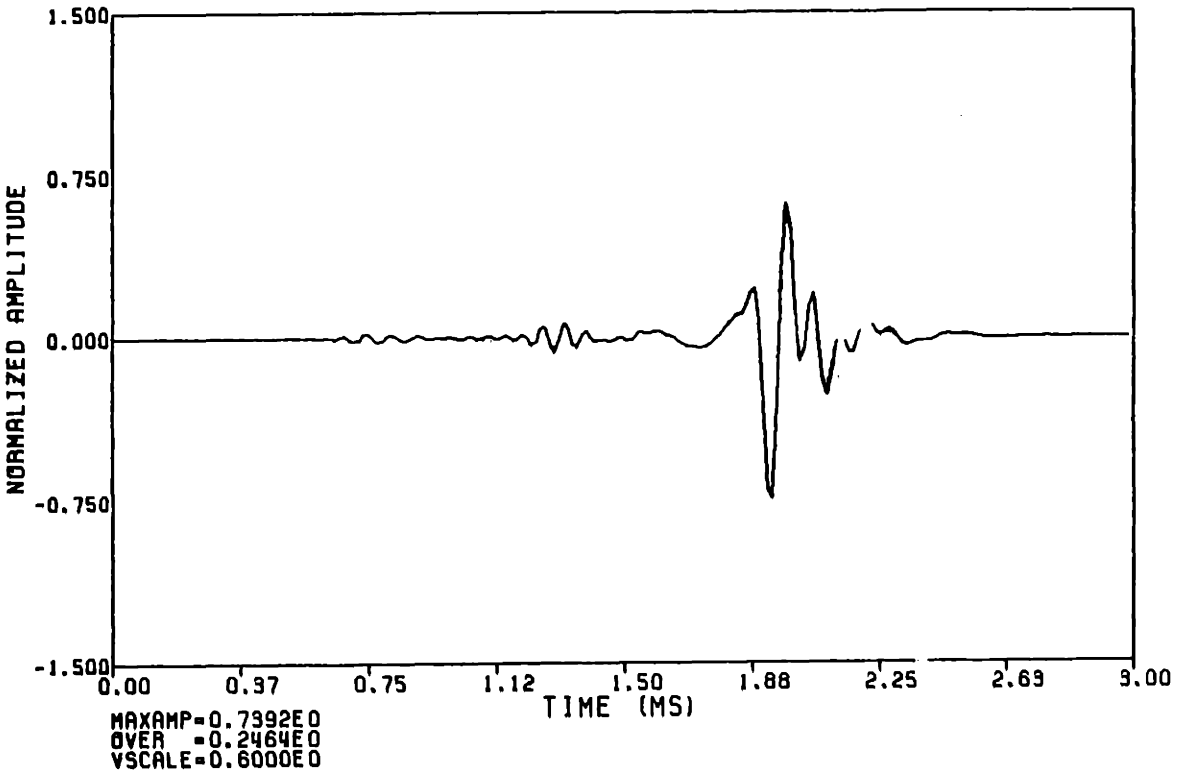

FIG. 3.5

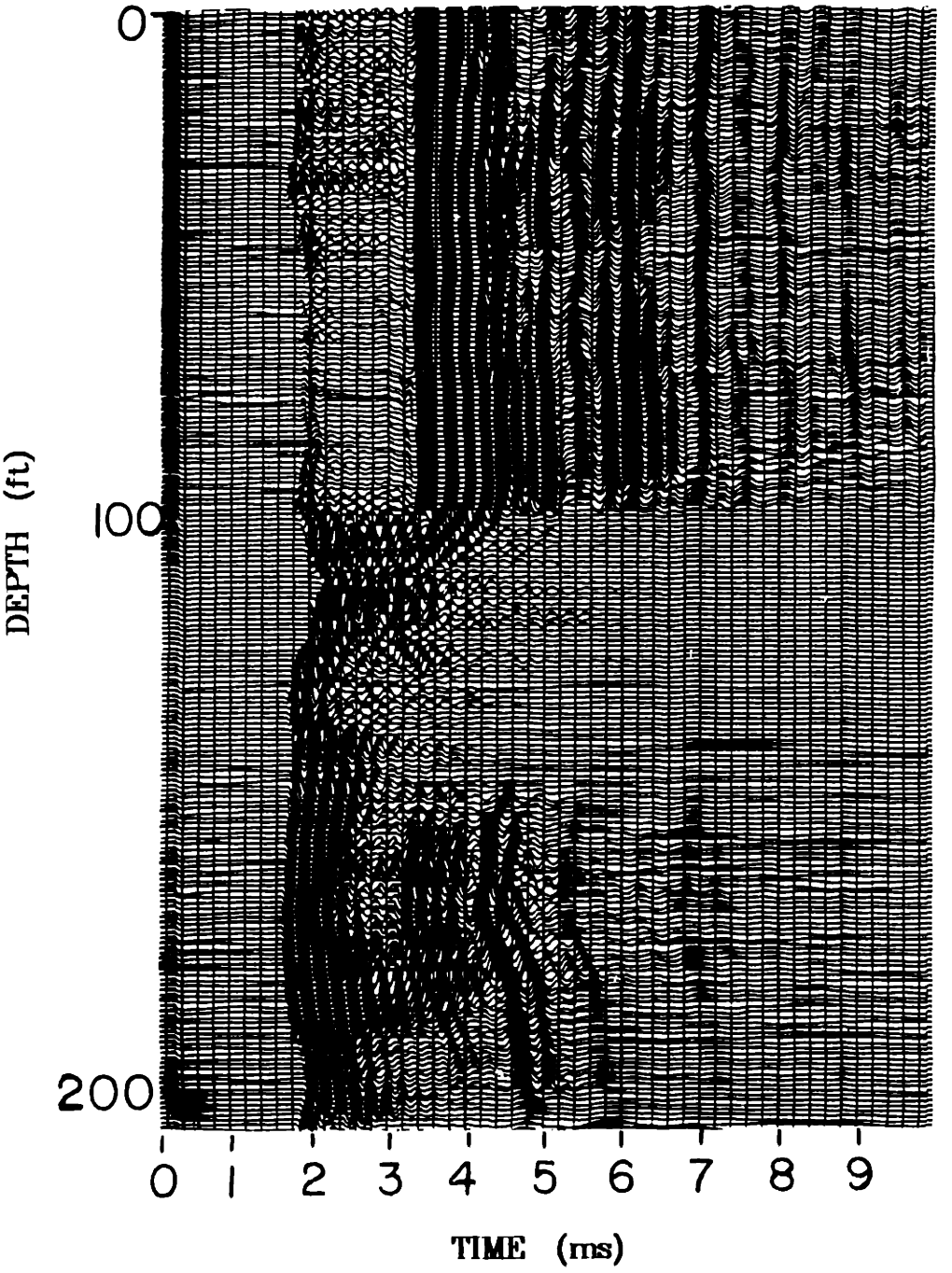

FIG. 3.6

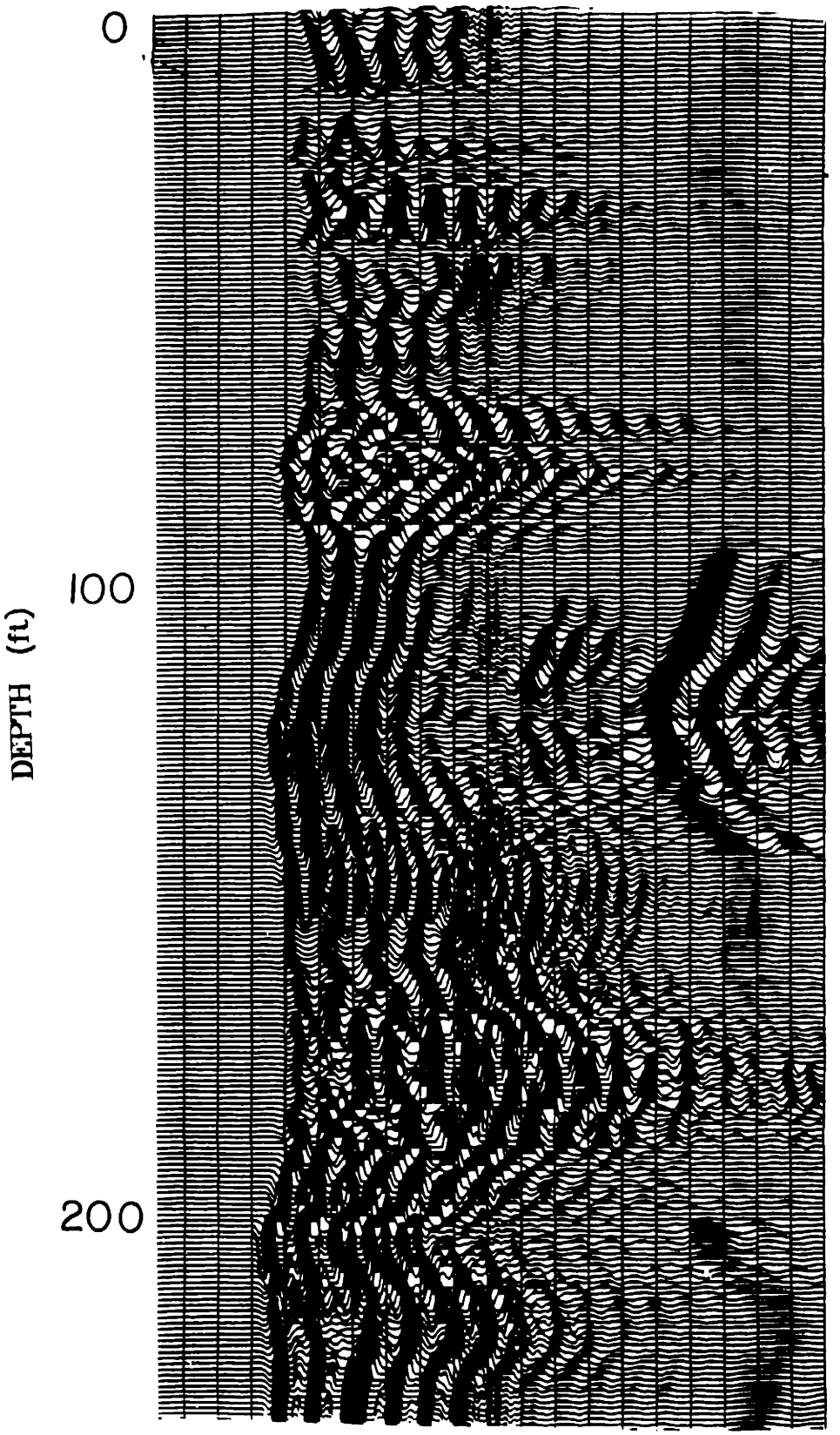

FIG. 3.7a

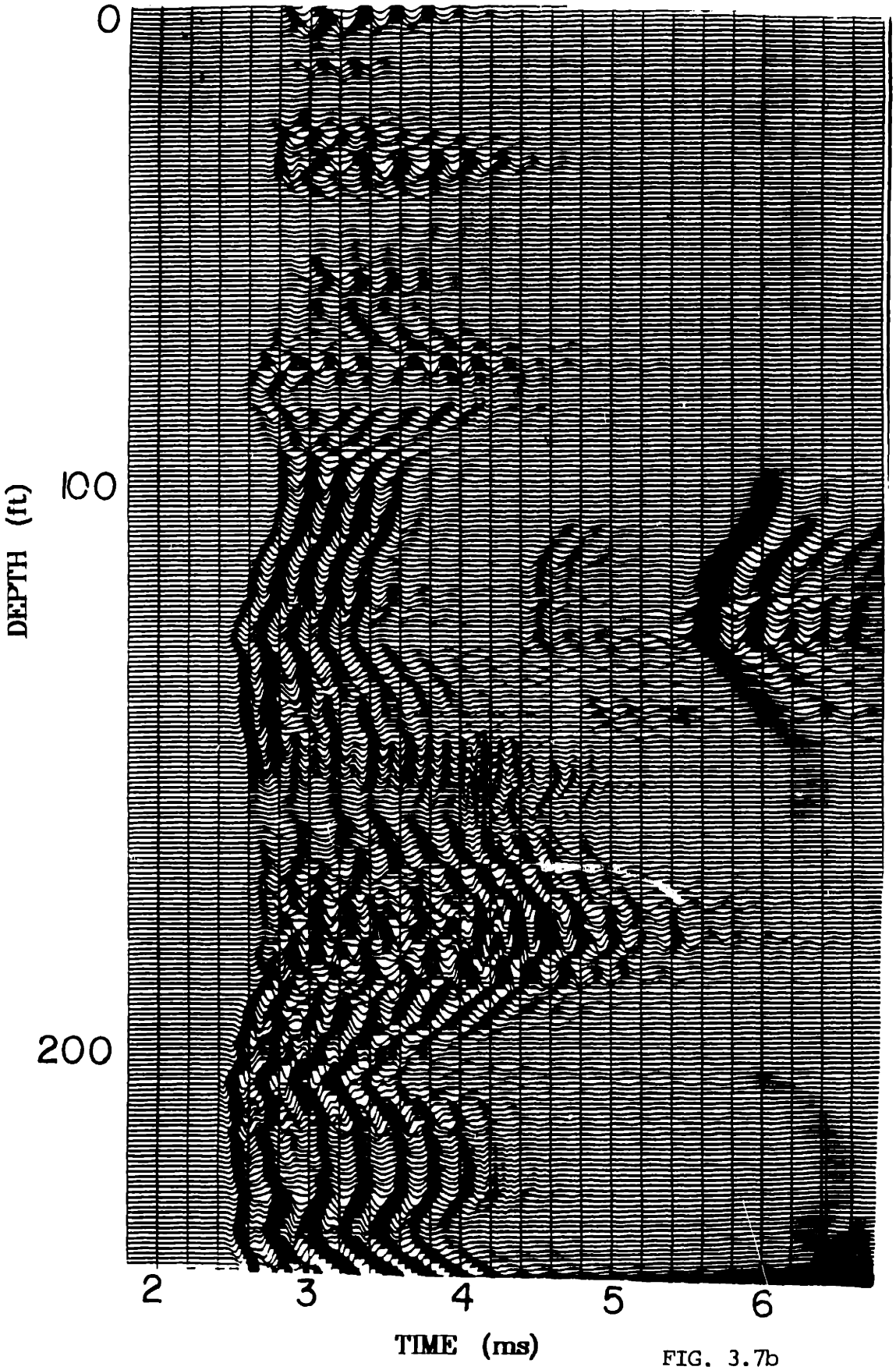

FIG. 3.7b

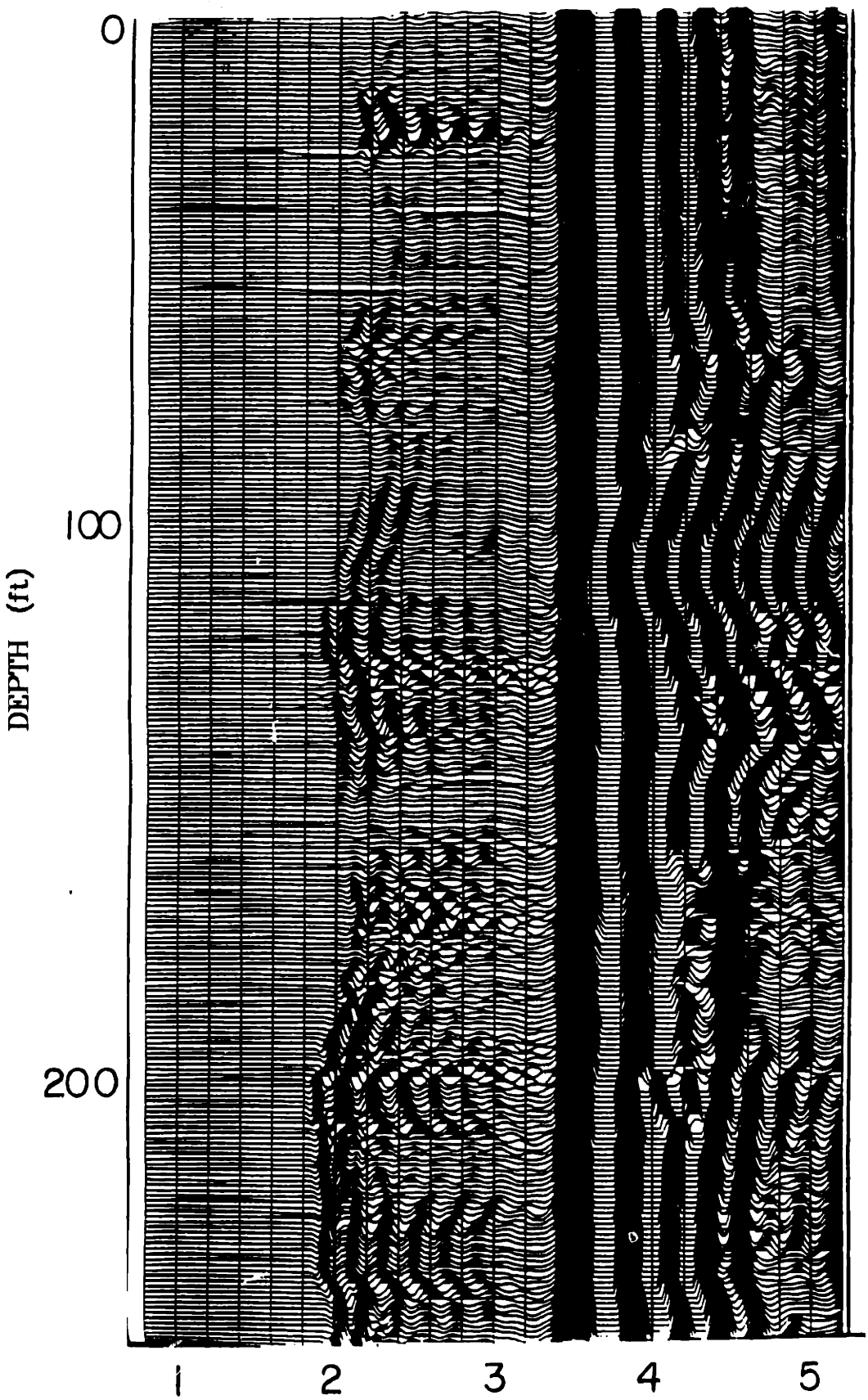

FIG. 3.7c

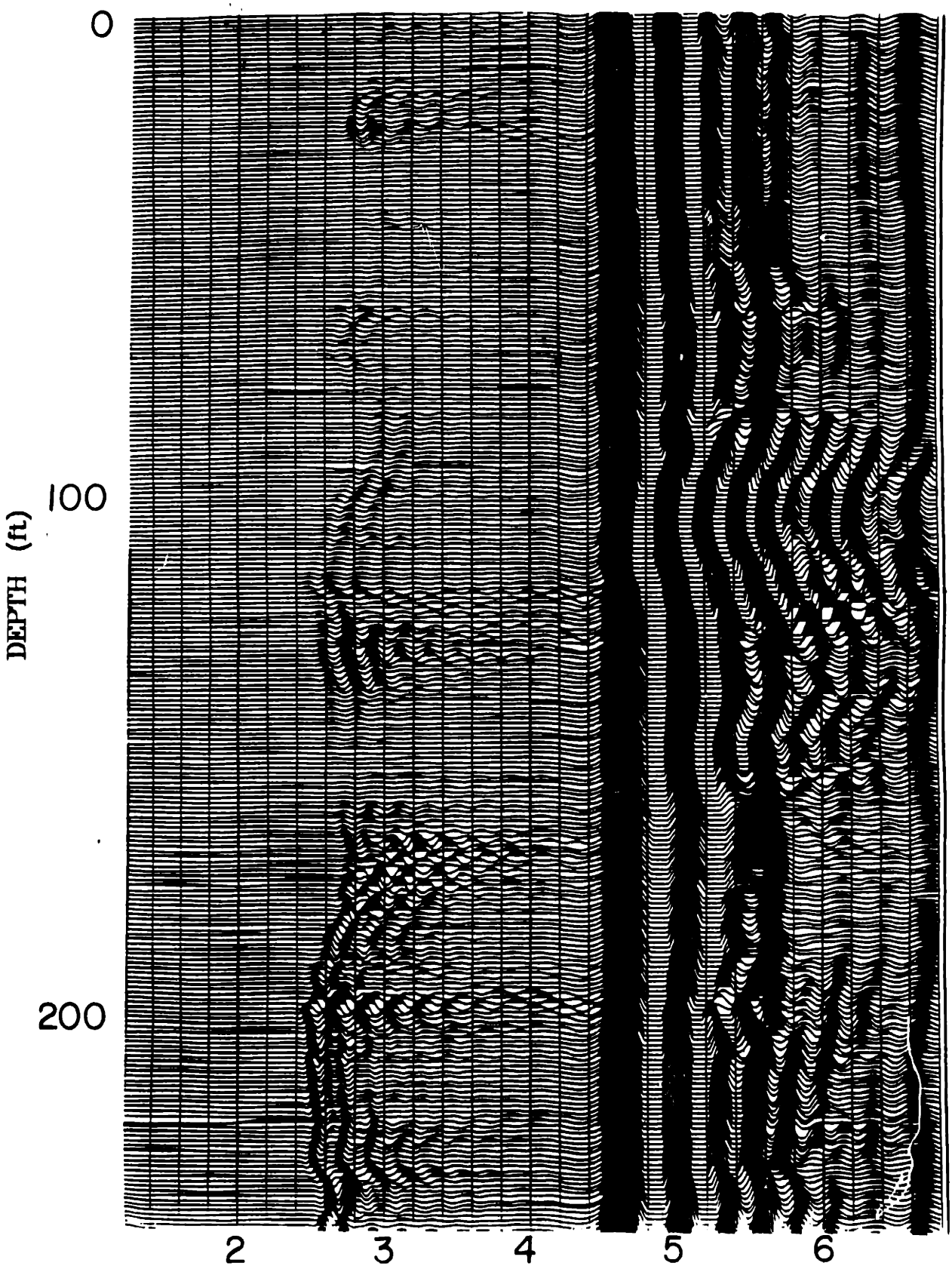

FIG. 3.7d

R (FT)	VP (FT/MS)	VS (FT/MS)	RHO (GM/CC)	QP	QS
0.333333	5.5000	0.	1.2000	20.00	0.
0.	9.5000	5.0000	2.0000	100.00	100.00

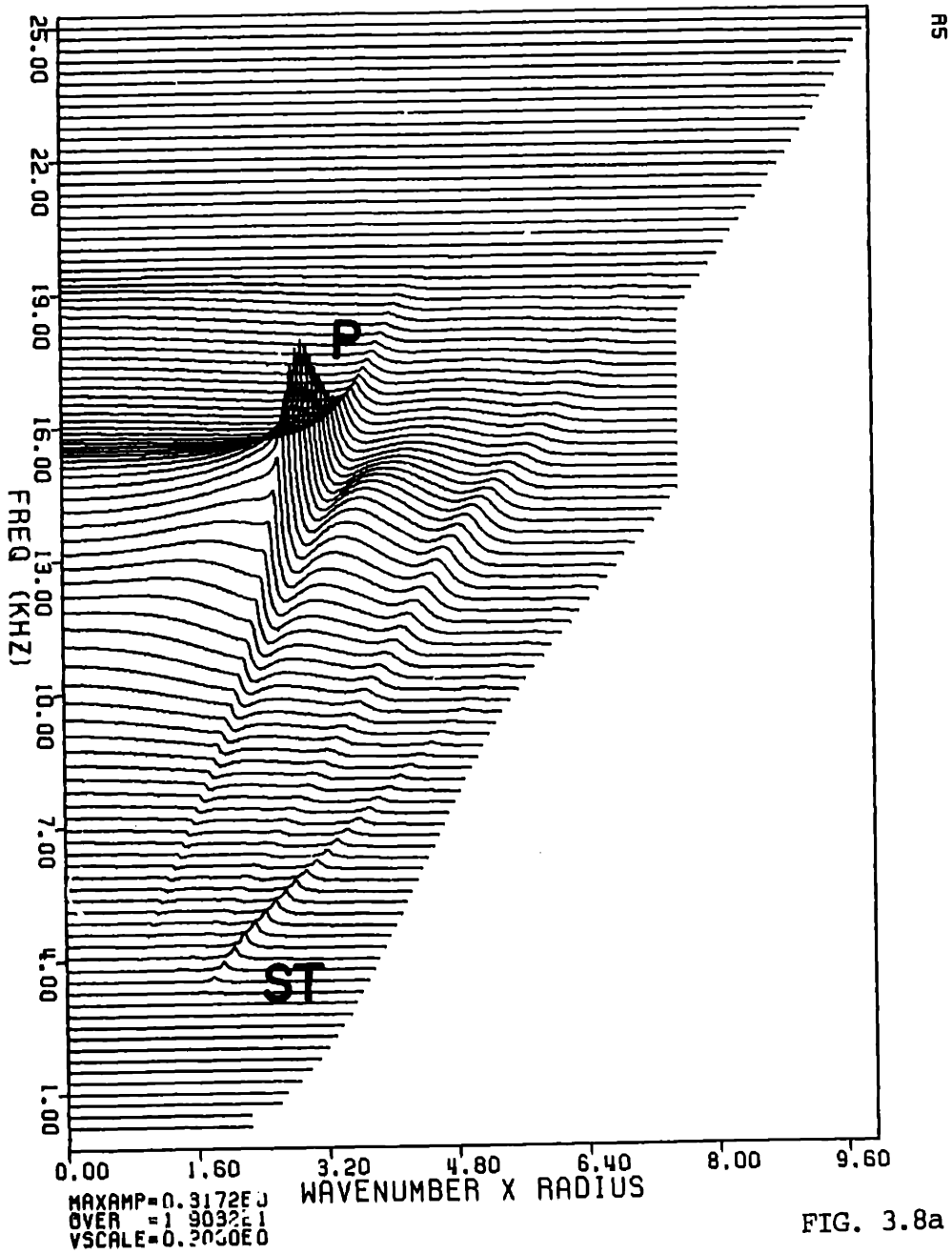

FIG. 3.8a

A (FT)	VP (FT/MS)	VS (FT/MS)	RHO (GM/CC)	QP	QS
0.154167	5.5000	0.	1.2000	20.00	0.
0.187500	20.0000	11.0000	7.5000	1000.00	1000.00
0.333333	9.2590	5.6700	1.9200	40.00	30.00
0.	9.5000	5.0000	2.0000	100.00	100.00

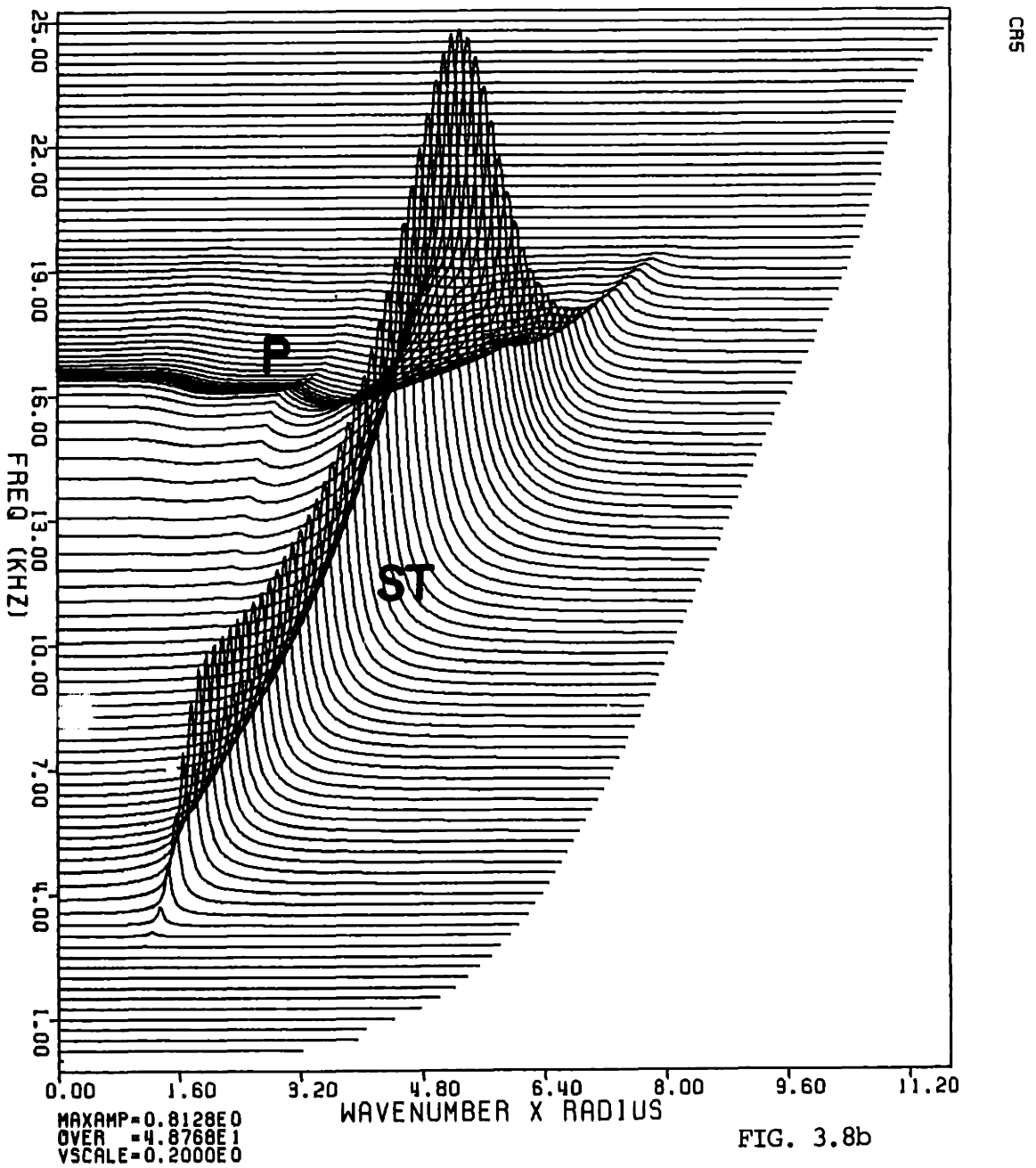

FIG. 3.8b

H (FT)	VP (FT/MS)	VS (FT/MS)	RHO (GM/CC)	QP	QS
0.154167	5.5000	0.	1.2000	20.00	0.
0.187500	20.0000	11.0000	7.5000	1000.00	1000.00
0.333333	9.2590	5.6700	1.9200	40.00	90.00
0.	19.5000	10.5000	2.3000	95.00	69.00

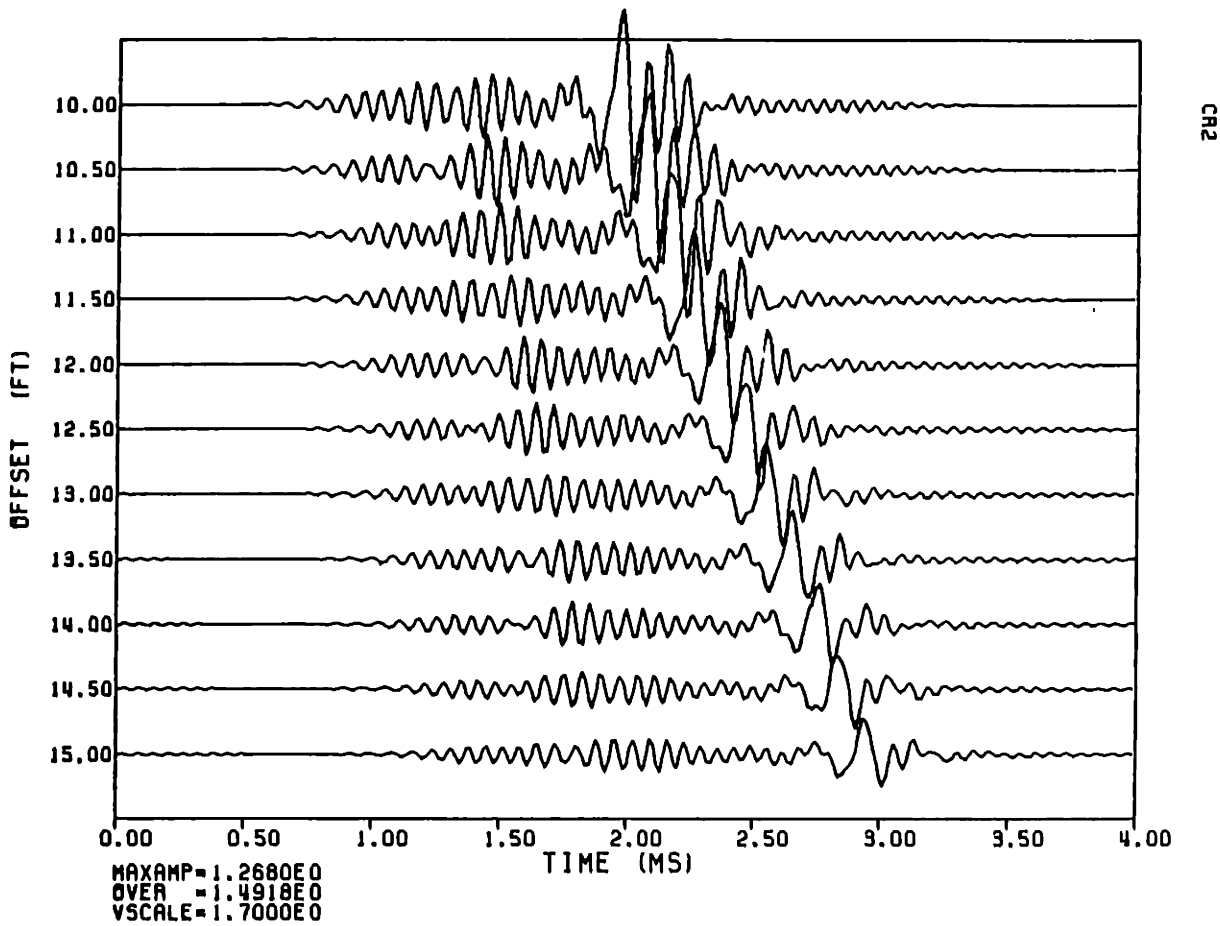

FIG. 3.9a

H (FT)	VP (FT/MS)	VS (FT/MS)	RHO (GM/CC)	QP	QS
0.154167	5.5000	0.	1.2000	20.00	0.
0.187500	20.0000	11.0000	7.5000	1000.00	1000.00
0.333333	9.2590	5.6700	1.9200	40.00	90.00
0.	19.5000	10.5000	2.3000	95.00	69.00

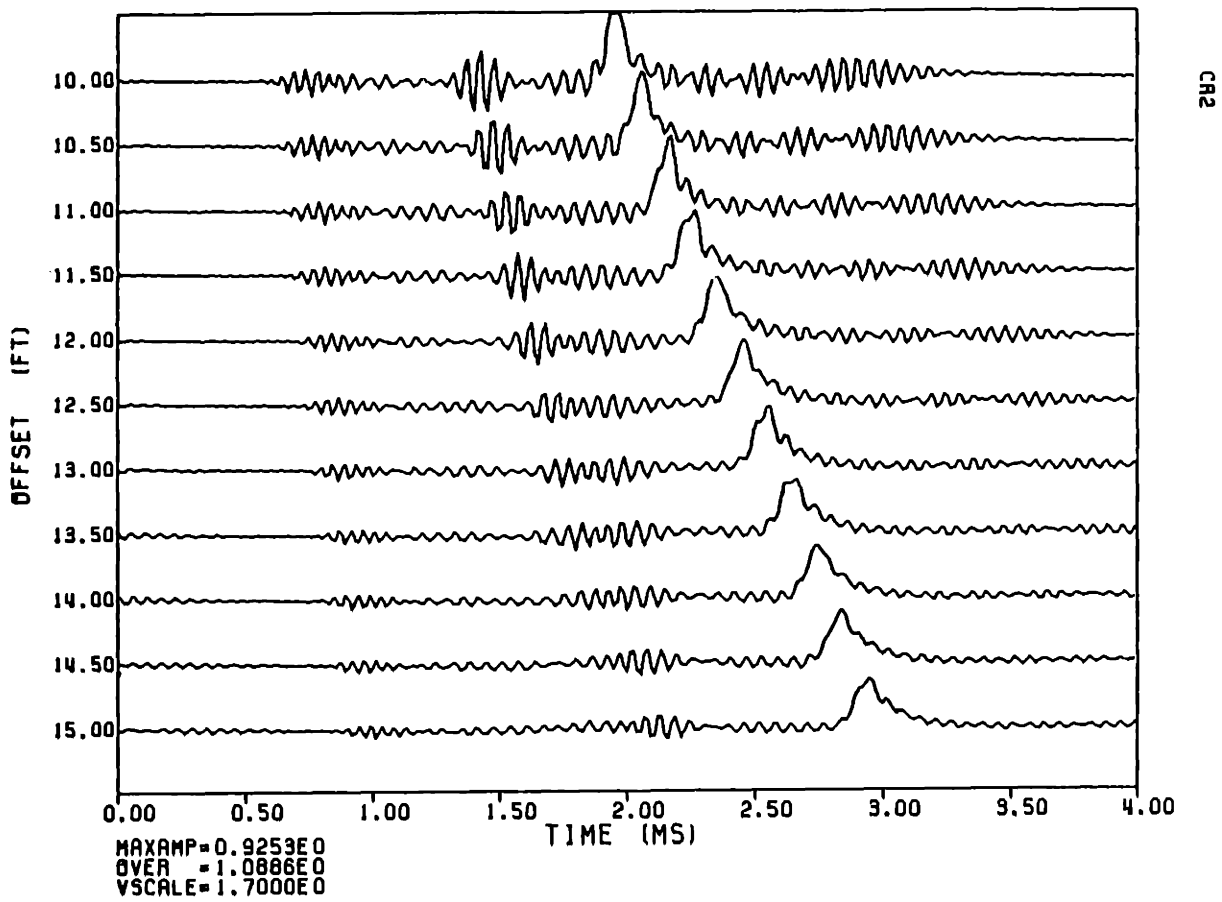

FIG. 3.9b

r	Vp	Vs	rho	Qp	Qs
0.333300	5.5000	0.	1.2000	20.00	0.
0.500000	16.0000	8.5300	2.1600	60.00	60.00
0.	16.0000	8.5300	2.1600	60.00	60.00

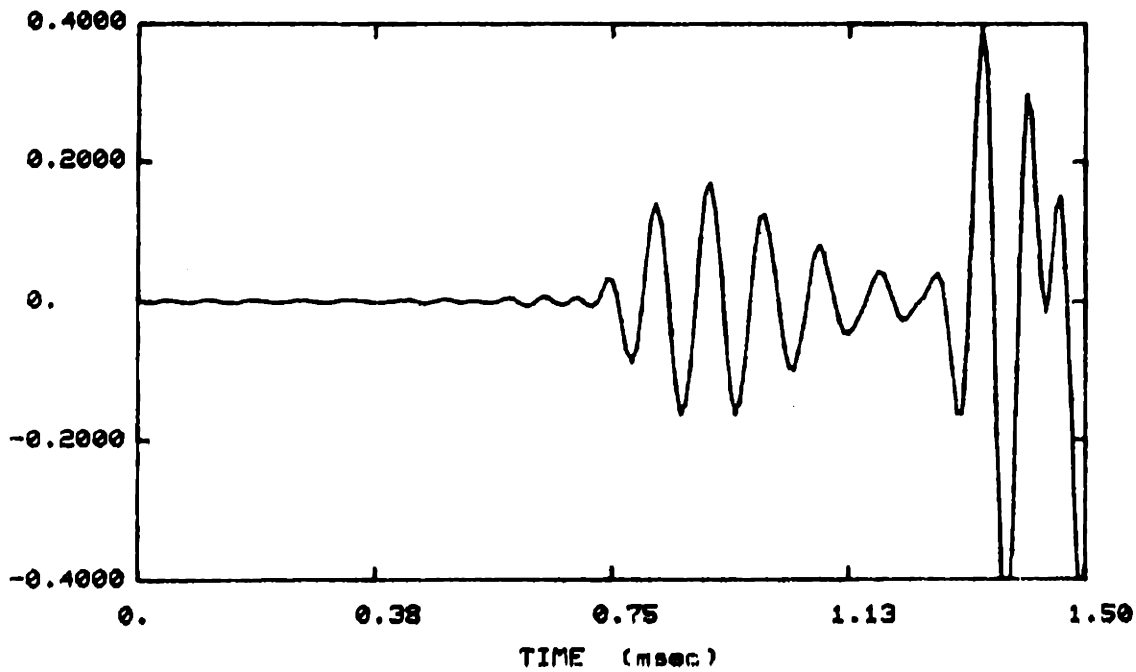

FIG. 3.10a

r	Vp	Vs	rho	Qp	Qs
0.154200	5.5000	0.	1.2000	20.00	0.
0.187500	20.0000	11.0000	7.5000	1000.00	1000.00
0.333300	13.5000	8.3000	1.9200	40.00	30.00
0.	16.0000	8.5300	2.1600	60.00	60.00

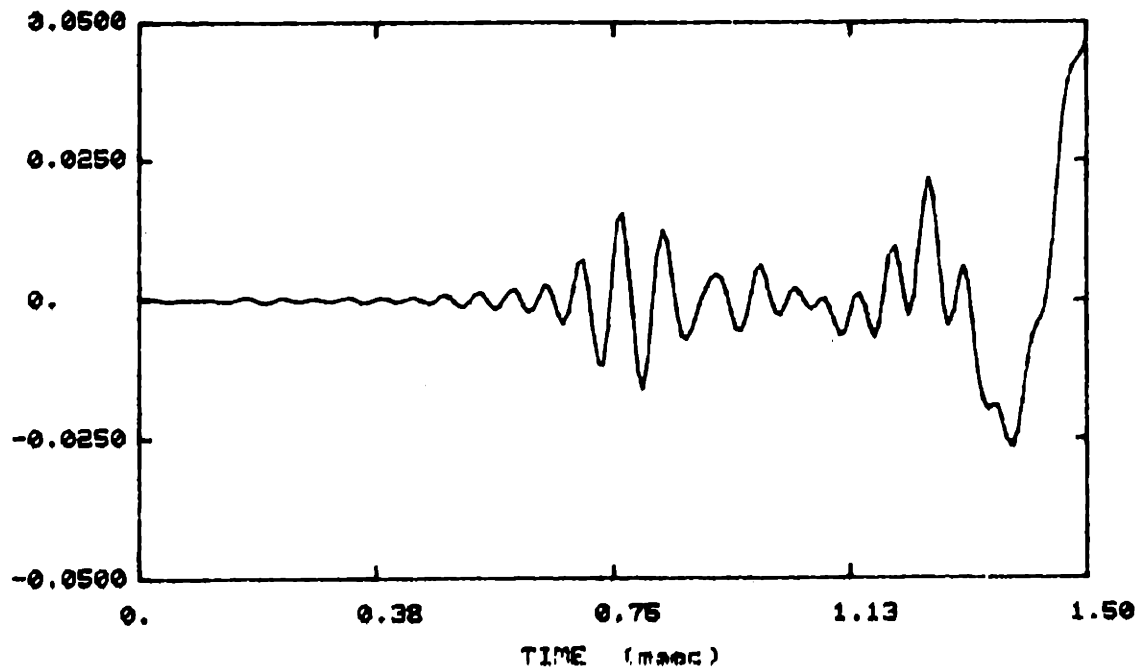

FIG. 3.10b

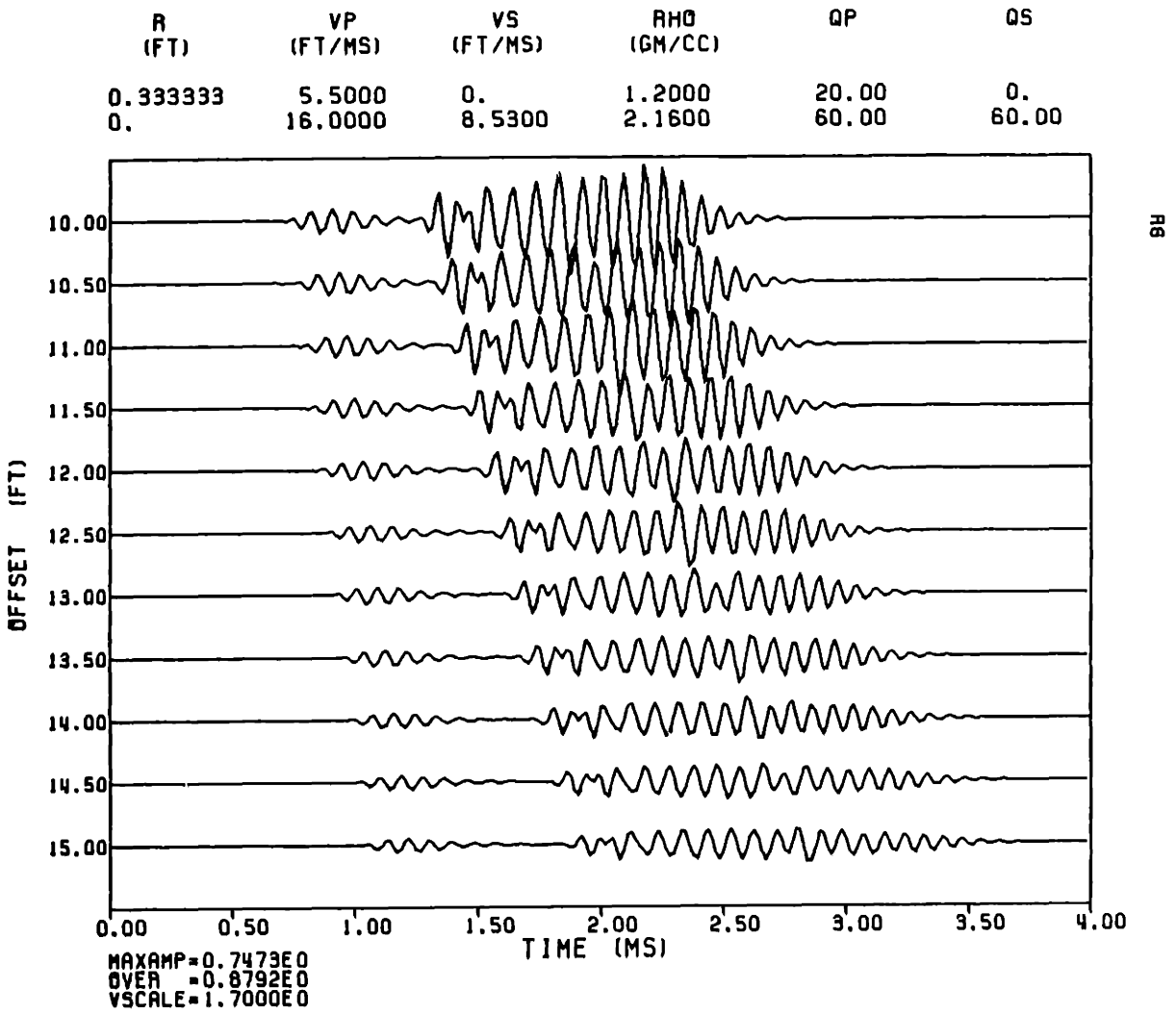
R (FT)
VP (FT/MS)
VS (FT/MS)
RHO (GM/CC)
QP
QS
0.333333 5.5000 0. 1.2000 20.00 0.
0. 16.0000 8.5300 2.1600 60.00 60.00
10.00
10.50
11.00
11.50
12.00
12.50
13.00
13.50
14.00
14.50
15.00
OFFSET (FT)
0.00 0.50 1.00 1.50 2.00 2.50 3.00 3.50 4.00
TIME (MS)
MAXAMP=0.7473E0
OVER =0.8792E0
VSCALE=1.7000E0
RG

FIG. 3.11

H (FT)	VP (FT/MS)	VS (FT/MS)	RHO (GM/CC)	QP	QS
0.154167	5.5000	0.	1.2000	20.00	0.
0.187500	20.0000	11.0000	7.5000	1000.00	1000.00
0.333333	9.2590	5.6700	1.9200	40.00	30.00
0.	16.0000	8.5300	2.1600	60.00	60.00

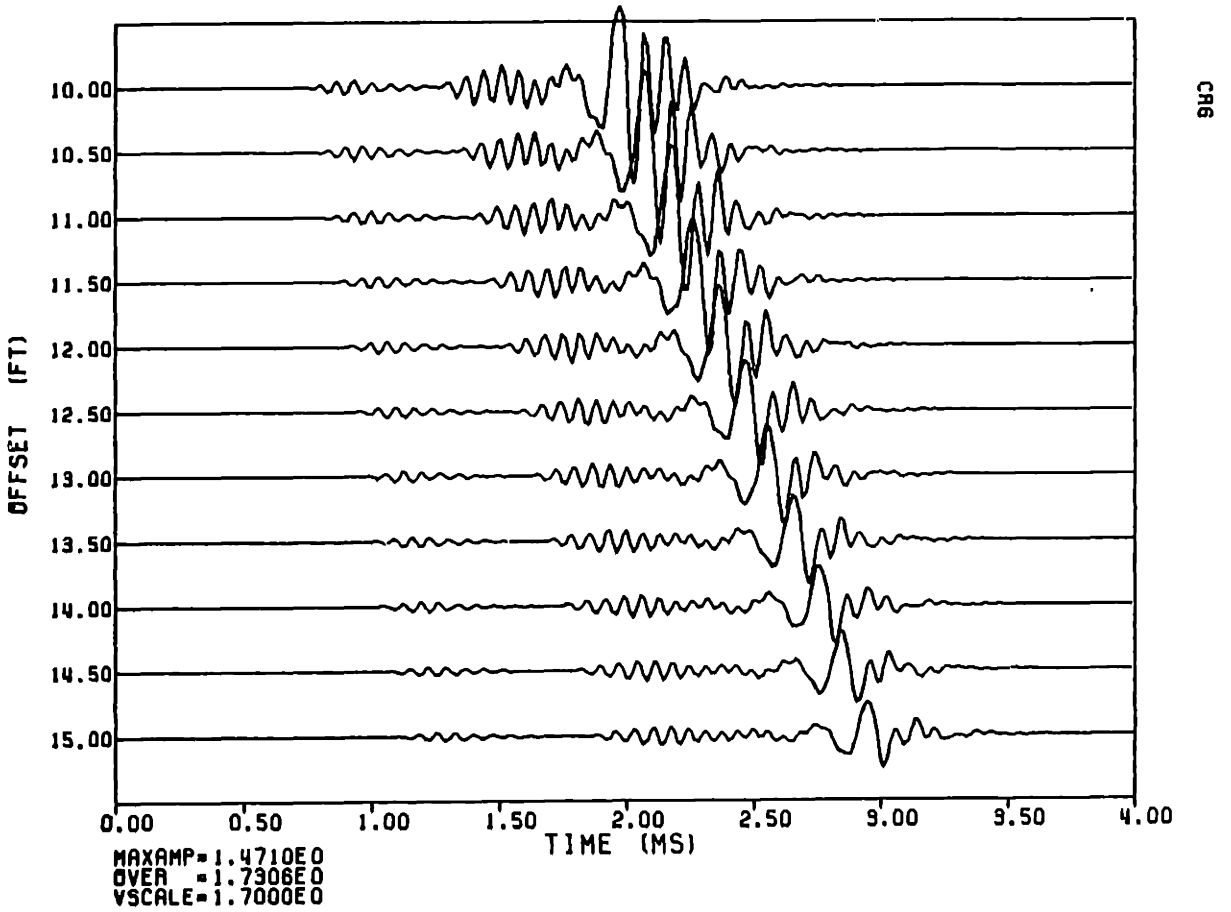

FIG. 3.12

H (FT)	VP (FT/MS)	VS (FT/MS)	RHO (GM/CC)	QP	QS
0.1542	5.5000	0.	1.2000	20.00	0.
0.1875	20.0000	11.0000	7.5000	1000.00	1000.00
0.3333	9.2590	5.6700	1.9200	40.00	90.00
0.	13.1200	8.5300	2.1600	60.00	60.00

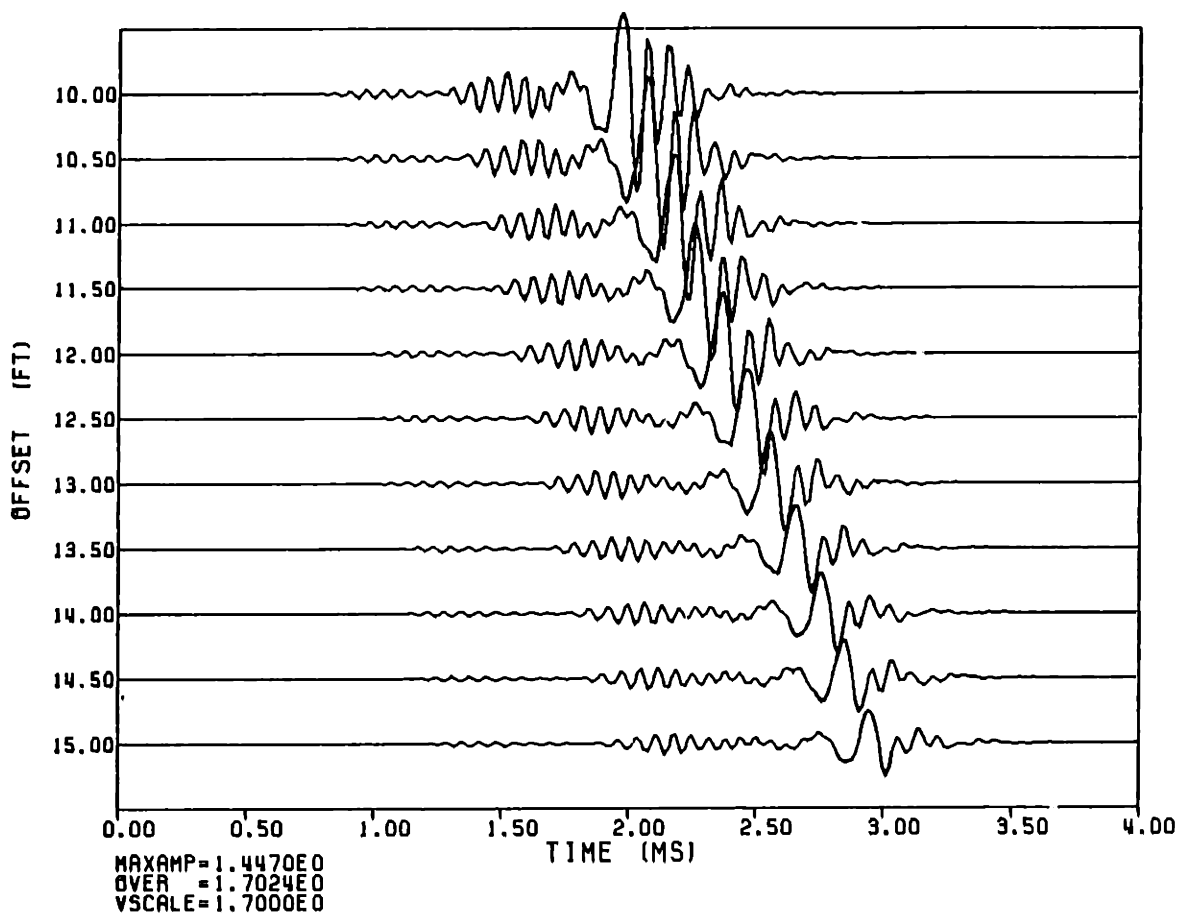

FIG. 3.13

R (FT)	VP (FT/MS)	VS (FT/MS)	RHO (GM/CC)	QP	QS
0.154167	5.5000	0.	1.2000	20.00	0.
0.187500	20.0000	11.0000	7.5000	1000.00	1000.00
0.333333	9.2590	5.6700	1.9200	40.00	30.00
0.	13.1200	7.0000	2.1600	60.00	80.00

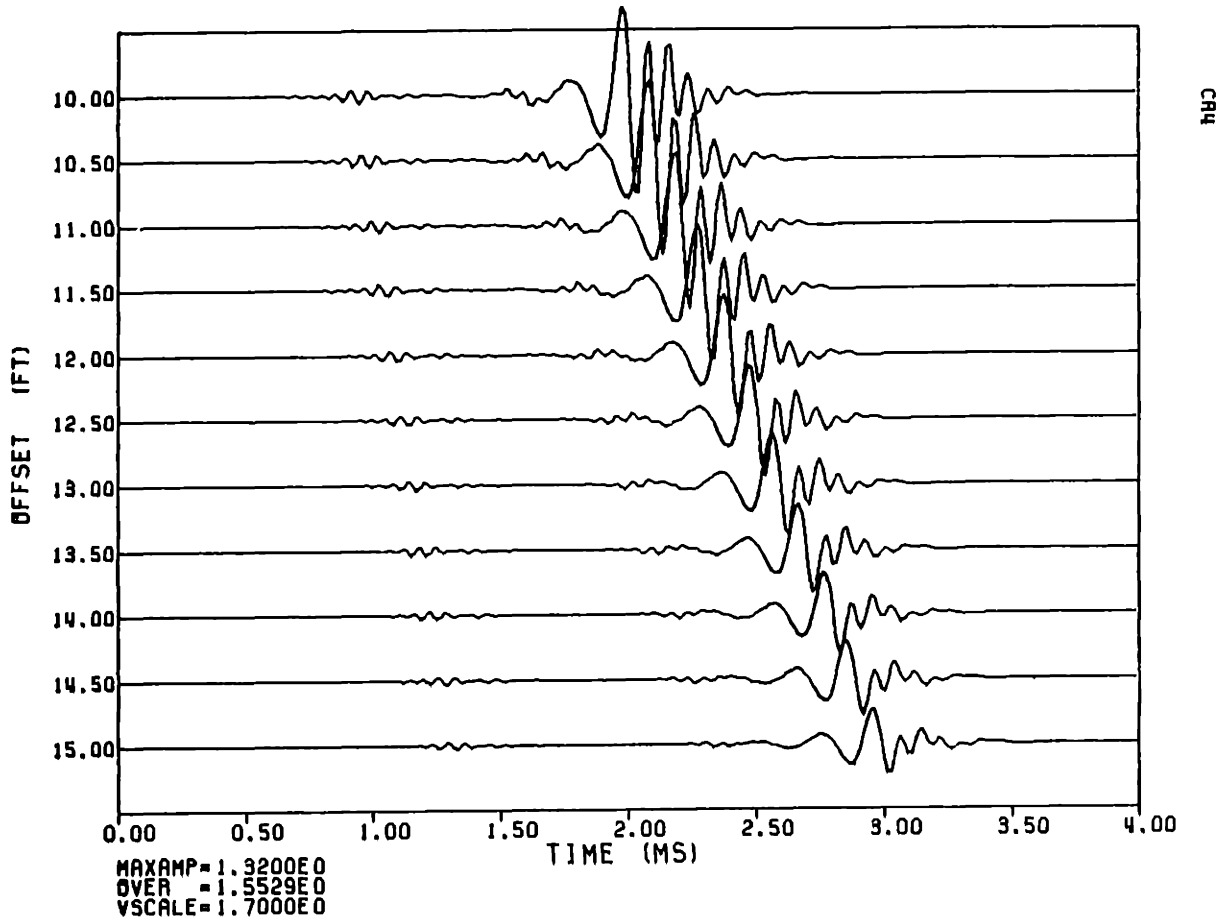

FIG. 3.14

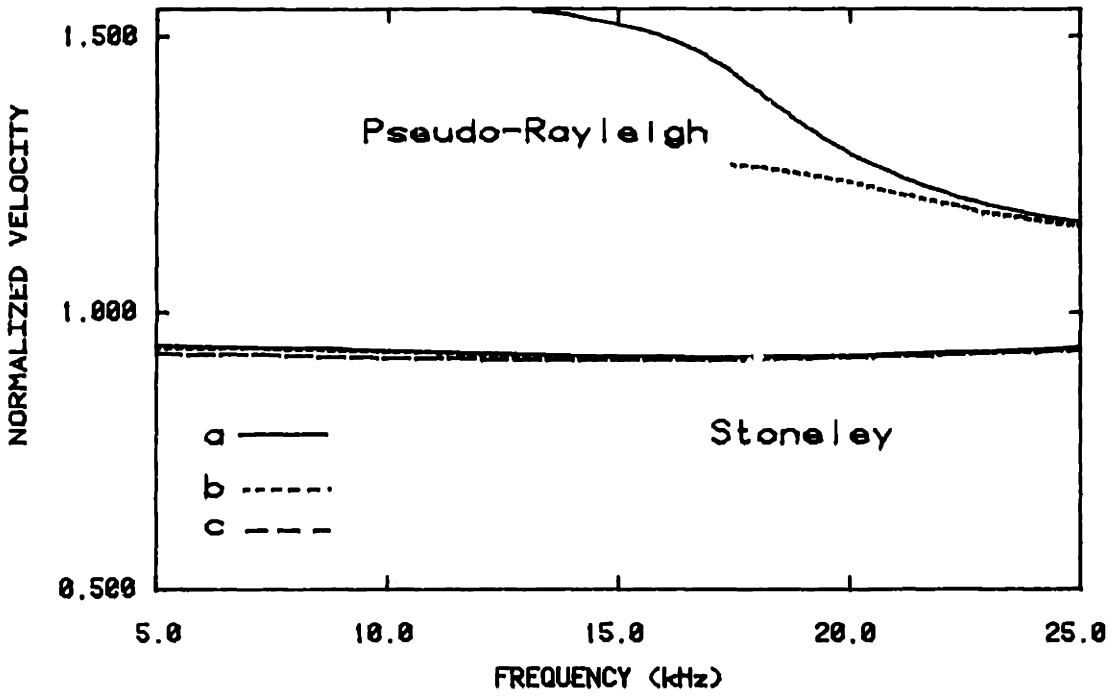
1.500
1.000
0.500
NORMALIZED VELOCITY
Pseudo-Rayleigh
Stoneley
a
b
c
5.0
10.0
15.0
20.0
25.0
FREQUENCY (kHz)

FIG. 3.15

R (FT)	VP (FT/MS)	VS (FT/MS)	RHO (GM/CC)	QP	QS
0.154167	5.5000	0.	1.2000	20.00	0.
0.187500	20.0000	11.0000	7.5000	1000.00	1000.00
0.333333	9.2590	5.6700	1.9200	40.00	30.00
0.	16.0000	8.5300	2.1600	60.00	60.00

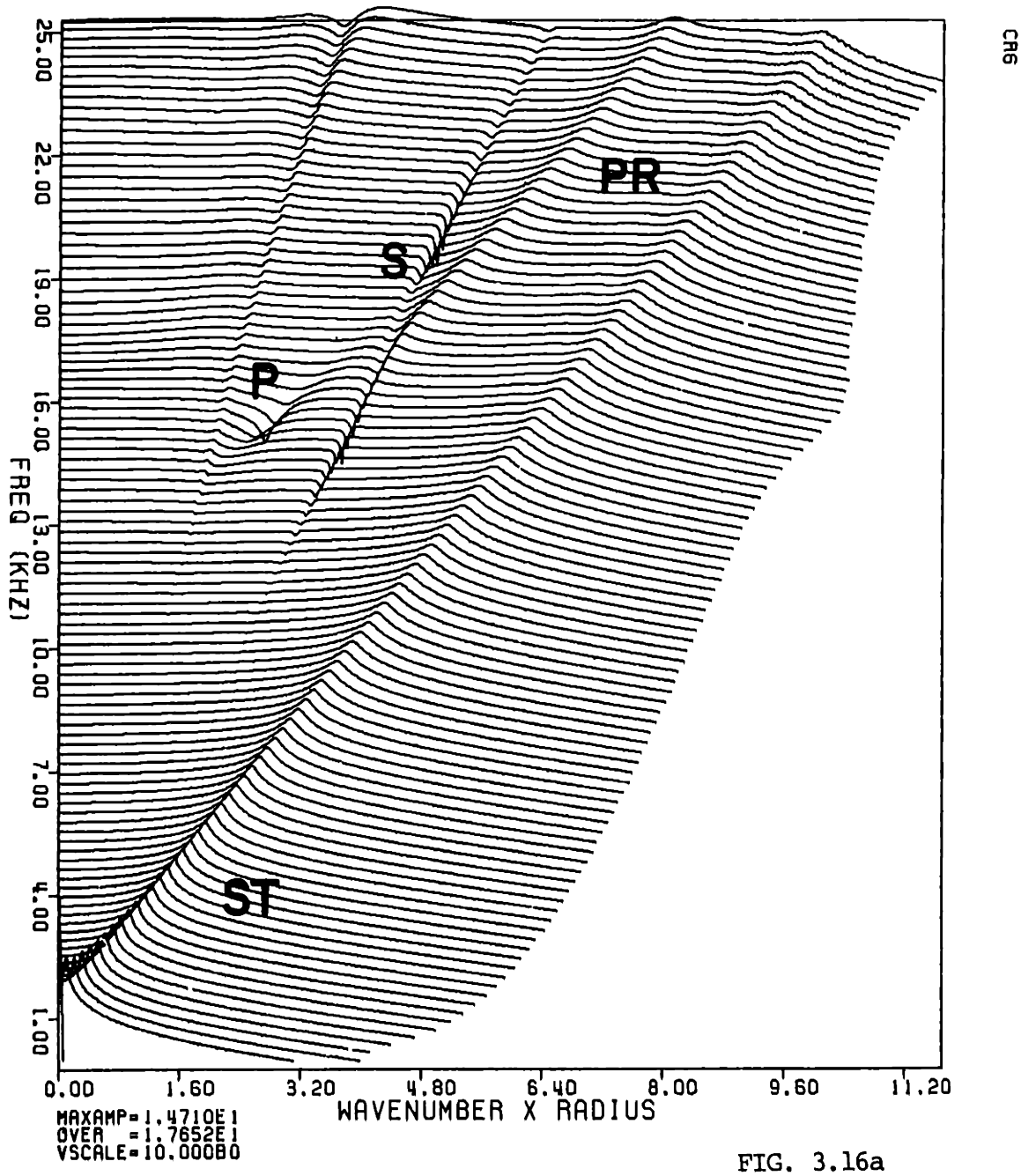

FIG. 3.16a

R (FT)	VP (FT/MS)	VS (FT/MS)	RHO (GM/CC)	QP	QS
0.154167	5.5000	0.	1.2000	20.00	0.
0.187500	20.0000	11.0000	7.5000	1000.00	1000.00
0.333333	9.2590	5.6700	1.9200	40.00	30.00
0.	13.1200	8.5300	2.1600	60.00	60.00

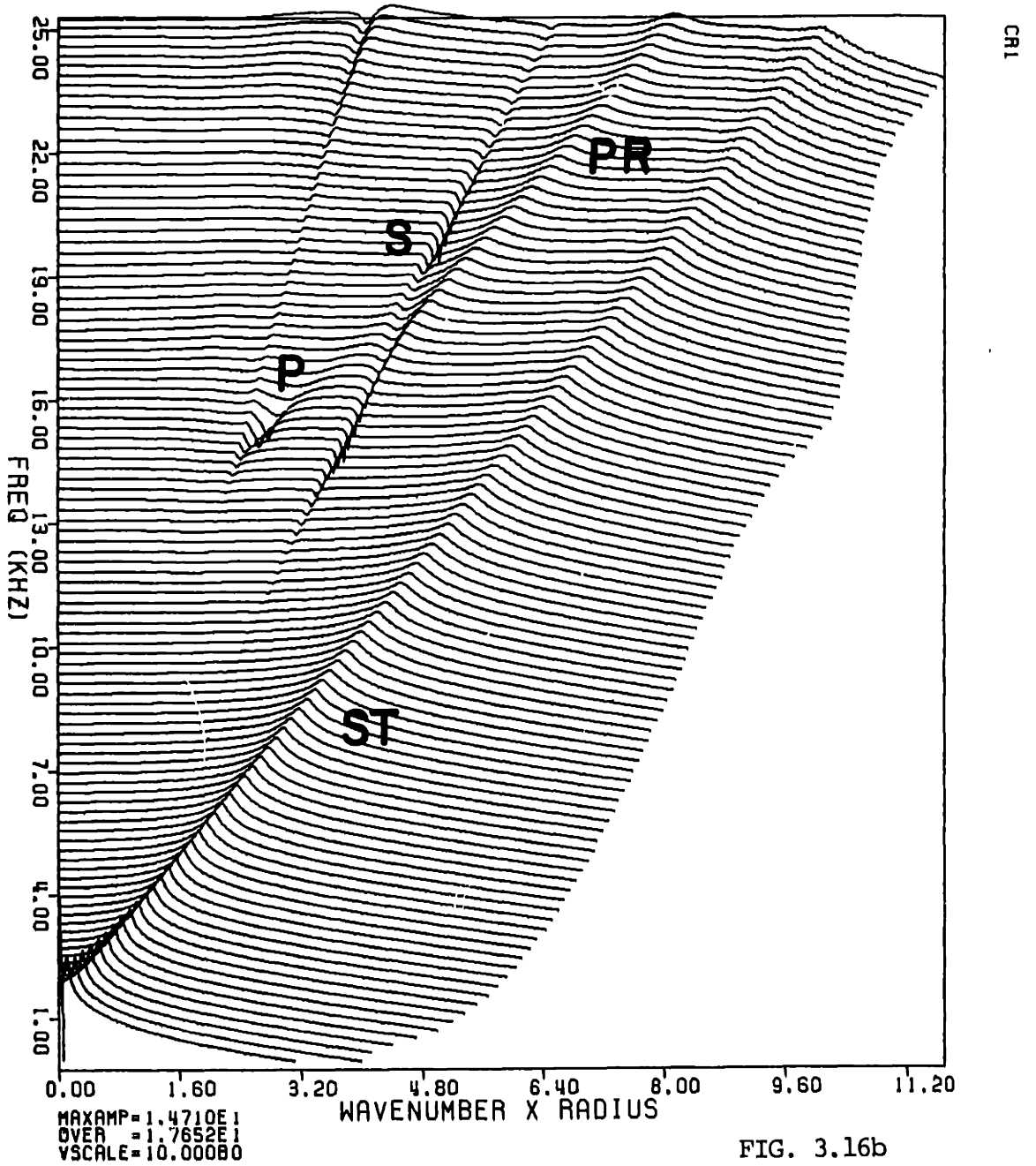

FIG. 3.16b

R (FT)	VP (FT/MS)	VS (FT/MS)	RHO (GM/CC)	QP	QS
0.154167	5.5000	0.	1.2000	20.00	0.
0.187500	20.0000	11.0000	7.5000	1000.00	1000.00
0.333333	9.2590	5.6700	1.9200	40.00	80.00
0.	13.1200	7.0000	2.1600	60.00	60.00

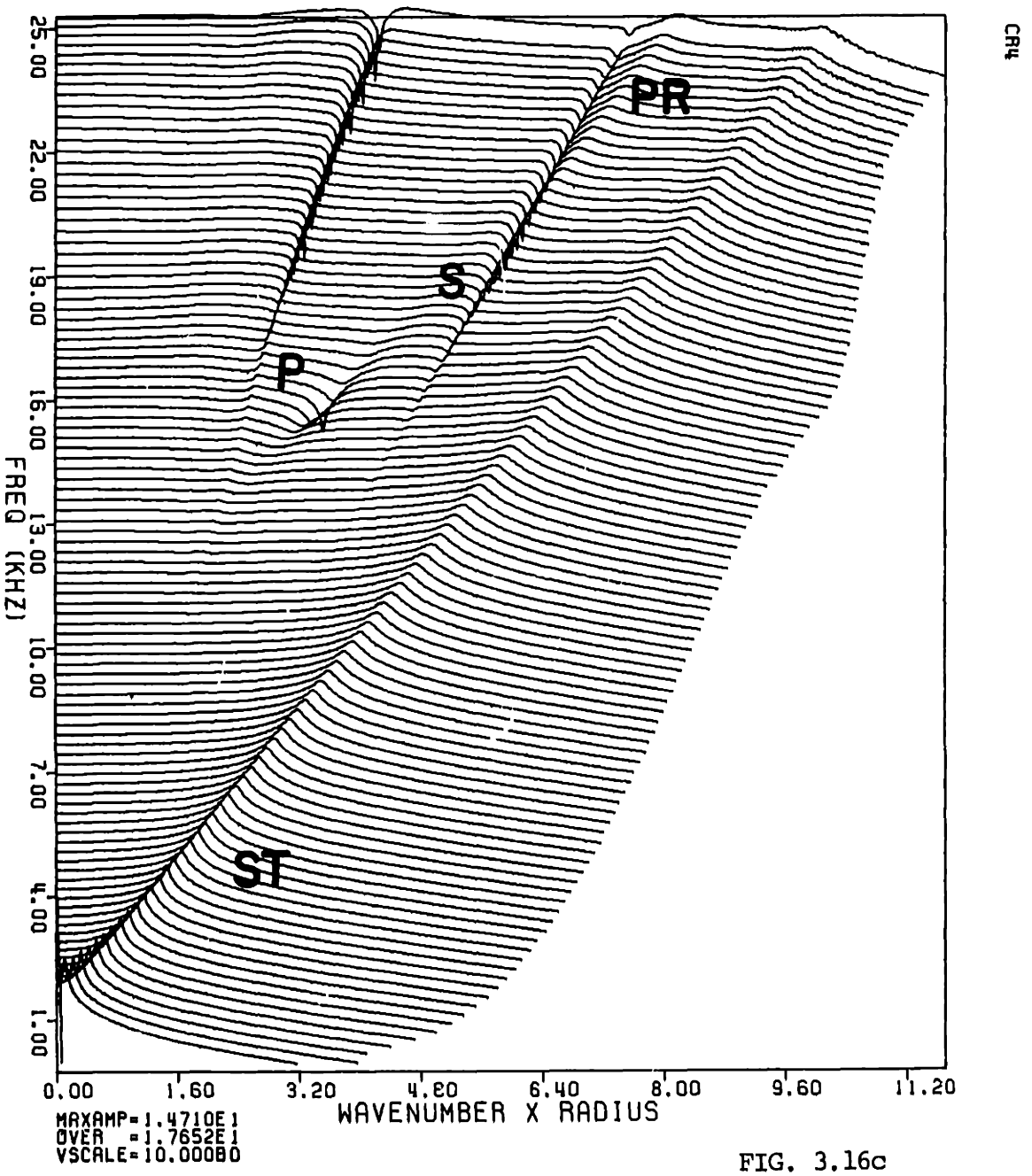

FIG. 3.16c

R (FT)	VP (FT/MS)	VS (FT/MS)	RHO (GM/CC)	QP	QS
0.154167	5.5000	0.	1.2000	20.00	0.
0.187500	20.0000	11.0000	7.5000	1000.00	1000.00
0.333333	9.2590	5.6700	1.9200	40.00	30.00
0.	9.5000	5.0000	2.0000	100.00	50.00

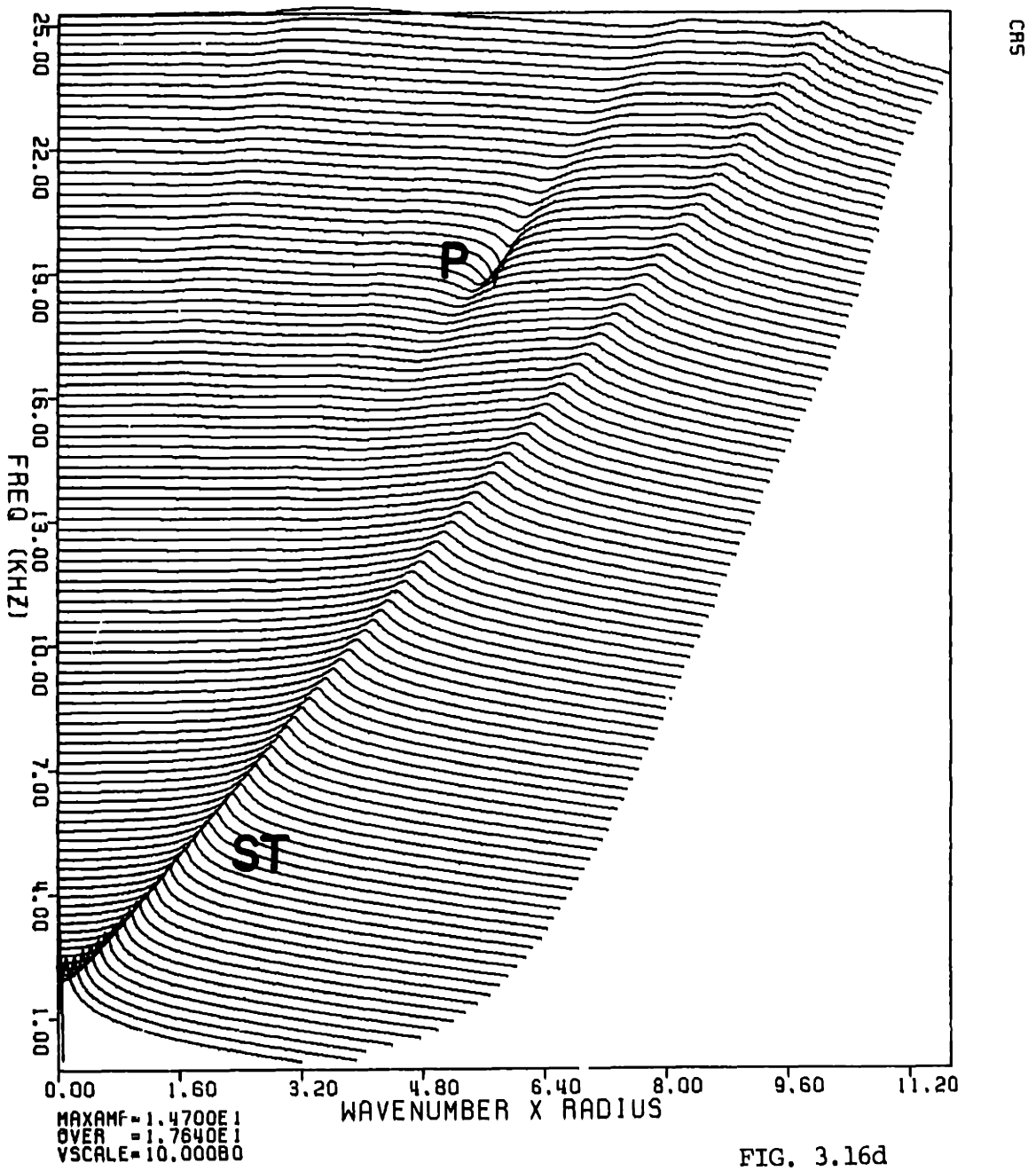

FIG. 3.16d

H (FT)	VP (FT/MS)	VS (FT/MS)	RHO (GM/CC)	QP	QS
0.1542	5.5000	0.	1.2000	20.00	0.
0.1875	20.0000	11.0000	7.5000	1000.00	1000.00
0.3333	9.2590	5.6700	1.9200	40.00	30.00
0.	9.5000	5.0000	2.0000	100.00	50.00

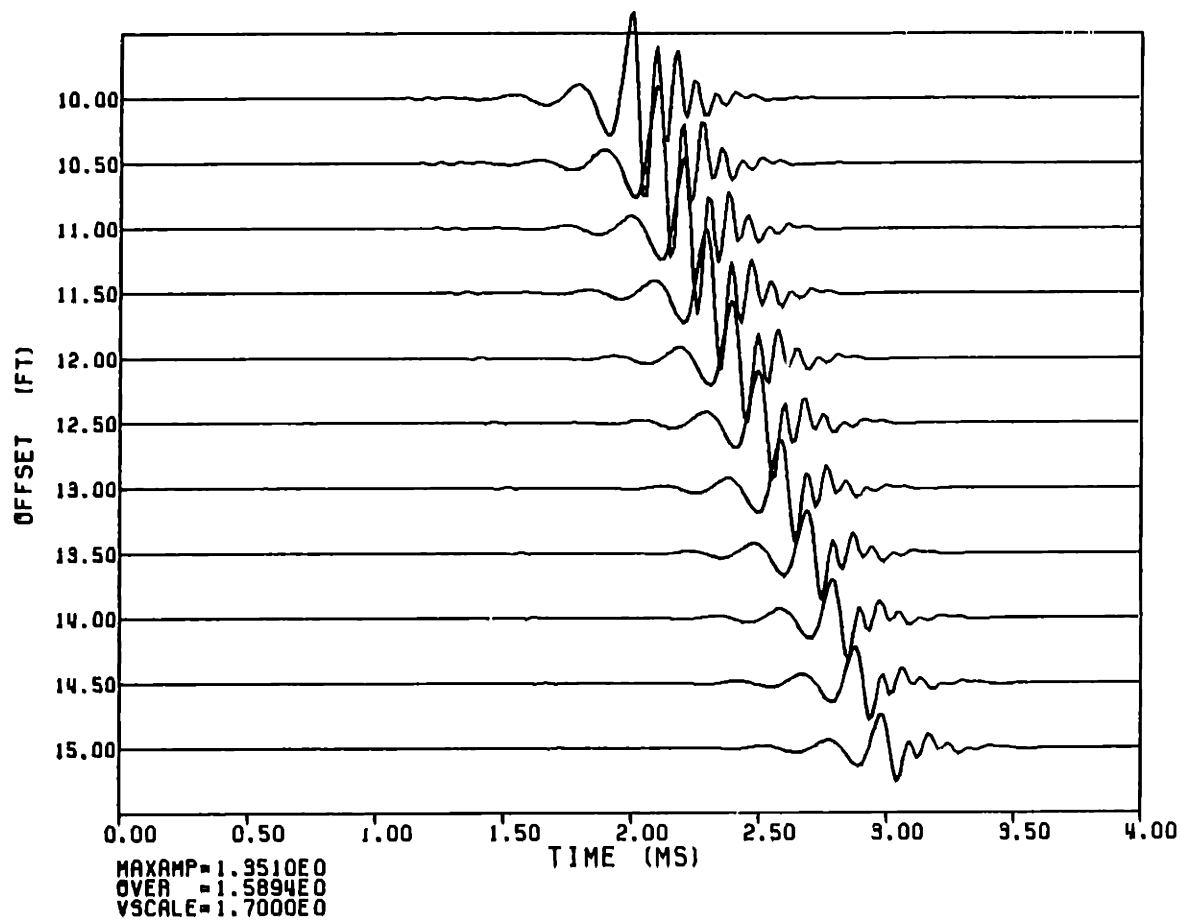

FIG. 3.17

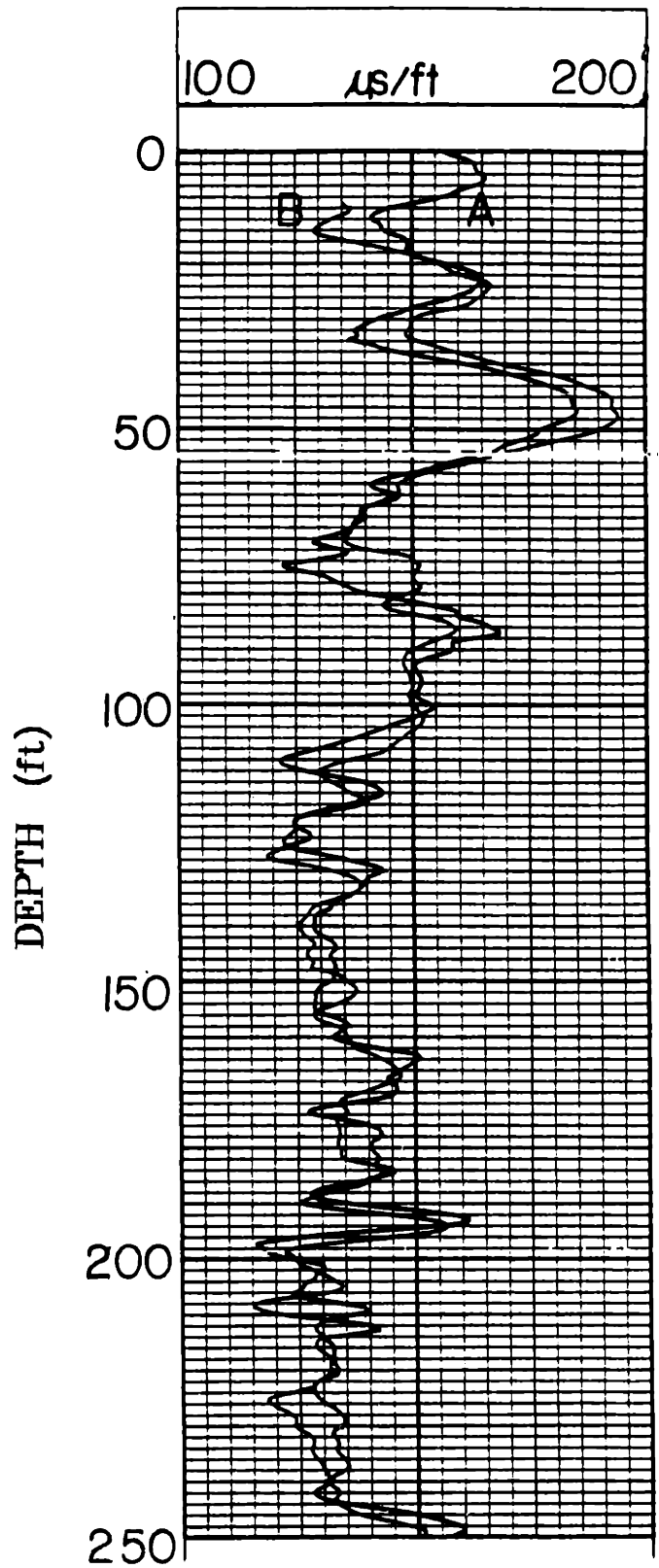

FIG. 3.18

H (FT)	VP (FT/MS)	VS (FT/MS)	RHO (GM/CC)	QP	QS
0.933333	5.5000	0.	1.2000	20.00	0.
0.	9.5000	5.0000	2.0000	100.00	100.00

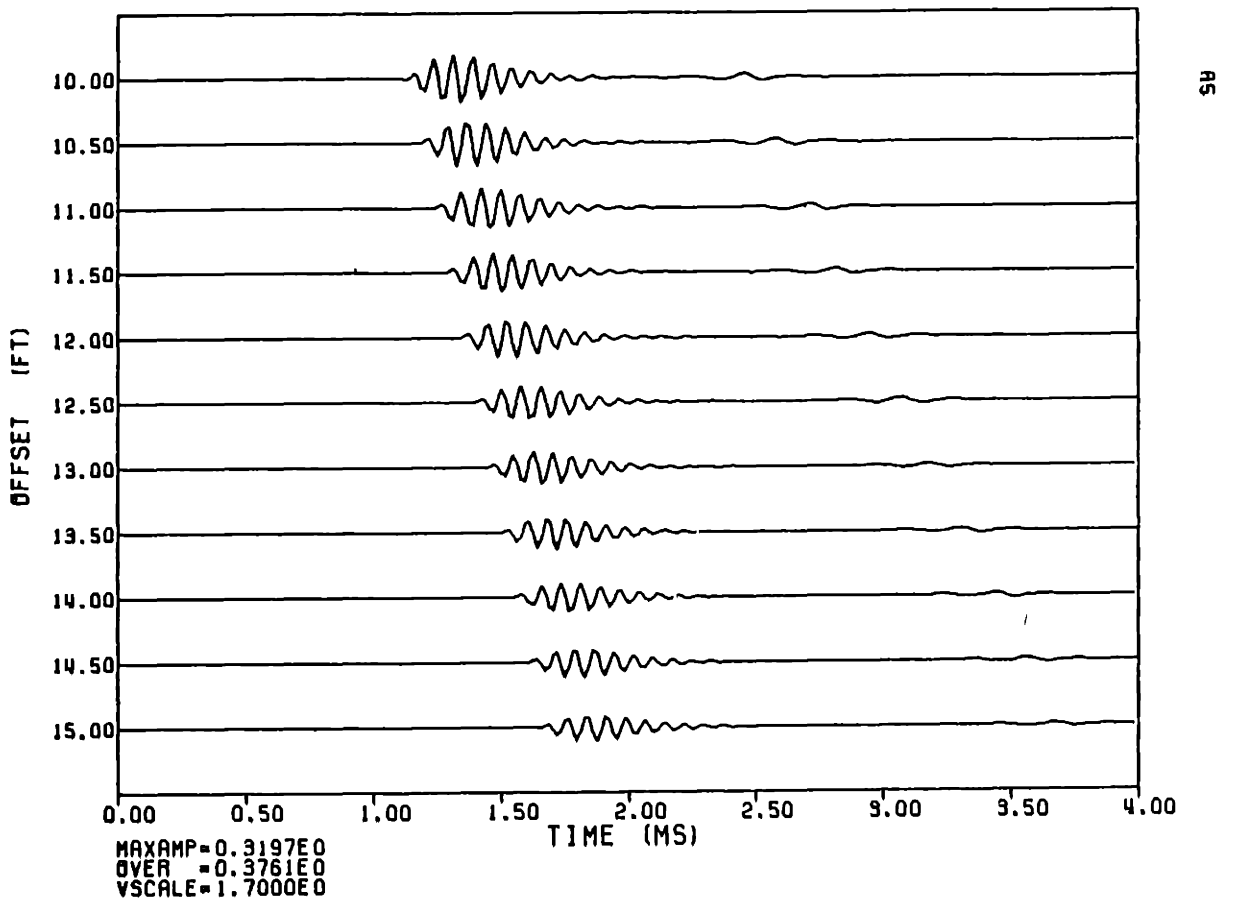

FIG. 3.19

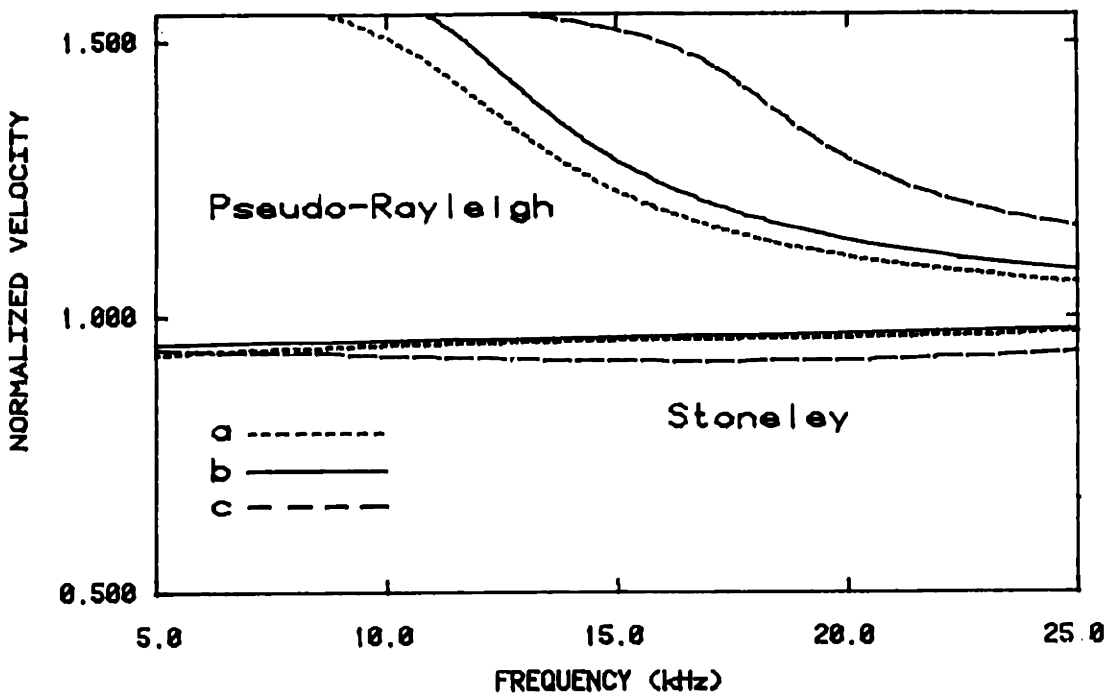
1.500
1.000
0.500
NORMALIZED VELOCITY
Pseudo-Rayleigh
Stoneley
a
b
c
5.0
10.0
15.0
20.0
25.0
FREQUENCY (kHz)

FIG. 3.20

R (FT)	VP (FT/MS)	VS (FT/MS)	RHO (GM/CC)	QP	QS
0.300000	5.5000	0.	1.2000	20.00	0.
0.333333	20.0000	11.0000	7.5000	1000.00	1000.00
0.	9.5000	5.0000	2.0000	100.00	50.00

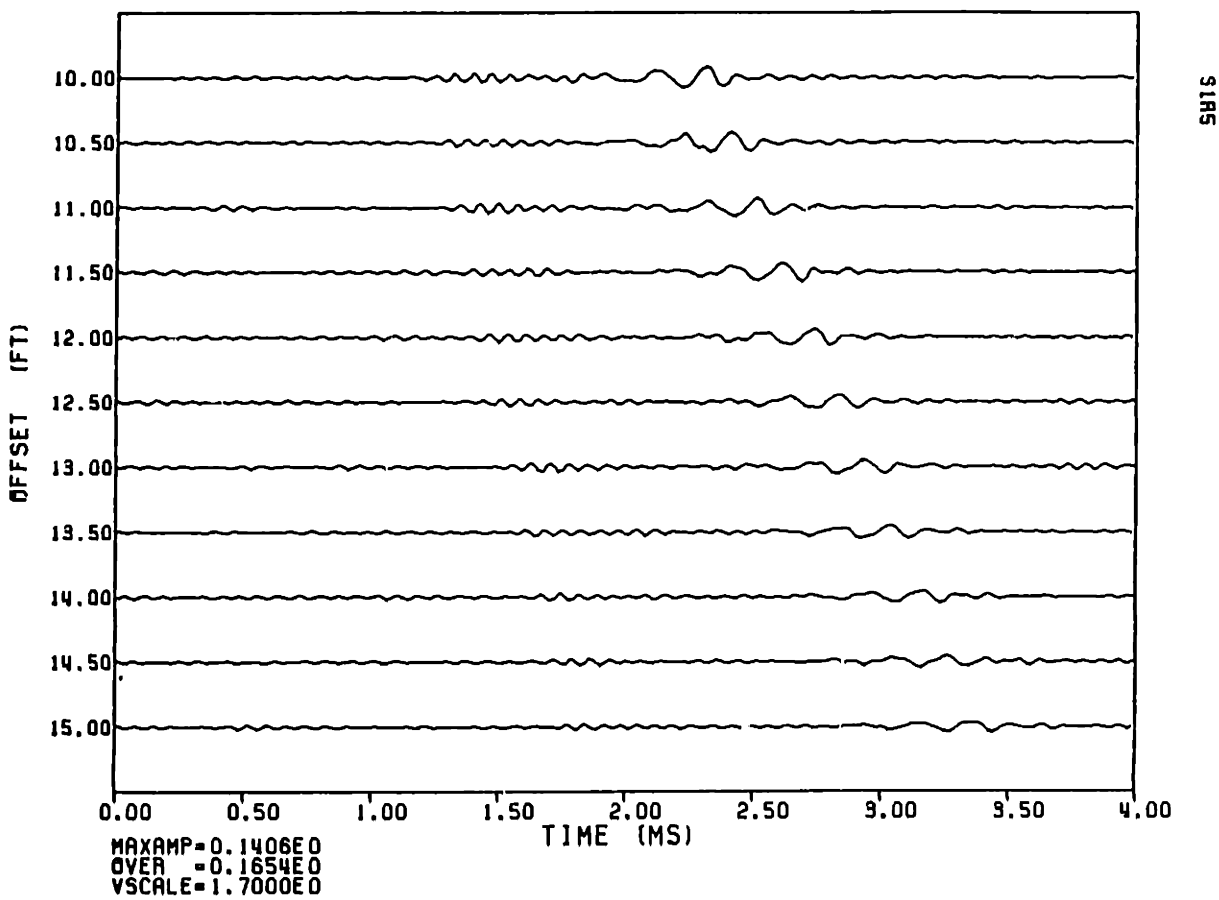

FIG. 3.21

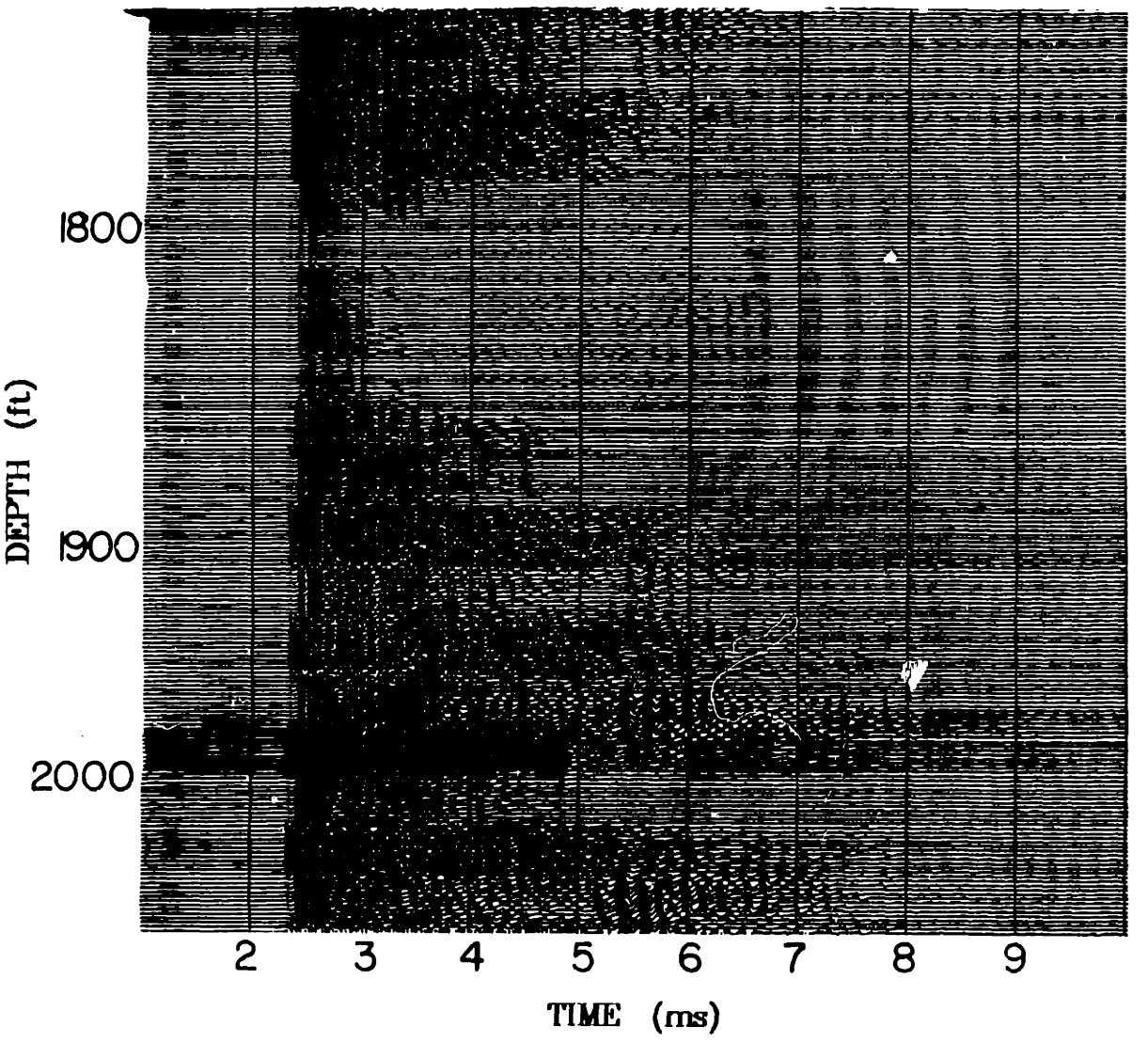

FIG. 3.22

H (FT)	VP (FT/MS)	VS (FT/MS)	RHO (GM/CC)	QP	QS
0.154167	5.5000	0.	1.2000	20.00	0.
0.187500	20.0000	11.0000	7.5000	1000.00	1000.00
0.333333	13.5000	8.3000	1.9200	40.00	90.00
0.	16.0000	8.5300	2.1600	60.00	60.00

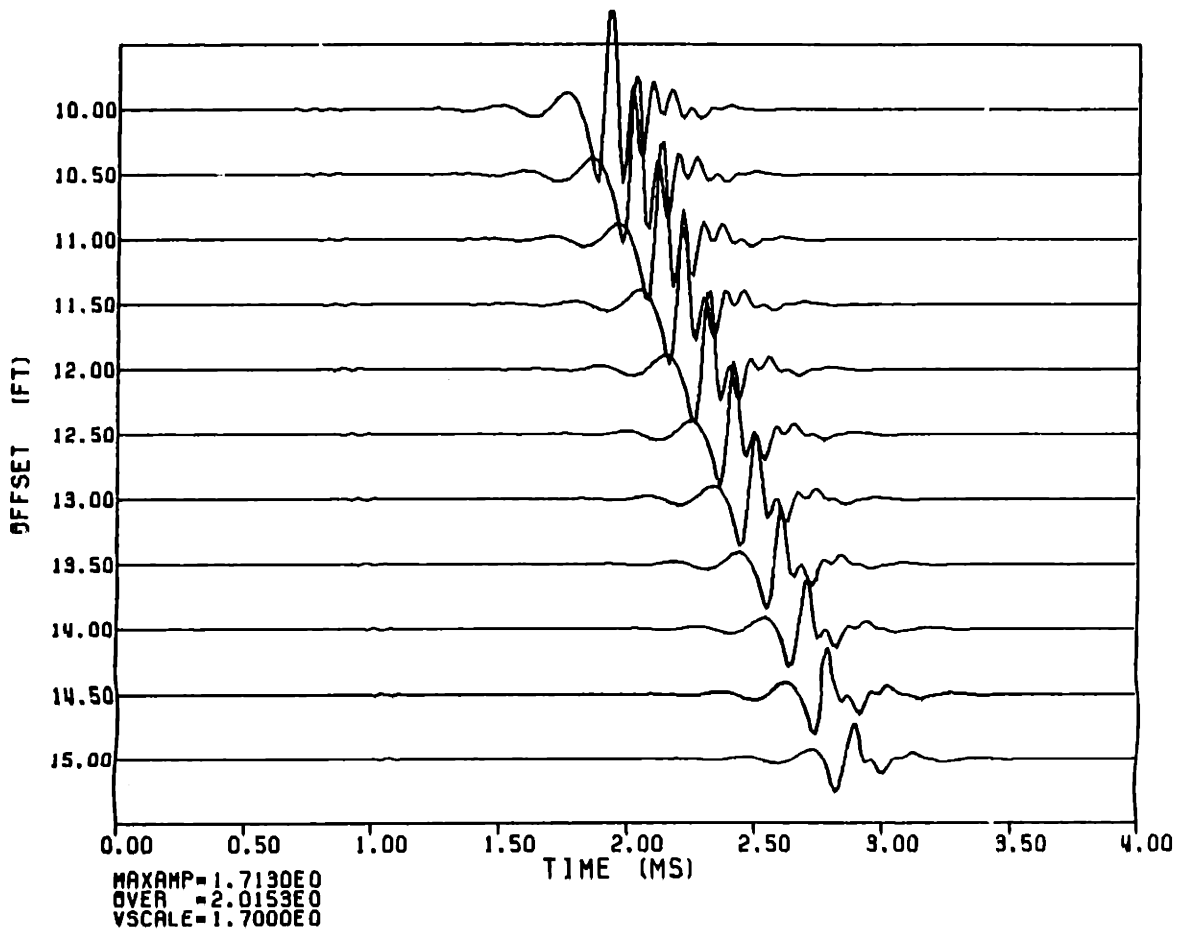

FIG. 3.23

H (FT)	VP (FT/MS)	VS (FT/MS)	RHO (GM/CC)	QP	QS
0.154167	5.5000	0.	1.2000	20.00	0.
0.220899	20.0000	11.0000	7.5000	1000.00	1000.00
0.933333	9.2590	5.6700	1.9200	40.00	90.00
0.	16.0000	8.5300	2.1600	60.00	60.00

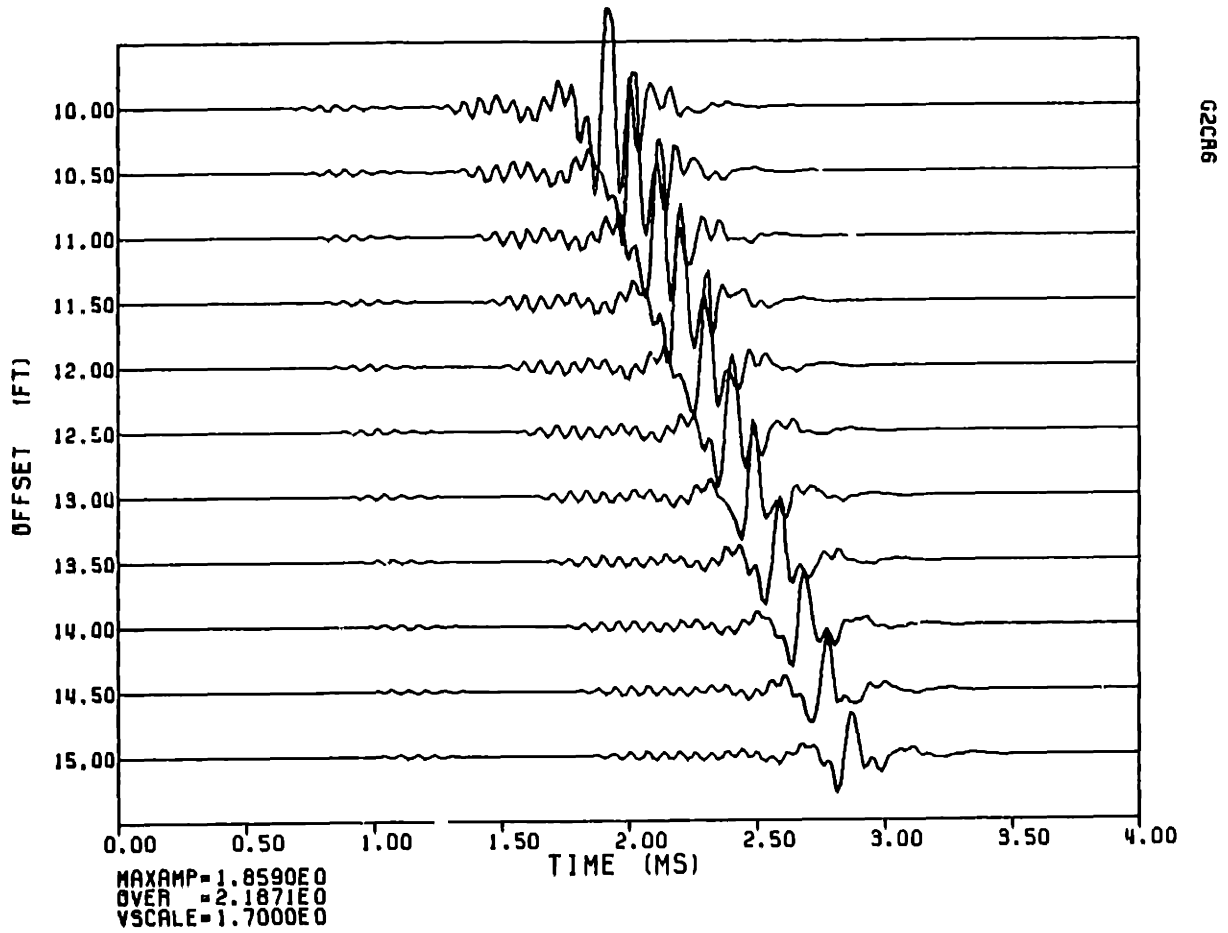

FIG. 3.24

A (FT)	VP (FT/MS)	VS (FT/MS)	RHO (GM/CC)	QP	QS
0.154167	5.5000	0.	1.2000	20.00	0.
0.187500	20.0000	11.0000	7.5000	1000.00	1000.00
0.333333	19.5000	8.3000	1.9200	40.00	30.00
0.	13.1200	7.0000	2.1600	60.00	60.00

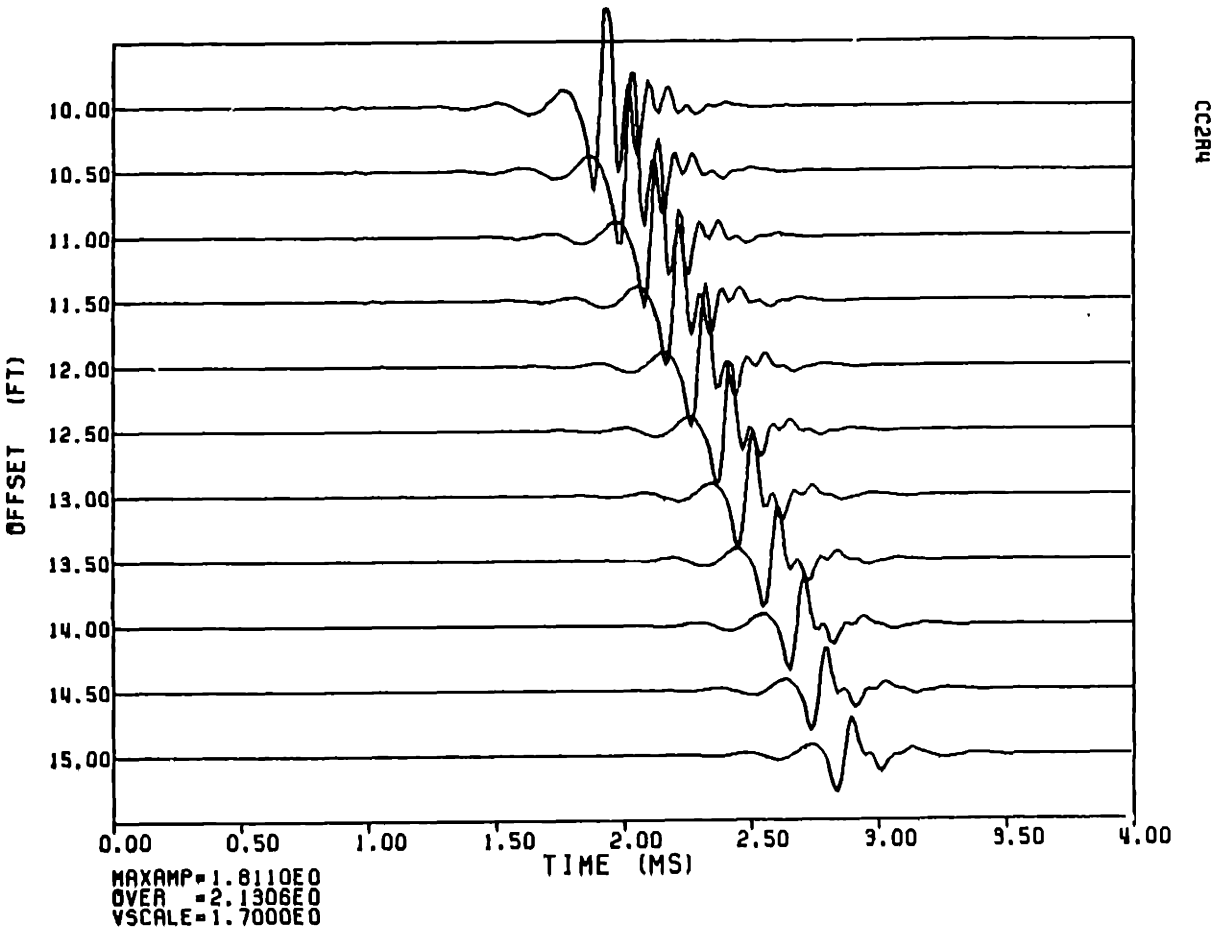

FIG. 3.25

R (FT)	VP (FT/MS)	VS (FT/MS)	RHO (GM/CC)	QP	QS
0.154167	5.5000	0.	1.2000	20.00	0.
0.187500	20.0000	11.0000	7.5000	1000.00	1000.00
0.333333	9.2590	5.6700	1.9200	40.00	30.00
0.	16.0000	8.5300	2.1600	120.00	120.00

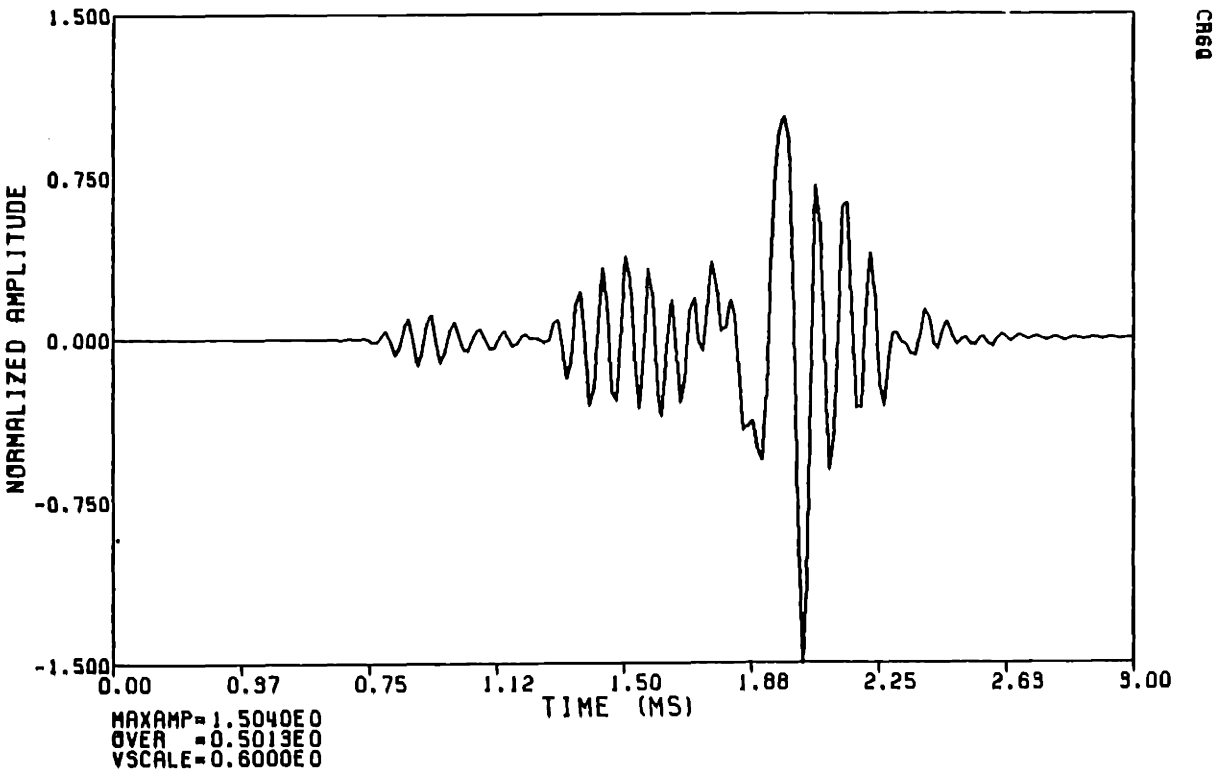

FIG. 3.26

A (FT)	VP (FT/MS)	VS (FT/MS)	RHO (GM/CC)	QP	QS
0.154167	5.5000	0.	1.2000	20.00	0.
0.187500	20.0000	11.0000	7.5000	1000.00	1000.00
0.333333	9.2590	5.6700	1.9200	80.00	60.00
0.	16.0000	8.5300	2.1600	60.00	60.00

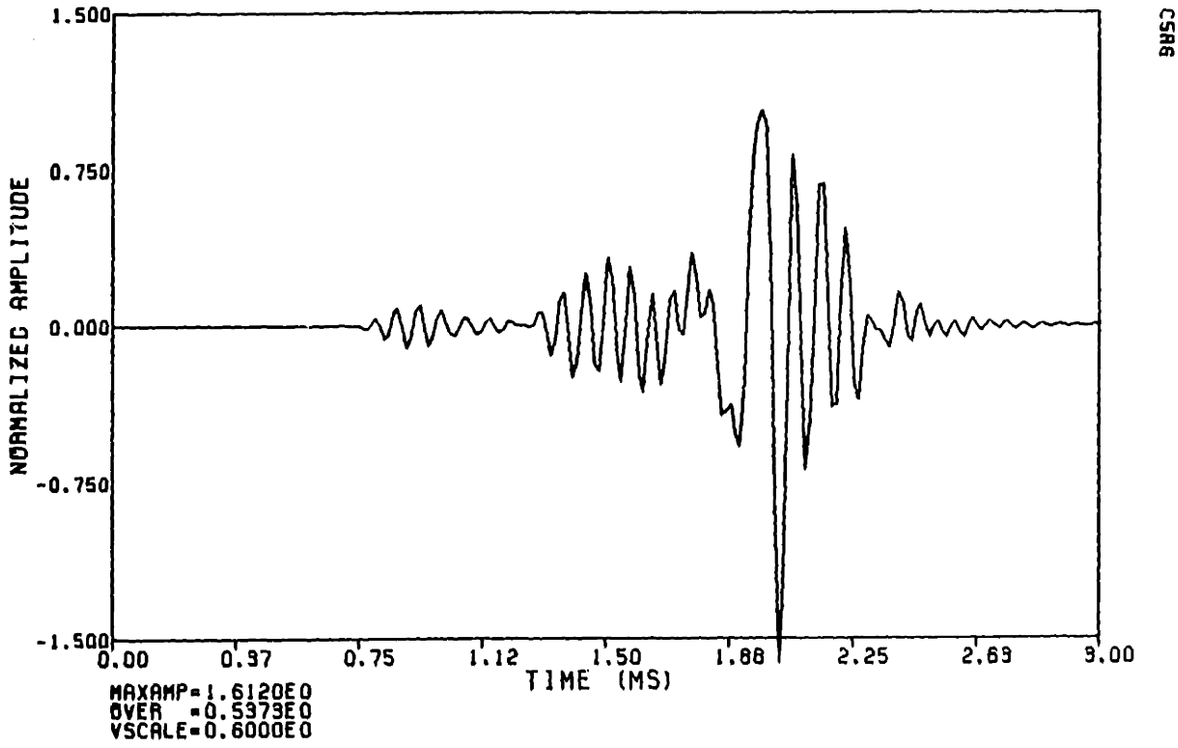

FIG. 3.27

Chapter 4

Poorly Bonded Cased Boreholes

4.1 Introduction

In the previous chapter the effects of adding a casing to the borehole were examined. The assumption was that the bonding conditions were ideal. Unfortunately, this is not always a reasonable approximation to the actual bonding conditions. There can be less than perfect bonding between any of the layers. The steel may not be bonded to the cement, and the cement may not be bonded to the formation. Fluid layers between the steel, cement, and formation can be large, as in the case of the free pipe hanging in the hole without being bonded to the formation or a zone were there is a large washout in the borehole wall. Thin layers are also possible. A coating of grease or imperfections on the outer wall of the casing can prevent the cement from bonding to the surface. The result is a thin layer between the steel and the cement commonly referred to as a microannulus.

The actual geometries in cased boreholes are difficult to know precisely. The radius and thickness of the pipe are usually given on the log report. A caliper log recorded in the hole before the casing is set gives

information on the hole radius. This, along with the casing dimensions can give an estimate of the cement thickness. It is often difficult though, to acquire any information about the type of cement used. Cement parameters vary greatly. Compressional velocities have been observed between 0.91 km/s (3 ft/ms) and 4.6 km/s (15 ft/ms) depending upon the composition, the curing time, and curing environment. Poisson's ratio for concrete as given by the American Concrete Institute ranges from about 0.18 to 0.22. Densities vary between 1.7 g/cm^3 and 2.0 g/cm^3.

Exact bonding conditions are also difficult to determine. The most common tool used to give a measure of the bonding conditions is the Cement Bond Log. This tool is similar in geometry to acoustic logging tools. The major differences are the much shorter source-receiver separations, typically 1-1.5m (3-5 feet), and the higher frequency source (20 kHz or higher). The conclusions about bonding conditions are based on relative amplitudes of arrivals at the beginning of the waveform and later arrivals. The source used in the modeling in this chapter is the same as that given in chapter 3. It is important to note that the slight non-causality of the source (described earlier) is more of a factor in the presence of the intermediate fluid layers in this chapter. The arrivals become emergent rather than impulsive. This is not a problem because velocities are determined between a number of offsets rather than from a single trace.

In this chapter we examine full waveform acoustic logs in boreholes with unbonded casing. The situation of unbonded casing and cement is modeled through the inclusion of fluid layers along with the solid layers of steel, cement, and formation. The fluid layers are placed in two common locations: between the steel and the cement, and between the cement and the formation. A fluid layer between the steel and the cement is used to study the free pipe situation. This is the case when there is no steel-cement bonding but good cement-formation bonding. Chang and Everhart (1983) studied the free pipe situation by allowing discontinuities in the axial displacement at the steel-cement interface and requiring zero axial stress at this boundary. There was no additional fluid layer though. The presence of the fluid layer in our model allows the investigation of the effects of the thickness of this layer rather than just its presence. A microannulus is modeled by having the thickness of the fluid layer become extremely thin.

The case of good steel-cement bonding but no cement-formation bonding is modeled with a fluid layer between the cement and the formation. This situation is more difficult to establish on field data. It is not able to be identified by a particular, consistent characteristic as in the free pipe situation where there is the obvious casing arrival.

4.2 No Steel-Cement Bond, Good Cement-Formation Bond

The situation of no steel-cement bonding but good cement-formation bonding is examined here by inserting a layer of fluid between the steel casing and the cement (see Figure 4.1) This is the free pipe situation.

In Figure 4.2, the fluid layer between the steel and the cement is taken to be 1.27 cm (0.5 inches) thick. This is the same formation used in Figure 3.12. With the addition of the intermediate fluid layer there is a large, distinct arrival at the beginning of the signal. The velocity of this arrival corresponds to the plate velocity of the steel, not the velocity of the formation. In the well bonded casing (Figure 3.12) the steel arrival was not obvious. With the pipe not well bonded to the cement, the casing arrival has a large amplitude and long duration. The formation P-wave arrival is overpowered by this signal. The above observation is consistent with field data (Walker, 1968; Grosmangin et al., 1961). Figure 4.3 shows data recorded in MIT's Burch well in Michigan using the EVA tool of Elf Acquitane. The source-receiver separation is 6.75 m (22.2 ft). The formation is the traverse limestone. This is a fast formation with a P-wave velocity of approximately 5 km/s (16.5 ft/ms). No cement was added to secure the pipe so the casing is hanging in the hole. The data display the characteristics described above. A large, ringing signal is the first arrival. This is the casing signal. There is no obvious arrival from the formation it is obscured by the casing arrival. Figure 4.4 is data that was recorded with

a 3.1 m (10 ft) offset. The tool passes from an uncased section into a region with poorly bonded casing. The beginning of the casing is indicated in the figure. Below the bottom of the casing, the first arrivals correspond to those of the formation. Above this point, a large signal from the casing is seen and the formation P-wave arrival is no longer identifiable.

Although the formation P-wave arrival is obscured by the casing signal in Figure 4.2, the formation shear arrival can be identified. There is still interference and overlap with casing arrivals though, and it would be difficult to distinguish the shear arrivals in field data.

The same geometry as Figure 4.2 is used in Figure 4.5 with different formation parameters. Here again, the first arrival is from the casing rather than from the formation. The character of the ringing first arrival is different here than in Figure 4.2 though. The duration of the signal has decreased. Changing the formation parameters has changed the nature of the microseismogram. This is due to the slower formation velocities in Figure 4.5 with respect to those in Figure 4.2. With the slower formation, the P-wave arrival time is at the tail end of the casing ringing. The P-wave arrival time for the formation in Figure 4.2 is earlier. This allows the formation energy to add in with the casing energy and cause a signal of longer duration. With the slower formation, the casing signal is starting to decay before the formation P-wave energy arrives. The duration of the first arrival decreases further if the formation is slower. The casing in

Figure 4.6 is the same as in Figures 4.2 and 4.5 but the formation is slow. The formation P-wave arrival is small and arrives after the casing arrival has ended.

Figures 4.7 and 4.8 further demonstrate the presence of the formation energy even with the free pipe. They are plots of the log-power of the frequency wavenumber information for the microseismograms in Figure 4.2 and 4.5. The location of the peaks corresponding to the casing energy is the same in both figures, but the peaks corresponding to the formation energy move as the formation parameters change.

The data in Figures 4.9 and 4.10 give an example of the formation arrivals being visible even with a poorly bonded casing. The source-receiver separation is 4.57 m (15 ft). These data were recorded in shales and soft, poorly consolidated sandstones. The formation velocities are slow, approximately 2.3 km/s (7.5 ft/ms) for V_p for the sandstone. The formation shear velocity is lower than the borehole mud velocity so there is no pseudo-Rayleigh wave. There are two zones in Figure 4.9 (at depths of 195 ft and 225 ft) where the bonding is poor. The formation arrival remains consistent through these regions. The upper section of Figure 4.10 was recorded with good bonding conditions. The formation arrival is clear and can be identified easily even down into the zone where the bonding deteriorates. The P-wave arrival can be followed through the entire section, but it is much more difficult at the lower depths where the

duration of the casing signal increases. It is feasible that the fluid layer between the steel and the cement is thin at the top of the unbonded section. This results in a casing arrival which decays before the arrival of the formation P-wave.

The differences in the character of the microseismograms is not as clear with a higher center frequency source (as is used for the Cement Bond Log). Figure 4.11 and 4.12 are the same models as Figure 4.2 and 4.5 with a different source function. The source spectrum retains the same shape but it is shifted so that the center frequency is 20 kHz. The higher frequency source puts much more energy into the thin, high velocity steel layer. The first arrivals in both cases are more similar and there is very little energy in the later portion of the time series.

A thin fluid layer yields results similar to the thicker layer geometry. Figures 4.13 and 4.14 present synthetic microseismograms in two different formations where the thickness of the fluid layer has been reduced to 2.54 $x10^{-3}$ cm (0.001 inches). This is the model of a microannulus. The first arrival is from the casing despite the very small thickness of the fluid layer. The velocities (both compressional and shear) of the formation in Figure 4.14 are less than those in Figure 4.13. The remainder of the model parameters are the same in both figures. There are no changes in the first arrivals in these cases as there were in the well bonded situations (Figures 3.12 and 3.14).

The model of Chang and Everhart (1983) is the same as this situation in the limit of the thickness of the fluid layer equal to zero. There was no actual fluid layer but they allow discontinuities in the axial displacement at the steel-cement interface. They demonstrated the same first arrival at the casing velocity even at the limit of zero fluid thickness.

Comparing Figures 4.2 and 4.13 (or 4.5 and 4.14) it is clear that the thickness of the fluid layer does affect the character of the microseismogram. While the first arrival in both cases corresponds to the steel signal, the amplitude and duration of the this arrival are different with the different fluid layer thicknesses. This can explain data reported by Brown et al. (1970) which displayed both the casing arrival and what were assumed to be formation arrivals. When the data were recorded with pressure in the well, the amplitude of the casing signal decreased. The additional pressure pushes out on the pipe decreasing the size of the fluid layer between the casing and the cement.

The thickness of the fluid layer between the steel and the cement has influence only on the duration and amplitude of the ringing casing signal, not its arrival time. The important factor in determining the first arrival is whether or not the pipe is bonded to the cement.

Figure 4.15 shows a number of microseismograms for the free pipe situation. All microseismograms are for the same source-receiver separation, 3.05 m (10 feet), and source, centered at 13 kHz. The

formation velocities are 4 km/s (13.12 ft/ms) for V_p and 2.12 km/s (7.0 ft/ms) for V_s (as in Figure 4.4). The difference in the models is the thickness of the fluid layer between the steel and the cement. The distance between the steel and the formation remains constant, so the cement thickness decreases as the fluid thickness increases. The fluid is replacing cement. The first microseismogram in Figure 4.15 has no fluid layer. This is the well bonded situation. The last waveform has no cement layer. The layers are just ones of fluid, steel, fluid, and the formation. Between these two extremes the thickness of the fluid layer increases in 0.64 cm (0.25 inch) increments (and the thickness of the cement layer decreases by this amount).

There is a large change in the character of the waveforms when the fluid layer is introduced. The microseismogram for the well bonded situation displays clear formation P-wave and S-wave arrivals. There is no distinct casing arrival. The additional fluid layer frees the pipe so the casing arrival is obvious. The ringing from the steel completely obscures the formation arrival. Little change occurs in the waveforms as the thickness of the fluid layer increases. The casing arrival dominates throughout, although an increase in the amplitude and duration of this pipe signal may be observed as the fluid layer becomes larger.

Phase velocity dispersion curves corresponding to some of the microseismograms of Figure 4.15 are shown in Figures 4.16 to 4.19. The

first one, Figure 4.16, gives the phase velocity dispersion relations for the well bonded cased hole situation. There are three distinct modes in the frequency range shown: the Stoneley and two for the pseudo-Rayleigh waves. (Only a small portion of the second pseudo-Rayleigh mode is seen.) The Stoneley wave is only slightly dispersive and is not cut off at low frequencies. The pseudo-Rayleigh curves are much more dispersive and have a cut off at the shear velocity of the formation.

A fluid layer of thickness 0.64 cm (0.25 inches) has been inserted between the steel and the cement in Figure 4.17. As before, the thickness of the cement is 0.64 cm (0.25 inches) less. The pseudo-Rayleigh curves are shifted to lower frequencies than in the well bonded situation. The extra fluid layer could be causing an effect similar to that produced by an increase in the borehole effective radius (Cheng and Toksöz, 1981; Tubman et al., 1984a). The Stoneley velocity is slightly lower at high frequencies but the curve has not changed substantially. The interesting thing to note in Figure 4.17 is the presence of an additional Stoneley mode. This additional mode is due to the presence of the intermediate fluid layer between the steel and the cement. This mode has significantly lower velocity and is more dispersive than the primary one which is observed in all situations.

In Figure 4.18 the thickness of the fluid layer is increased to 3.81 cm (1.5 inches). The pseudo-Rayleigh curves have moved to still lower frequencies but the general shape of the curves has not changed. The first

Stoneley mode has lower velocities in a small region about 20 kHz but the shift is not significant. The second Stoneley mode has moved to much higher velocities. The Stoneley modes are now almost identical to those that observed in the case of no cement layer (Figure 4.19.)

The fluid layer has been decreased in thickness in Figure 4.20. This is the model of the microannulus. The fluid layer has a thickness of only 2.54 $x\,10^{-3}$ cm (0.001 inches). The pseudo-Rayleigh velocities have shifted back slightly to higher frequencies. The first Stoneley mode shows minor changes but the additional mode is now gone. The fluid layer is now too thin to support the propagation of the addition mode.

It is important to note that this additional Stoneley mode has not been observed in the microseismograms. This can be understood by looking at the frequency-wavenumber information (Figure 4.21). The arrival in question is the first encountered (counter-clockwise) from the kr axis. Clearly, there is very little energy associated with this wave. The power is not sufficient to be observable in the time domain. Figures 4.22 and 4.23 show the radial displacements for the two Stoneley modes as a function of radius. The peak displacements are less for the additional mode than for the primary mode by more than a factor of 35. At the center of the borehole, where the signals are measured, the amplitude of the displacement has decayed to almost zero.

4.3 Good Steel-Cement Bond, No Cement-Formation Bond

Another common occurrence in cased holes is good steel-cement bonding but poor cement-formation bonding. The intermediate fluid layer is between the cement and the formation so the steel casing is now clad with a layer of cement (see Figure 4.24). This cement layer strongly affects the behavior of the pipe.

In Figure 4.25 the thickness of the fluid layer is 0.16 cm (0.0625 inches) and the thickness of the cement layer is 4.29 cm (1.6875 inches). The arrival from the casing is very small and is difficult to identify. The velocity of the first obvious arrival corresponds to the P-wave velocity of the formation. The formation S-wave arrival is also clear. To check that these are indeed the formation arrivals, the casing parameters and geometry are held constant as the formation velocities are modified. The microseismograms shown in Figure 4.26 are for a formation with lower P- and S-wave velocities than in Figure 4.25. It is clear from this figure that the arrival times and velocities of the body waves have changed as the formation velocities change. Velocities determined from this figure confirm that the observed arrivals are from the formation and not from the casing. The cement is sufficiently thick here to damp out the ringing of the casing. The pipe can not generate a signal with large amplitude and long duration as is observed in the free pipe geometry so the formation arrivals are clear.

A thick cement layer bonded to the pipe is not sufficient to ensure that the formation arrival will be clear and distinct. Figures 4.27 and 4.28 have the same amount of cement (4.29 cm, 1.6875 inches) bonded to the pipe as in the previous geometry (Figure 4.25 and 4.26). The fluid layers are of different thicknesses though. The hole radius is larger in Figures 4.27 and 4.28 so that the fluid layer thickness is 3.18 cm (1.25 inches) compared with 0.16 cm (0.0625 inches) in Figure 10. While the formation signals are small in Figures 4.25 and 4.26, they are clear and able to be distinguished. The first arrivals with the thicker intermediate fluid layer are difficult to identify. The cement is sufficiently thick to prevent the casing from ringing, but the fluid layer (with low Q values) is sufficiently thick to cause a large reduction in the formation amplitudes.

If the amount of cement bonded to the steel is small it will not be able to damp out the casing arrivals effectively. Figure 4.29 shows the synthetic microseismograms for a model with a cement layer thickness of 1.27 cm (0.5 inches) and a fluid layer thickness of 3.18 cm (1.25 inches). The amplitude of the first arrival has increased relative to the previous cases of thicker cement. The duration of this portion of the waveform has also increased substantially. (When we discuss the first arrival, we are referring to the earliest arrivals on the microseismogram consisting of approximately 6 cycles over a span of about .7 ms). The formation shear and pseudo-Rayleigh wave arrivals are now much more difficult to identify due to overlapping with the ringing of the earlier arrival.

The velocity determined for the first arrival is 4.94 km/s (16.2 ft/ms), very close to the formation P-wave velocity of 4.88 km/s (16 ft/ms). Changing the formation parameters has little effect on the shape or velocity of this first arrival though. This is seen in Figure 4.30, which was calculated with the same geometry but with a slower formation and Figure 4.31 where the formation is soft. The first wave packets on waveforms in Figures 4.29, 4.30 and 4.31 are virtually identical. This arrival is behaving independently from the formation parameters. The velocity of this first arrival is determined to be between the plate velocity of the steel and the velocity of the cement. In Figure 4.32 the velocities of the cement have been increased so that they are now comparable to the formation velocities. This relationship between the cement and formation velocities in the well-bonded cased hole resulted in significantly reduced amplitudes of the first arrival (Figure 3.26). Here, the amplitudes and shape of the first arrival are almost unchanged. The velocity has increased though, to 5.43 km/s (17.8 ft/ms), due to the faster cement.

It is interesting to note the complexity of the first arrival observed on the microseismograms in Figures 4.29-4.32. The steel and cement are ringing together as a composite two layered cylinder. The nature of the propagation in such geometries is complicated by the presence of a large number of modes (Whittier and Jones, 1967). This results in the various peaks associated with the combined steel and cement propagation.

Figure 4.33 is the same as Figure 4.15 except that the intermediate fluid layer is now located between the cement and the formation. The first microseismogram has no intermediate fluid layer and the last has no cement layer. (These are the same waveforms shown in Figure 4.15.) Here it is clear that the character of the waveform changes as the thicknesses of the fluid and cement layers change. With the thick cement layer and thin fluid layer the formation arrival can be distinguished. At the other extreme, with a thin cement layer and a thick fluid layer, the waveform has basically the same appearance as that in the free pipe situation. The first arrival varies as the amount of cement bonded to the steel varies. This first arrival appears to be a signal due to the combination of the steel and the cement. A larger amount of cement damps out the ringing of the pipe decreasing the amplitude and duration of the first arrival. The cement is also much slower than the steel, so increased influence on the velocity of the first arrival (due to the greater thickness) results in a lower velocity. It should be noted that while the change in velocity of the first arrival is fairly clear in Figure 4.33, the cement velocity used is much less than the velocity of the steel. If the cement was faster, the change in velocity would be much less apparent. The cement only influences the velocity of the first arrival to be less than that of the steel. The steel velocity still is an important factor. The amplitude and velocity of this arrival increase with decreasing thickness of the cement layer. A similar amplitude variation of the casing signal with cement thickness was

observed by Walker (1968) using data from test wells with controlled bonding situations. Pardue et al. (1962) found the amplitude of the casing arrival decreases with increasing cement compressive strength. A stronger cement is able to damp out the ringing of the steel more efficiently.

Riddle (1962) refers to the geometry considered here (good steel-cement bonding with poor cement-formation bonding). In both experimental data and field data he observes a wave which he identifies as a body wave along the cement. Figures 4.34 and 4.35 are taken from his paper and all display a wave arriving after the expected time of the casing arrival, but before the formation arrival time. Rather than a cement wave, this could be explained as the signal from the steel and cement combined. Figure 4.35 is field data and so the cement composition is not known but Figure 4.34 is from experimental conditions. The steel is bonded to the cement and immersed in a large water filled testing tank. Because of the long curing time, the velocity of the cement is high. Data is given showing the velocity of cement to be approximately 3.66 km/s (12 ft/ms) after a few days of curing. The high cement velocities would result in a higher combined velocity.

Figures 4.36 to 4.38 show similar behavior for the dispersion curves as in the free pipe situation. A thicker intermediate fluid layer shifts the pseudo-Rayleigh dispersion curves to lower frequencies relative to the thin layer (Figures 4.36 and 4.37). The primary Stoneley mode changes only

slightly and the additional Stoneley mode has significantly higher phase velocity with the thicker fluid layer. Again, the second Stoneley mode disappears completely when the thickness of the fluid layer is very small (Figure 4.38). A thick fluid layer yields curves that are virtually the same as those with no cement layer.

4.4 Summary

The addition of an intermediate fluid layer can have a large effect on the observed waveforms. More surprisingly, this additional layer may have only minor effects, indicating possible difficulties in establishing its presence. The location and thickness of the fluid layer, and the thickness of the accompanying cement layer are all important factors in determining the character of the microseismogram.

A fluid layer between the steel and cement essentially frees the steel casing. The result is that the casing arrival becomes larger in amplitude and longer in duration than in the well bonded geometry. The casing signal in this situation can obscure the formation P-wave arrival. The amplitude and duration of the ringing are affected by the thickness of the fluid layer between the steel and the cement. A large layer yields a long, high amplitude arrival. A very thin layer, or microannulus, results in a relatively small casing signal. The first arrival is from the casing though, regardless of the thickness of the fluid layer. It is the the existence of this layer, not its thickness, that is the most important factor in determining

the presence of an observable casing arrival.

When there is good bonding between the steel and the cement but poor bonding between the cement and the formation the situation is more complicated. It may be possible to discern the formation body wave arrivals even in the presence of a fluid layer between the cement and the formation. If the fluid layer is thin and there is a large amount of cement bonded to the steel, the cement will act to damp out the ringing of the pipe, making the formation arrivals clear. If the cement layer is sufficiently thin, it will ring along with the steel casing. The first arrival in this situation will be from the combination of the steel and the cement and will have a velocity intermediate to their velocities. The velocity of this wave is controlled by the velocities and thicknesses of the steel and the cement layers. A thicker cement layer will have more influence on the velocity causing it to be lower.

An intermediate fluid layer is shown to have the additional effect of introducing another Stoneley wave mode provided that the layer is of sufficient thickness. This mode contains only a small amount of energy and so it does not contribute significantly to the observed microseismograms.

Figure	thickness cm (inches)	V_p km/s (ft/ms)	V_s km/s (ft/ms)	ρ gm/cm^3	Q_α	Q_β
all figures	4.7 (1.85)	1.68 (5.50)	–	1.2	20.	–

Table 4.1. Borehole fluid parameters for theoretical models.

Figure	thickness cm (inches)	V_p km/s (ft/ms)	V_s km/s (ft/ms)	ρ gm/cm^3	Q_α	Q_β
all figures	1.02 (0.40)	6.1 (20.0)	3.35 (11.00)	7.5	1000.	1000.

Table 4.2. Steel parameters for theoretical models.

Figure	thickness cm (inches)	V_p km/s (ft/ms)	V_s km/s (ft/ms)	ρ gm/cm^3	Q_α	Q_β
13,14, 20,38	2.54×10^{-3} (0.001)	1.68 (5.50)	–	1.2	20.	–
25,26	0.16 (0.0625)	1.68 (5.50)	–	1.2	20.	–
17,36	0.64 (0.25)	1.68 (5.50)	–	1.2	20.	–
2,5-8,11, 12,21-23	1.27 (0.5)	1.68 (5.50)	–	1.2	20.	–
27,28-32	3.18 (1.25)	1.68 (5.50)	–	1.2	20.	–
18,37	3.81 (1.5)	1.68 (5.50)	–	1.2	20.	–
19	4.44 (1.75)	1.68 (5.50)	–	1.2	20.	–

Table 4.3. Intermediate fluid layer parameters for theoretical models. Note that the variations are in thickness only.

Figure	thickness cm (inches)	V_p km/s (ft/ms)	V_s km/s (ft/ms)	ρ gm/cm^3	Q_α	Q_β
32	1.27 (0.50)	4.11 (13.5)	2.53 (8.30)	1.92	40.	30.
15,33	variable	2.82 (9.26)	1.73 (5.67)	1.92	40.	30.
18,37	0.64 (0.25)	2.82 (9.26)	1.73 (5.67)	1.92	40.	30.
29-31	1.27 (0.50)	2.82 (9.26)	1.73 (5.67)	1.92	40.	30.
2,5-8,11, 12,21-23	3.18 (1.25)	2.82 (9.26)	1.73 (5.67)	1.92	40.	30.
17,36	3.81 (1.50)	2.82 (9.26)	1.73 (5.67)	1.92	40.	30.
25-28	4.29 (1.6875)	2.82 (9.26)	1.73 (5.67)	1.92	40.	30.
13,14, 20,38	4.4425 (1.749)	2.82 (9.26)	1.73 (5.67)	1.92	40.	30.
16	4.445 (1.750)	2.82 (9.26)	1.73 (5.67)	1.92	40.	30.

Table 4.4 Cement parameters for theoretical models. Note that aside from the first case, all the variations are in thickness only.

Figure	thickness cm (inches)	V_p km/s (ft/ms)	V_s km/s (ft/ms)	ρ gm/cm^3	Q_α	Q_β
6,31	∞	2.9 (9.5)	1.52 (5.00)	2.0	100.	50.
5,8,12, 14-21,26, 28,30,32, 33,36-38	∞	4.0 (13.12)	2.13 (7.00)	2.16	60.	60.
2,7,11, 13,22,23, 25,27,29	∞	4.88 (16.00)	2.6 (8.53)	2.16	60.	60.

Table 4.5. Formation parameters for theoretical models.

Figure Captions

Figure. 4.1. Geometry of the free pipe model. The intermediate fluid layer is between the steel and the cement.

Figure 4.2 Microseismograms for the free pipe situation. There is a 1.27 cm (0.5 inch) fluid layer between the steel and the cement.

Figure 4.3 Data recorded with EVA in MIT's Burch well. There is no cement bonding the pipe to the formation. The source-receiver separation is 6.75 m (22.1 ft).

Figure 4.4 Data recorded as the tool passes from an open hole into a poorly bonded cased section. The source-receiver separation is 3.05 m (10 ft).

Figure 4.5 Microseismograms for the free pipe situation. The geometry is the same as in Figure 4.2 but the formation velocities are lower.

Figure 4.6 Microseismograms for the free pipe situation. The geometry is the same as in Figure 4.2 but the formation velocities are slow.

Figure 4.7 Log of the power of the ω–k information for Figure 4.2.

Figure 4.8 Log of the power of the ω–k information for Figure 4.5.

Figure 4.9 Data recorded in a cased borehole. The bonding is poor above 100 ft. and the formation arrivals are obscured. At depths of approximately 195 and 225 there are zones where the bonding is poor

but the formation P-wave arrivals are clear. The casing (C), formation P-wave (P), and Stoneley wave (ST) arrivals are indicated. The formation is slow so there is no unattenuated pseudo-Rayleigh wave.

Figure 4.10 Data recorded in cased borehole. The bonding conditions are good above 100 ft and the formation arrivals are clear. The formation P-wave arrival can be distinguished even below 100 ft where the bonding conditions worsen. The casing (c), formation P-wave (P), and Stoneley wave (ST) arrivals are indicated.

Figure 4.11 The same as Figure 4.2 except the center frequency is raised to 20 kHz. The vertical scale increased by a factor of 4.

Figure 4.12 The same as Figure 4.2 except the center frequency is raised to 20 kHz. The vertical scale increased by a factor of 4.

Figure 4.13 Microseismograms for the model of a microannulus. The formation is the same as that in Figure 4.2. The thickness of the fluid layer between the steel and the cement is 2.54×10^{-3} cm (0.001 inches).

Figure 4.14 Microseismograms for the model of a microannulus. The formation is the same as that in Figure 4.5. The thickness of the fluid layer between the steel and the cement is 2.54×10^{-3} cm (0.001 inches).

Figure 4.15. Microseismograms for various thicknesses of the fluid layer between the steel and the cement. This is the free pipe situation. The

source-receiver separation is 3.05 m (10 ft). The fluid layer thickness increases in 0.64 cm (0.25 inch) increments. The cement layer thickness decreases by this amount. The first microseismogram has no fluid layer (the well bonded case) and the last has no cement layer. The formation is the same as that in Figure 4.5.

Figure 4.16 Phase velocity dispersion curves for the well bonded situation. The Stoneley mode (ST) and two modes of the pseudo-Rayleigh (PR) are present in this frequency range. The velocities are normalized to the borehole fluid velocity.

Figure 4.17 Phase velocity dispersion curves for the free pipe situation where the thickness of the intermediate fluid layer is 0.64 cm (0.25 inches). There is an additional, lower velocity Stoneley mode due to the extra fluid layer.

Figure 4.18 Phase velocity dispersion curves for the free pipe situation where the thickness of the intermediate fluid layer is 3.81 cm (1.5 inches).

Figure 4.19 Phase velocity dispersion curves for the free pipe situation where there is not cement between the steel and the cement.

Figure 4.20 Phase velocity dispersion curves for the case of a microannulus. The thickness of the intermediate fluid layer is 2.54 $x\,10^{-3}$ cm (0.001 inches).

Figure 4.21 $\omega-k$ information for the free pipe situation. The fluid layer between the steel and the cement is 1.27 cm (0.5 inches) thick. The spectrum has been multiplied by the source function. The additional Stoneley mode (B) is significantly smaller amplitude than the other Stoneley mode (A) due to the central fluid cylinder.

Figure 4.22 Amplitude of the radial component of the Stoneley wave displacement for the Stoneley mode in the central fluid cylinder. The layer boundaries are indicated by vertical lines.

Figure 4.23 Amplitude of the radial component of the Stoneley wave displacement for the Stoneley mode in the intermediate fluid cylinder. The layer boundaries are indicated by vertical lines.

Figure 4.24 Geometry for the situation of good steel-cement bonding but poor cement-formation bonding. The intermediate fluid layer is between the cement and the formation.

Figure 4.25 Microseismograms for a case of good steel-cement bonding but poor cement-formation bonding. The thickness of the intermediate fluid layer is 0.16 cm (0.0625 inches). The formation is the same as in Figure 4.2. There is a large amount of cement bonded to the steel so there is not obvious casing arrival.

Figure 4.26 Same as Figure 4.25 except the formation velocities are lower. The formation is the same as in Figure 4.5.

Figure 4.27 Same as Figure 4.25 except the borehole radius is larger so the fluid layer between the cement and the formation is now 3.18 cm (1.25 inches) thick.

Figure 4.28 Same as Figure 4.27 with the lower formation velocities.

Figure 4.29 Microseismograms for a case of good steel-cement bonding but poor cement-formation bonding. The thickness of the cement is 1.27 cm (0.5 inches) and the thickness of the intermediate fluid layer is 3.18 cm (1.25 inches). The cement is not sufficiently thick to damp the ringing of the steel. The formation is the same as in Figure 4.2.

Figure 4.30 Same as Figure 4.29 with lower formation velocities.

Figure 4.31 Same as Figure 4.29 with a slow formation.

Figure 4.32 Same as Figure 4.29 with higher cement velocities. The velocity of the first arrival increases as a result of the change in cement velocities.

Figure 4.33 Microseismograms for various thicknesses of the fluid layer between the cement and the formation. The fluid layer thickness increases in 0.64 cm (0.25 inch) increments. The cement layer thickness decreases by this amount. The first microseismogram has no fluid layer (the well bonded case) and the last has no cement layer. The P velocity of the formation is 13.12 ft/ms and the S velocity is 7.0

ft/ms. The formation is the same as that in Figure 4.5.

Figure 4.34 Waveforms were recorded under experimental conditions. Steel is bonded to cement and immersed in a water filled tank. Taken from Riddle (1962).

Figure 4.35 Field data displaying an arrival with a velocity intermediate to those of the steel and the formation. Taken from Riddle (1962)

Figure 36. Phase velocity dispersion curves for the case of good steel-cement bonding but no cement-formation bonding. The intermediate fluid layer thickness is 0.64 cm (0.25 inches).

Figure 37. Phase velocity dispersion curves for the case of good steel-cement bonding but no cement-formation bonding. The intermediate fluid layer thickness is 3.81 cm (1.5 inches).

Figure 37. Phase velocity dispersion curves for a very thin (2.54×10^{-3} cm, 0.001 inch) fluid layer between the cement and the formation.

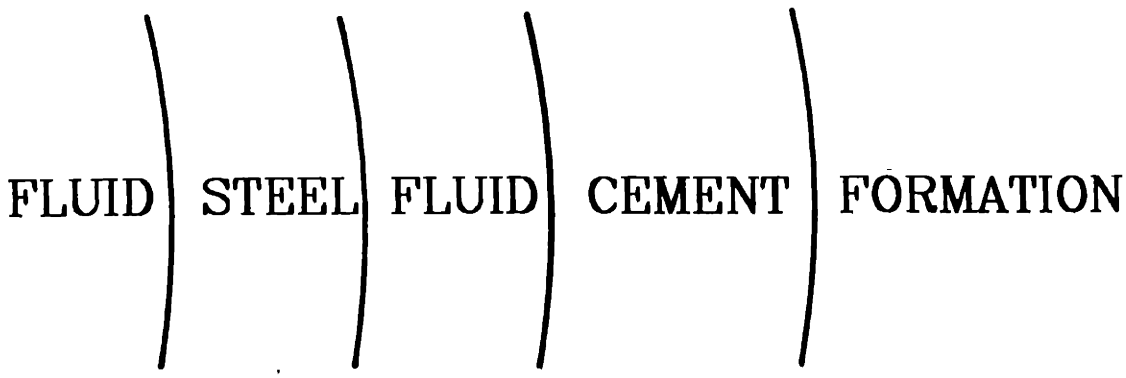
FLUID
STEEL
FLUID
CEMENT
FORMATION
ORIGINAL
BOREHOLE
RADIUS

FIG. 4.1

R (FT)	VP (FT/MS)	VS (FT/MS)	RHO (GM/CC)	QP	QS
0.154167	5.5000	0.	1.2000	20.00	0.
0.187500	20.0000	11.0000	7.5000	1000.00	1000.00
0.229167	5.5000	0.	1.2000	20.00	0.
0.333333	9.2590	5.6700	1.9200	40.00	30.00
0.	16.0000	8.5300	2.1600	60.00	60.00

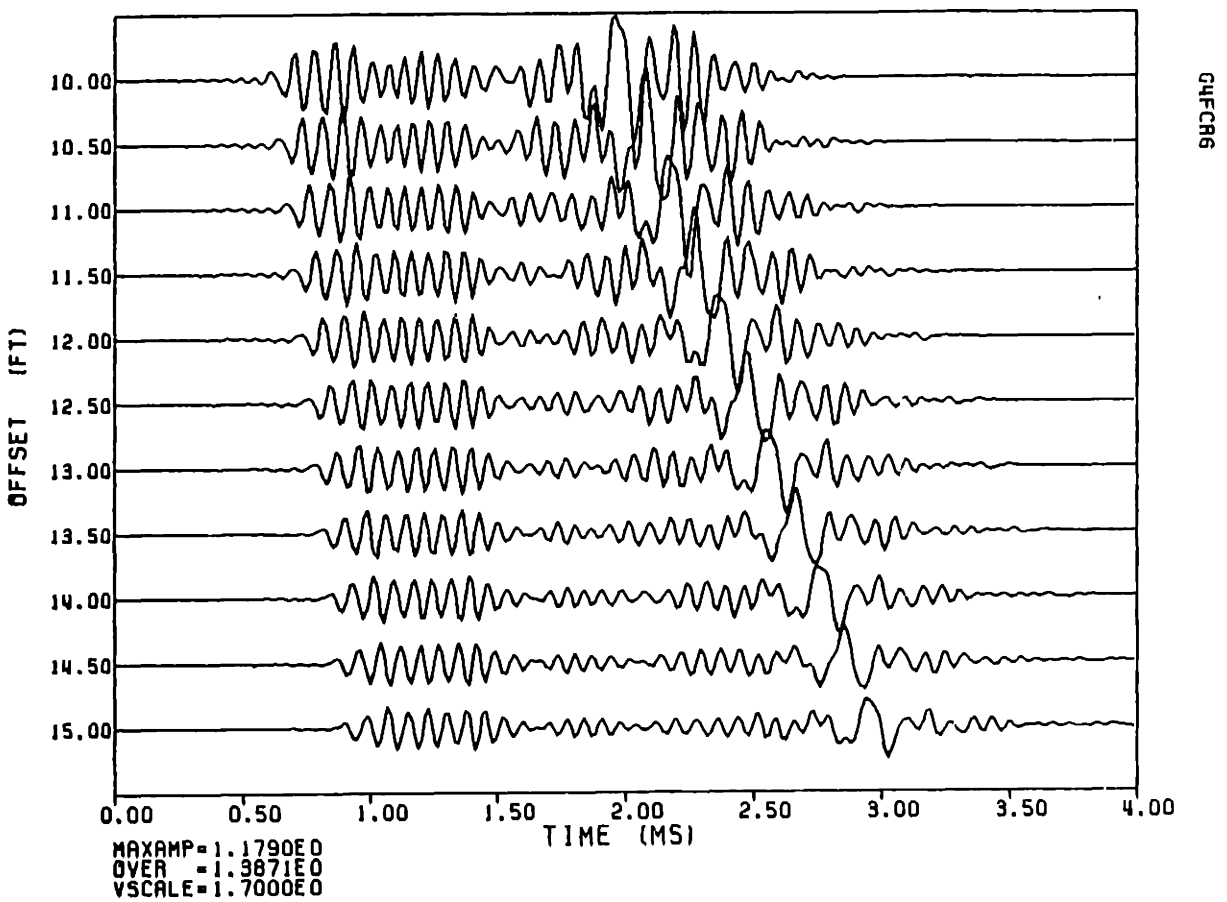

FIG. 4.2

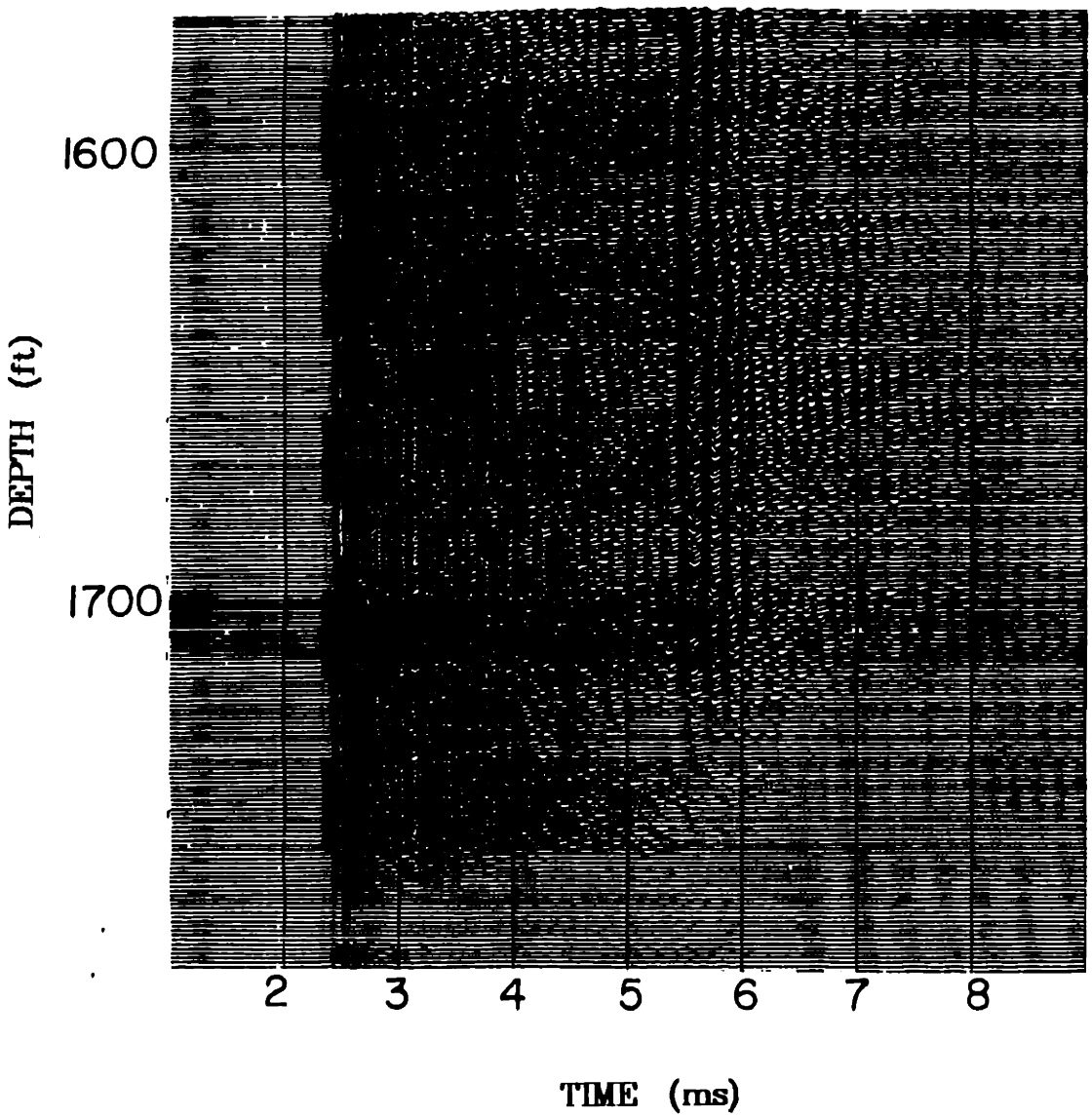

FIG. 4.3

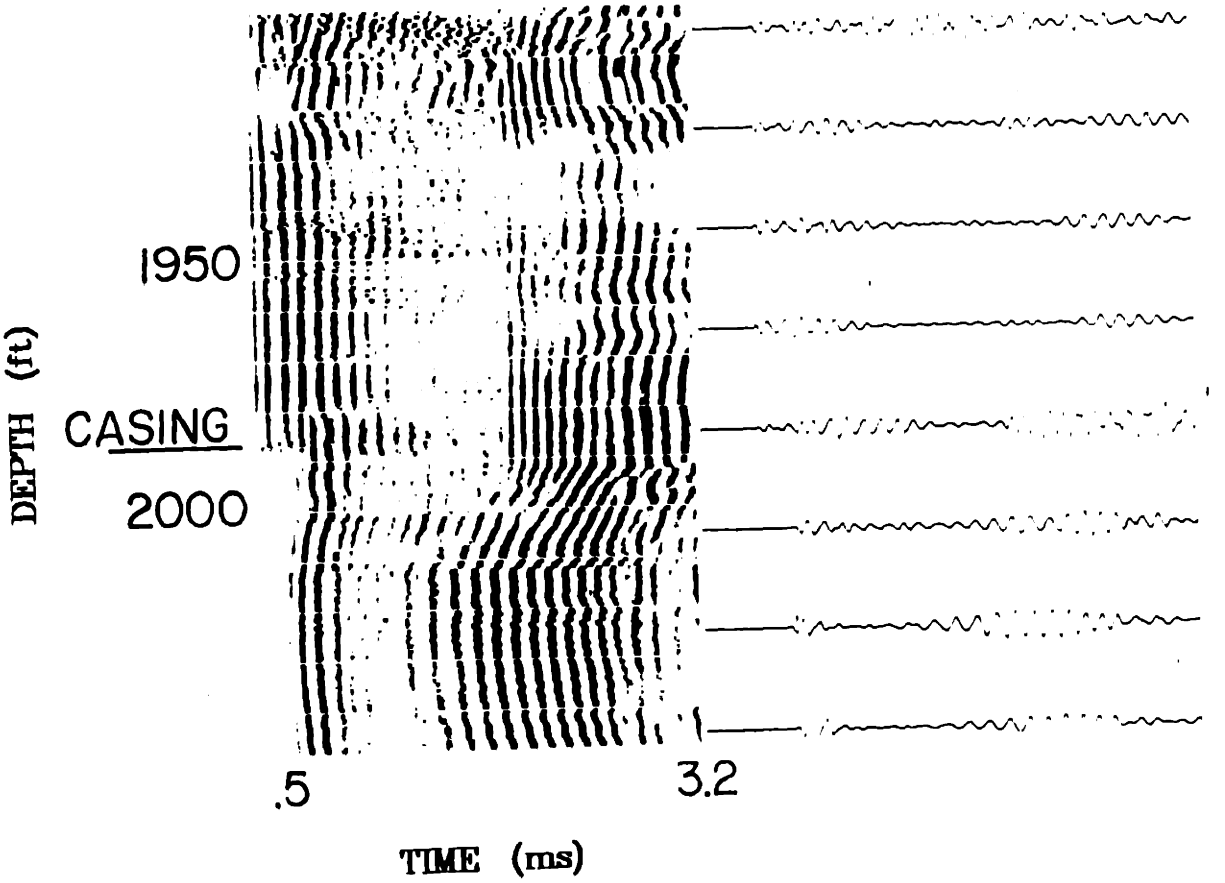

FIG. 4.4

R (FT)	VP (FT/MS)	VS (FT/MS)	RHO (GM/CC)	QP	QS
0.154167	5.5000	0.	1.2000	20.00	0.
0.187500	20.0000	11.0000	7.5000	1000.00	1000.00
0.229167	5.5000	0.	1.2000	20.00	0.
0.333333	9.2590	5.6700	1.9200	40.00	30.00
0.	13.1200	7.0000	2.1600	60.00	60.00

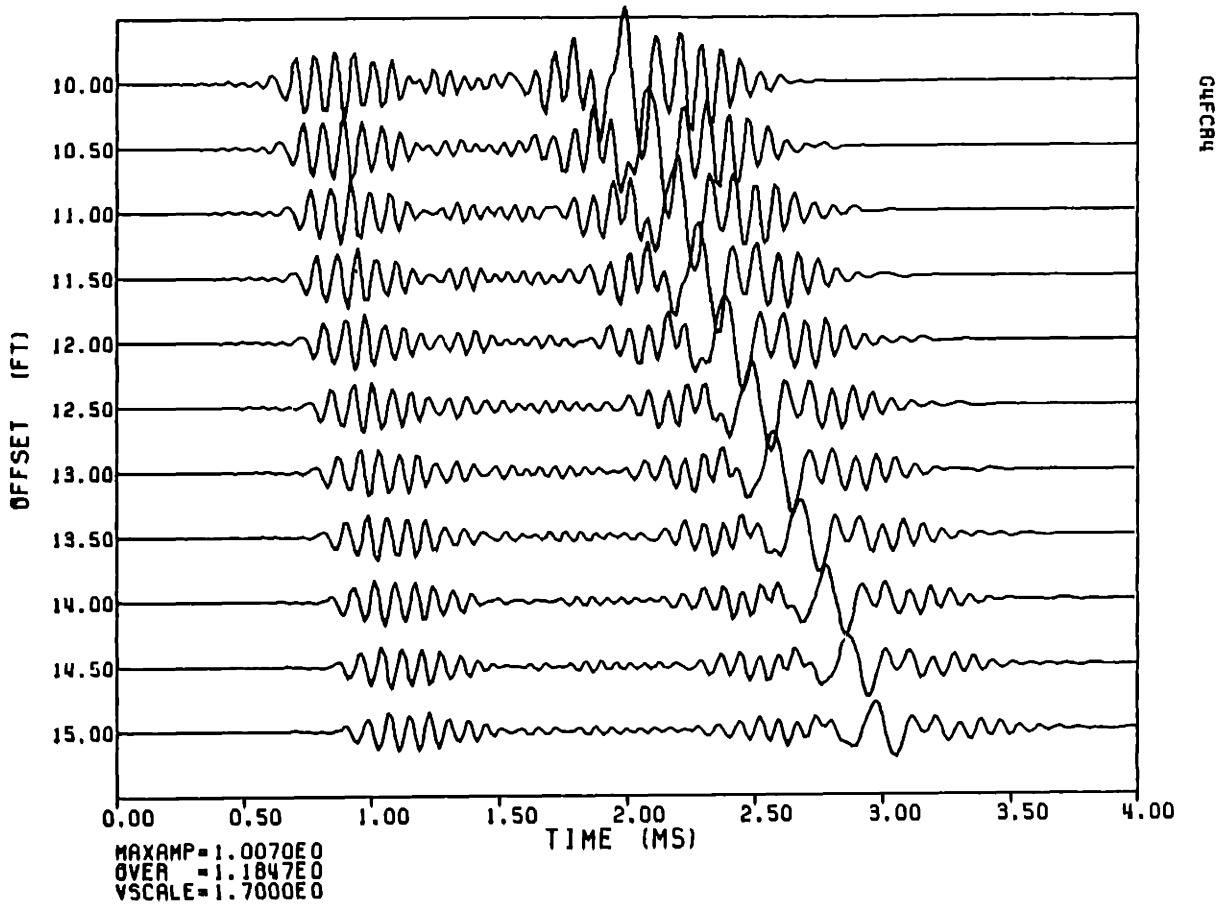

FIG. 4.5

H (FT)	VP (FT/MS)	VS (FT/MS)	RHO (GM/CC)	QP	QS
0.154167	5.5000	0.	1.2000	20.00	0.
0.187500	20.0000	11.0000	7.5000	1000.00	1000.00
0.229167	5.5000	0.	1.2000	20.00	0.
0.333333	9.2590	5.6700	1.9200	40.00	30.00
0.	9.5000	5.0000	2.0000	100.00	50.00

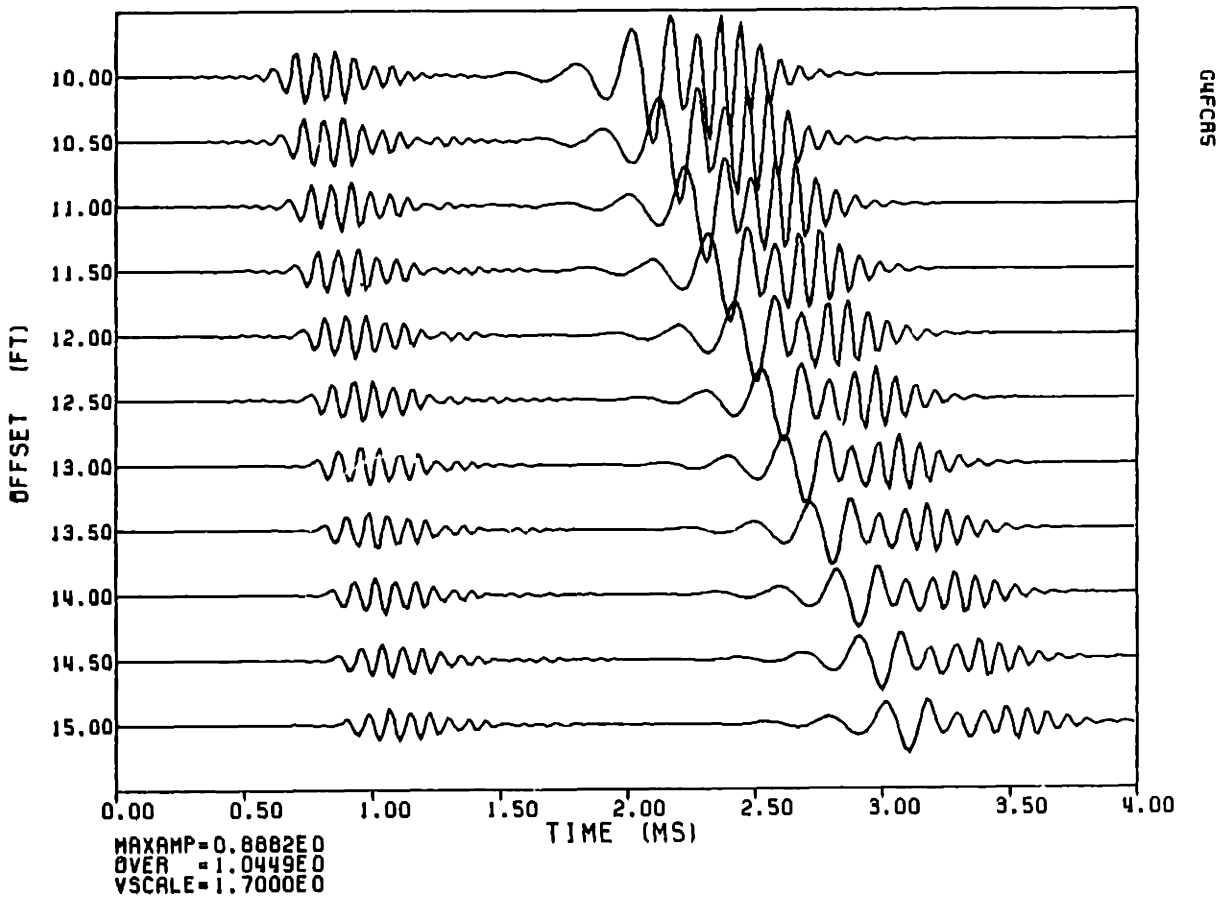

FIG. 4.6

R (FT)	VP (FT/MS)	VS (FT/MS)	RHO (GM/CC)	QP	QS
0.154167	5.5000	0.	1.2000	20.00	0.
0.187500	20.0000	11.0000	7.5000	1000.00	1000.00
0.229167	5.5000	0.	1.2000	20.00	0.
0.933333	9.2590	5.6700	1.9200	40.00	30.00
0.	16.0000	8.5300	2.1600	60.00	60.00

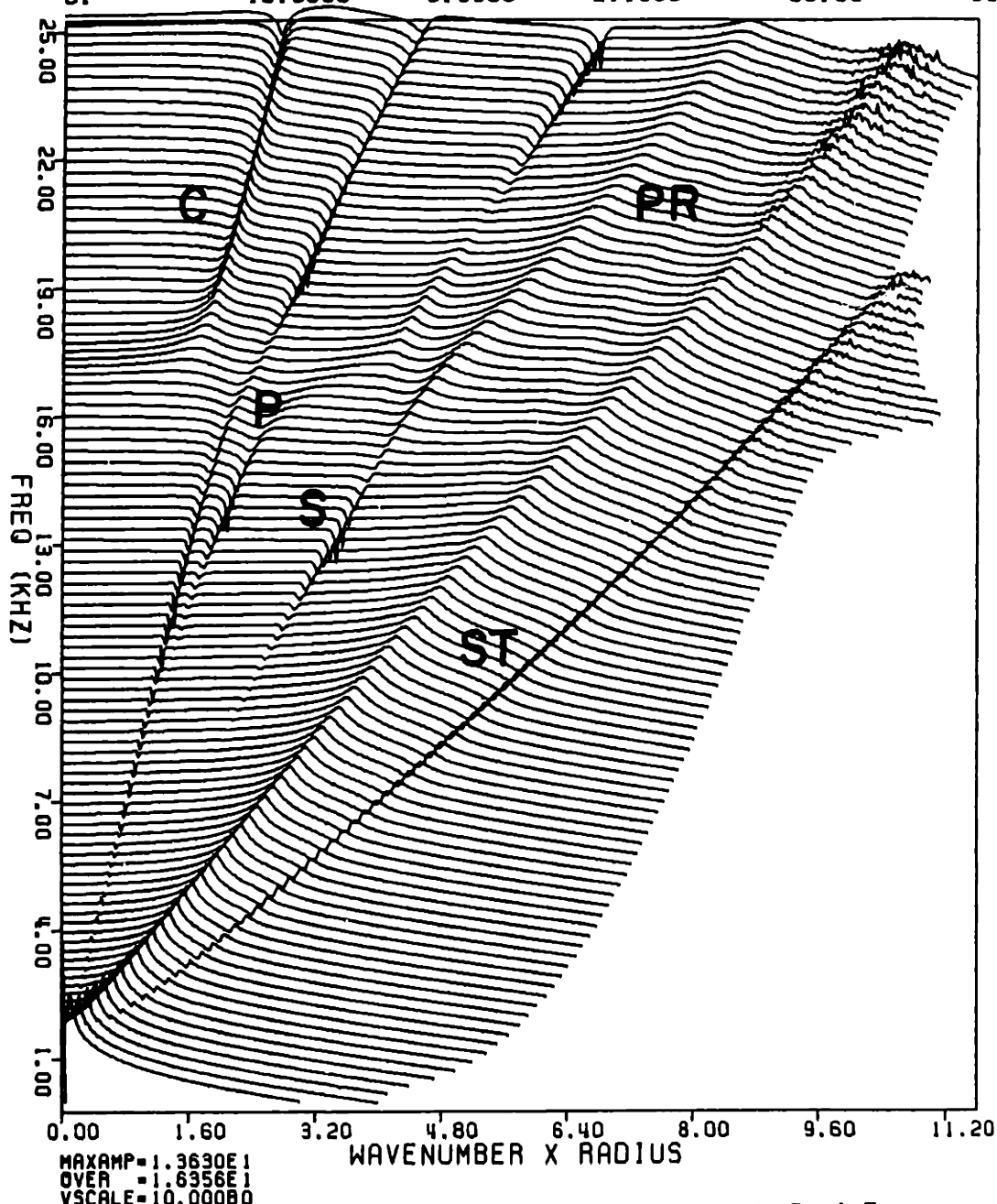

FIG. 4.7

R (FT)	VP (FT/MS)	VS (FT/MS)	RHO (GM/CC)	QP	QS
0.154167	5.5000	0.	1.2000	20.00	0.
0.187500	20.0000	11.0000	7.5000	1000.00	1000.00
0.229167	5.5000	0.	1.2000	20.00	0.
0.333333	9.2590	5.6700	1.9200	40.00	30.00
0.	13.1200	7.0000	2.1600	60.00	60.00

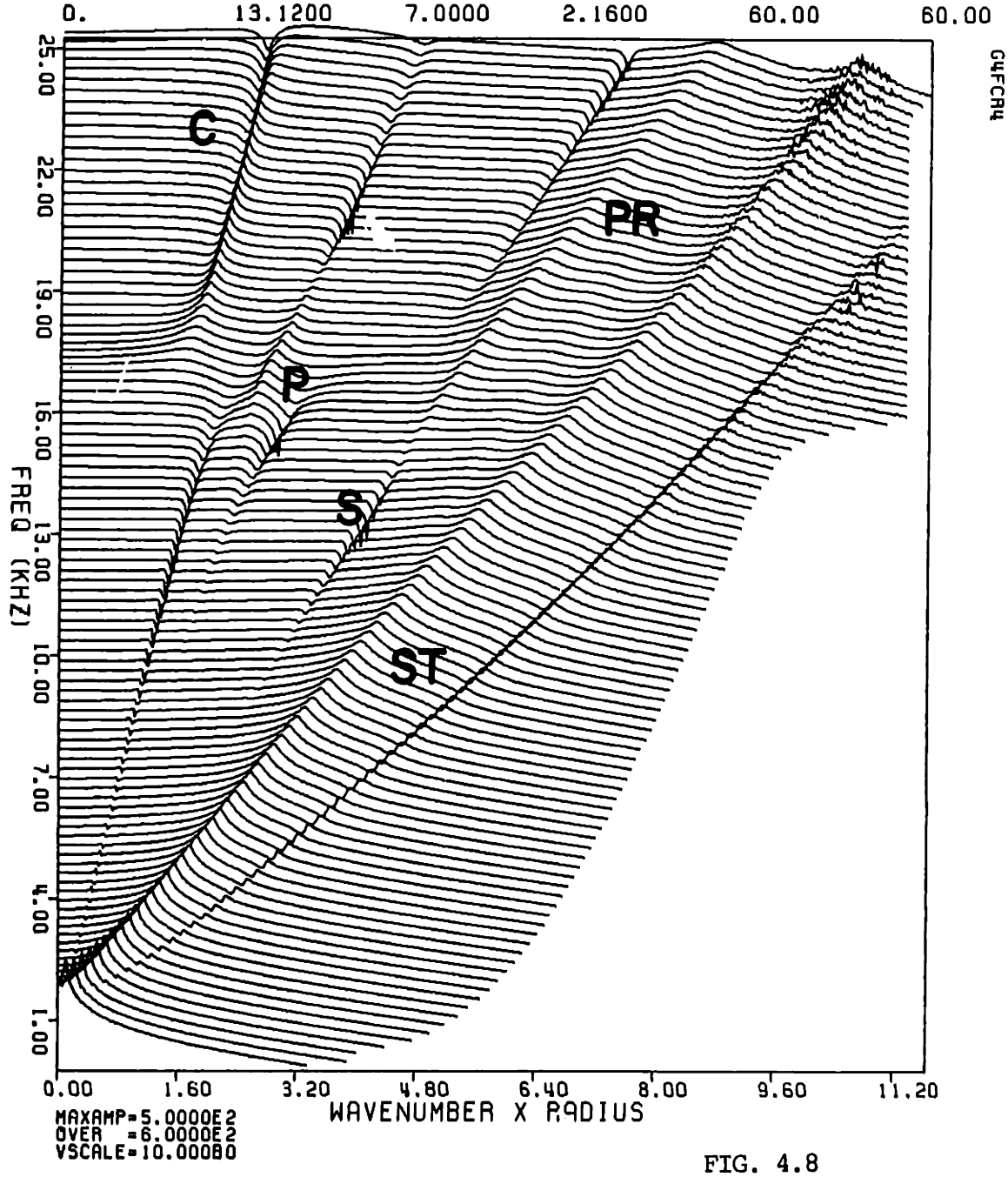

FIG. 4.8

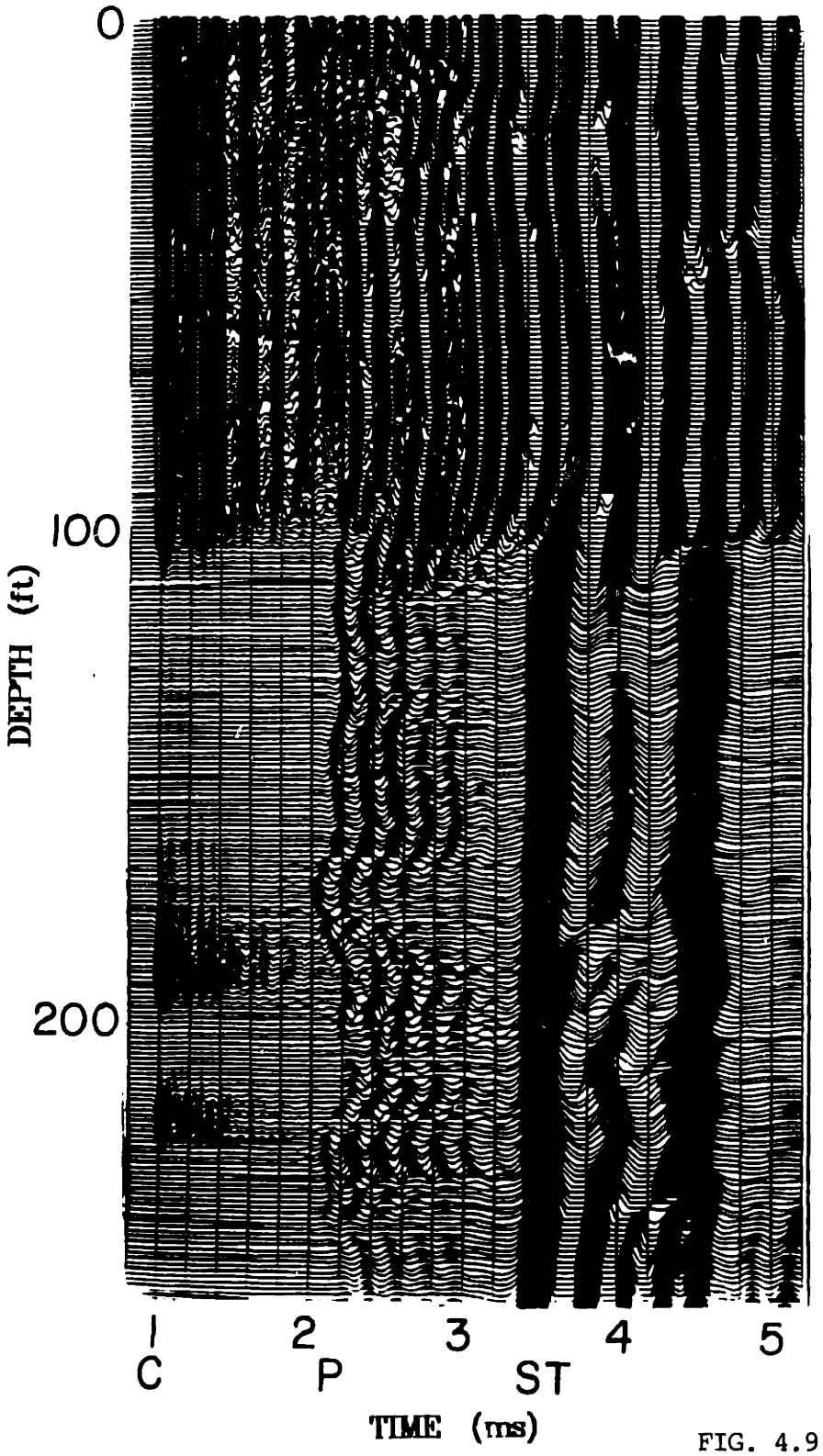

FIG. 4.9

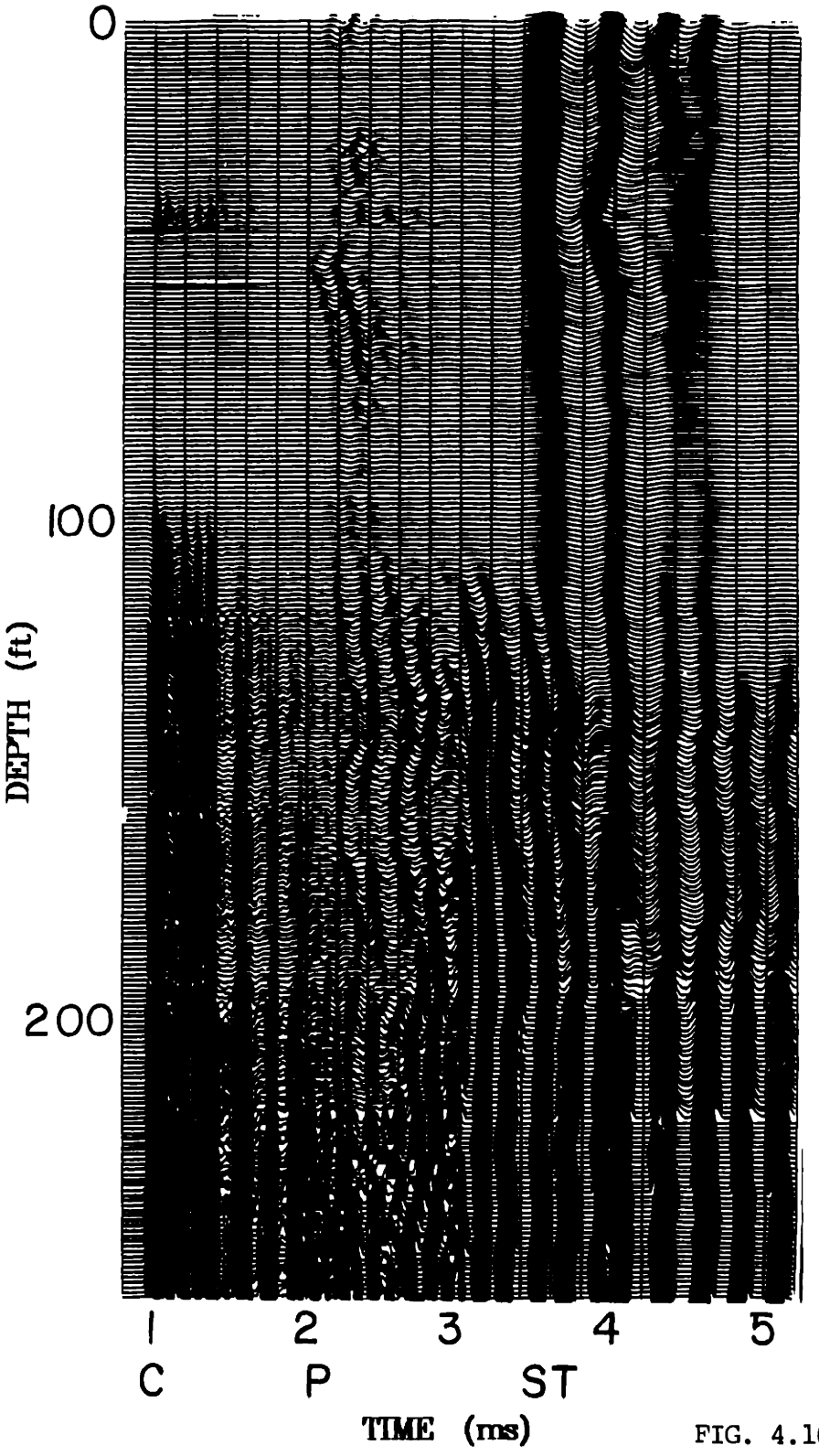

FIG. 4.10

H (FT)	VP (FT/MS)	VS (FT/MS)	RHO (GM/CC)	QP	QS
0.154167	5.5000	0.	1.2000	20.00	0.
0.187500	20.0000	11.0000	7.5000	1000.00	1000.00
0.229167	5.5000	0.	1.2000	20.00	0.
0.333333	9.2590	5.6700	1.9200	40.00	30.00
0.	16.0000	8.5300	2.1600	60.00	60.00

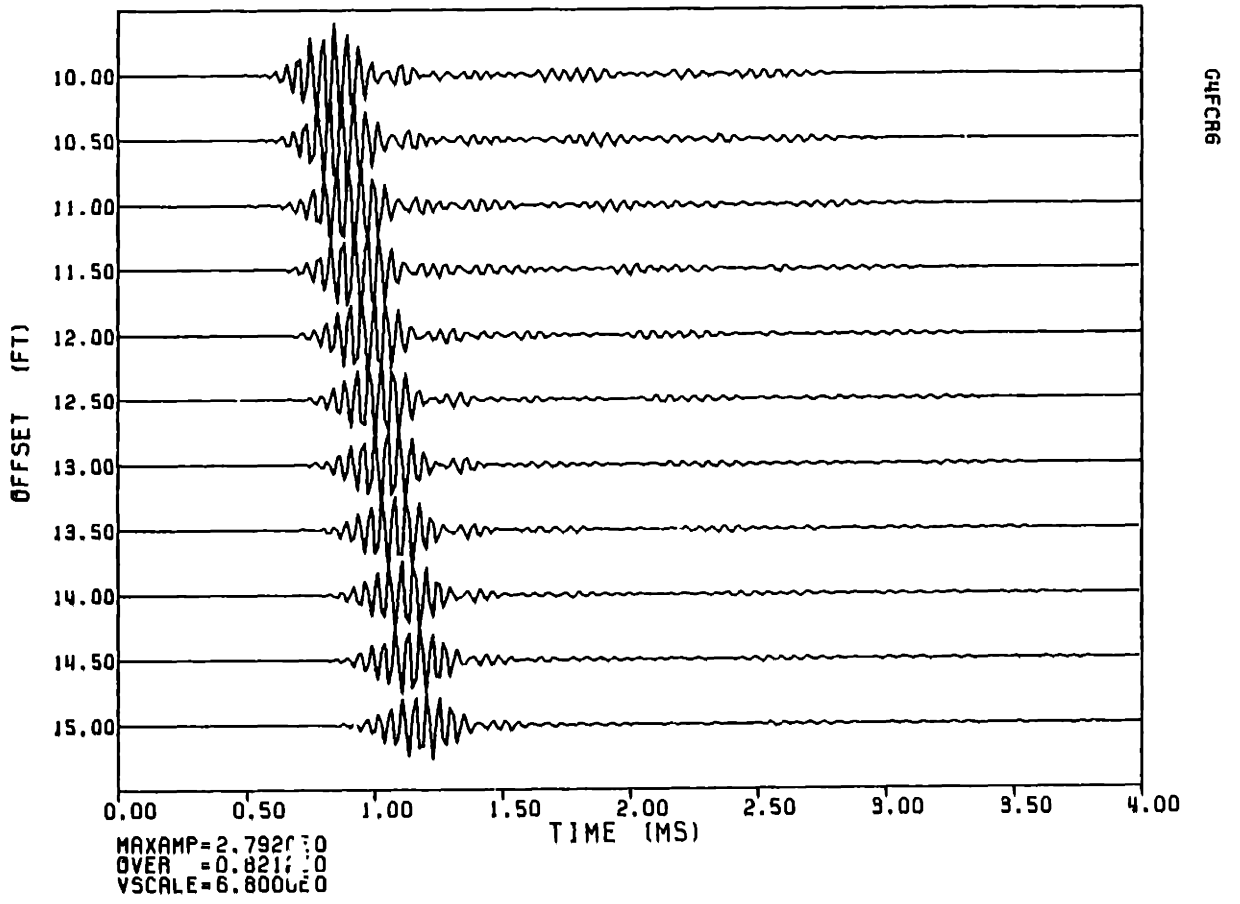

FIG. 4.11

R (FT)	VP (FT/MS)	VS (FT/MS)	RHO (GM/CC)	QP	QS
0.154167	5.5000	0.	1.2000	20.00	0.
0.187500	20.0000	11.0000	7.5000	1000.00	1000.00
0.229167	5.5000	0.	1.2000	20.00	0.
0.333333	9.2590	5.6700	1.9200	40.00	30.00
0.	13.1200	7.0000	2.1600	60.00	60.00

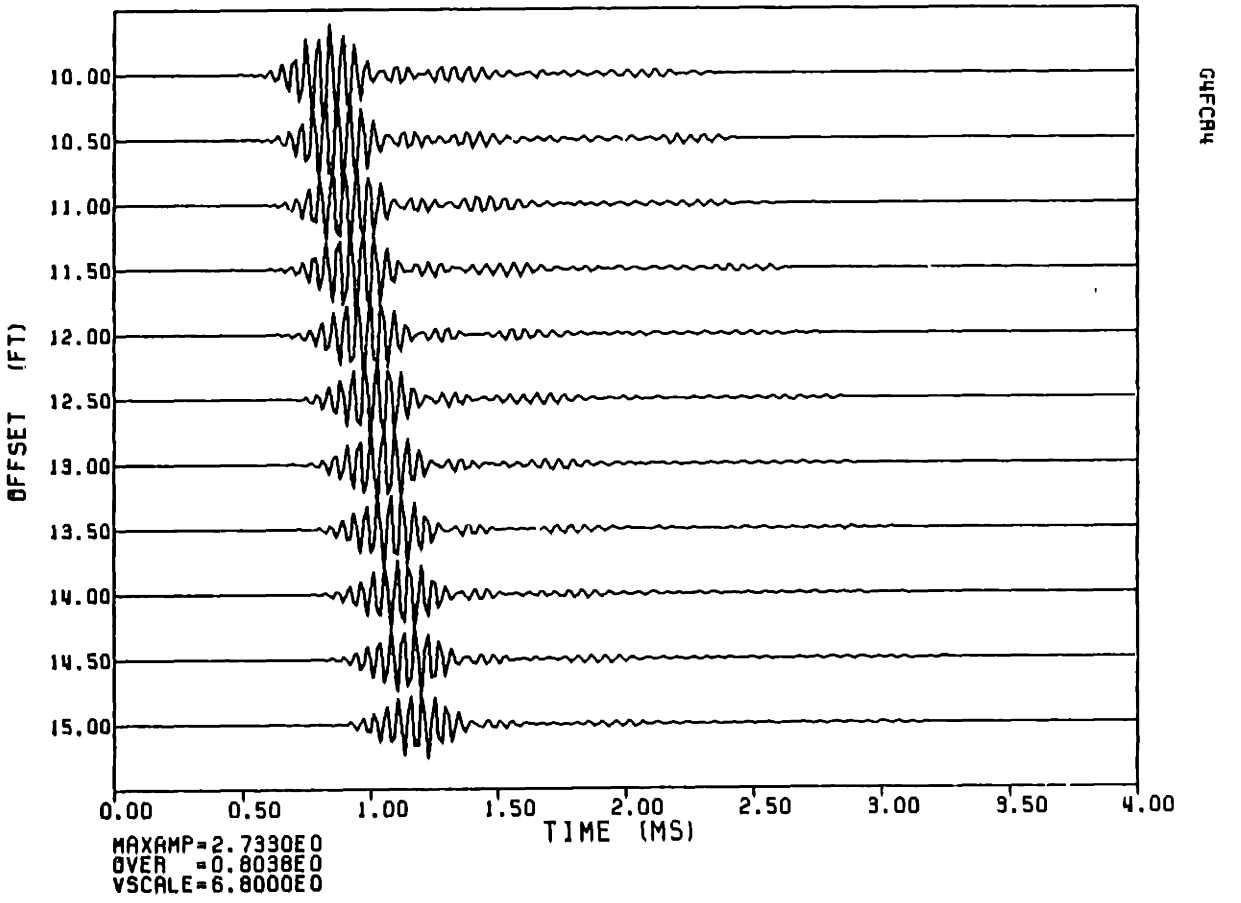

FIG. 4.12

R (FT)	VP (FT/MS)	VS (FT/MS)	RHO (GM/CC)	QP	QS
0.154167	5.5000	0.	1.2000	20.00	0.
0.187500	20.0000	11.0000	7.5000	1000.00	1000.00
0.187583	5.5000	0.	1.2000	20.00	0.
0.333333	9.2590	5.6700	1.9200	40.00	30.00
0.	16.0000	8.5300	2.1600	60.00	60.00

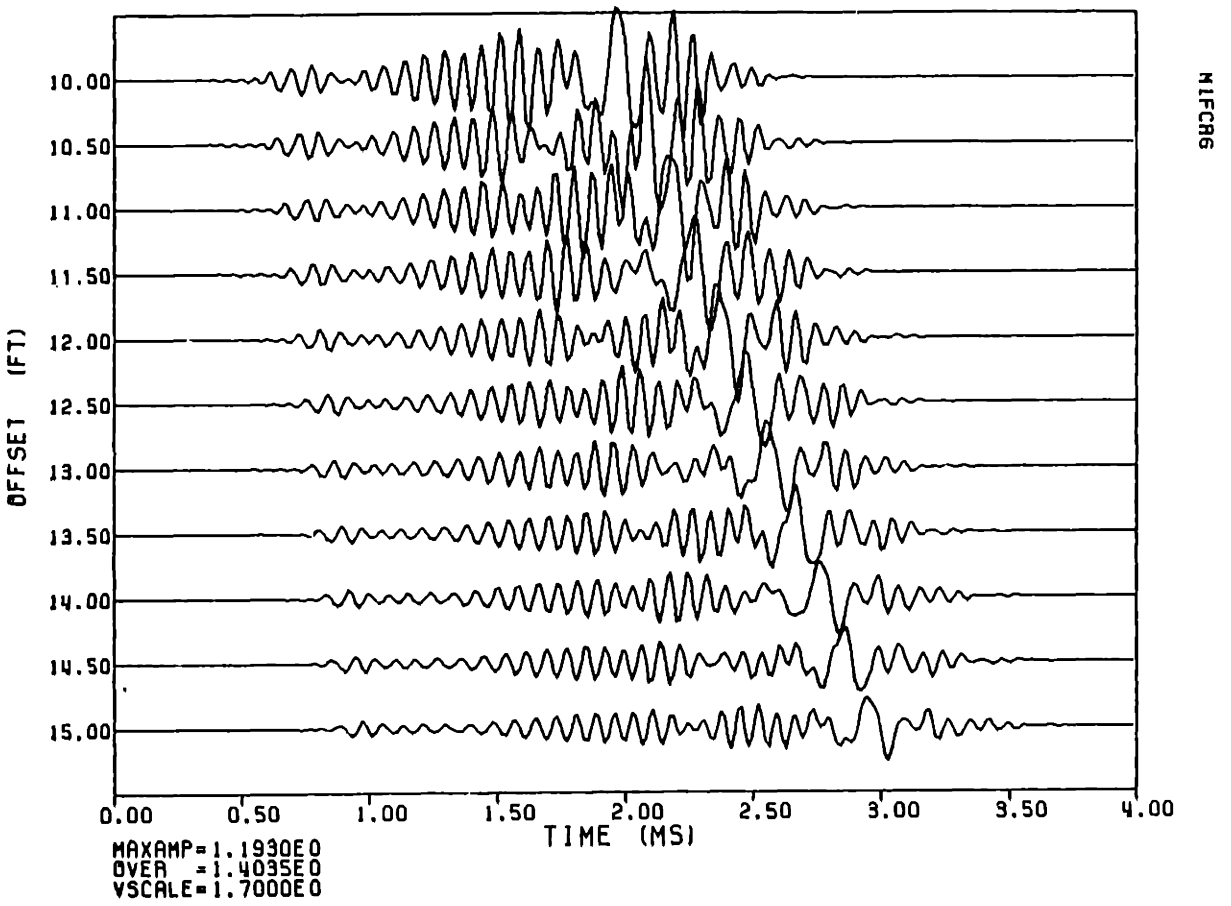

FIG. 4.13

R (FT)	VP (FT/MS)	VS (FT/MS)	RHO (GM/CC)	QP	QS
0.154167	5.5000	0.	1.2000	20.00	0.
0.187500	20.0000	11.0000	7.5000	1000.00	1000.00
0.187583	5.5000	0.	1.2000	20.00	0.
0.333333	9.2590	5.6700	1.9200	40.00	30.00
0.	13.1200	7.0000	2.1600	60.00	60.00

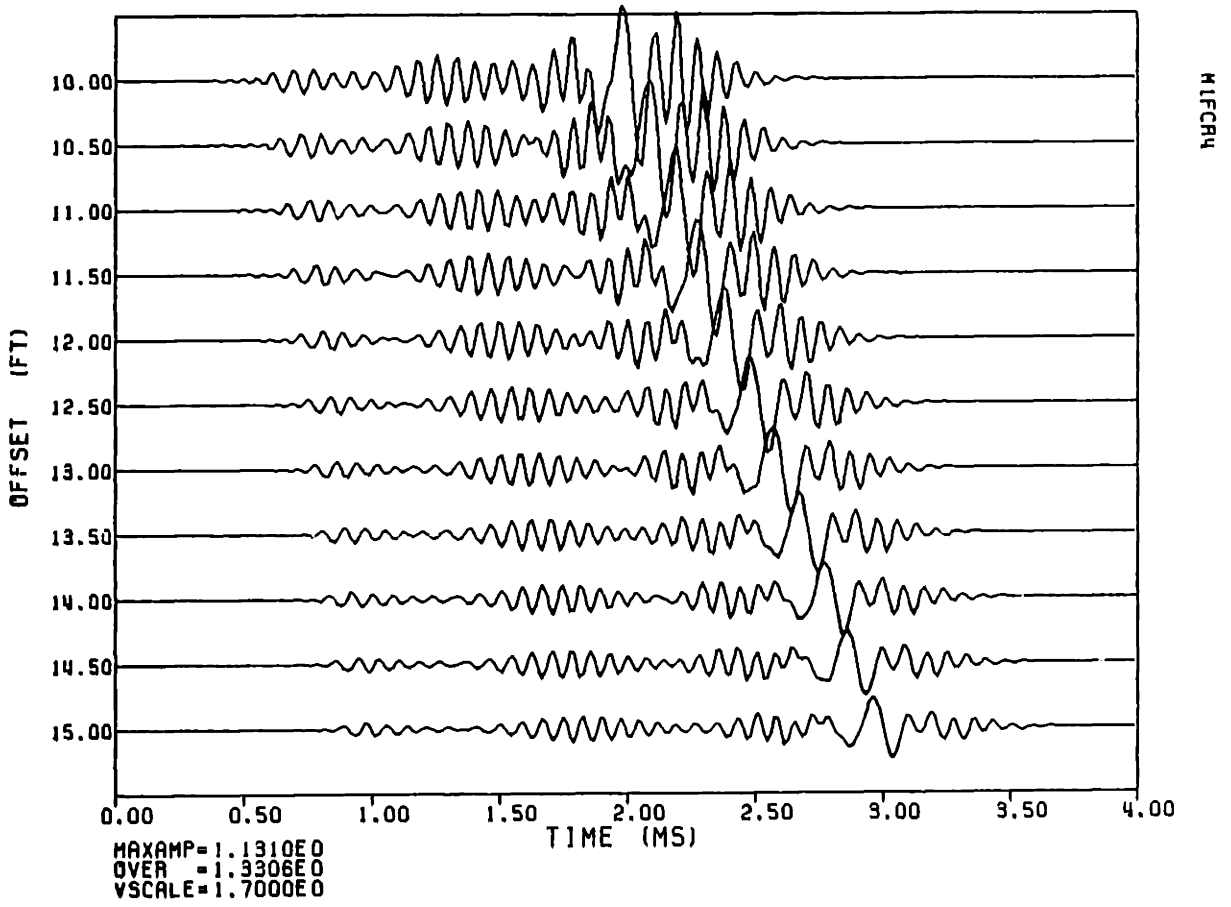

FIG. 4.14

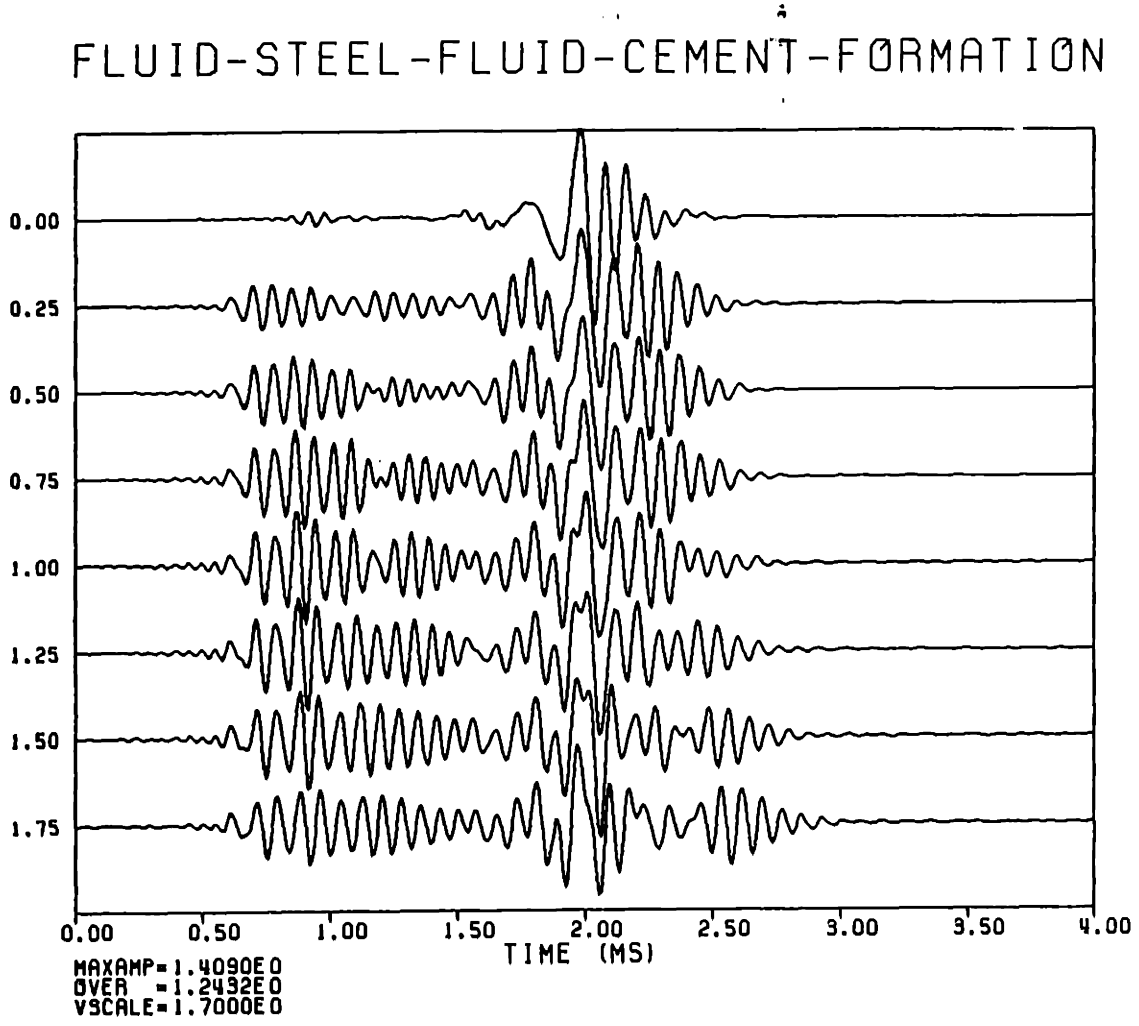
FLUID-STEEL-FLUID-CEMENT-FORMATION
0.00
0.25
0.50
0.75
1.00
1.25
1.50
1.75
0.00
0.50
1.00
1.50
2.00
2.50
3.00
3.50
4.00
TIME (MS)
MAXAMP=1.4090E0
OVER =1.2432E0
VSCALE=1.7000E0

FIG. 4.15

Portions of the text
on the following page(s)
are not legible in the
original.

r	Vp	Vs	rho
0.154167	5.500	0.	1.200
0.157500	20.000	11.000	7.500
0.333333	9.259	5.670	1.920
0.	19.120	7.000	2.100

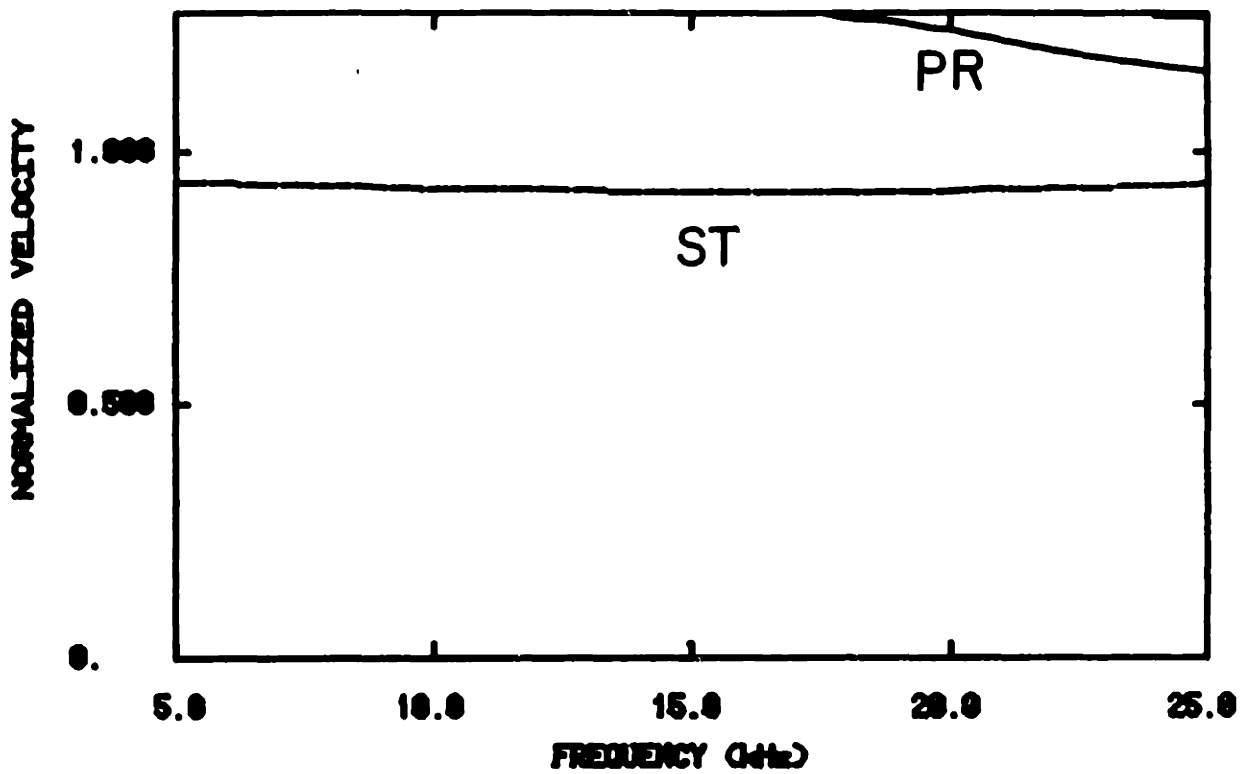

FIG. 4.16

r	Vp	Vs	rho
0.154167	5.500	0.	1.200
0.167500	20.000	11.000	7.500
0.200000	5.500	0.	1.200
0.333333	9.250	5.670	1.920
0.	13.120	7.000	2.100

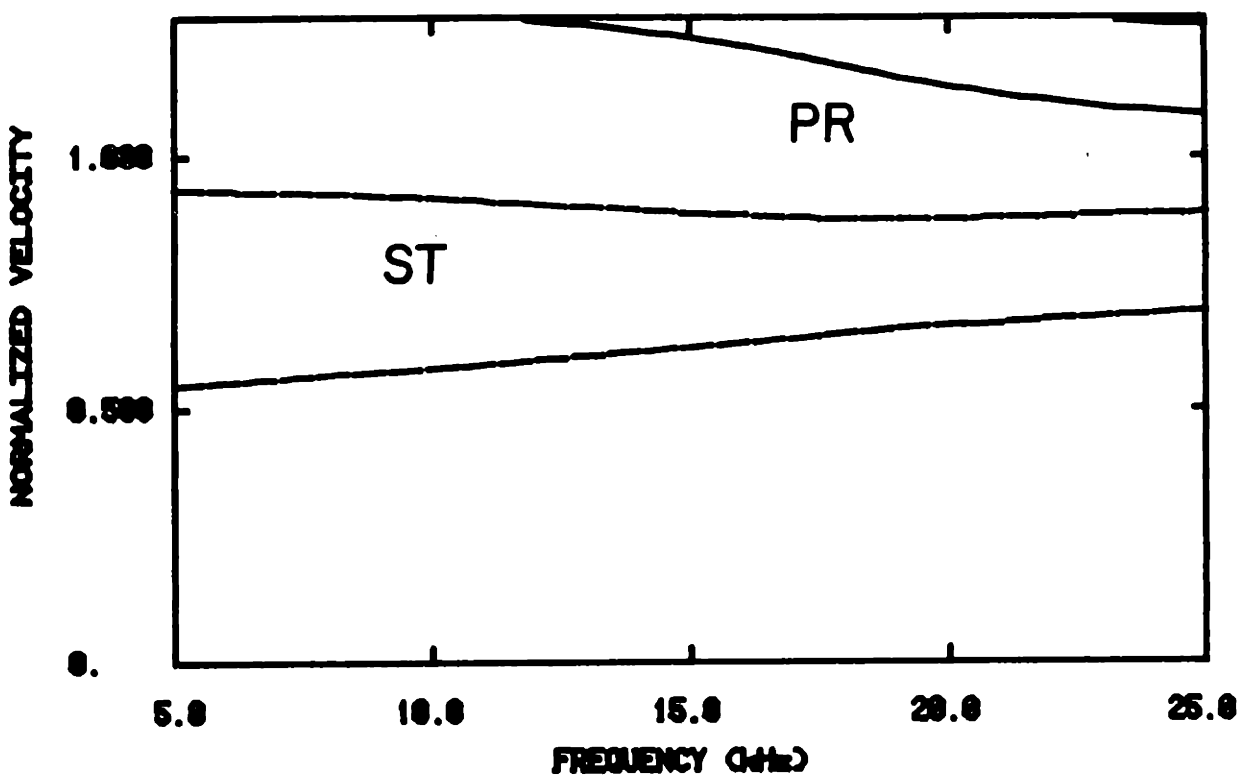

FIG. 4.17

r	Vp	Vs	rho
0.154167	5.500	0.	1.200
0.187500	20.000	11.000	7.500
0.312500	5.500	0.	1.200
0.500000	9.250	5.670	1.020
0.	13.120	7.000	2.100

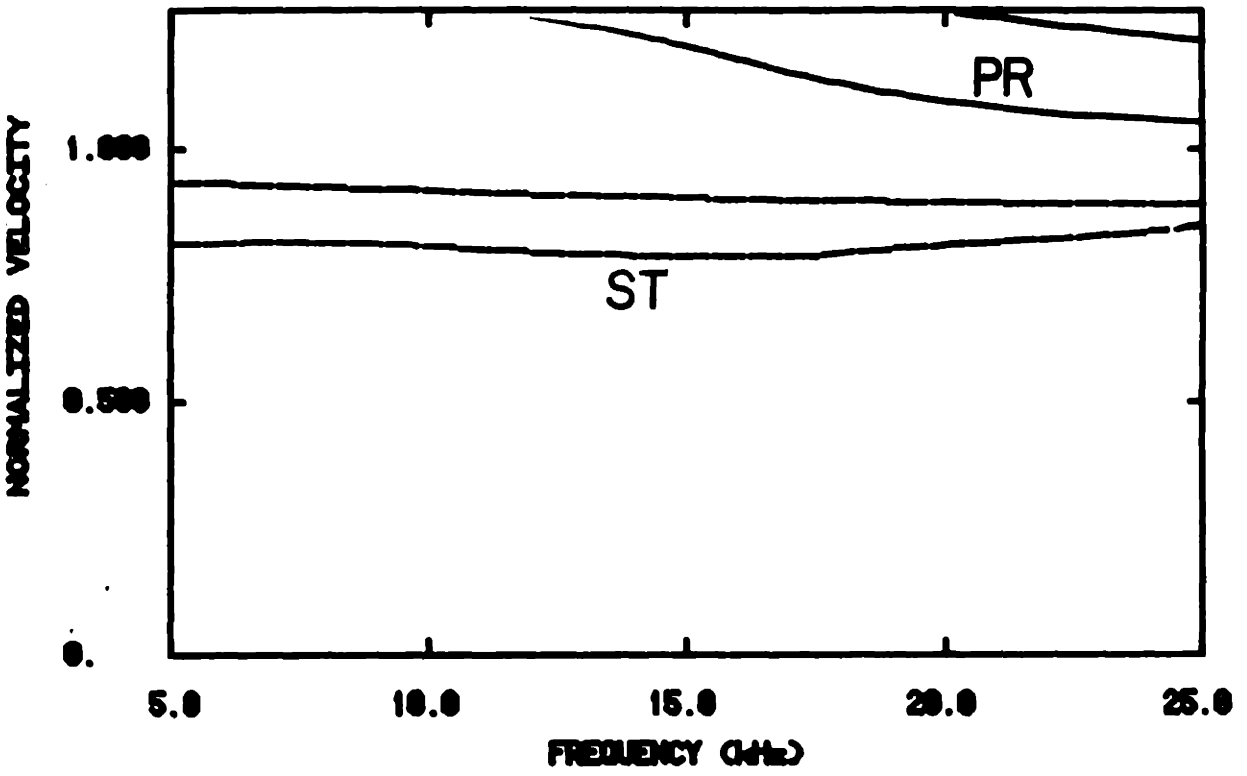

FIG. 4.18

r	Vp	Vs	rho
0.154167	5.500	0.	1.200
0.187500	20.000	11.000	7.500
0.333333	5.500	0.	1.200
0.	13.120	7.000	2.100

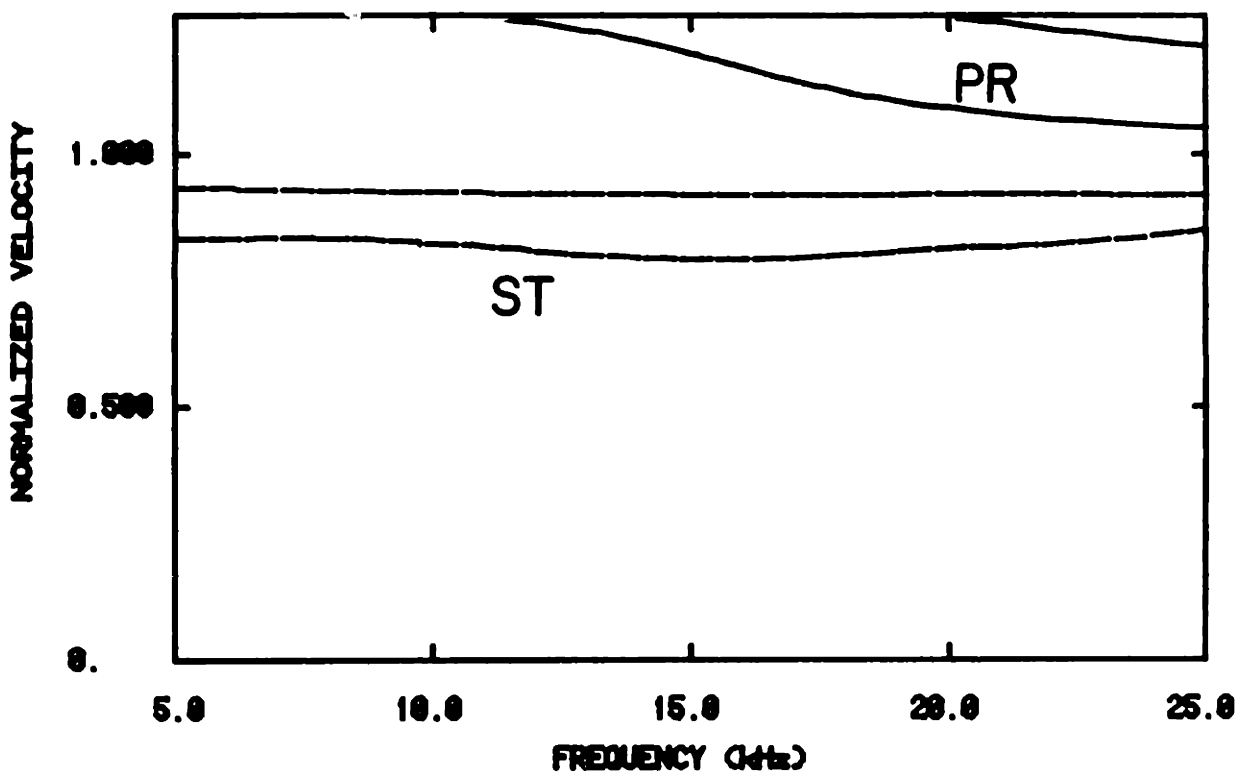

FIG. 4.19

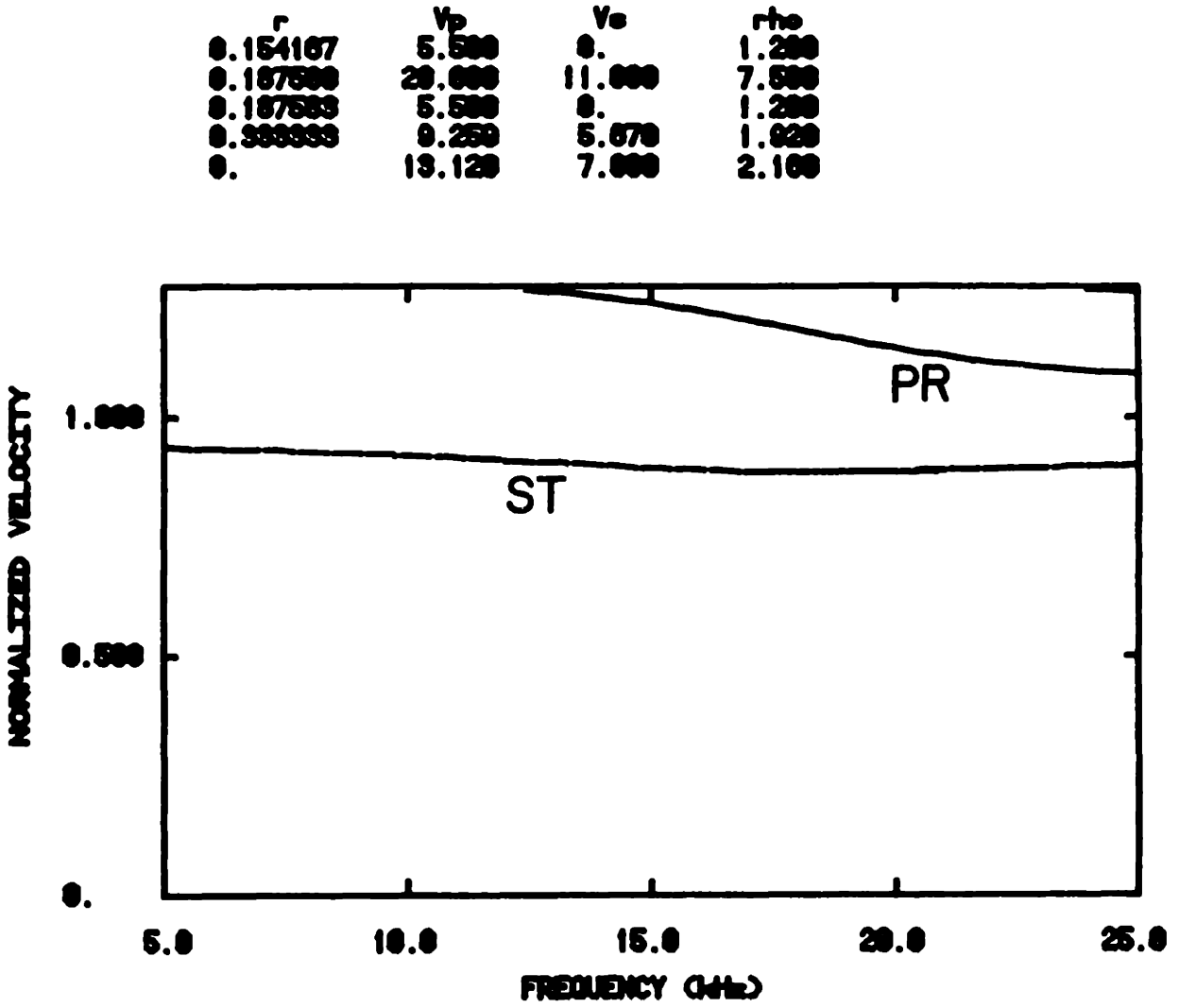
r
Vp
Vs
rho
0.154167
5.500
0.
1.200
0.187500
20.000
11.000
7.500
0.187500
5.500
0.
1.200
0.366333
9.250
5.670
1.920
0.
13.120
7.000
2.100
PR
ST
NORMALIZED VELOCITY
1.000
0.500
0.
5.0
10.0
15.0
20.0
25.0
FREQUENCY (kHz)

FIG. 4.20

R (FT)	VP (FT/MS)	VS (FT/MS)	RHO (GM/CC)	QP	QS
0.154167	5.5000	0.	1.2000	20.00	0.
0.187500	20.0000	11.0000	7.5000	1000.00	1000.00
0.229167	5.5000	0.	1.2000	20.00	0.
0.333333	9.2590	5.6700	1.9200	40.00	30.00
0.	13.1200	7.0000	2.1600	60.00	60.00

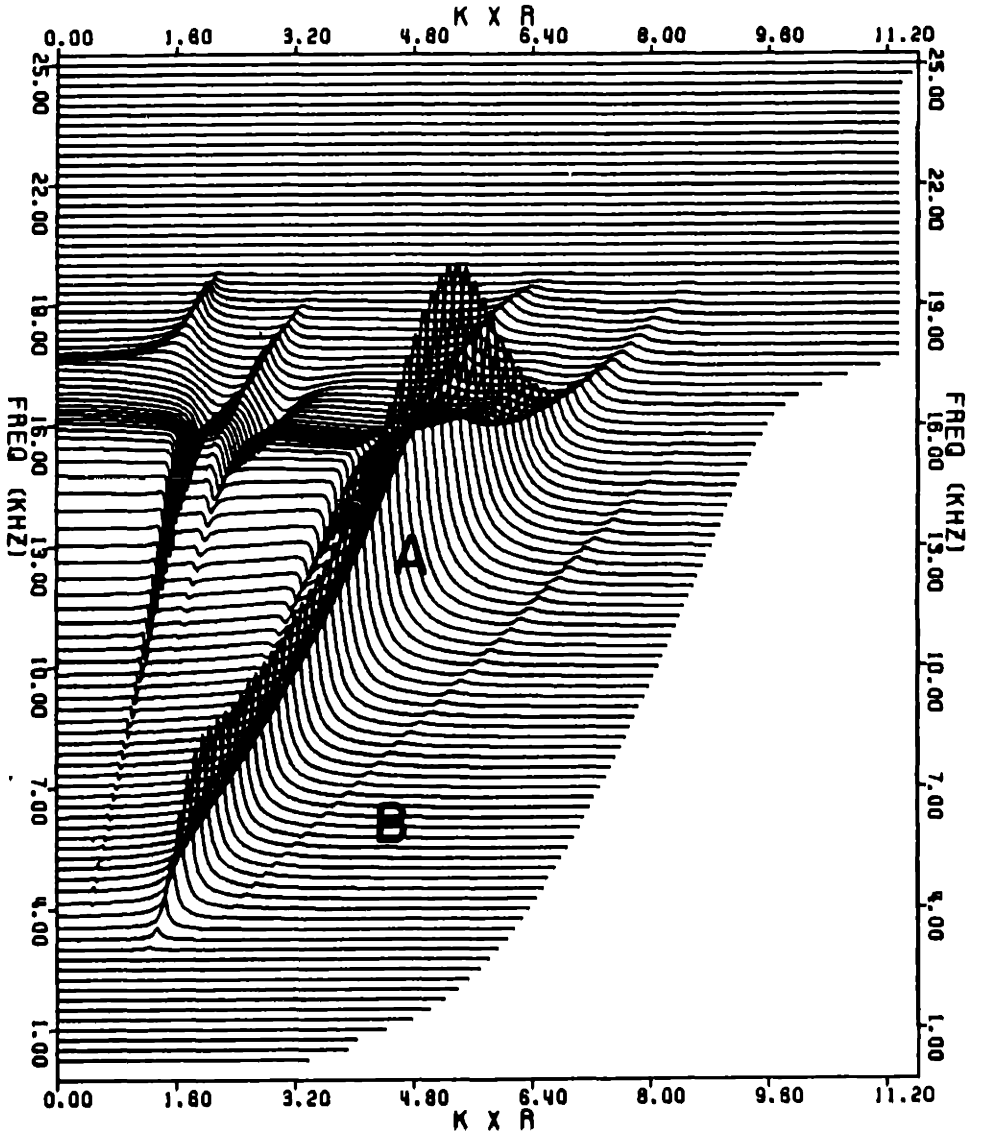

FIG. 4.21

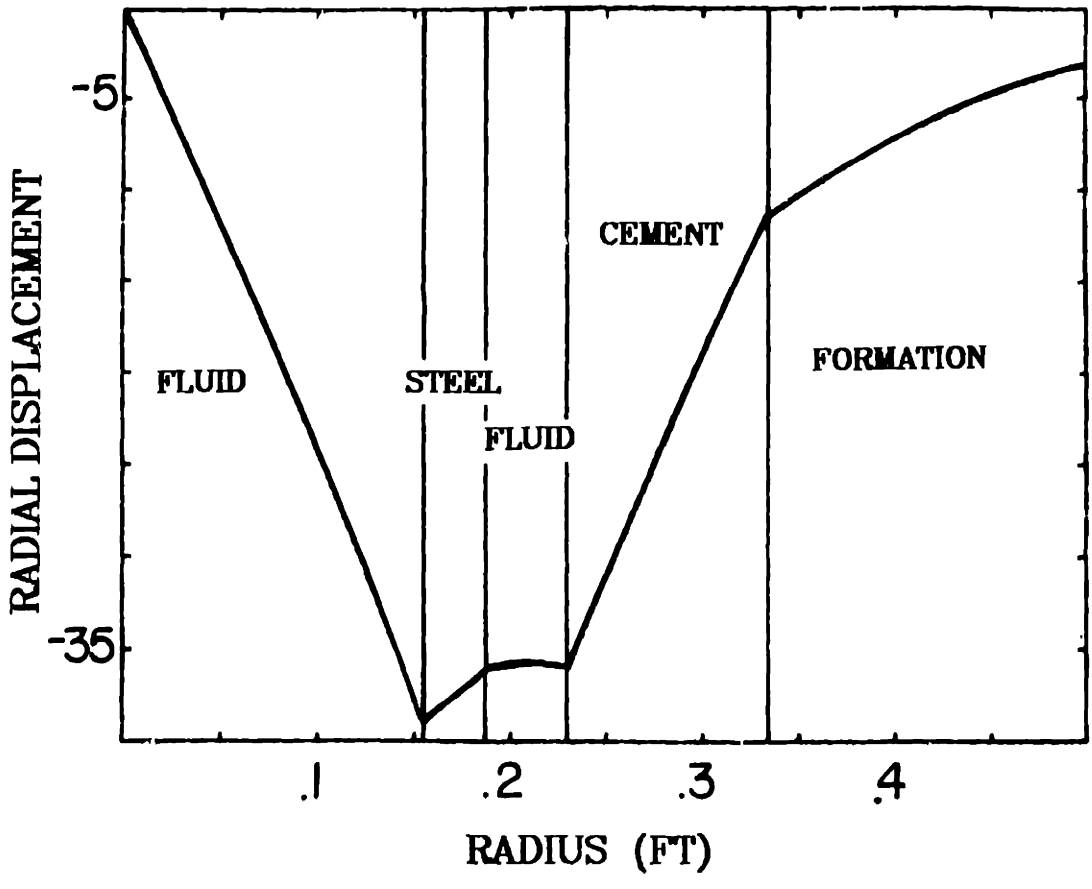
RADIAL DISPLACEMENT
-5
-35
FLUID
STEEL
FLUID
CEMENT
FORMATION
.1
.2
.3
.4
RADIUS (FT)

FIG. 4.22

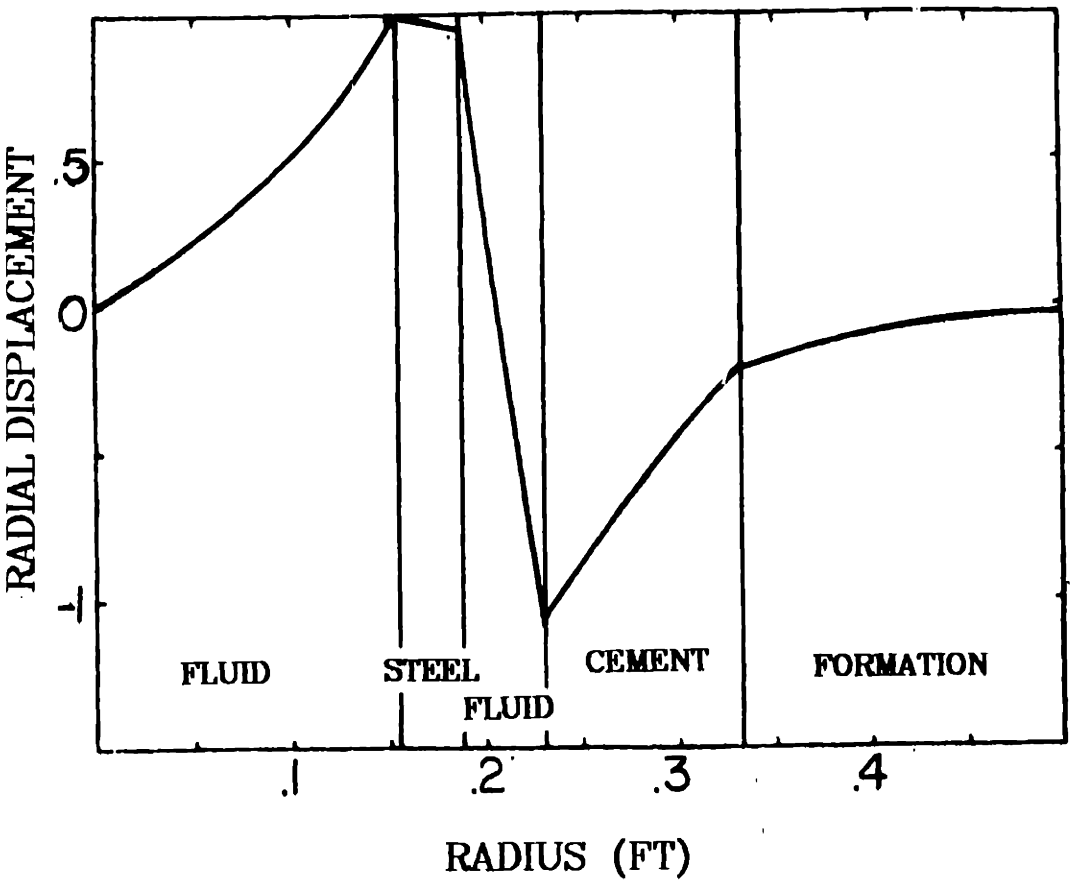
RADIAL DISPLACEMENT
.5
0
-1
FLUID
STEEL
FLUID
CEMENT
FORMATION
.1
.2
.3
.4
RADIUS (FT)

FIG. 4.23

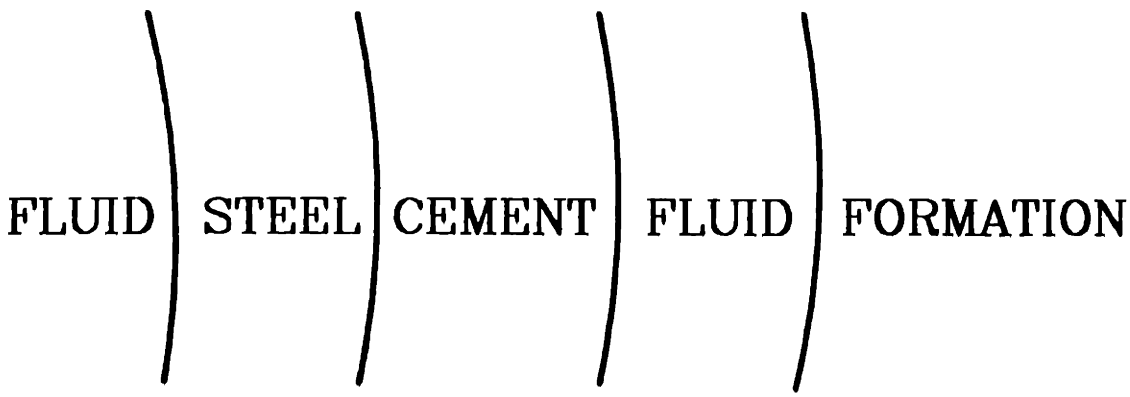
FLUID
STEEL
CEMENT
FLUID
FORMATION
ORIGINAL
BOREHOLE
RADIUS

FIG. 4.24

H (FT)	VP (FT/MS)	VS (FT/MS)	RHO (GM/CC)	QP	QS
0.154167	5.5000	0.	1.2000	20.00	0.
0.187500	20.0000	11.0000	7.5000	1000.00	1000.00
0.328125	9.2590	5.6700	1.9200	40.00	30.00
0.333333	5.5000	0.	1.2000	20.00	0.
0.	16.0000	8.5300	2.1600	60.00	60.00

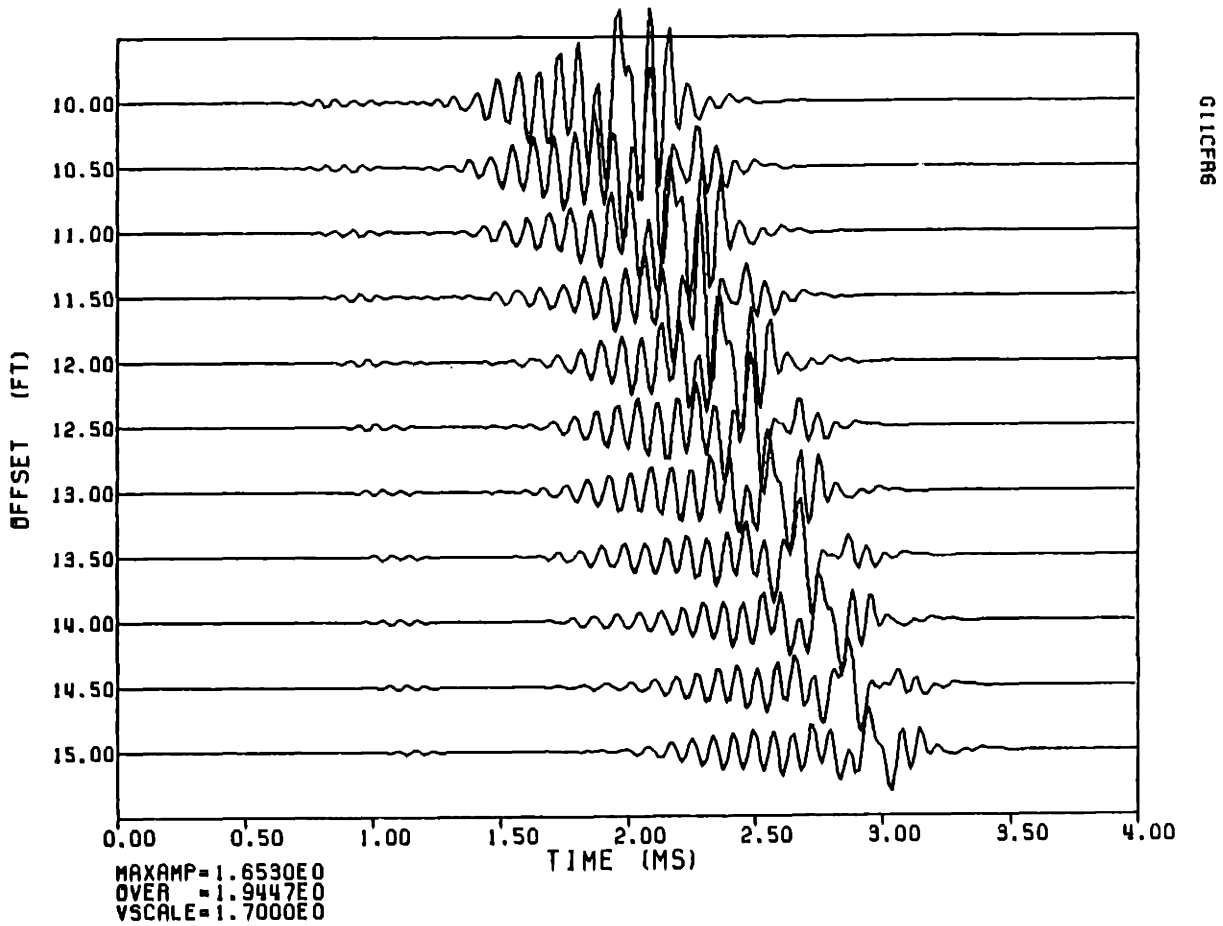

FIG. 4.25

R (FT)	VP (FT/MS)	VS (FT/MS)	RHO (GM/CC)	QP	QS
0.154167	5.5000	0.	1.2000	20.00	0.
0.187500	20.0000	11.0000	7.5000	1000.00	1000.00
0.328125	9.2590	5.6700	1.9200	40.00	30.00
0.333333	5.5000	0.	1.2000	20.00	0.
0.	13.1200	7.0000	2.1600	60.00	60.00

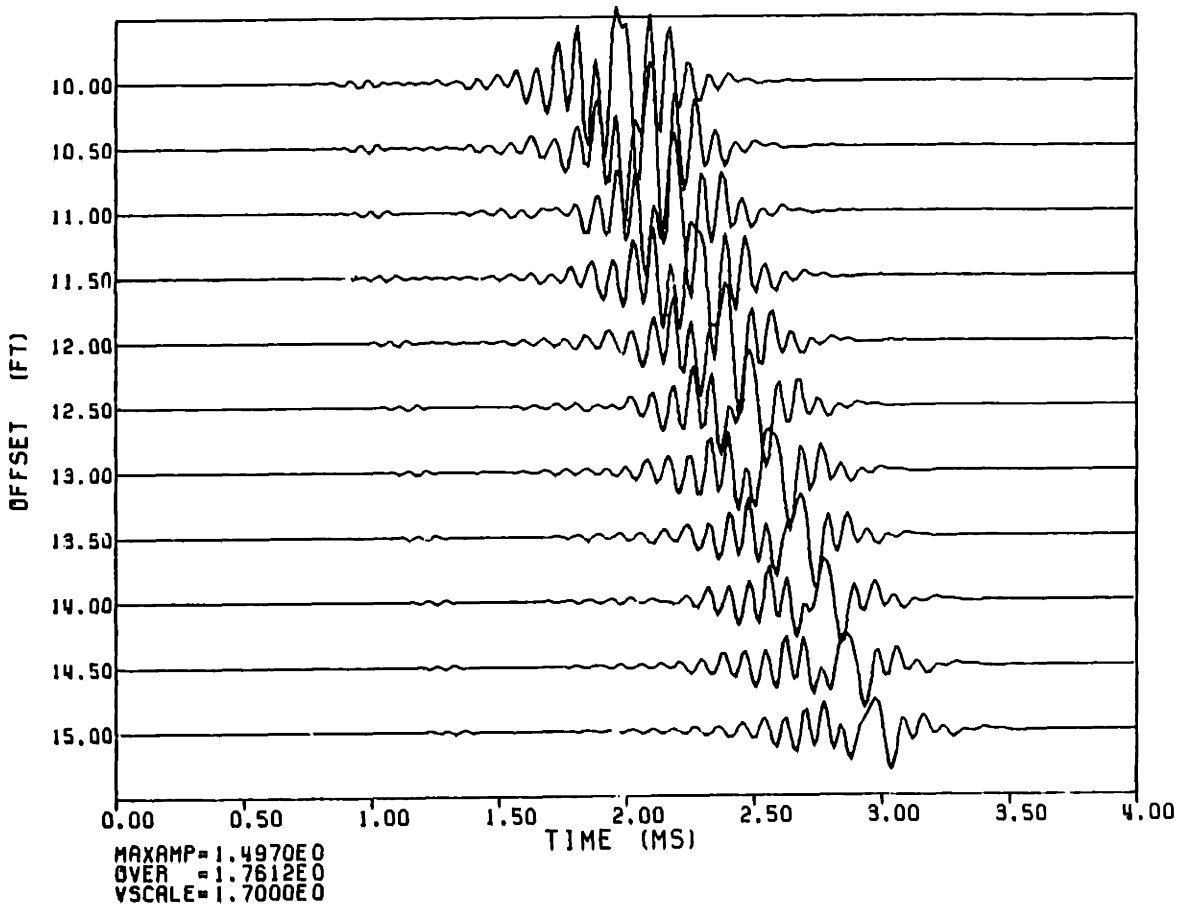

FIG. 4.26

R (FT)	VP (FT/MS)	VS (FT/MS)	RHO (GM/CC)	QP	QS
0.154167	5.5000	0.	1.2000	20.00	0.
0.187500	20.0000	11.0000	7.5000	1000.00	1000.00
0.328125	9.2590	5.6700	1.9200	40.00	30.00
0.432267	5.5000	0.	1.2000	20.00	0.
0.	16.0000	8.5300	2.1600	60.00	60.00

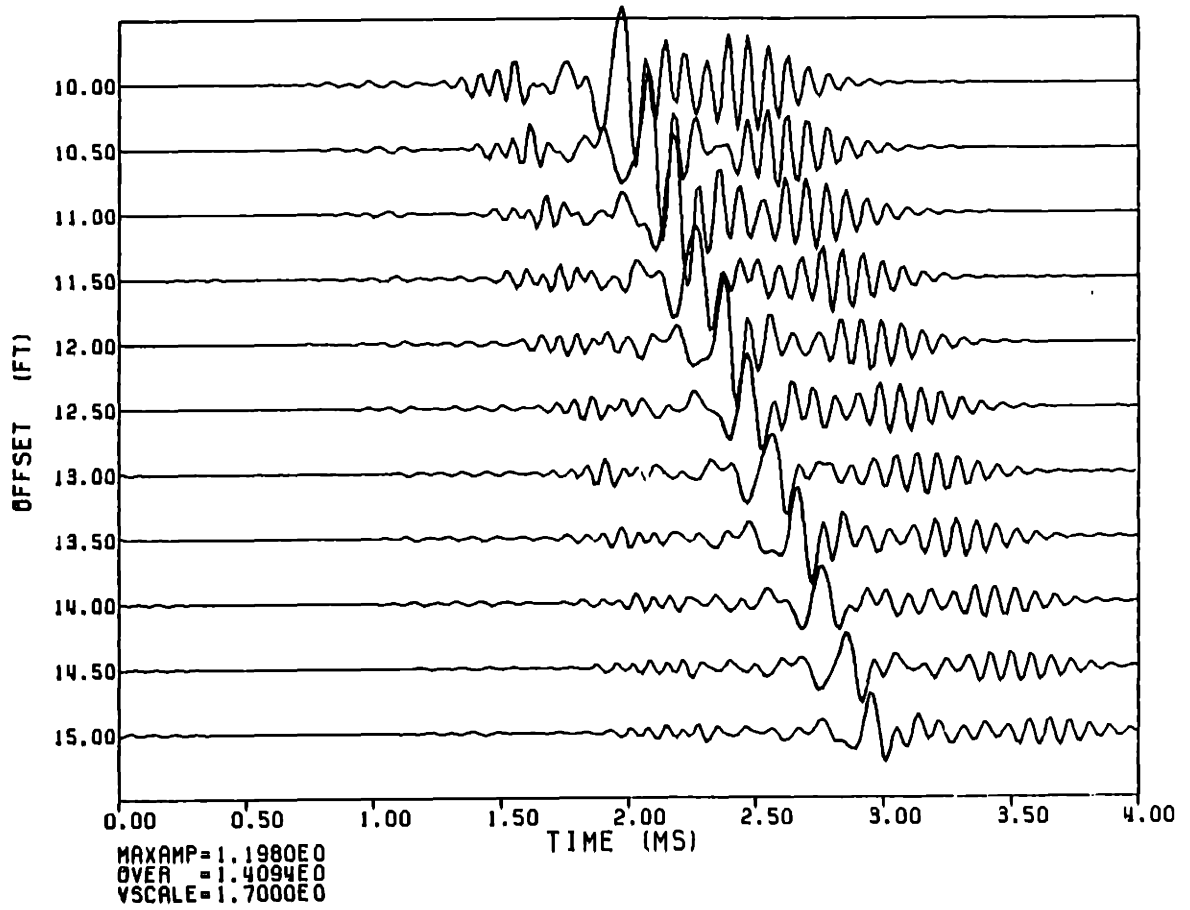

FIG. 4.27

H (FT)	VP (FT/MS)	VS (FT/MS)	RHO (GM/CC)	QP	QS
0.154167	5.5000	0.	1.2000	20.00	0.
0.187500	20.0000	11.0000	7.5000	1000.00	1000.00
0.328125	9.2590	5.6700	1.9200	40.00	30.00
0.432267	5.5000	0.	1.2000	20.00	0.
0.	13.1200	7.0000	2.1600	60.00	60.00

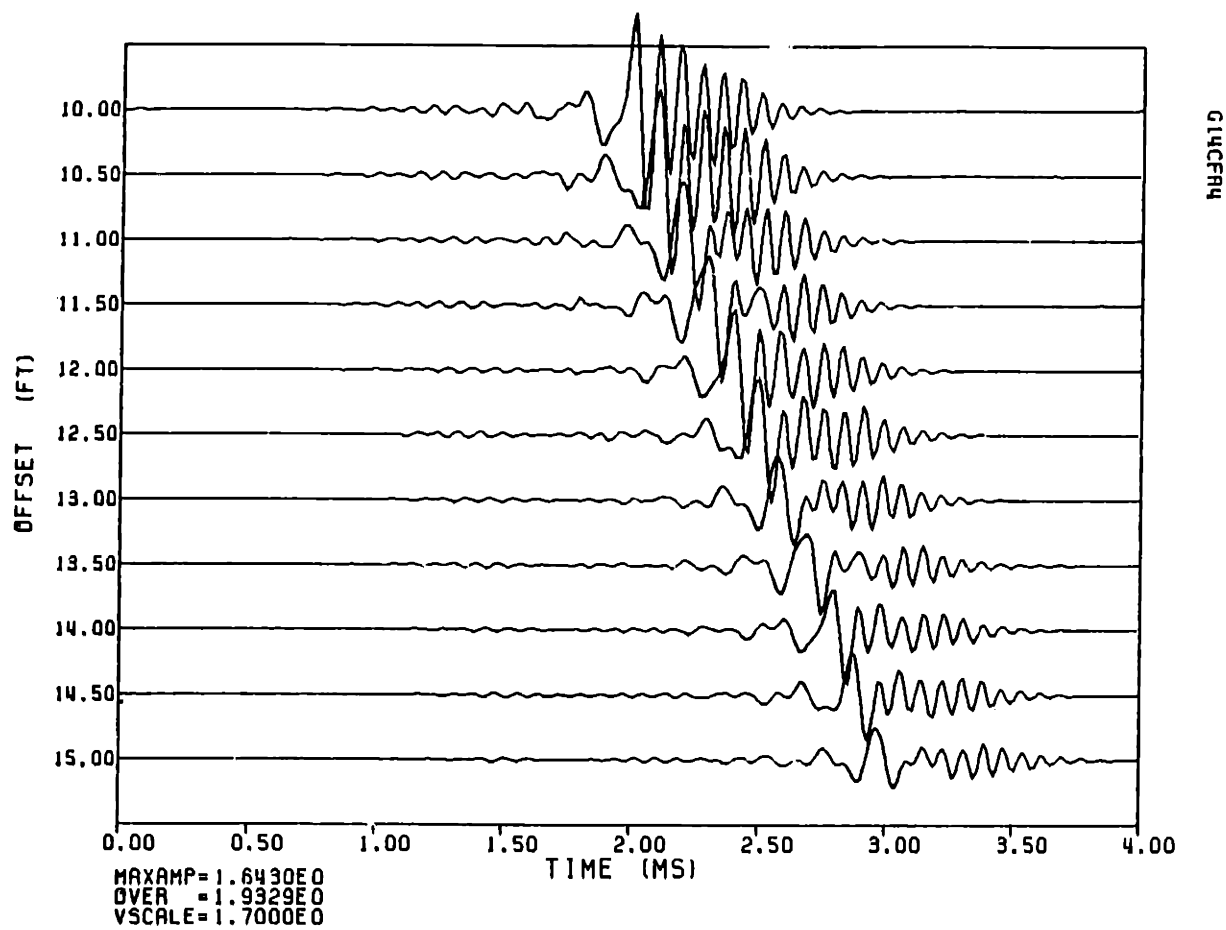

FIG. 4.28

R (FT)	VP (FT/MS)	VS (FT/MS)	RHO (GM/CC)	QP	QS
0.154167	5.5000	0.	1.2000	20.00	0.
0.187500	20.0000	11.0000	7.5000	1000.00	1000.00
0.229167	9.2590	5.6700	1.9200	40.00	30.00
0.333333	5.5000	0.	1.2000	20.00	0.
0.	16.0000	8.5300	2.1600	60.00	60.00

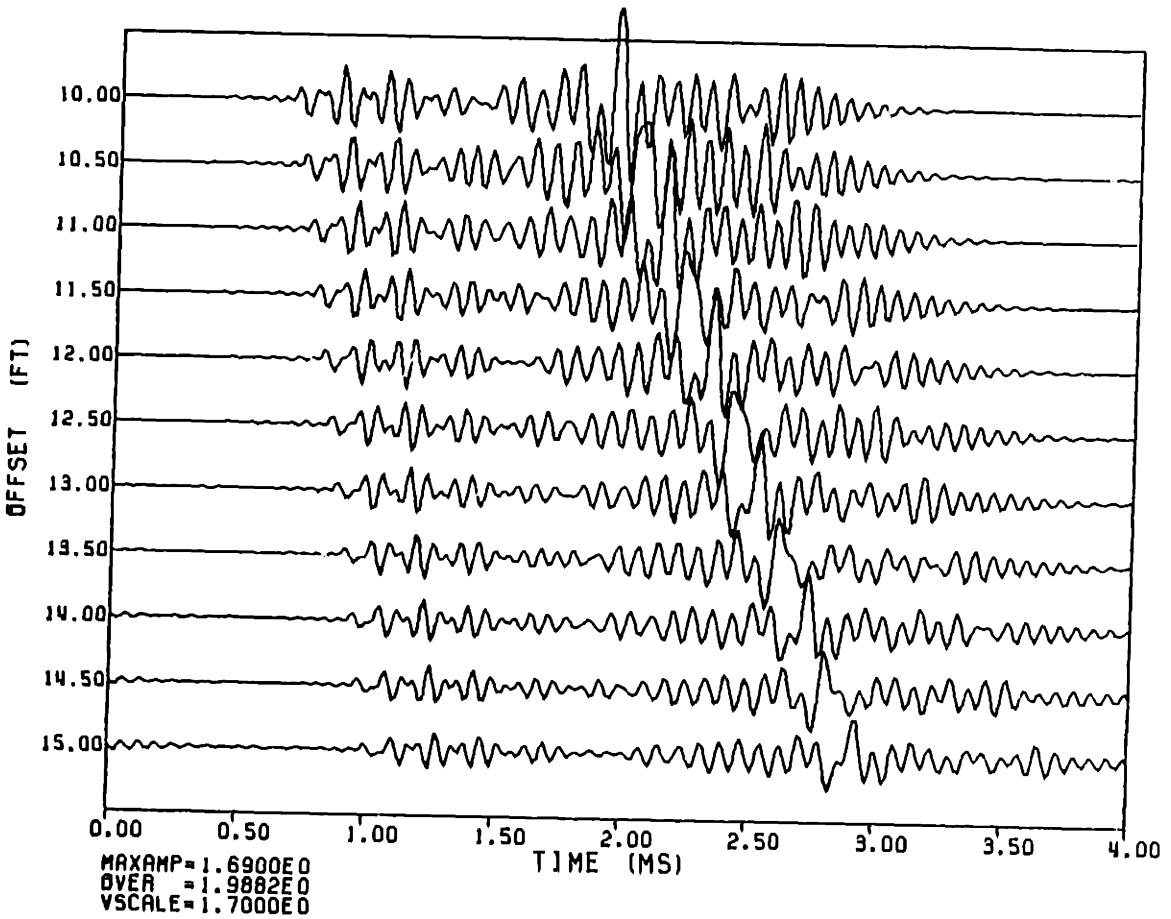

FIG. 4.29

H (FT)	VP (FT/MS)	VS (FT/MS)	RHO (GM/CC)	QP	QS
0.154167	5.5000	0.	1.2000	20.00	0.
0.187500	20.0000	11.0000	7.5000	1000.00	1000.00
0.229167	9.2590	5.6700	1.9200	40.00	30.00
0.333333	5.5000	0.	1.2000	20.00	0.
0.	13.1200	7.0000	2.1600	60.00	60.00

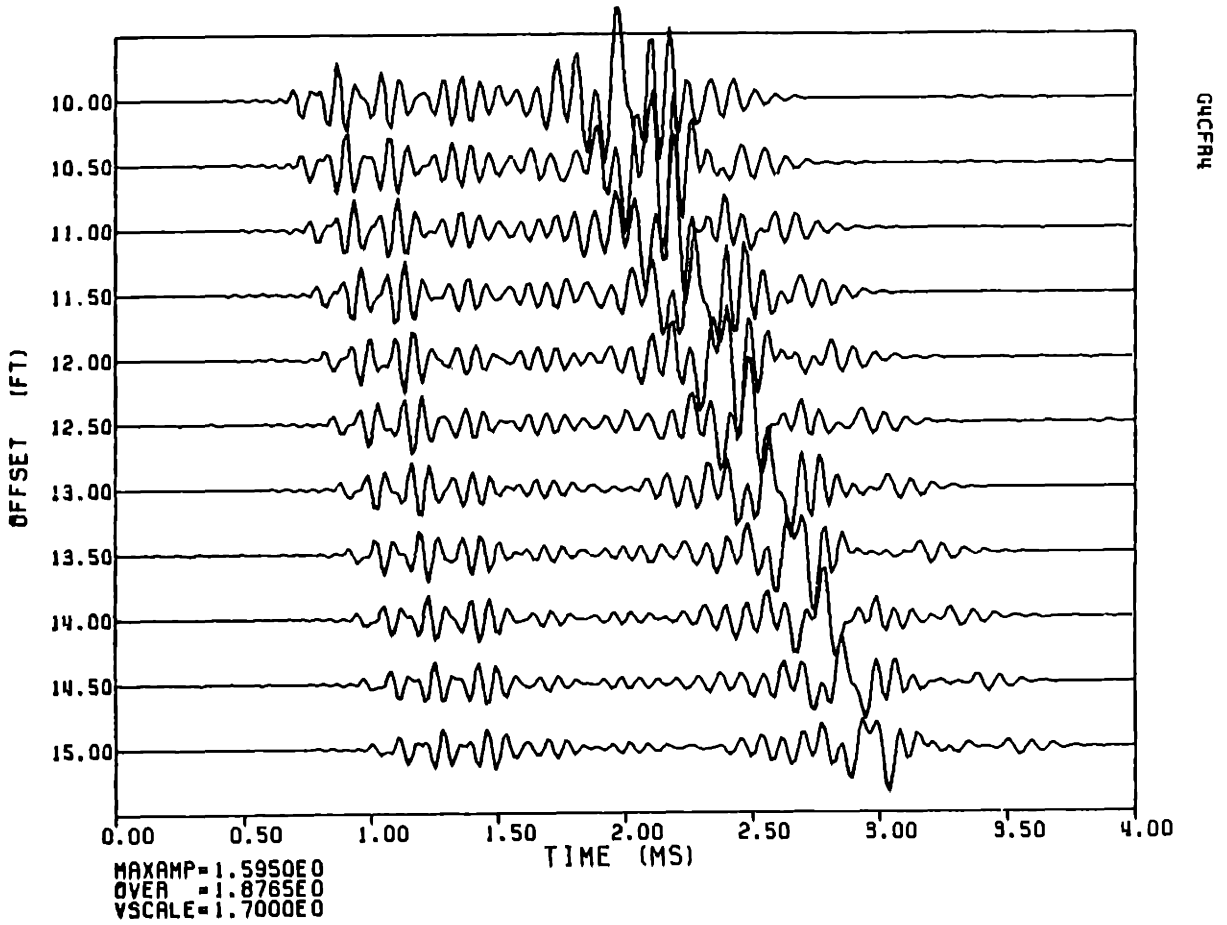

FIG. 4.30

R (FT)	VP (FT/MS)	VS (FT/MS)	RHO (GM/CC)	QP	QS
0.154167	5.5000	0.	1.2000	20.00	0.
0.187500	20.0000	11.0000	7.5000	1000.00	1000.00
0.229167	9.2590	5.6700	1.9200	40.00	30.00
0.333333	5.5000	0.	1.2000	20.00	0.
0.	9.5000	5.0000	2.0000	100.00	50.00

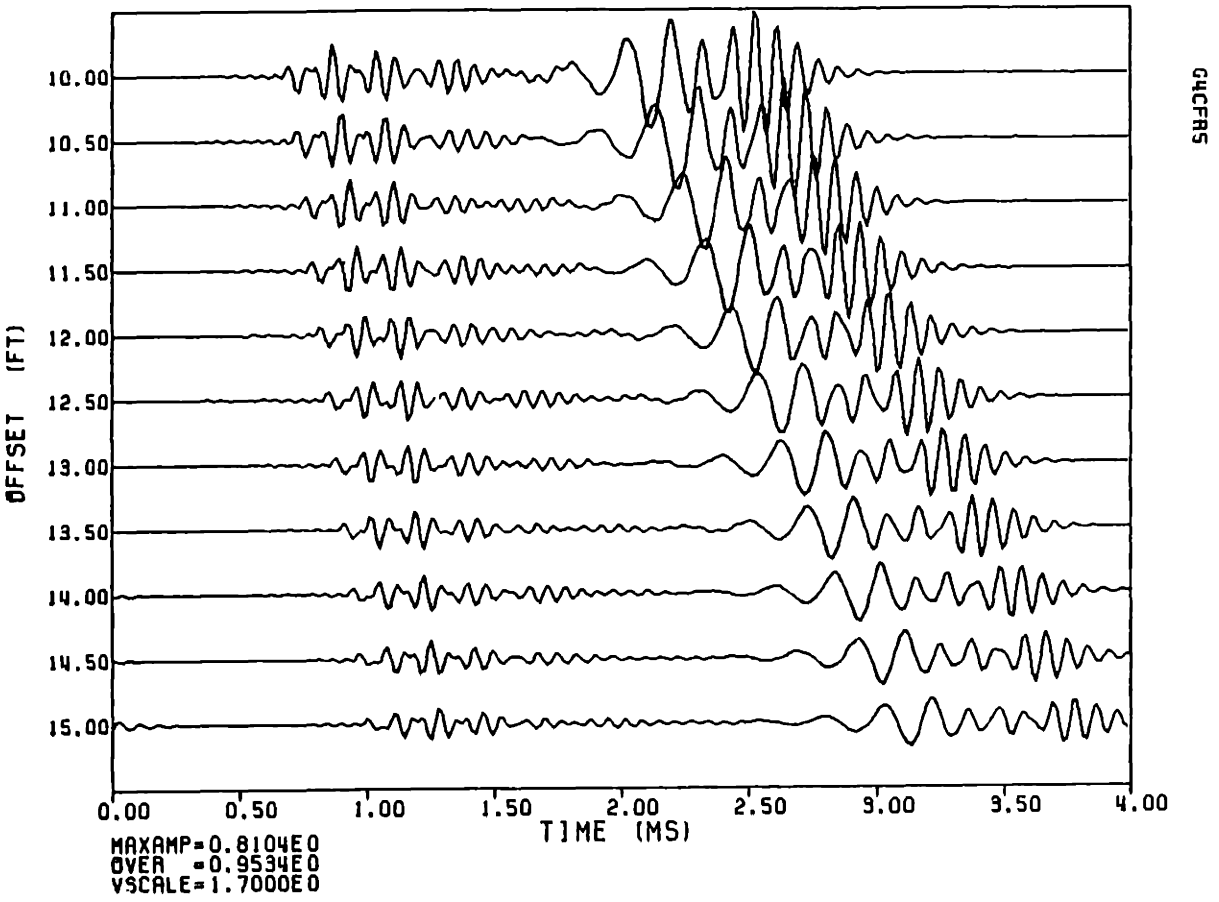

FIG. 4.31

R (FT)	VP (FT/MS)	VS (FT/MS)	RHO (GM/CC)	QP	QS
0.154167	5.5000	0.	1.2000	20.00	0.
0.187500	20.0000	11.0000	7.5000	1000.00	1000.00
0.229167	13.5000	8.3000	1.9200	40.00	30.00
0.333333	5.5000	0.	1.2000	20.00	0.
0.	13.1200	7.0000	2.1600	60.00	60.00

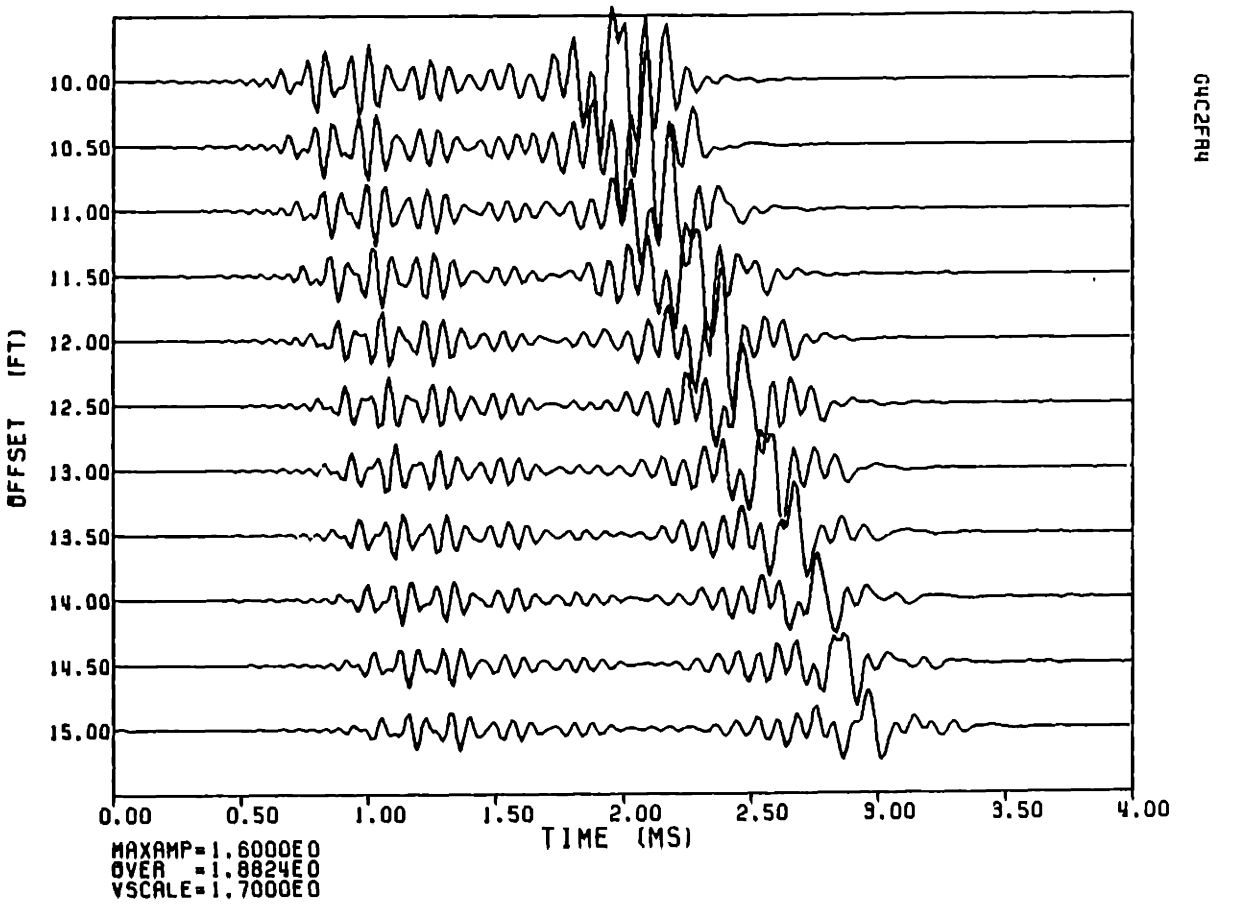

FIG. 4.32

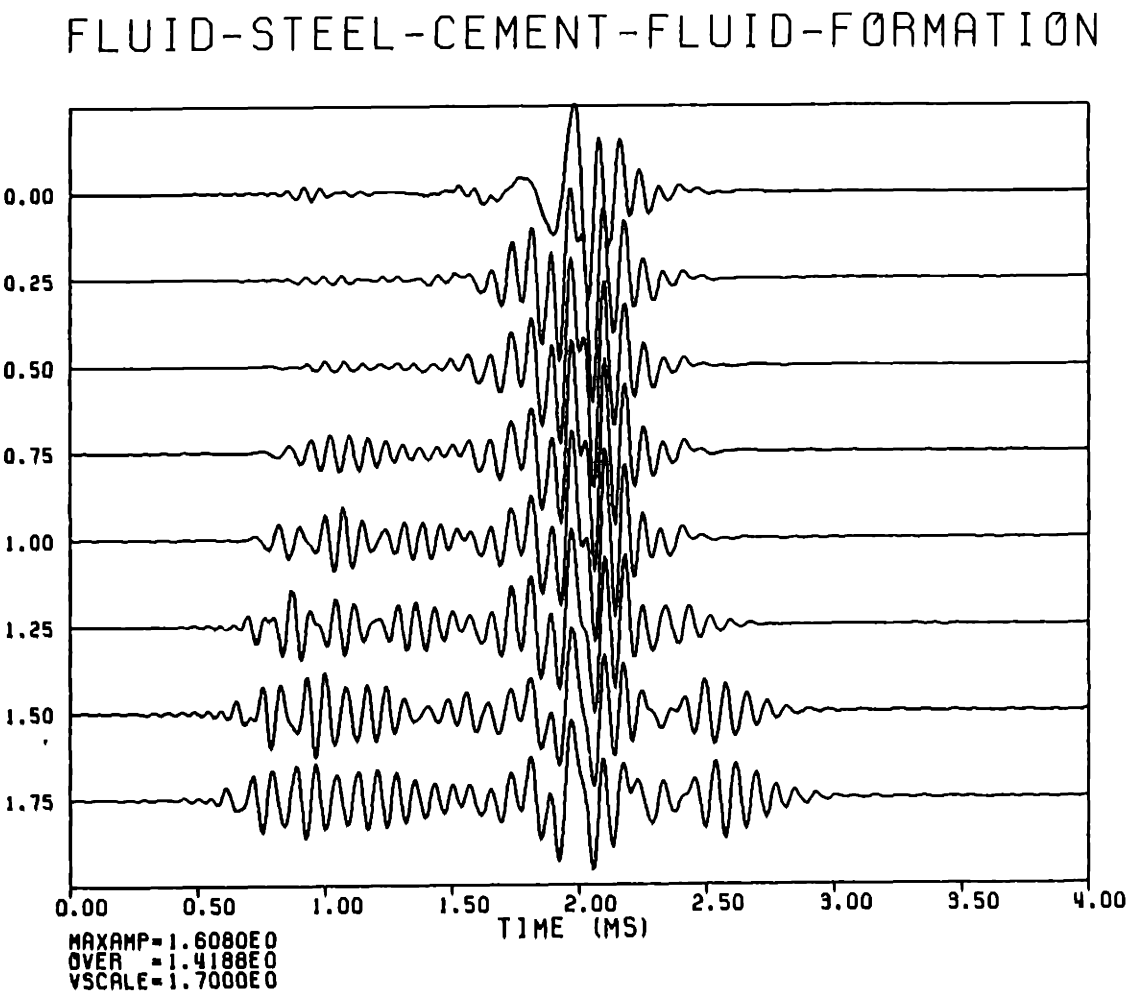
FLUID-STEEL-CEMENT-FLUID-FORMATION
0.00
0.25
0.50
0.75
1.00
1.25
1.50
1.75
0.00
0.50
1.00
1.50
2.00
2.50
3.00
3.50
4.00
TIME (MS)
MAXAMP=1.6080E0
OVER =1.4188E0
VSCALE=1.7000E0

FIG. 4.33

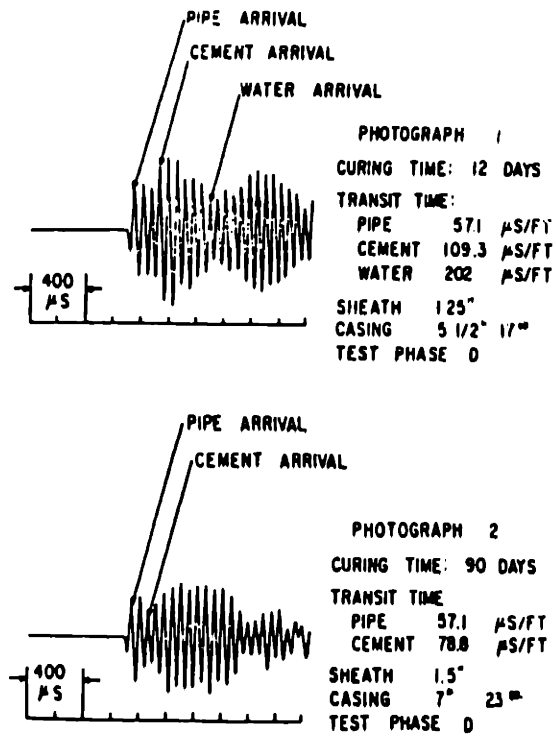

CEMENT WAVE RESPONSE IN PIPE BC ID TESTS

FIG. 4.34

TIME AFTER TRANSMITTER FIRE

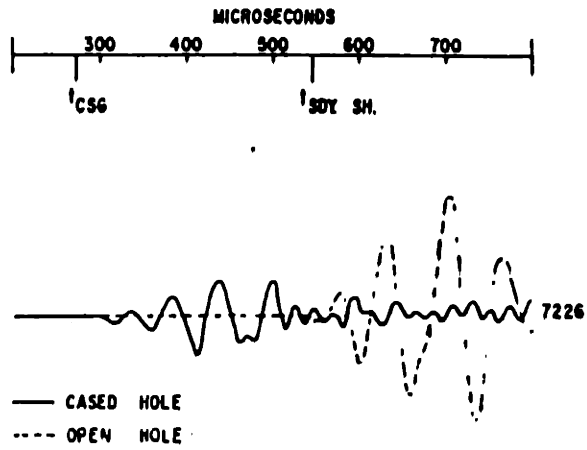

NO MUD CAKE - HOLE DIA. = 10 5/8"
SANDY SHALE - 125 μS/FT. DELTA - t

CEMENT WAVE SIGNAL

FIG. 4.35a

TIME AFTER TRANSMITTER FIRE

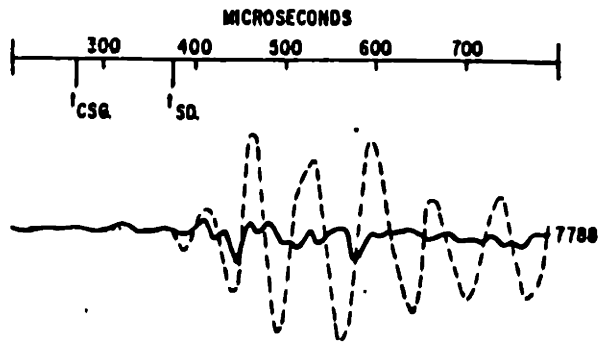

——CASED HOLE

- - - OPEN HOLE

CSG. – 5 1/2"

HOLE SIZE – 12"

FORMATION DELTA-t – 95 μS/FT.

RESPONSE TO GOOD PIPE – CEMENT BOND AND NO CEMENT – FORMATION BOND

FIG. 4.35b

TIME AFTER TRANSMITTER FIRE

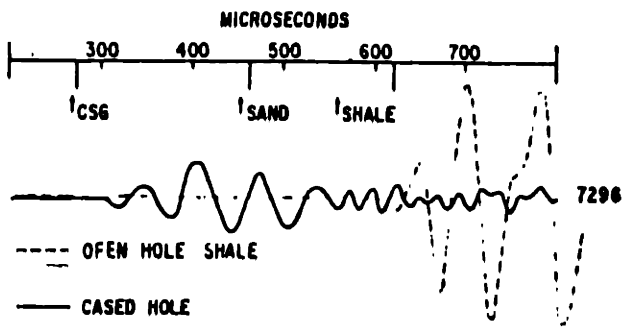

RESPONSE TO GOOD PIPE - CEMENT BOND
AND POOR CEMENT - FORMATION BOND

FIG. 4.35c

r	Vp	Vs	rho
0.154167	5.500	0.	1.200
0.187500	20.000	11.000	7.500
0.312500	9.259	5.670	1.920
0.333333	5.500	0.	1.200
0.	13.120	7.000	2.100

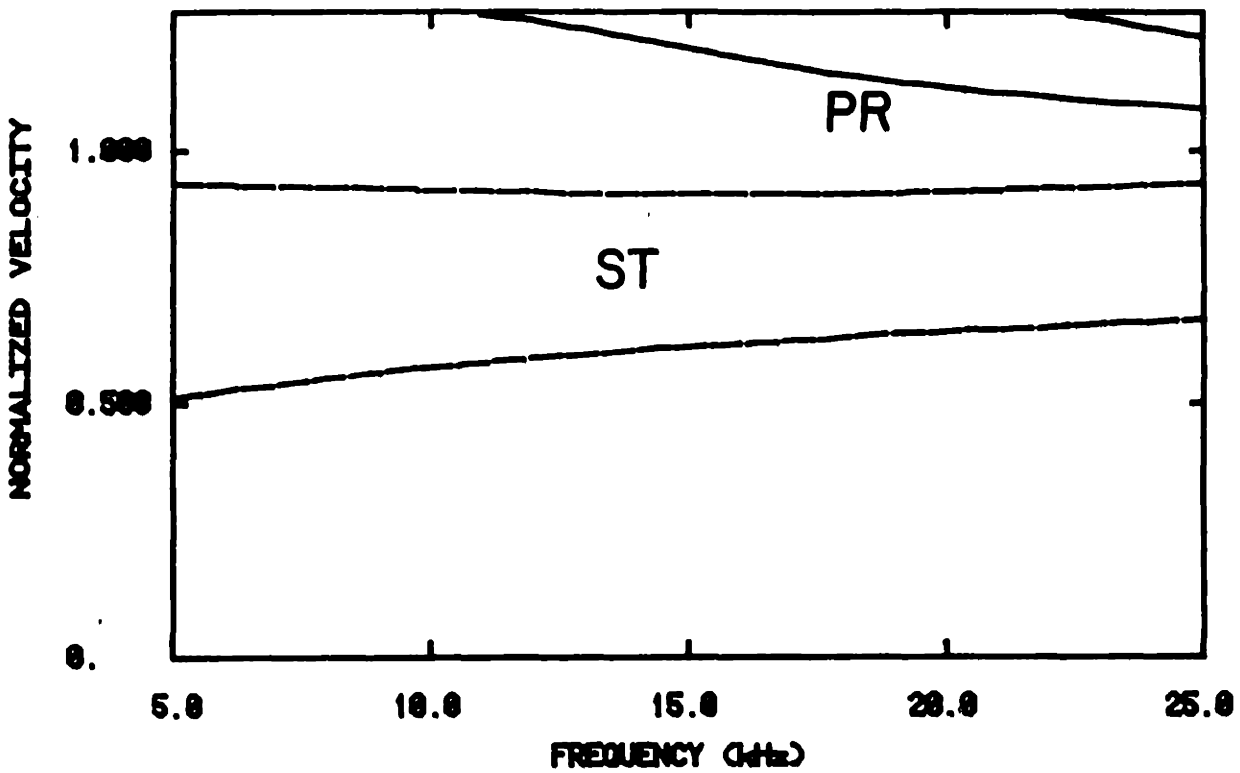

FIG. 4.36

r	Vp	Vs	rho
0.154167	5.500	0.	1.200
0.167500	20.000	11.663	7.500
0.200333	9.250	5.676	1.920
0.333333	5.500	0.	1.200
0.	13.120	7.661	2.100

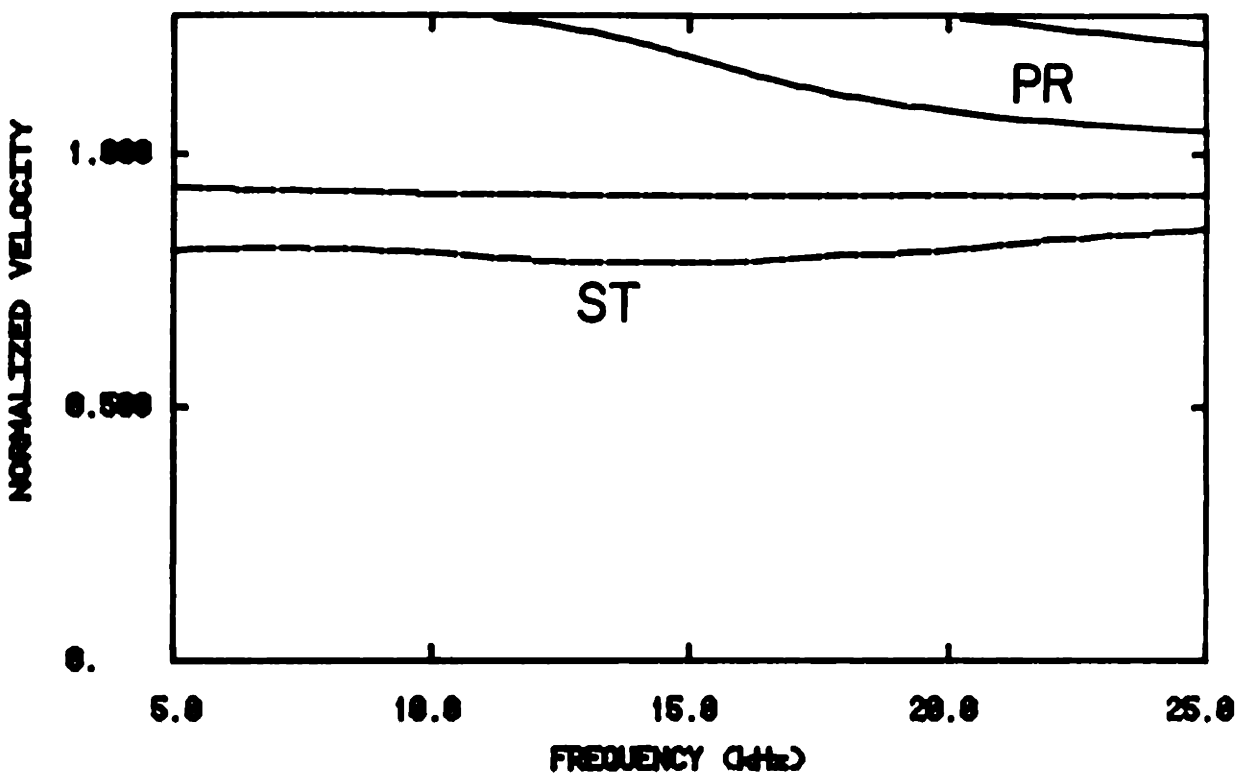

FIG. 4.37

r	Vp	Vs	rho
0.154167	5.500	0.	1.200
0.167500	20.000	11.000	7.500
0.333250	9.250	5.670	1.920
0.333333	5.500	0.	1.200
0.	13.120	7.000	2.100

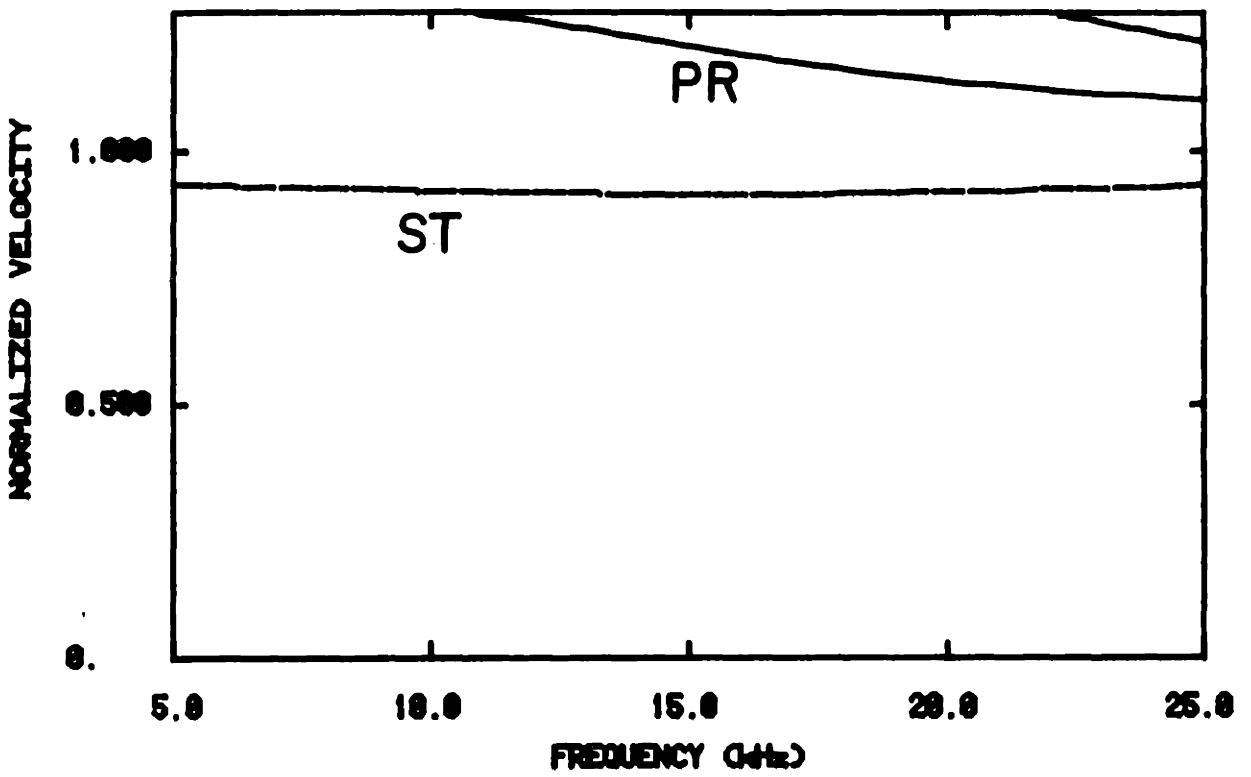

FIG. 4.38

Chapter 5

Open Boreholes With Radial Layering

5.1 Introduction

Even without casing layers of steel and cement present, actual open borehole environments are more complex than a simple infinite formation surrounding a fluid cylinder. The process of drilling introduces a variety of radial layers into the geometry. After the drilling process is complete, the drilling fluid itself can alter the parameters of the formation immediately adjacent to the borehole. In the worst case, this alteration can penetrate deep into the formation. The parameters desired are those of the *insitu* unaltered formation. In the case of extreme alteration it would be difficult to determine whether the measured values are those of the virgin formation or some perturbation away from those values. In this chapter we will investigate the effects on full waveform acoustic logs of some commonly occurring layers. The geometry is shown in Figure 5.1. The altered layers considered here are those of an invaded zone, a damaged zone, and a mud cake.

An invaded zone is formed as the borehole fluid seeps into the formation. The depth of the penetration depends greatly on the porosity and permeability of the formation. High permeability facilitates the migration of the fluid away from the borehole. The mud properties are also important. A highly viscous mud will not flow easily into the pore space of the surrounding formation resulting in an invaded zone of a few centimeters or less. If the permeability of the formation is high, and the mud is able to flow freely, the invaded zone can be as much as a meter or more. The formation of the mud cake layer can also reduce the flow of the borehole fluid into the surrounding formation. The mud cake is a layer of precipitate that forms along the inside of the borehole. The liquid components (filtrate) of the drilling mud migrate into the formation but the solid components are deposited as a coating along the fluid-solid interface. The characteristics of the mud cake will depend largely on the type of fluid used but the formation properties are important as well.

In addition to simply producing the borehole itself, the drilling process also damages a portion of the formation. This can create a zone with a large amount of micro-fractures or otherwise altered properties immediately along the borehole wall. This layer is called the damaged zone. Its thickness and parameters depend on the type of formation.

There is some ambiguity in the modeling of these different layers. The invaded zone, the damaged zone, and the mud cake can all be modeled as

lower velocity layers between the borehole fluid and the formation. The differences are in the amount of velocity change and the thickness of the layer over which the parameters are altered. A badly damaged layer may yield higher variations than a small amount of invasion. Conversely, a large amount of invasion can produce more velocity contrast than a small damaged zone. In field situations, the formation properties resulting in a large damaged zone will generally also be associated with a large invaded layer. It is not the formation parameters exclusively that control invasion, though, the mud properties affect the alteration also. There is a difference in the geometries as well. The invaded and damaged zones are both alterations of the formation. Part of the formation is replaced by the altered layer. The borehole radius (outer radius of the central fluid layer) is the same as in the simple infinite formation model. The radius at which the virgin formation is encountered is larger. The mud cake is deposited within the borehole so the borehole radius decreases by the thickness of this layer. The radius of the original formation does not change but the radius of the fluid does.

5.2 Invaded Zone

After the borehole has been drilled, the borehole mud remains in the hole. After some time, the fluid permeates a region of the formation surrounding the borehole. In this section we model this altered, or flushed zone as if the process is one where the borehole fluid fills the pores of a

gas saturated formation. This results in P-wave velocities which are higher and S-wave velocities which are lower for the saturated (post-invasion) state than for the dry (pre-invasion) state (Johnston and Toksöz, 1980).

For a first model of an invaded zone we raise the P-wave velocity 15 percent from 4 km/s (13.12 ft/ms) to 4.57 km/s (15 ft/ms). The S-wave velocity is lowered by 10 percent from 2.13 km/s (7 ft/ms) to 1.92 km/s (6.3 ft/ms). These contrasts are very large but they are used for demonstration purposes. The resulting microseismograms are shown in Figure 5.2. The thickness of the invaded zone is thin, 7.6 cm (3 inches). There is little difference in the character of the waveform due to the introduction of the invaded zone. Figure 5.3 shows the microseismograms for the homogeneous formation case. The P-wave arrivals overlay and there are only minor changes in the guided wave packet. The wavelengths involved here are more than 30 cm (1 ft). Because the P-wave velocity is higher in the invaded zone than in the formation, the thin invaded zone is not sufficient to affect the observed waveforms. The energy is directed out, away from the borehole.

As the thickness of the invaded zone increases its influence increases as well. Figure 5.4a shows microseismograms for a model with the thickness of the invaded zone doubled while the other parameters are held constant. The body wave arrival times still correspond to those of the formation, not the invaded zone. The thickness of the layer is now 15.2 cm

(6 inches) but it is still much less than a wavelength. The amplitude of the P-waves have decreased substantially though. There is no obvious wave from the invaded zone itself. but the layer is now sufficient to direct energy away from the borehole. It is necessary to expand the scale of these waveforms in order to see the formation P-wave arrivals (see Figure 5.4b). As the velocity contrast between the formation and the invaded zone decreases, the amplitude of the formation P-wave arrivals increases. The high velocity contrast is very efficient in causing energy to leak away from the borehole. This efficiency diminishes as the velocities of the two layers approach each other. In Figure 5.5 the invaded zone P-wave velocity is reduced to approximately 5 percent above the formation velocity. The shear velocity difference is just over 4 percent. The thickness remains unchanged at 15.2 cm. The P-wave arrival can be easily followed over the entire range of offsets in Figure 5.5. In Figure 5.6 the velocity contrasts are reduced still further. The waveforms are now indistinguishable from the simple infinite formation model (Figure 5.3).

As the invaded layer becomes thicker it becomes closer to the scale of the wavelengths involved. The thickness has been increased to 30.5 cm (1 ft) in Figure 5.7. Here, the very thick layer allows some energy from the invaded zone to be seen at short source-receiver separations (see Figure 5.7b). The waveforms approach those for an infinite invaded zone (Figure 5.8) with increasing thickness of the altered layer. Since Poisson's ratio changes (increases) with invasion, P-wave amplitudes also should increase

(Cheng and Toksöz, 1981). It also contributes to the difficulty of interpreting P-wave amplitudes in intermediate cases.

Looking back at the previous models and comparing with the infinite invaded zone model (Figure 5.8) it is clear that the guided waves are more strongly affected by presence of the invaded zone than are the body waves. The pseudo-Rayleigh arrivals appear similar to those in the infinite invaded zone even when the invasion is not strongly influencing the velocity of the first arrival.

Invasion can still take place when the formation is saturated with a fluid. Drilling mud density is generally adjusted so that the borehole fluid pressure is higher than the pore pressure in the formation. Drilling fluid invasion increases pore pressure in the formation reducing the effective pressure. The velocities of the invaded zone decrease relative to those of the unaltered formation. This results in a situation with the borehole fluid surrounded by a zone of relatively slow, modified formation which is in turn surrounded by the original medium with faster velocities.

Classical refraction seismology relies on head wave arrivals from various layer boundaries in order to obtain information about the subsurface. The geometry we have here is similar to this method. The most strongly observed body wave arrivals are the waves refracted along the interface.

The ability of standard refraction profile arrival time equations to correctly predict the first arrivals in the presence of a invaded zone is tested by examining waveforms at a large number of closely spaced receivers. Microseismograms for models with a highly invaded zone are shown in Figures 5.9 and 5.10. The virgin formation has velocities of 4 km/s (13.12 ft/ms) for V_p and 2.13 km/s (7 ft/ms) for V_s. The invaded layer has a P-wave velocity of 2.9 km/s (9.5 ft/ms) and a shear velocity of 1.52 km/s (5 ft/ms). The contrast between the invaded zone and the virgin formation in this model is very large, almost thirty percent. It is unlikely that alteration of this magnitude would occur. The parameters are chosen here so as to be an extreme case in order to separate various arrivals.

The thickness of the invaded layer in Figure 5.9 is 18.3 cm (7.2 inches) and in Figure 5.10 it is 27.2 cm (10.7 inches). All other parameters are the same in both figures. The observed first arrivals are indicated on the figures. Two distinct lines can be drawn connecting the first arrivals. These are compared with the expected arrival times as determined using equations for refraction profiles in stratified media (Dobrin, 1976). The agreement between the observed and calculated arrival times is excellent. The location of the intersection of the lines changes as expected with the increase in the thickness of the invaded zone. This intersection is marked as the crossover distance in Figures 5.9 and 5.10. This is the distance at which the first arrival switches from the first interface to the second. At distances less than the crossover distance, the first arrival is from (in this

case) the fluid-invaded zone boundary. At source-receiver separations greater than this distance, the first arrival corresponds to the wave refracted along the invaded zone-formation interface. Within the accuracy of the measurement, the observed crossover distance matches the calculated point very closely.

Figures 5.11 and 5.12 show models similar to the previous cases. The parameters of the invaded zone are the same but the thicknesses are now 5.1 cm (2 inches) and 18.3 cm (7.2 inches) for Figures 5.11 and 5.12 respectively. The center frequency of the source has been lowered to 5 kHz in order to examine the guided wave portion of the time series. As expected, the thicker invaded layer affects the waveform more than the thin layer. Stoneley wave velocity calculations from the two models yield 1.48 km/s (4.86 ft/ms) for the model with the 5.1 cm (2 inch) layer and 1.28 km/s (4.2 ft/ms) for the model with the 18.3 cm (7.2 inch) thick layer. Since the velocities of the invaded layer are lower than those of the formation, a larger layer results in lower velocities.

It is important to note that in Figures 5.9 and 5.10 the offsets and the source-receiver spacing are both small. The receivers are separated by only 6 cm (.2 feet). This is much smaller than the inter-receiver distance on actual tools. Also, the velocity contrast between the invaded zone and the formation is very large. If the velocity difference is not as great and the receiver spacing is larger, it is difficult to observe separate arrivals

corresponding to the different layers. A more realistic model of an invaded zone is shown in Figure 5.13. The invaded zone is 15.2 cm (6 inches) with velocities 10 percent lower, V_p = 3.6 km/s (11.8 ft/ms) and V_s = 1.92 km/s (6.3 ft/ms), than those of the formation. The invaded zone is modeled with six layers with a linear velocity variation rather than one layer as in the previous case. The receivers are now spaced 15.2 cm (0.5 feet) apart. The presence of the invaded zone is not obvious here. It is not possible to distinguish arrivals from the different layers. This is in agreement with Chan and Tsang (1983) and Pardo (1984). They observed the first arrival from the formation even in the presence of an invasion layer. Baker (1984) also measures the formation velocities provided that the source-receiver separation is sufficiently large. The only clear change in the waveforms of Figure 5.13 from the homogeneous solid case (Figure 5.3) is an increase in the P-wave amplitudes. This increase in amplitude is due to the focusing of energy because of the increasing velocities.

5.3 Damaged Zone

The process of drilling can alter some amount of the formation surrounding the borehole. The drill bit does not simply create the hole itself, it also disturbs a region of formation bordering the hole. This region can be fractured and altered into what is commonly referred to as a damaged zone. The thickness of the damaged zone, as well as its properties, depends on the original properties of the formation and the

specific drilling process. A very strong formation, such as a granite, would be altered very little while a shale can be greatly affected by the drilling process.

In this section a damaged zone is modeled as a region of lowered velocities, densities, and Q values. The damaged zone model is similar to the previous one of an invaded zone with velocities lower than those of the formation. The damaged zone generally does not extend as far into the formation but the invaded zone model could also be considered to be a model of a large damaged zone.

As before, at very short offsets the first arrival will be from the damaged zone, but at longer, more reasonable offsets, the first arrival will be from the formation. Figure 5.14 shows a damaged zone of thickness 0.64 cm (0.25 inches). The waveforms are very similar to the simple formation model (Figure 5.3). There is a very slight increase in the P-wave amplitude. This is due to the focusing of the energy because of the velocity increase. The shear wave and guided wave packets are virtually unchanged. A thicker damaged zone results in a larger increase in the amplitude of the P-wave. The thickness has been increased to 2.5 cm (1 inch) in Figure 5.15. Here the increase in the P-wave amplitude is significant, approximately double. This is consistent with the observations of Bhasavanija (1983) in the same situation. He modeled a damaged zone with the finite difference technique. His results indicate an increase in the

P-wave amplitude of more than 2 times. The damaged zone in his model was almost 5 cm (2 inches) thick rather than the 2.5 cm (1 inch) in our model, but the velocity contrast was much less, (9 percent versus 20 percent). Despite the change in the amplitudes of the P-wave arrival, the first arrivals correspond to those of the formation, not the damaged zone.

The character of the guided wave portion of the microseismograms displays minor changes with the thicker damaged zone. The layer appears to be sufficient to make the pseudo-Rayleigh wave slightly more dispersive. The first peak, generally taken to be the shear arrival, is at the velocity of the formation S-wave velocity. The remainder of the peaks are delayed by approximately one quarter cycle at the longest offsets.

Similar results are obtained with different formation and damaged zone parameters. Figure 5.16 shows the microseismograms for a model with formation velocities of 4.88 km/s (16 ft/ms) for V_p and 2.6 km/s (8.53 ft/ms) for V_s. The contrast between the formation velocities and the damaged zone velocities remains 20 percent.

The thin (0.64 cm, 0.25 inch) damaged zone again produces very little effect on the waveforms as compared with the simple geometry (Figure 5.17). A slight increase in the P-wave amplitude is observed but the remainder of the time series is unchanged. The 2.5 cm (1 inch) thick damaged layer results in larger P-wave amplitudes and minor changes in the guided wave arrivals (see Figure 5.18).

5.4 Mud Cake Layer

As the borehole fluid permeates the formation creating the invaded zone the mud precipitate settles along the borehole wall. This precipitate forms a layer along the borehole wall referred to as the mud cake. The properties of the mud cake are not well known, although the caliper log can give a good measure of its thickness. The mud cake layer is modeled in this section as a low velocity material with low density and Q factors. Since the mud cake forms on the inside of the borehole wall, the outer radius of the fluid is less in the presence of a mud cake than without one.

The properties of the mud cake are controlled mainly by the nature of the drilling mud in the borehole. If the borehole fluid moves into the formation quickly, a layer of precipitate will soon form on the borehole wall. This layer seals the interface, inhibiting further invasion. A different type of mud can deposit more slowly, allowing the layer of mud cake to become much thicker. Generally the amount of mud cake ranges from 0.3 cm (1/8 inch) to about 1.3 cm (0.5 inch). In a bad case the mud cake thickness can reach 2 cm (0.75 inch). The rate at which the mud can enter the formation is also affected by formation itself. A formation with high permeability and porosity will allow the mud to filter in easily. Low permeability will inhibit the flow.

Figure 5.19 shows a geometry with the same formation as in Figure 5.3 only there is now a mud cake layer within the borehole. The mud cake

velocities are taken to be slow, 2.29 km/s (7.5 ft/ms) for V_p and 1.14 km/s (3.75 ft/ms) for V_s. The thickness is 1.27 cm (0.5 inches) so this is a fairly thick mud cake. The arrival times and velocities of the observed body waves, both the P- and the S-wave are the same as in the simple homogeneous formation case (Figure 5.3). The P-wave amplitudes are significantly larger though. As in the damaged zone model, the difference is approximately a factor of two. This is not surprising since the models of the damaged zone and mud cake are not fundamentally different. They are both low velocity layers between the fluid and the formation. The geometries are different though. The damaged zone replaces part of the formation while the mud cake replaces part of the fluid. The reduction in borehole size would yield slightly smaller P-wave amplitudes (Zhang and Cheng, 1984) but the higher velocity contrast produces more amplitude increase than the damaged zone model. The final result is similar amplitude changes in the damaged zone and mud cake models.

The guided wave arrivals are only slightly affected by the addition of the mud cake. The pseudo-Rayleigh and Stoneley amplitudes are unchanged although the pseudo-Rayleigh wave is mildly more dispersive.

The basic observations remain the same as the amount of the mud cake increases. The thickness of the mud cake layer in Figure 5.20 is 2.5 cm (1 inch). This corresponds to an extremely thick mud cake. The arrival times of the body wave arrivals do not change but there is a change in

amplitudes. The pseudo-Rayleigh wave becomes more dispersive also. The nature of the effects observed due to the mud cake does not change, only the degree to which they influence the waveforms.

The observed effects of the mud cake do not change as the parameters of the mud cake change. Figure 5.21 shows a model with a mud cake layer thickness of 0.64 cm (0.25 inches). The shear velocity of the mud cake has been raised to 1.37 km/s (4.5 ft/ms). A comparison of this figure with Figure 5.19 reveals that the only change is in the amplitude of the P-wave. This is most likely caused by the change in layer thickness as was observed in the previous models. The amplitudes are smaller with the thinner layer even though the mud cake Q values are increased in Figure 5.21.

Figures 5.22, 5.23, and 5.24 show a simple formation model and this same formation with mud cake layers of 1.27 cm (0.5 inch) and 2.5 cm (1 inch). The conclusions about the effects of the mud cake do not differ with the different formation.

5.5 Summary

The introduction of a thin altered layer into the borehole environment does not restrict the ability to determine the properties of the virgin formation. At very short offsets a distinction can be seen between the different layers but at longer offsets the observed arrivals have velocities corresponding to those of the formation.

As the thickness of the altered layer increases, its influence becomes more noticeable. Longer offsets become necessary in order to measure the properties of the unaltered formation. Classical refraction relations can satisfactorily predict the arrival times of signals from the different layers in the case where the altered zone has lower velocities than the original formation (such as a damaged zone or mud cake layer). Lower velocities in the altered layer result in interference between arrivals from the different layers which produce increase P-wave amplitudes. The guided wave portion of the microseismograms remain basically unchanged although it does become slightly more dispersive.

In the model of a flushed zone the P-wave velocity increases and the S-wave velocity decreases relative to the formation. A thin layer is almost transparent because the wavelengths are much longer than the thickness of the layer. Since the velocities decrease away from the borehole wall, the energy leaks away and is trapped by the infinite formation. Thus the velocities observed are those of the formation, not those of the invaded zone. In the case of lower velocities for the altered layer, there is the higher velocity formation to contain the energy and direct it back into the borehole. In this situation the altered layer only acts to direct the energy out from the borehole. As the thickness of the flushed zone increases the situation becomes more what is expected and observed in flat earth seismology: the arrival from the formation decreases substantially and the arrival from the fluid-invaded zone interface increases. In the limit that

the flushed zone thickness goes to infinity, there is only the arrival from this layer and there is no significant contribution from the formation. Although velocities are not changed, changes in the waveforms could be significant.

Figure	thickness cm (inches)	V_p km/s (ft/ms)	V_s km/s (ft/ms)	ρ gm/cm^3	Q_α	Q_β
20,23,	7.62 (3.00)	1.68 (5.50)	–	1.2	20.	–
19,24	8.89 (3.5)	1.68 (5.50)	–	1.2	20.	–
21	9.53 (3.75)	1.68 (5.50)	–	1.2	20.	–
2-18,22	10.16 (4.00)	1.68 (5.50)	–	1.2	20.	–

Table 5.1. Borehole fluid parameters for theoretical models. Note that the variations are in thickness only.

Figure	thickness cm (inches)	V_p km/s (ft/ms)	V_s km/s (ft/ms)	ρ gm/ cm^3	Q_α	Q_β
2	7.62 (3.00)	4.57 (15.0)	1.92 (6.30)	2.36	70.	50.
4	15.24 (6.00)	4.57 (15.0)	1.92 (6.30)	2.36	70.	50.
5	15.24 (6.00)	4.21 (13.8)	2.04 (6.70)	2.24	65.	55.
6	15.24 (6.00)	4.02 (13.2)	2.12 (6.95)	2.17	61.	59.
7	30.48 (12.00)	4.57 (15.0)	1.92 (6.30)	2.36	70.	50.
8	∞	4.57 (15.0)	1.92 (6.30)	2.36	70.	50.
9	18.3 (7.2)	2.9 (9.5)	1.52 (5.00)	2.0	100.	50.
10	27 (10.7)	2.9 (9.5)	1.52 (5.00)	2.0	100.	50.
11	5.08 (2.00)	2.9 (9.5)	1.52 (5.00)	2.0	100.	50.
12	18.03 (7.2)	2.9 (9.5)	1.52 (5.00)	2.0	100.	50.

Table 5.2. Invaded zone parameters for theoretical models.

Figure	thickness cm (inches)	V_p km/s (ft/ms)	V_s km/s (ft/ms)	ρ gm/cm^3	Q_α	Q_β
14	.64 (0.25)	3.2 (10.5)	1.71 (5.60)	1.8	50.	40.
15	2.54 (1.00)	3.2 (10.5)	1.71 (5.60)	1.8	50.	40.
16	.64 (0.25)	3.9 (12.8)	2.08 (6.825)	1.8	50.	40.
18	2.54 (1.00)	3.9 (12.8)	2.08 (6.825)	1.8	50.	40.

Table 5.3. Damaged zone parameters for theoretical models.

Figure	thickness cm (inches)	V_p km/s (ft/ms)	V_s km/s (ft/ms)	ρ gm/cm^3	Q_α	Q_β
19,24	1.27 (0.50)	2.29 (7.50)	1.14 (3.75)	1.6	30.	20.
20,23	2.54 (1.00)	2.29 (7.50)	1.14 (3.75)	1.6	30.	20.
21	.64 (0.25)	2.29 (7.50)	1.37 (4.50)	2.4	50.	40.

Table 5.4. Mud cake parameters for theoretical models.

Figure	thickness cm (inches)	V_p km/s (ft/ms)	V_s km/s (ft/ms)	ρ gm/cm^3	Q_α	Q_β
22-24	∞	5.94 (19.50)	3.2 (10.5)	2.16	60.	60.
6,7, 9-15, 19-21	∞	4.0 (13.12)	2.13 (7.00)	2.16	60.	60.
16-18	∞	4.88 (16.00)	2.6 (8.53)	2.16	60.	60.

Table 5.5. Formation parameters for theoretical models.

Figure Captions

Figure 5.1 Geometry of the a) invaded or damaged zone model. A portion of the original formation is replaced by the altered zone b) mud cake model. The mud cake is deposited on the borehole wall so the radius of the fluid layer decreases.

Figure 5.2 Microseismograms for a model with a 7.62 cm (3 inch) flushed zone. The flushed zone is model as the borehole fluid permeating a gas saturated formation. The resulting velocities are higher for the P-wave and lower for the S-wave.

Figure 5.3 Microseismograms for a homogeneous formation without an altered zone. The formation is the same as that in Figure 5.2. The source-receiver separations range from a) 3.05 m (10 ft) to 4.57 m (15 ft) b) 0.61 m (2 ft) to 3.05 m (10 ft) at 0.15 m (0.5 ft) intervals.

Figure 5.4 Same as Figure 5.2 except the thickness of the invaded zone is increased to 15.2 cm (6 inches). The vertical scale is a) the same as the other figures b) increases by a factor of 5.

Figure 5.5 Microseismograms for a model with a 15.2 cm (6 inch) invaded zone. The velocity contrast is now smaller than in Figure 5.2.

Figure 5.6 Microseismograms for a model with a 15.2 cm (6 inch) invaded zone. The velocity contrast is now smaller than in Figure 5.5 so the

invaded zone parameters are close to those of the formation.

Figure 5.7 Microseismograms for an invaded zone with a thickness of The invaded zone parameters are the same as those in Figure 5.2. The source-receiver separations range from a) 3.05 m (10 ft) to 4.57 m (15 ft) b) .61 m (2 ft) to 3.05 m (10 ft) at 0.15 m (0.5 ft) intervals.

Figure 5.8 Microseismograms for a model of a homogeneous formation. The formation properties are those of the invaded zone in Figure 5.2. This is a model of infinite invasion.

Figure 5.9 Microseismograms for a model of an invaded zone with much lower velocities than those of the unaltered formation. The invaded zone velocities are 2.9 km/s (9.5 ft/ms) for V_p and 1.52 km/s (5 ft/ms) for V_s. The formation velocities are 4 km/s (13.12 ft/ms) and 2.13 km/s (7 ft/ms) for V_p and V_s. Offsets range from 0.30 m (1 ft) to 3.05 m (10 ft) at intervals of 0.06 m (0.2 ft). The first arrivals due to the different layers are marked. The thickness of the invaded zone is 18.3 cm (7.2 inches) so the expected crossover distance is 3.39 ft.

Figure 5.10 Same as Figure 5.9 except the thickness of the invaded zone is 27 cm (10.7 inches). The expected crossover is at 4.86 ft.

Figure 5.11 Microseismograms from 2.13 m (7 ft) to 3.05 m (10 ft) with a source center frequency of 5 kHz. The thickness of the invaded zone is 5.08 cm (2 inches) and the velocities are the same as in Figure 5.9 The

Stoneley wave velocity determined from the indicated peaks is 1.49 km/s (4.89 ft/ms).

Figure 5.12 Same as Figure 5.11 except the thickness of the invaded zone is 18.3 cm (7.2 inches). The velocity determined for the Stoneley wave is 1.31 km/s (4.29 ft/ms).

Figure 5.13 Microseismograms for an invaded zone modeled as 6 layers with a linear velocity change. The source-receiver separations range from a) 3.05 m (10 ft) to 4.57 m (15 ft) b) 0.61 m (2 ft) to 3.05 m (10 ft) at 0.15 m (0.5 ft) intervals.

Figure 5.14 Microseismograms for a model of a borehole with a .64 cm (.25 inch) damaged zone. The formation parameters are the same as those in Figure 5.2.

Figure 5.15 Same as Figure 5.14 except the thickness of the damaged zone has been increased to 2.54 cm (1 inch).

Figure 5.16 Microseismograms for a model of a borehole with a .64 cm (.25 inch) damaged zone. The formation has higher velocities than in Figure 5.14.

Figure 5.17 Microseismograms for the unaltered formation of Figure 5.16.

Figure 5.18 Same as Figure 5.16 except the thickness of the invaded zone is increased to 2.54 cm (1 inch).

Figure 5.19 Microseismograms for the formation of Figure 5.3 with a 1.27 cm (.5 inch) mud cake layer on the borehole wall. Note the large increase in P-wave amplitudes.

Figure 5.20 Same as Figure 5.19 except the thickness of the mud cake has been increased to 2.5 cm (1 inch).

Figure 5.21 Microseismograms for the formation of Figure 5.3 with a 1.27 cm (.5 inch) mud cake layer. The mud cake S-wave velocity, density, and Q values are higher than those in Figure 5.19.

Figure 5.22 Microseismograms for unaltered formation with high velocities.

Figure 5.23 Microseismograms for the formation of Figure 5.22 with a 2.5 cm (1 inch) thick mud cake layer.

Figure 5.24 Same as Figure 5.23 except the mud cake thickness is 1.27 cm (.5 inches).

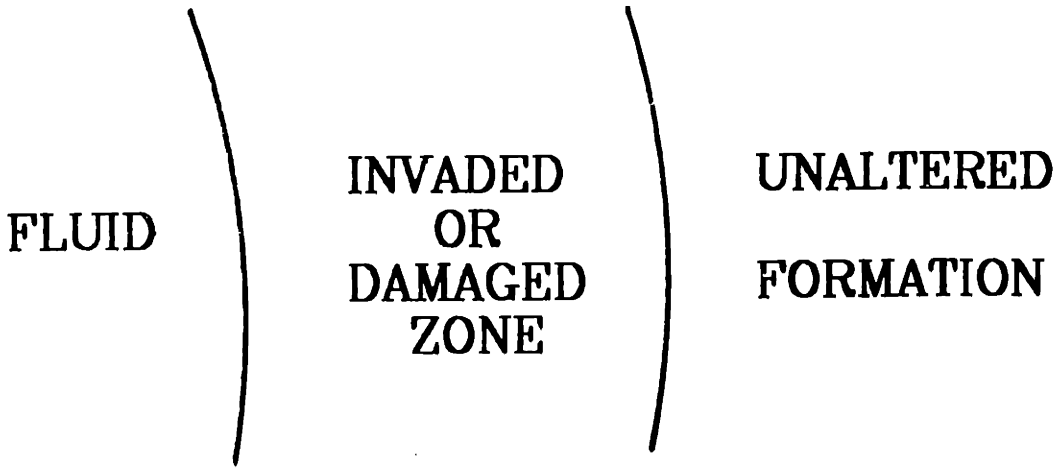

ORIGINAL
BOREHOLE
RADIUS

FIG. 5.1a

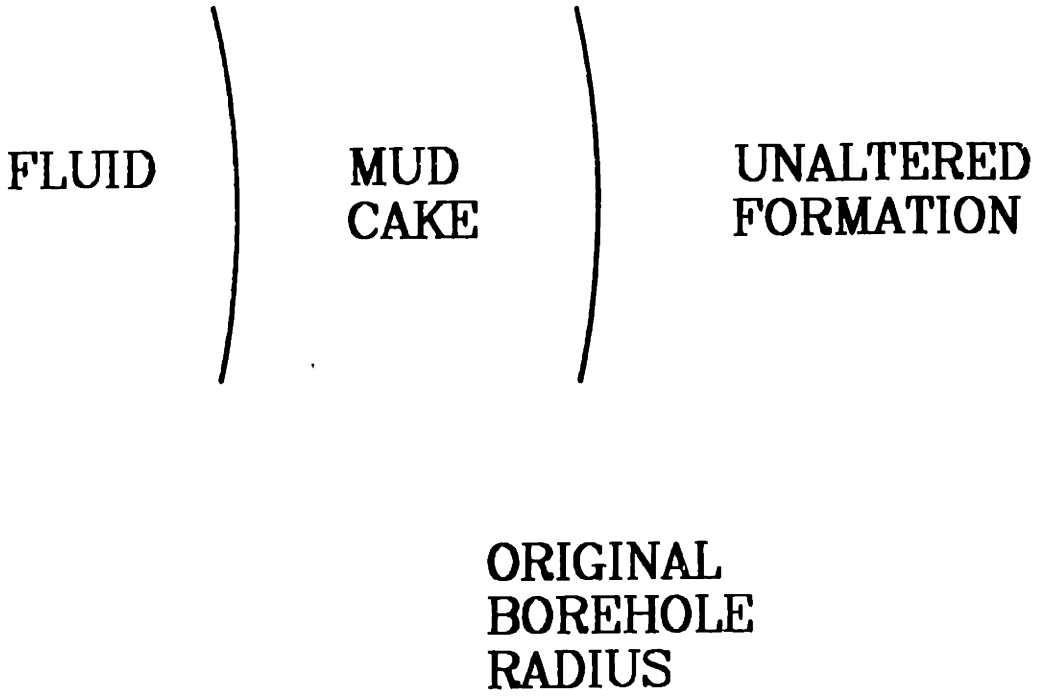
FLUID
MUD
CAKE
UNALTERED
FORMATION
ORIGINAL
BOREHOLE
RADIUS

FIG. 5.1b

H (FT)	VP (FT/MS)	VS (FT/MS)	RHO (GM/CC)	QP	QS
0.333333	5.5000	0.	1.2000	20.00	0.
0.583300	15.0000	6.3000	2.3600	70.00	50.00
0.	19.1200	7.0000	2.1600	60.00	60.00

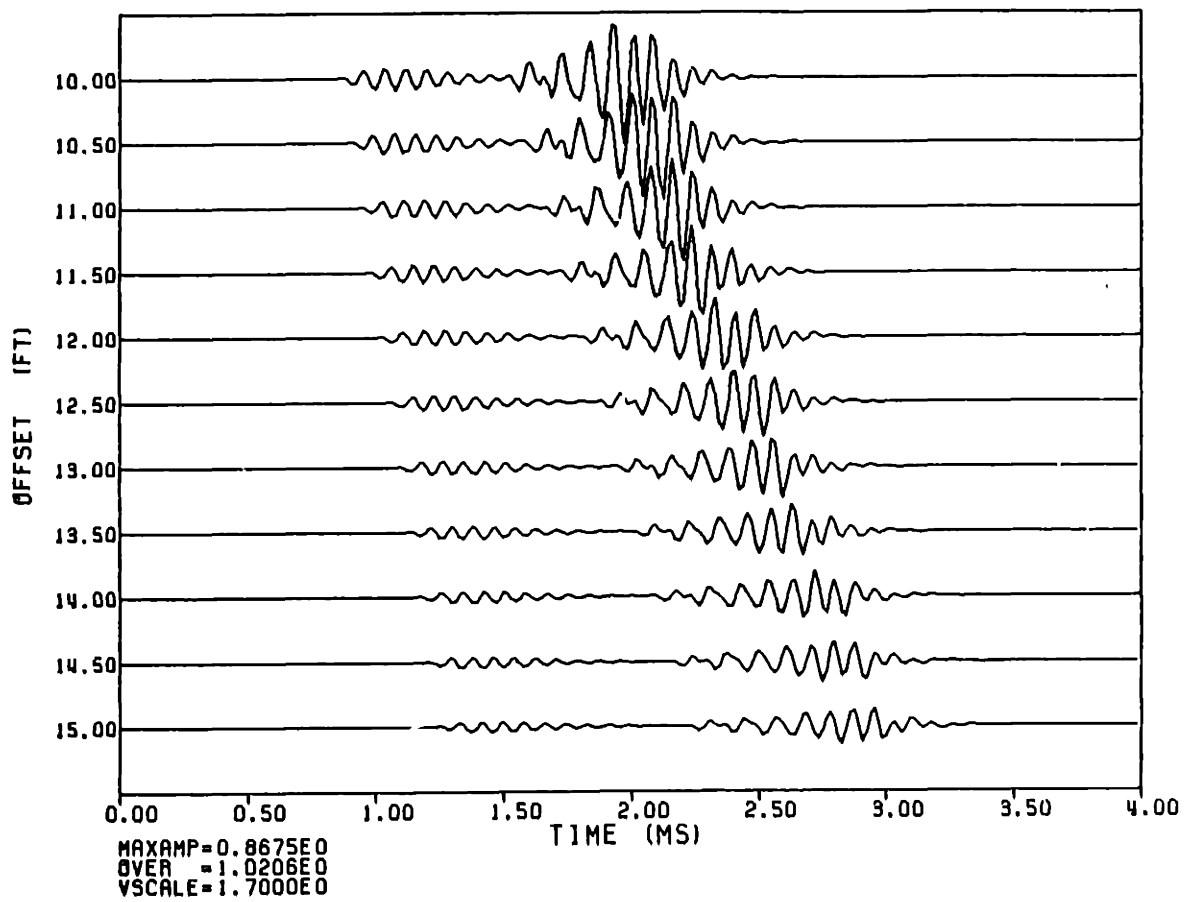

FIG. 5.2

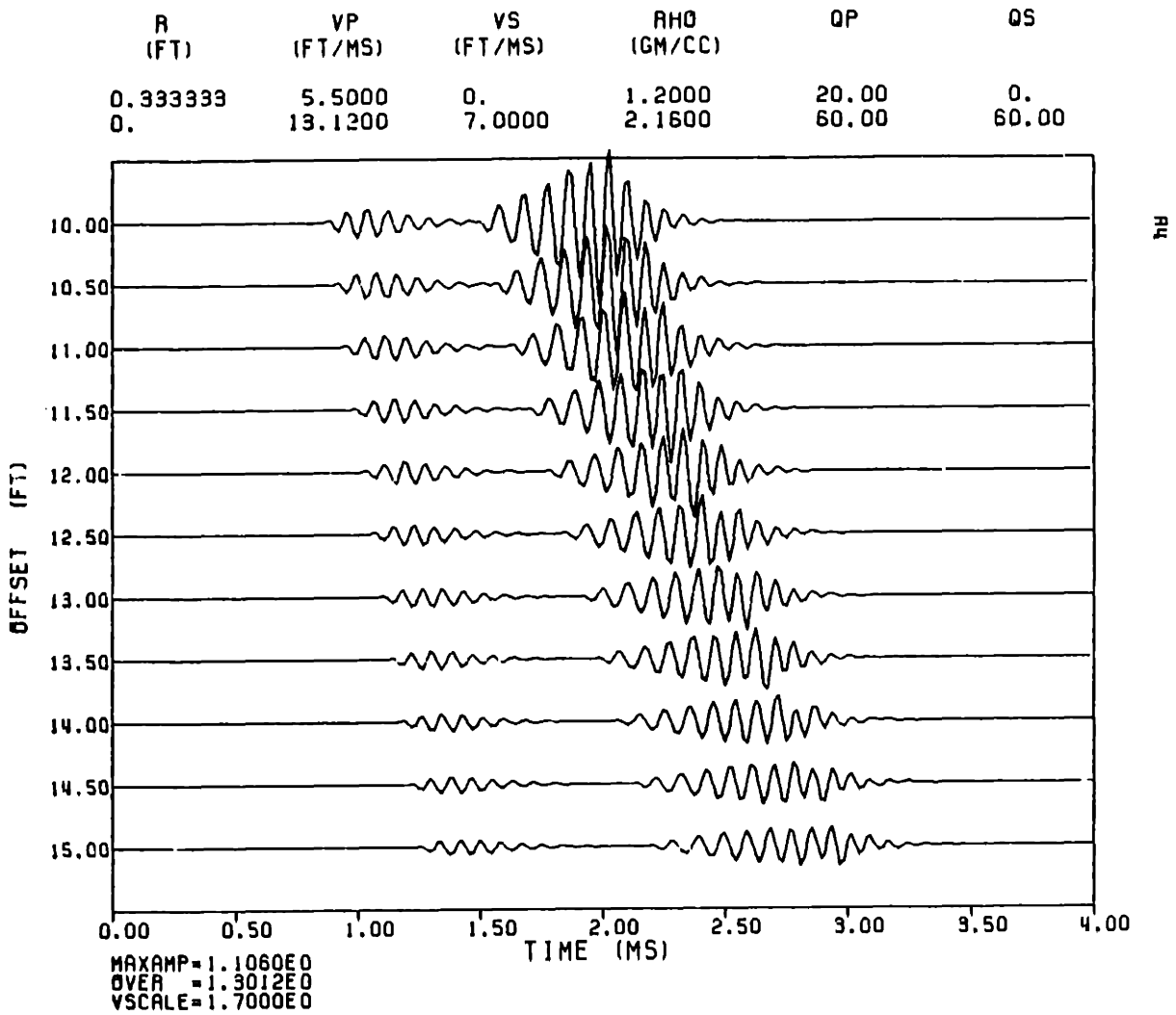
R (FT)
VP (FT/MS)
VS (FT/MS)
RHO (GM/CC)
QP
QS
0.333333 5.5000 0. 1.2000 20.00 0.
0. 13.1200 7.0000 2.1600 60.00 60.00
10.00
10.50
11.00
11.50
12.00
12.50
13.00
13.50
14.00
14.50
15.00
OFFSET (FT)
0.00 0.50 1.00 1.50 2.00 2.50 3.00 3.50 4.00
TIME (MS)
MAXAMP=1.1060E0
OVER =1.3012E0
VSCALE=1.7000E0

FIG. 5.3a

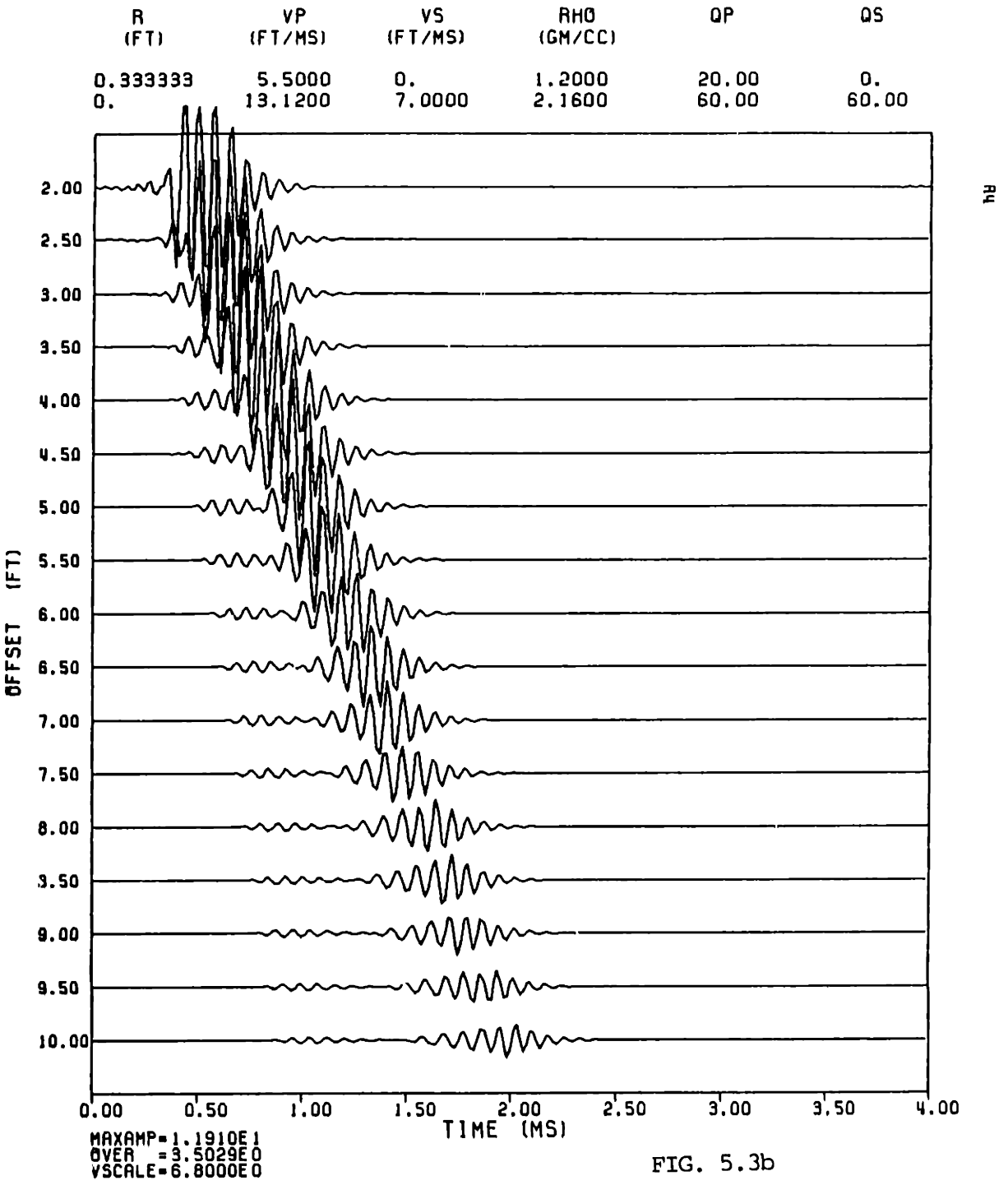
R (FT)
VP (FT/MS)
VS (FT/MS)
RHO (GM/CC)
QP
QS
0.333333 5.5000 0. 1.2000 20.00 0.
0. 13.1200 7.0000 2.1600 60.00 60.00
OFFSET (FT)
2.00
2.50
3.00
3.50
4.00
4.50
5.00
5.50
6.00
6.50
7.00
7.50
8.00
8.50
9.00
9.50
10.00
0.00 0.50 1.00 1.50 2.00 2.50 3.00 3.50 4.00
TIME (MS)
MAXAMP=1.1910E1
OVER =3.5029E0
VSCALE=6.8000E0

FIG. 5.3b

R (FT)	VP (FT/MS)	VS (FT/MS)	RHO (GM/CC)	QP	QS
0.333333	5.5000	0.	1.2000	20.00	0.
0.833333	15.0000	6.3000	2.3600	70.00	50.00
0.	13.1200	7.0000	2.1600	60.00	60.00

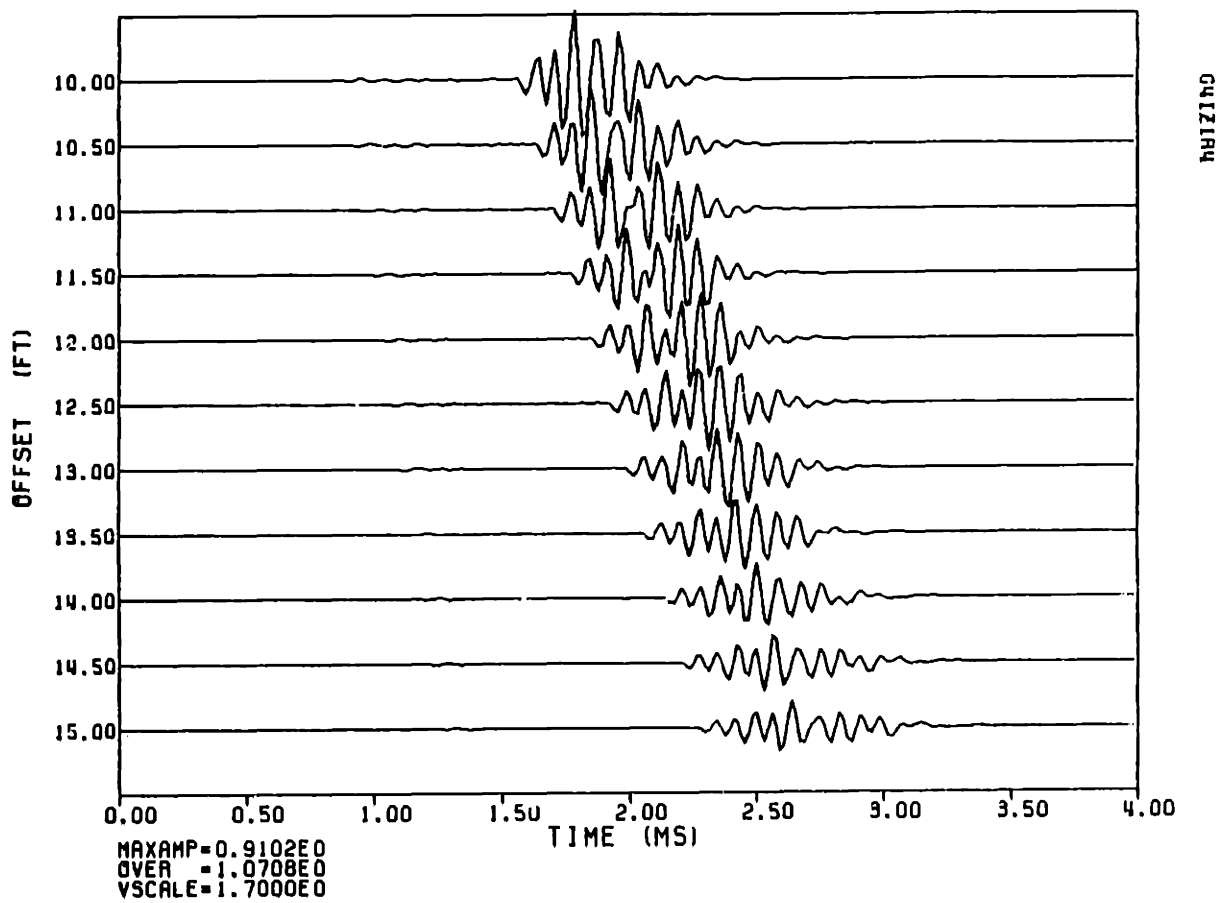

FIG. 5.4a

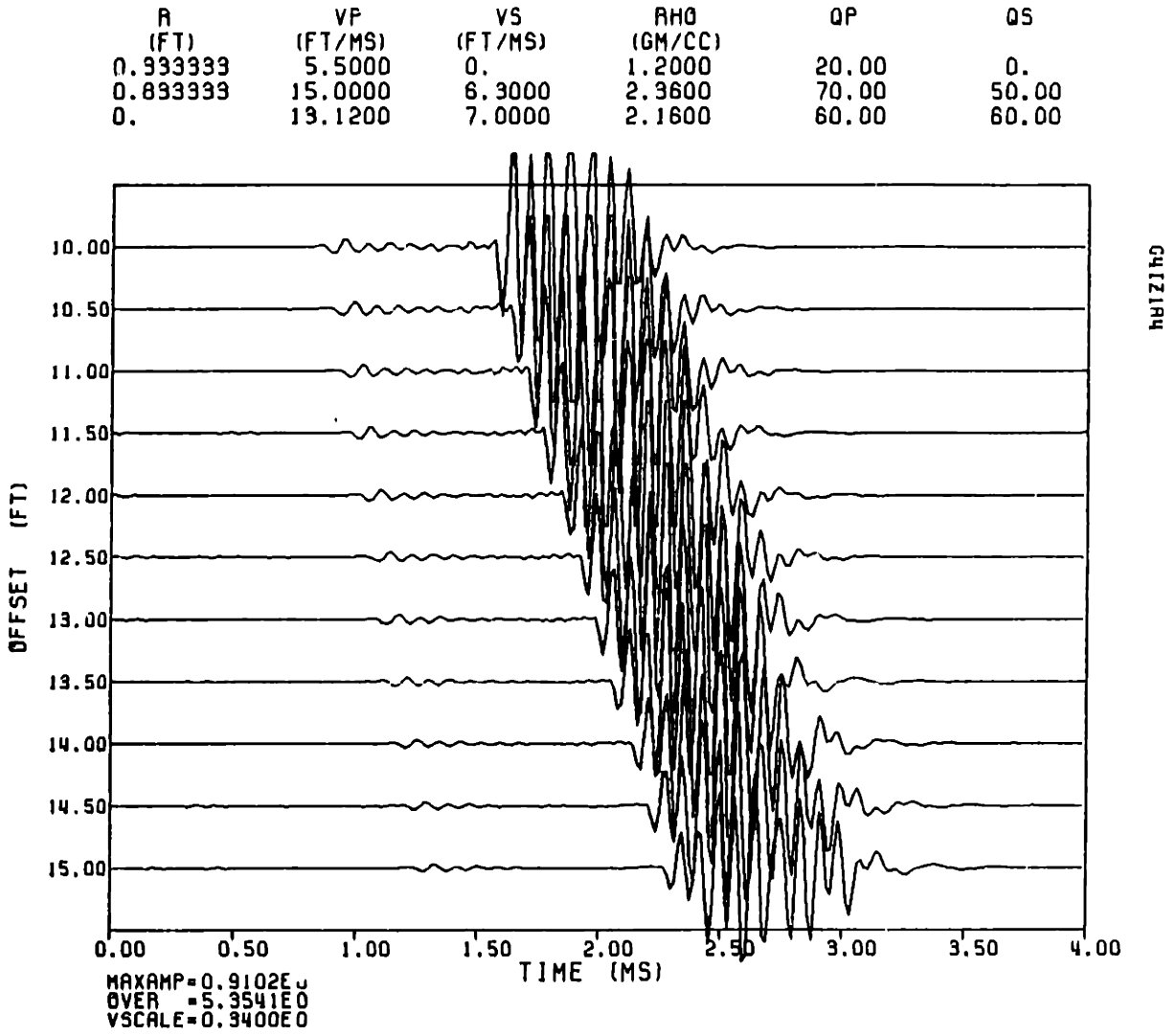
H (FT) VP (FT/MS) VS (FT/MS) RHO (GM/CC) QP QS
0.933333 5.5000 0. 1.2000 20.00 0.
0.833333 15.0000 6.3000 2.3600 70.00 50.00
0. 13.1200 7.0000 2.1600 60.00 60.00
OFFSET (FT)
10.00
10.50
11.00
11.50
12.00
12.50
13.00
13.50
14.00
14.50
15.00
0.00 0.50 1.00 1.50 2.00 2.50 3.00 3.50 4.00
TIME (MS)
MAXAMP=0.9102E
OVER =5.3541E0
VSCALE=0.9400E0

FIG. 5.4b

H (FT)	VP (FT/MS)	VS (FT/MS)	RHO (GM/CC)	QP	QS
0.333333	5.5000	0.	1.2000	20.00	0.
0.833333	13.8000	6.7000	2.2400	65.00	55.00
0.	13.1200	7.0000	2.1600	60.00	60.00

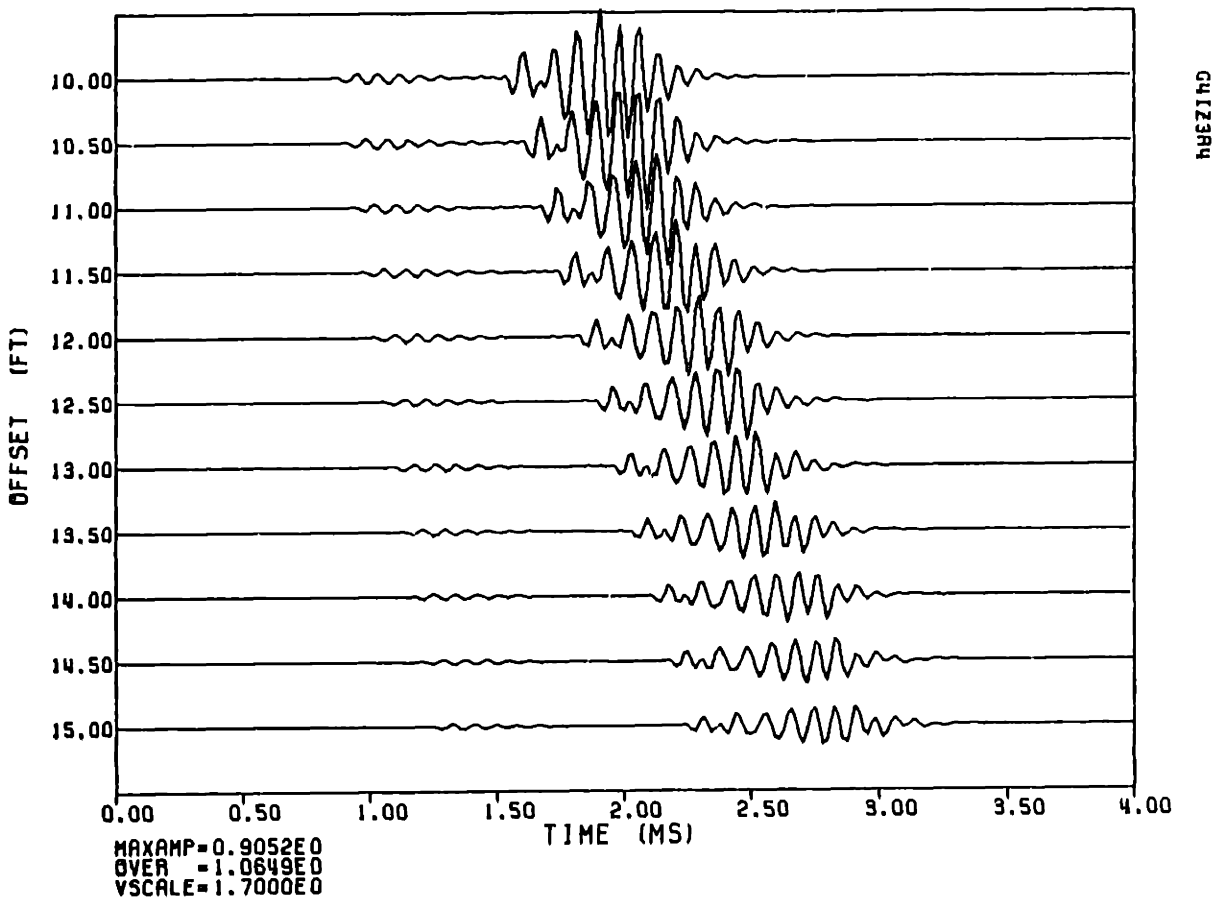

FIG. 5.5

H (FT)	VP (FT/MS)	VS (FT/MS)	RHO (GM/CC)	QP	QS
0.333333	5.5000	0.	1.2000	20.00	0.
0.833333	13.2000	6.9500	2.1700	61.00	59.00
0.	13.1200	7.0000	2.1600	60.00	60.00

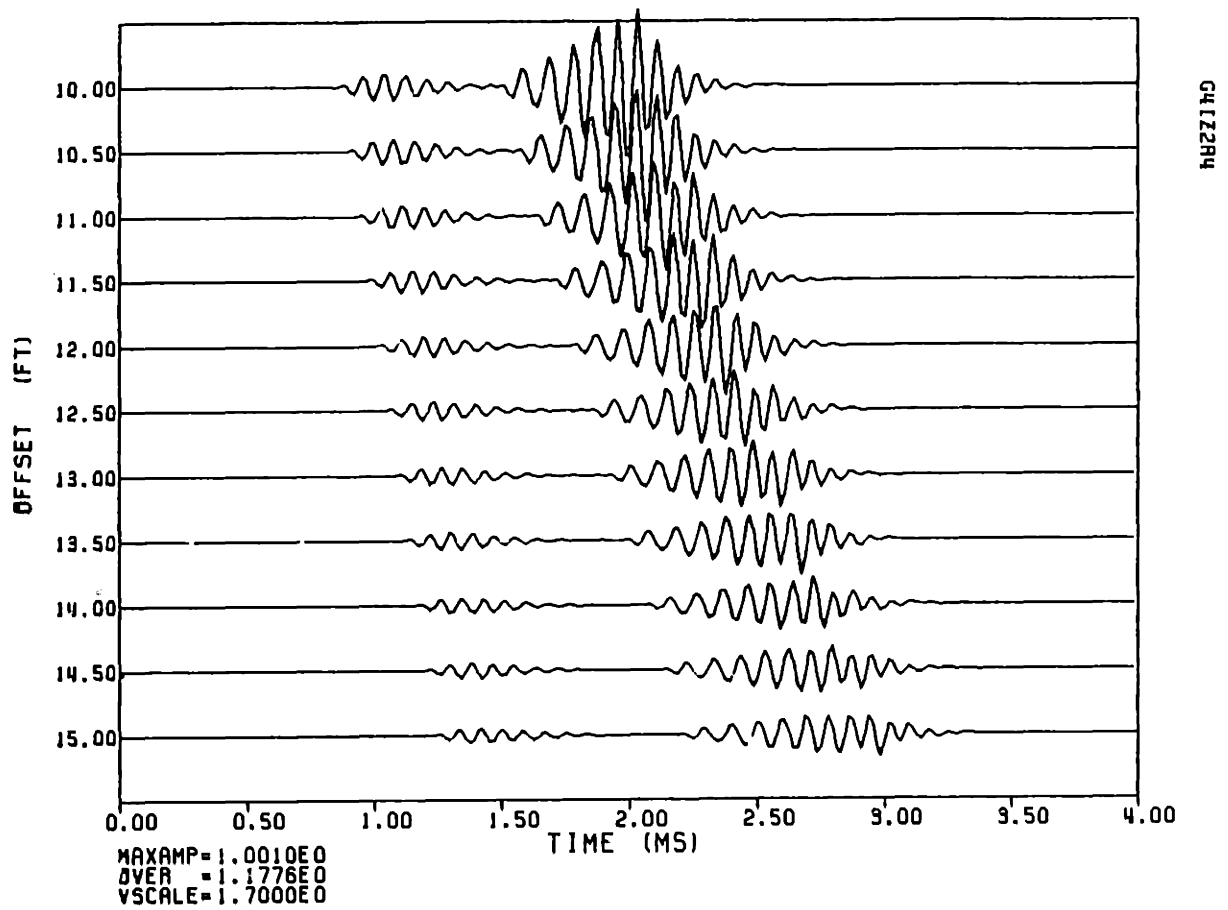

FIG. 5.6

H (FT)	VP (FT/MS)	VS (FT/MS)	RHO (GM/CC)	QP	QS
0.333333	5.5000	0.	1.2000	20.00	0.
1.333330	15.0000	6.3000	2.3600	70.00	50.00
0.	19.1200	7.0000	2.1600	60.00	60.00

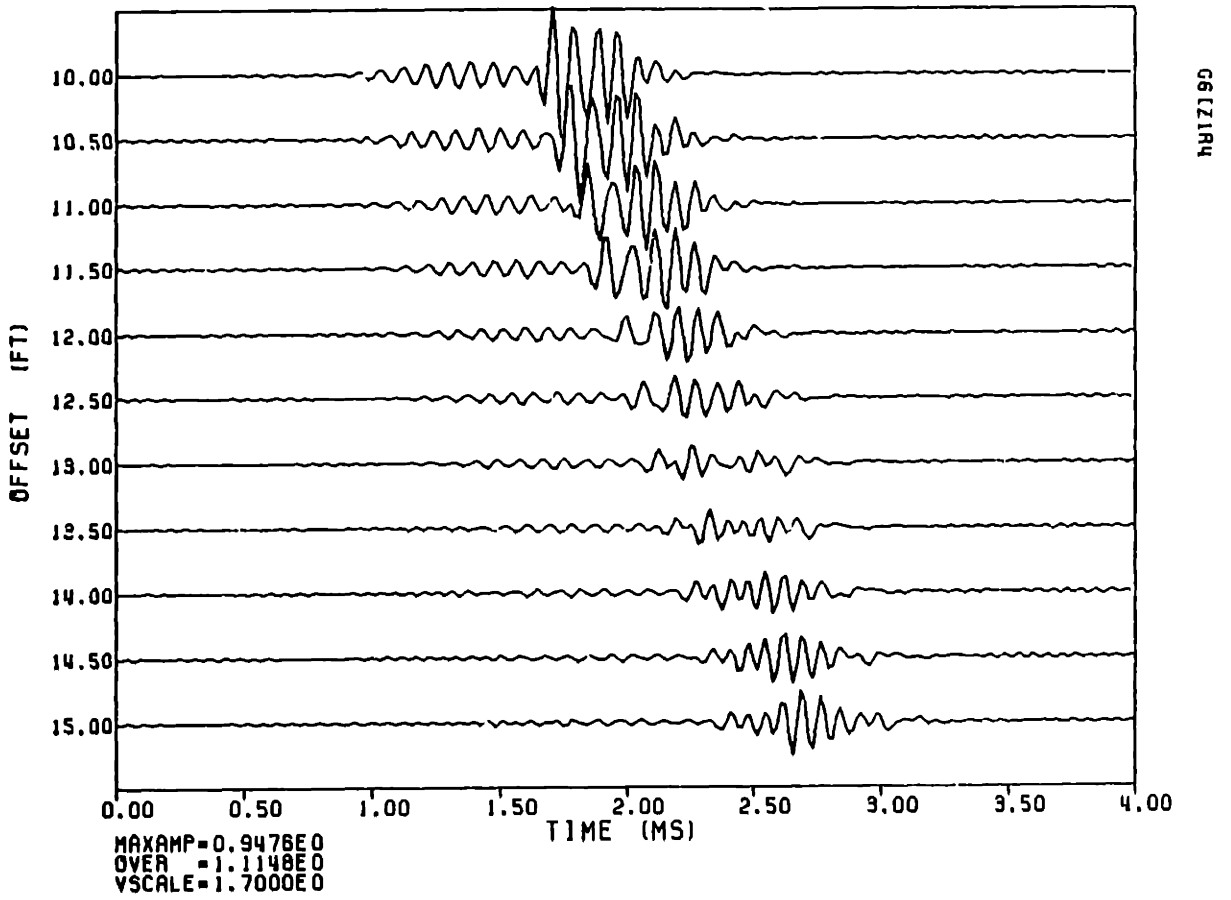

FIG. 5.7a

R (FT)	VP (FT/MS)	VS (FT/MS)	RHO (GM/CC)	QP	QS
0.333333	5.5000	0.	1.2000	20.00	0.
1.333330	15.0000	6.3000	2.3600	70.00	50.00
0.	13.1200	7.0000	2.1600	60.00	60.00

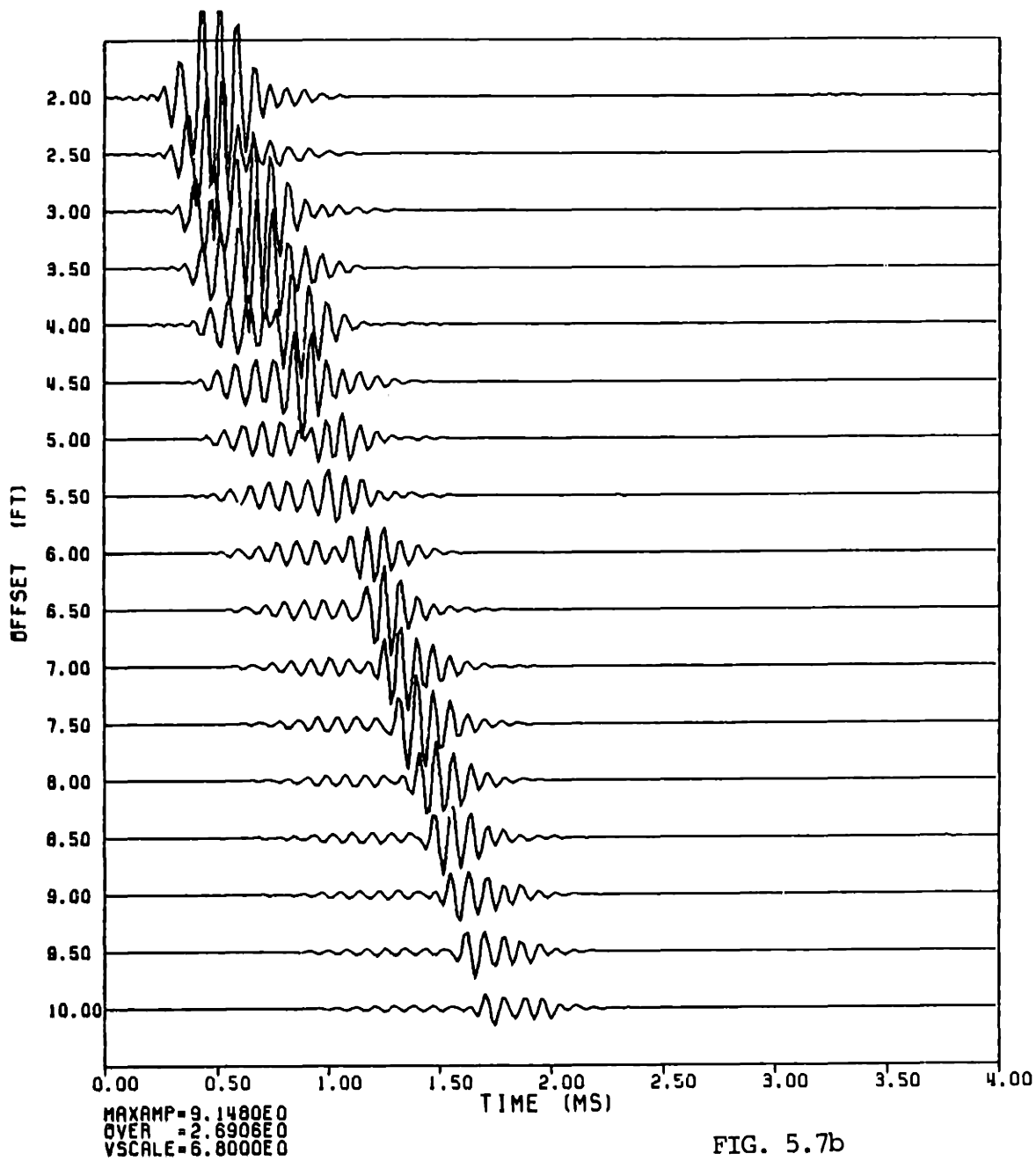

FIG. 5.7b

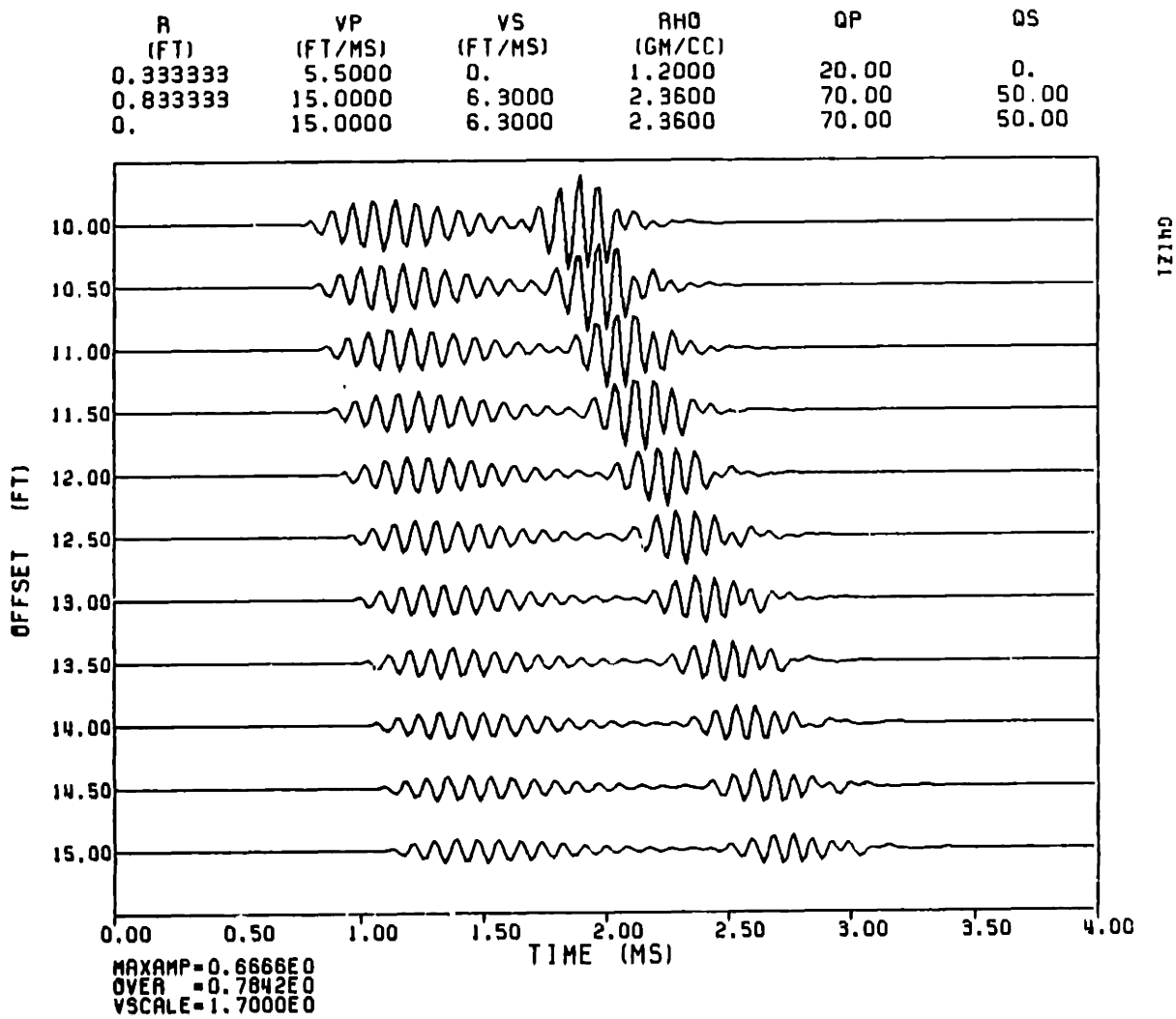
R (FT) VP (FT/MS) VS (FT/MS) RHO (GM/CC) QP QS
0.333333 5.5000 0. 1.2000 20.00 0.
0.833333 15.0000 6.3000 2.3600 70.00 50.00
0. 15.0000 6.3000 2.3600 70.00 50.00
OFFSET (FT)
10.00
10.50
11.00
11.50
12.00
12.50
13.00
13.50
14.00
14.50
15.00
0.00 0.50 1.00 1.50 2.00 2.50 3.00 3.50 4.00
TIME (MS)
MAXAMP=0.6666E0
OVER =0.7842E0
VSCALE=1.7000E0
CH121

FIG. 5.8

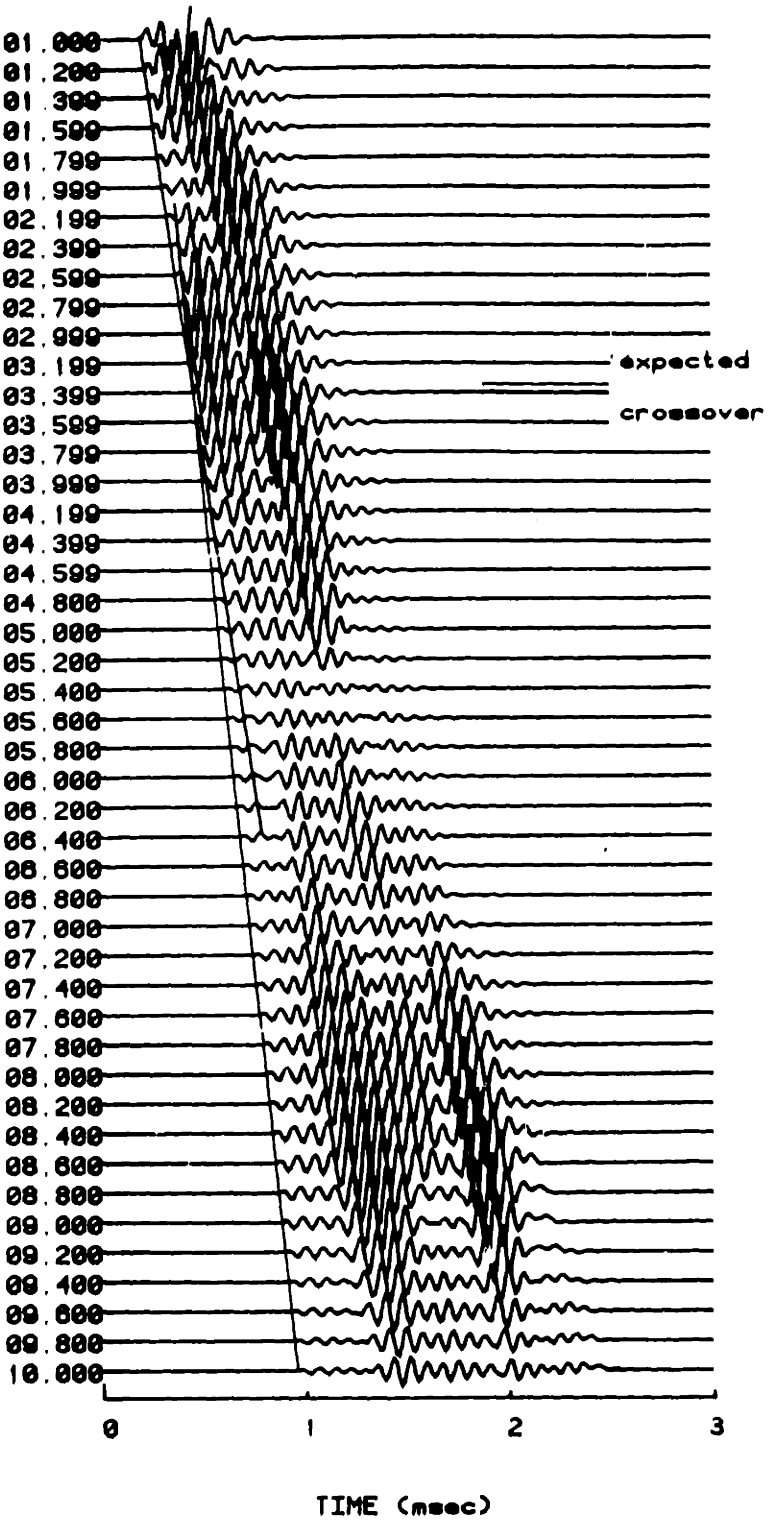
01.000
01.200
01.300
01.500
01.700
01.900
02.100
02.300
02.500
02.700
02.900
03.100
03.300
03.500
03.700
03.900
04.100
04.300
04.500
04.800
05.000
05.200
05.400
05.600
05.800
06.000
06.200
06.400
06.600
06.800
07.000
07.200
07.400
07.600
07.800
08.000
08.200
08.400
08.600
08.800
09.000
09.200
09.400
09.600
09.800
10.000
expected
crossover
0
1
2
3
TIME (msec)

FIG. 5.9

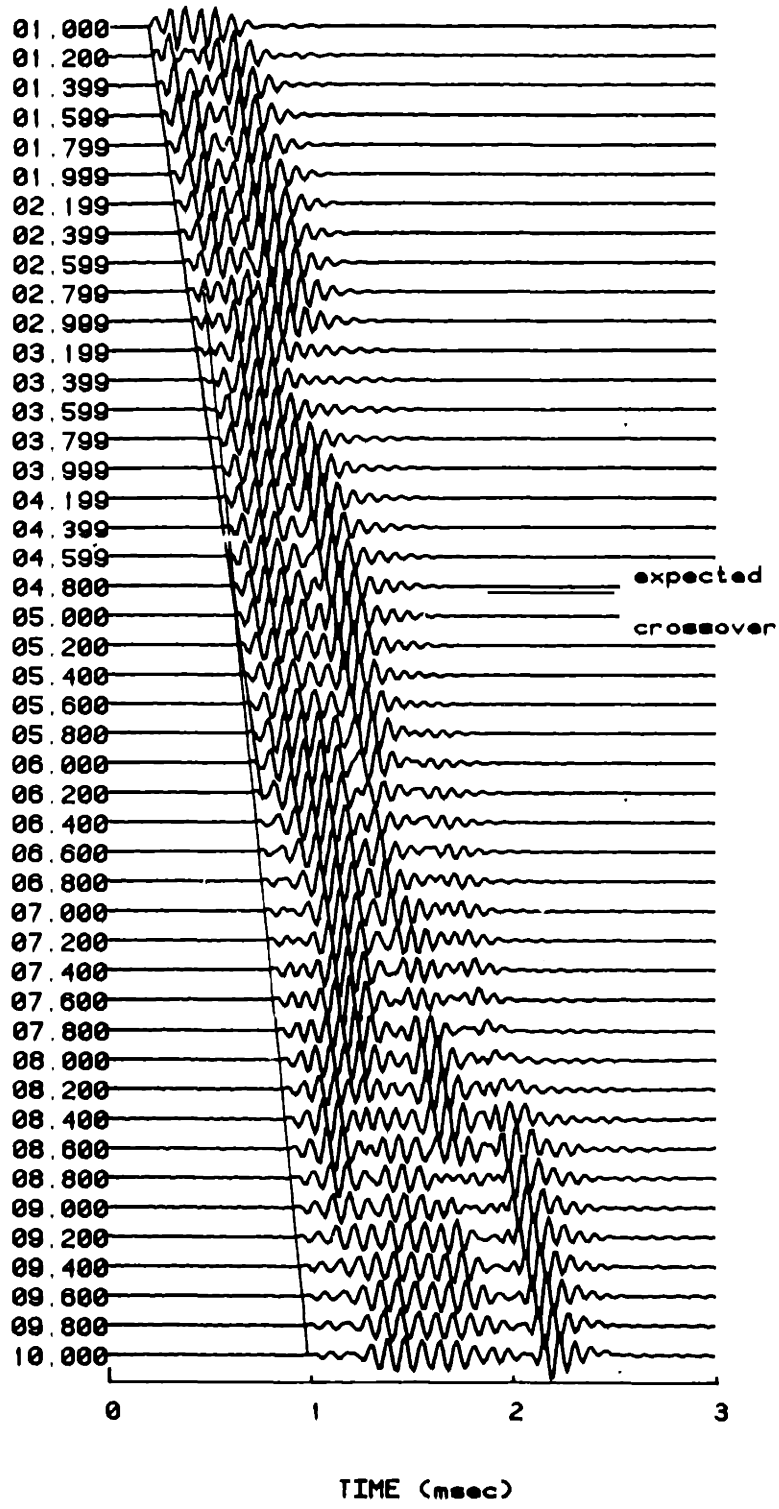
01.000
01.200
01.399
01.599
01.799
01.999
02.199
02.399
02.599
02.799
02.999
03.199
03.399
03.599
03.799
03.999
04.199
04.399
04.599
04.800
05.000
05.200
05.400
05.600
05.800
06.000
06.200
06.400
06.600
06.800
07.000
07.200
07.400
07.600
07.800
08.000
08.200
08.400
08.600
08.800
09.000
09.200
09.400
09.600
09.800
10.000
expected
crossover
0
1
2
3
TIME (msec)

FIG. 5.10

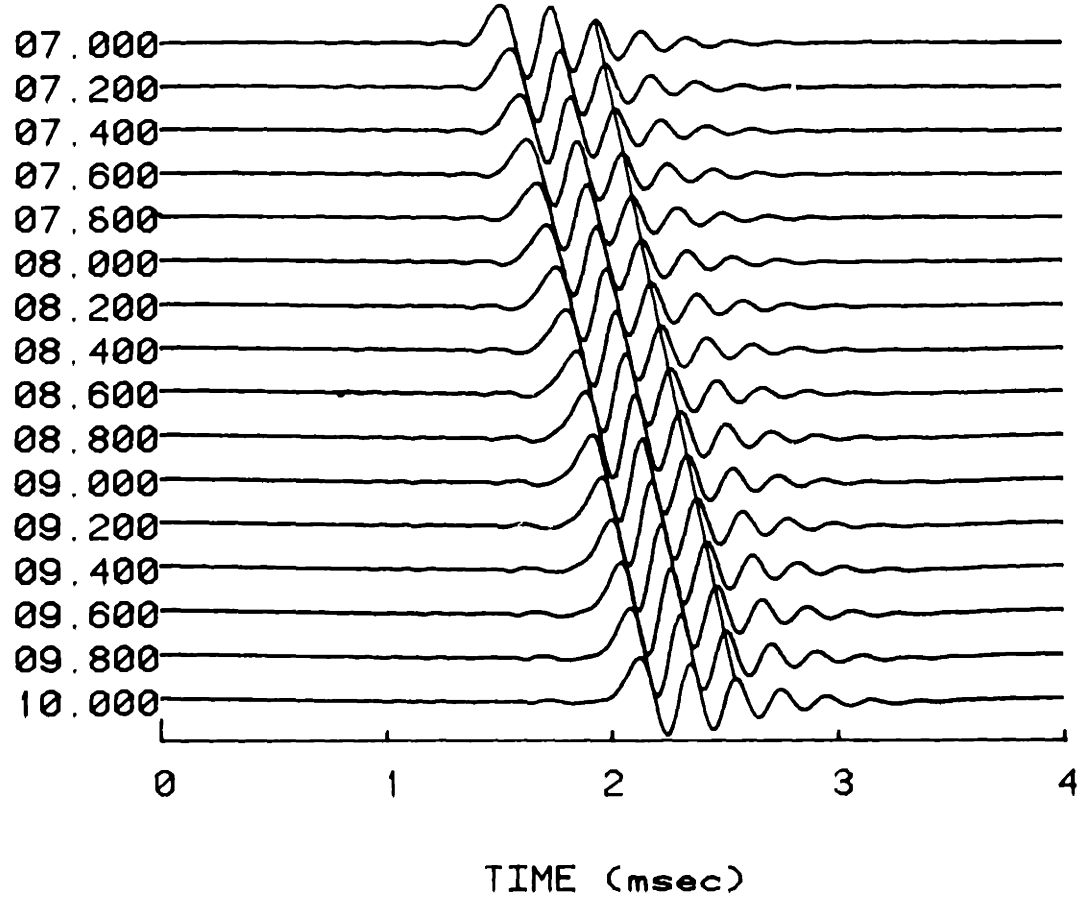
07.000
07.200
07.400
07.600
07.800
08.000
08.200
08.400
08.600
08.800
09.000
09.200
09.400
09.600
09.800
10.000
0
1
2
3
4
TIME (msec)

FIG. 5.11

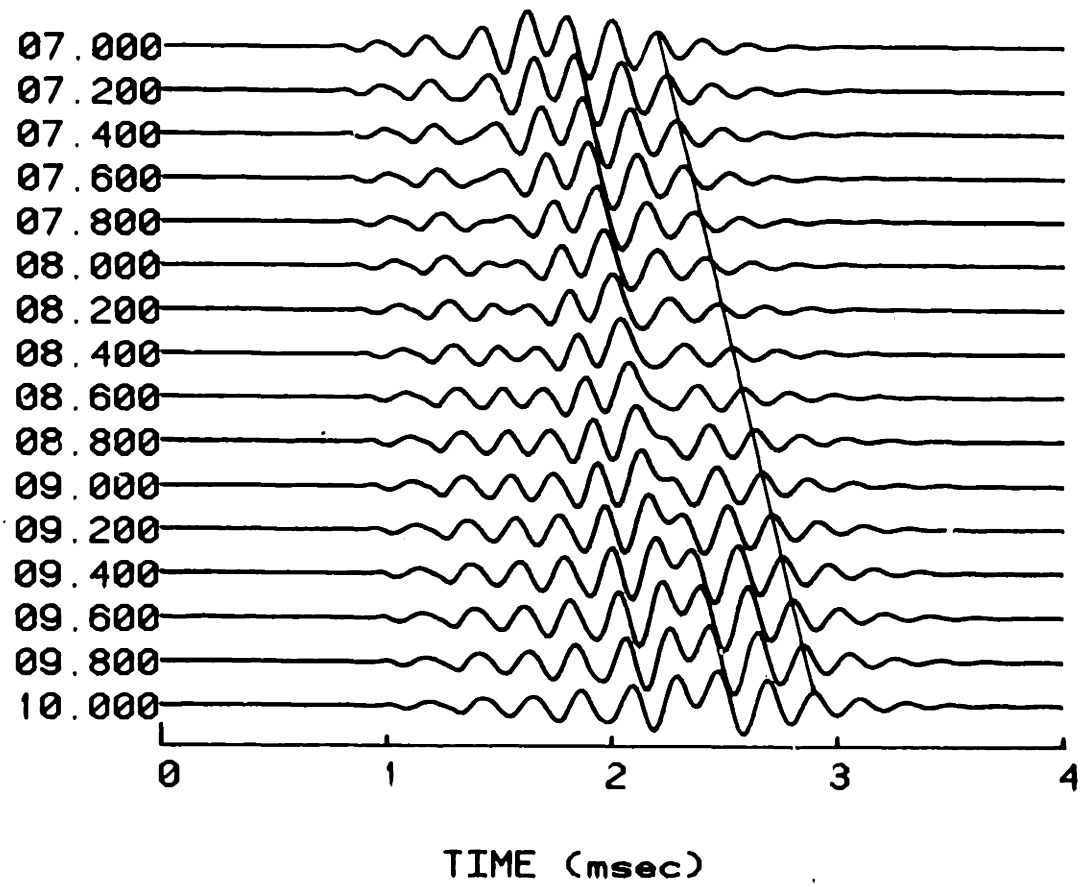
07.000
07.200
07.400
07.600
07.800
08.000
08.200
08.400
08.600
08.800
09.000
09.200
09.400
09.600
09.800
10.000
0
1
2
3
4
TIME (msec)

FIG. 5.12

R (FT)	VP (FT/MS)	VS (FT/MS)	RHO (GM/CC)	QP	QS
0.333333	5.5000	0.	1.2000	20.00	0.
0.416667	11.8000	6.3000	2.0400	60.00	60.00
0.500000	12.0200	6.4200	2.0600	60.00	60.00
0.583333	12.2400	6.5300	2.0800	60.00	60.00
0.666667	12.4600	6.6500	2.1000	60.00	60.00
0.750000	12.6800	6.7700	2.1200	60.00	60.00
0.833333	12.9000	6.8800	2.1400	60.00	60.00
0.	13.1200	7.0000	2.1600	60.00	60.00

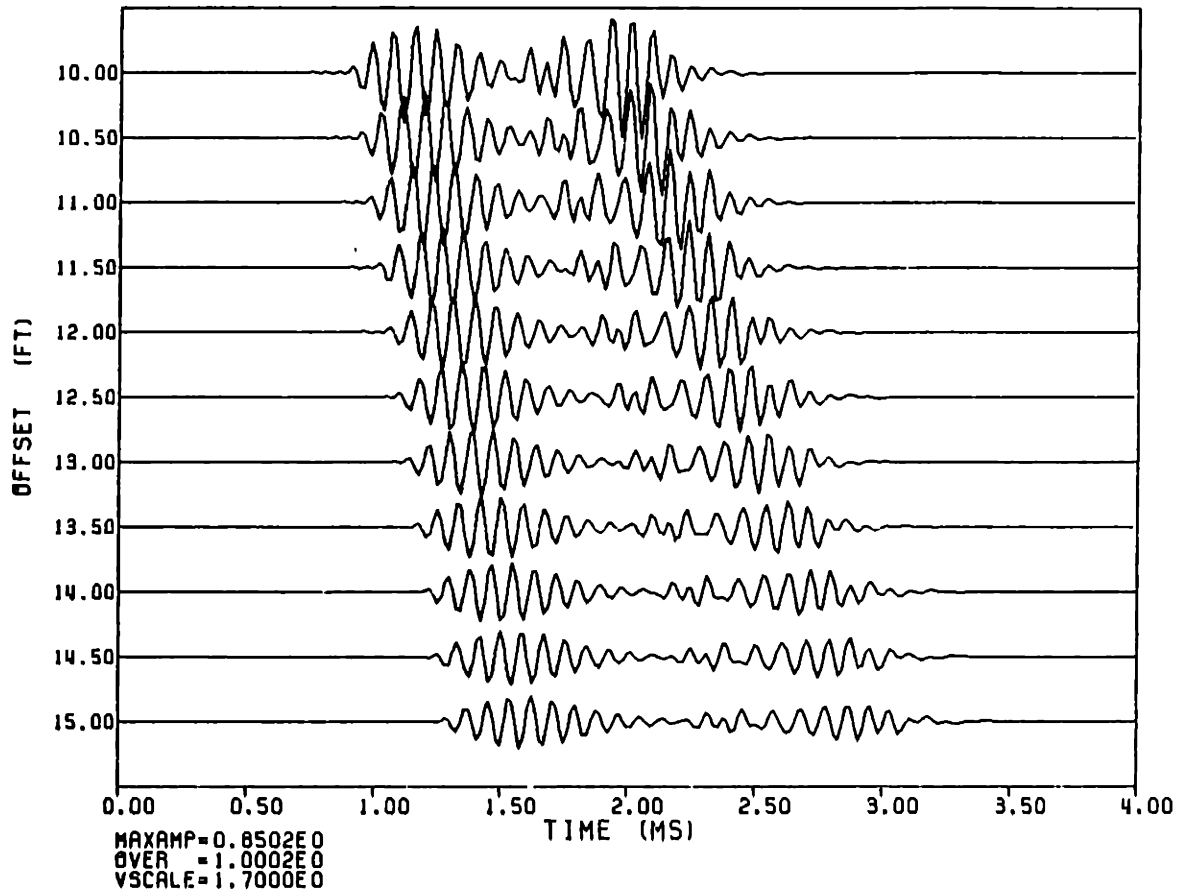

FIG. 5.13a

R (FT)	VP (FT/MS)	VS (FT/MS)	RHO (GM/CC)	QP	QS
0.333333	5.5000	0.	1.2000	20.00	0.
0.416667	11.8000	6.3000	2.0400	60.00	60.00
0.500000	12.0200	6.4200	2.0600	60.00	60.00
0.583333	12.2400	6.5300	2.0800	60.00	60.00
0.666667	12.4600	6.6500	2.1000	60.00	60.00
0.750000	12.6800	6.7700	2.1200	60.00	60.00
0.833333	12.9000	6.8800	2.1400	60.00	60.00
0.	13.1200	7.0000	2.1600	60.00	60.00

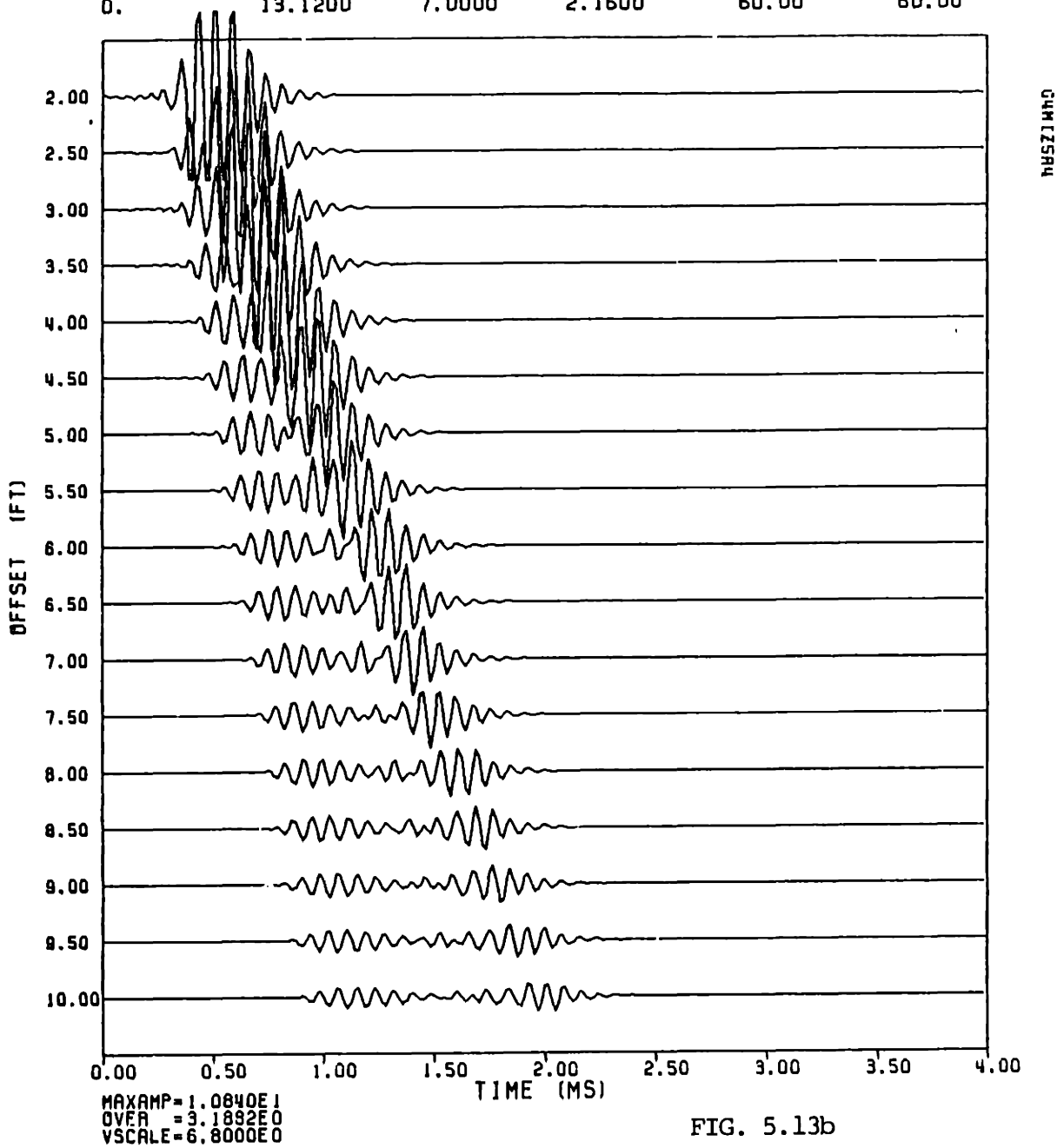

FIG. 5.13b

R (FT)	VP (FT/MS)	VS (FT/MS)	RHO (GM/CC)	QP	QS
0.333333	5.5000	0.	1.2000	20.00	0.
0.354166	10.5000	5.6000	1.8000	50.00	40.00
0.	13.1200	7.0000	2.1600	60.00	60.00

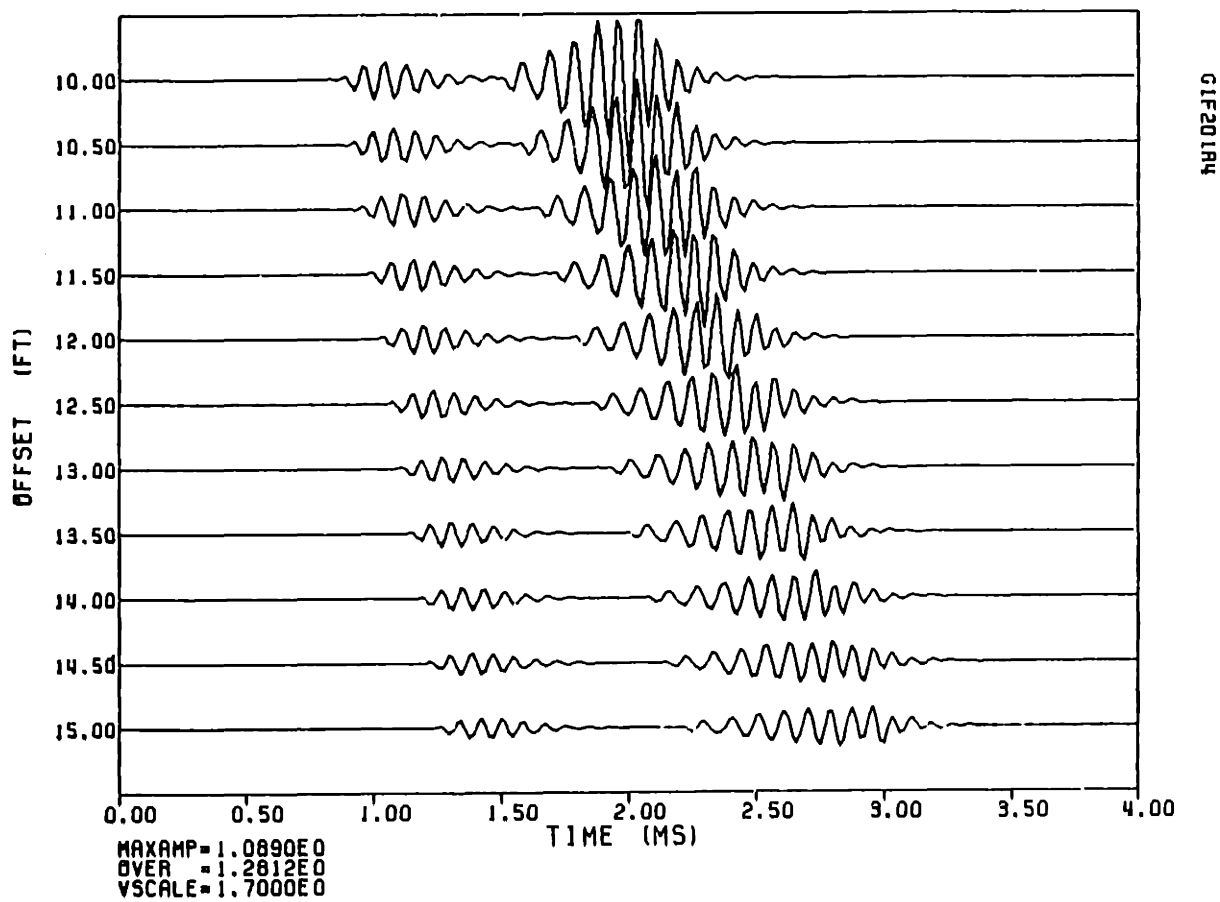

FIG. 5.14

R (FT)	VP (FT/MS)	VS (FT/MS)	RHO (GM/CC)	QP	QS
0.333333	5.5000	0.	1.2000	20.00	0.
0.416700	10.5000	5.6000	1.8000	50.00	40.00
0.	13.1200	7.0000	2.1600	60.00	60.00

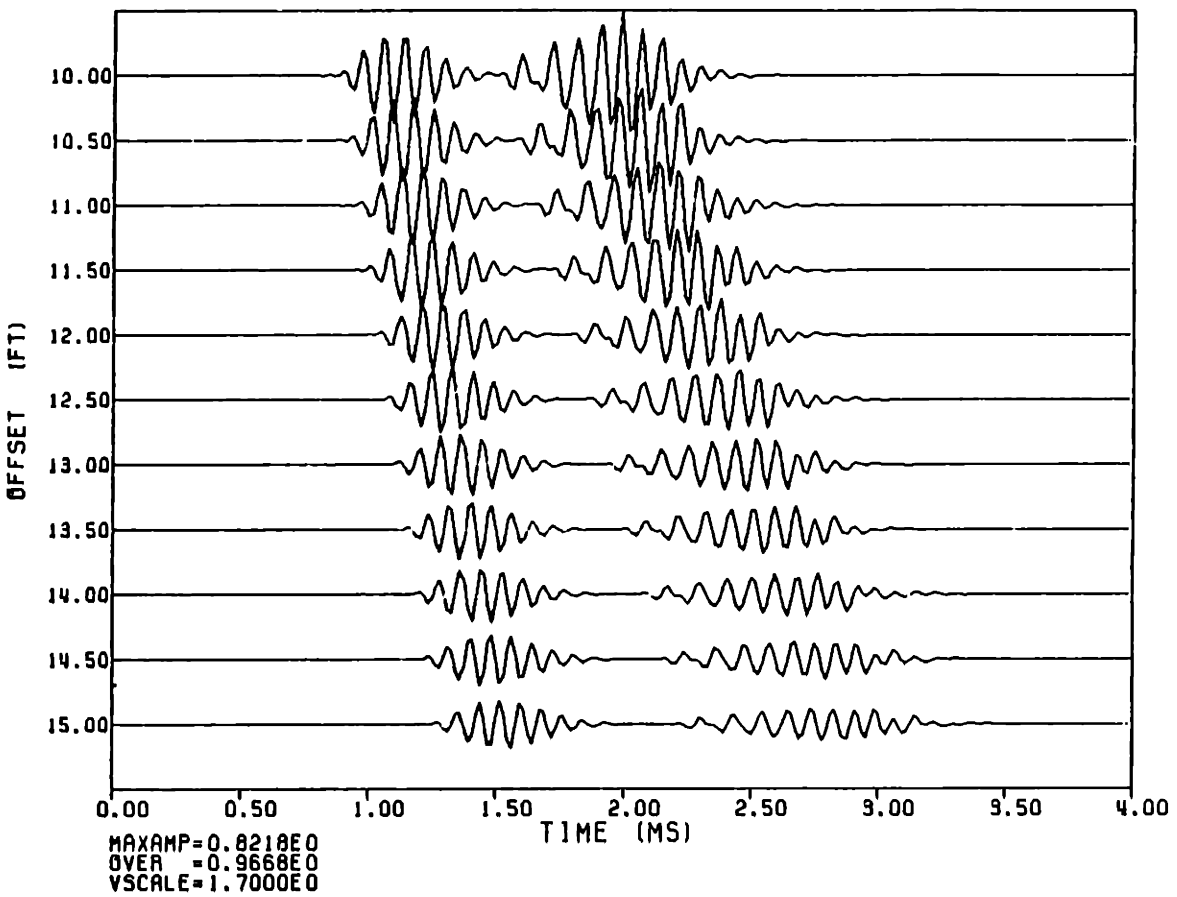

FIG. 5.15

R (FT)	VP (FT/MS)	VS (FT/MS)	RHO (GM/CC)	QP	QS
0.333333	5.5000	0.	1.2000	20.00	0.
0.354166	12.8000	6.8250	1.8000	50.00	40.00
0.	16.0000	8.5300	2.1600	60.00	60.00

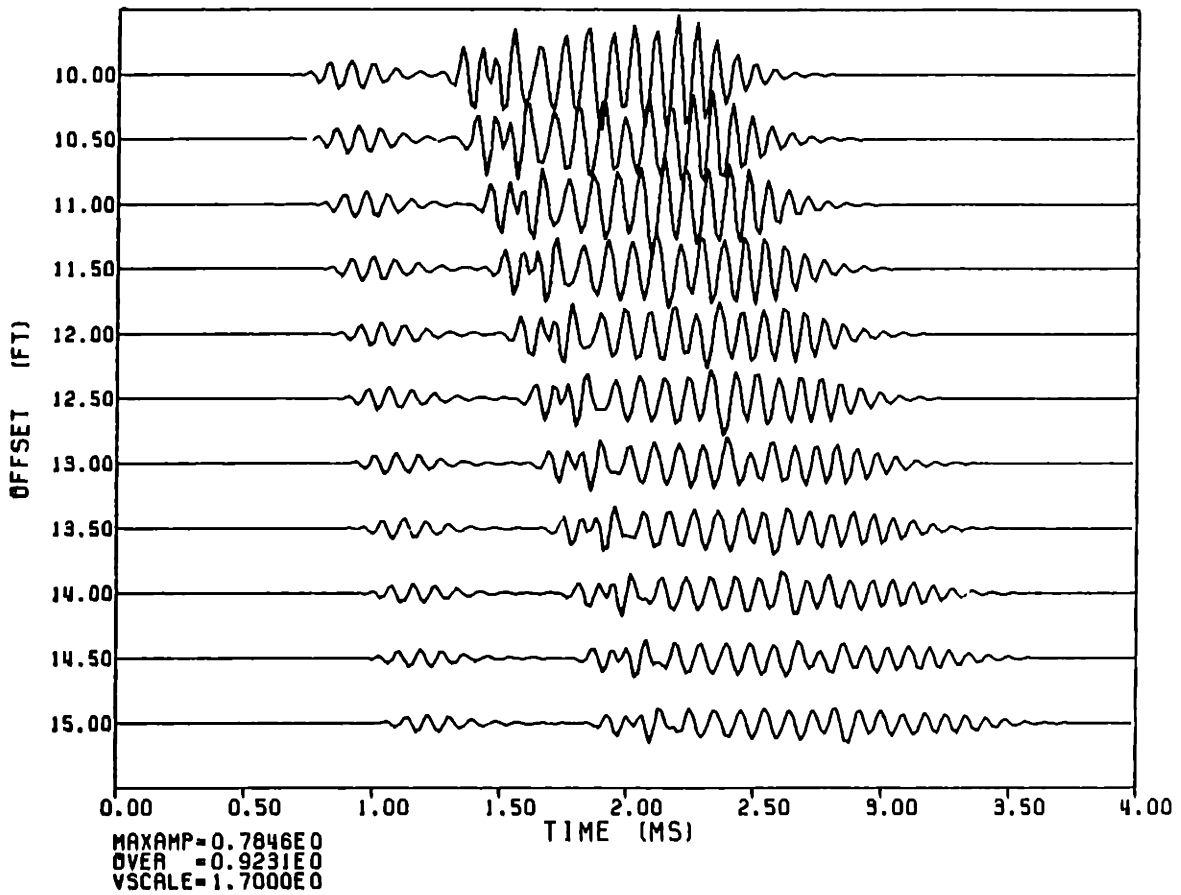

FIG. 5.16

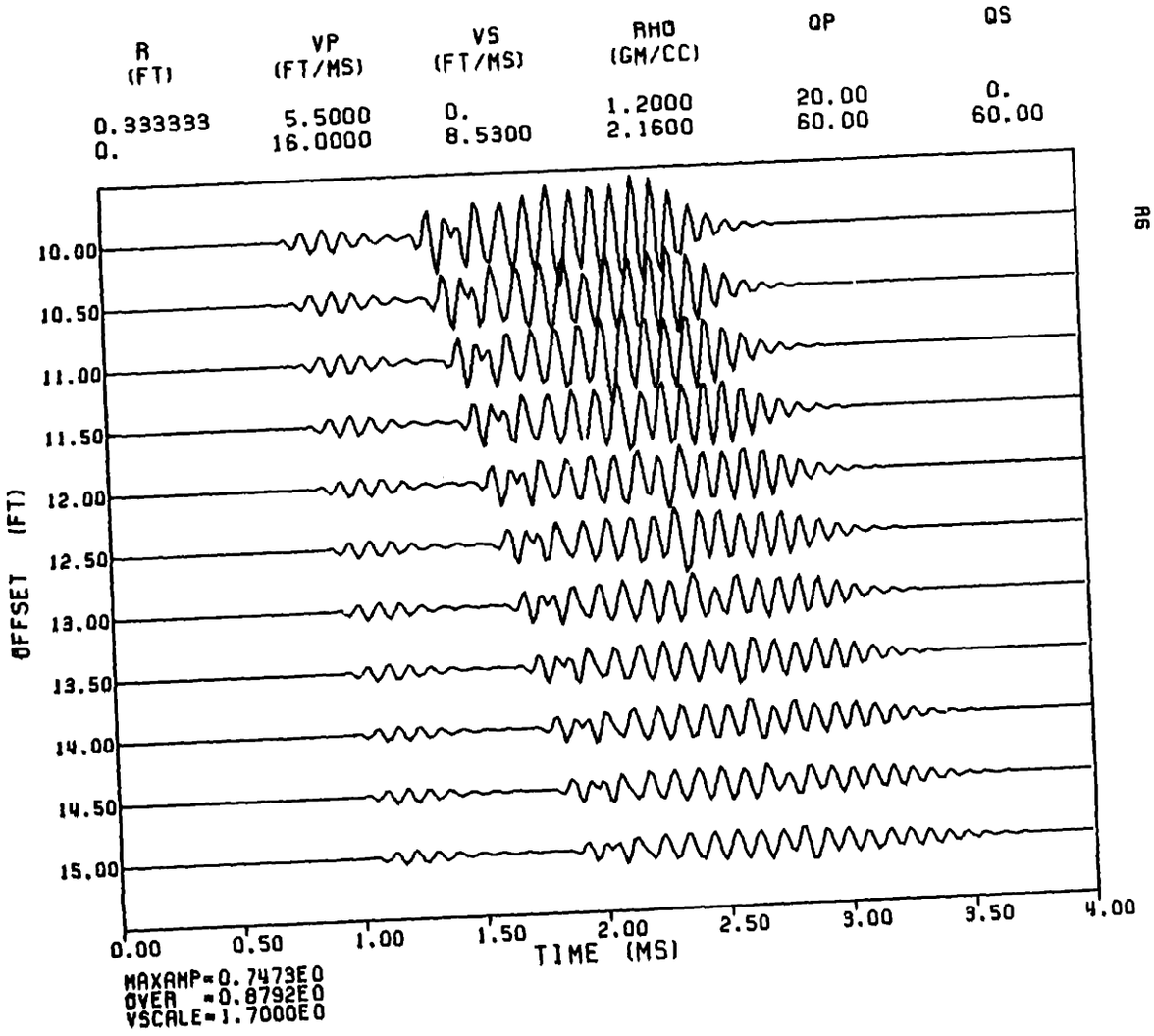
R (FT)
VP (FT/MS)
VS (FT/MS)
RHO (GM/CC)
QP
QS
0.333333 5.5000 0. 1.2000 20.00 0.
0. 16.0000 8.5300 2.1600 60.00 60.00
AG
OFFSET (FT)
10.00
10.50
11.00
11.50
12.00
12.50
13.00
13.50
14.00
14.50
15.00
0.00
0.50
1.00
1.50
2.00
2.50
3.00
3.50
4.00
TIME (MS)
MAXAMP=0.7473E0
OVER =0.8792E0
VSCALE=1.7000E0

FIG. 5.17

R (FT)	VP (FT/MS)	VS (FT/MS)	RHO (GM/CC)	QP	QS
0.333333	5.5000	0.	1.2000	20.00	0.
0.416666	12.8000	6.8250	1.8000	50.00	40.00
0.	16.0000	8.5300	2.1600	60.00	60.00

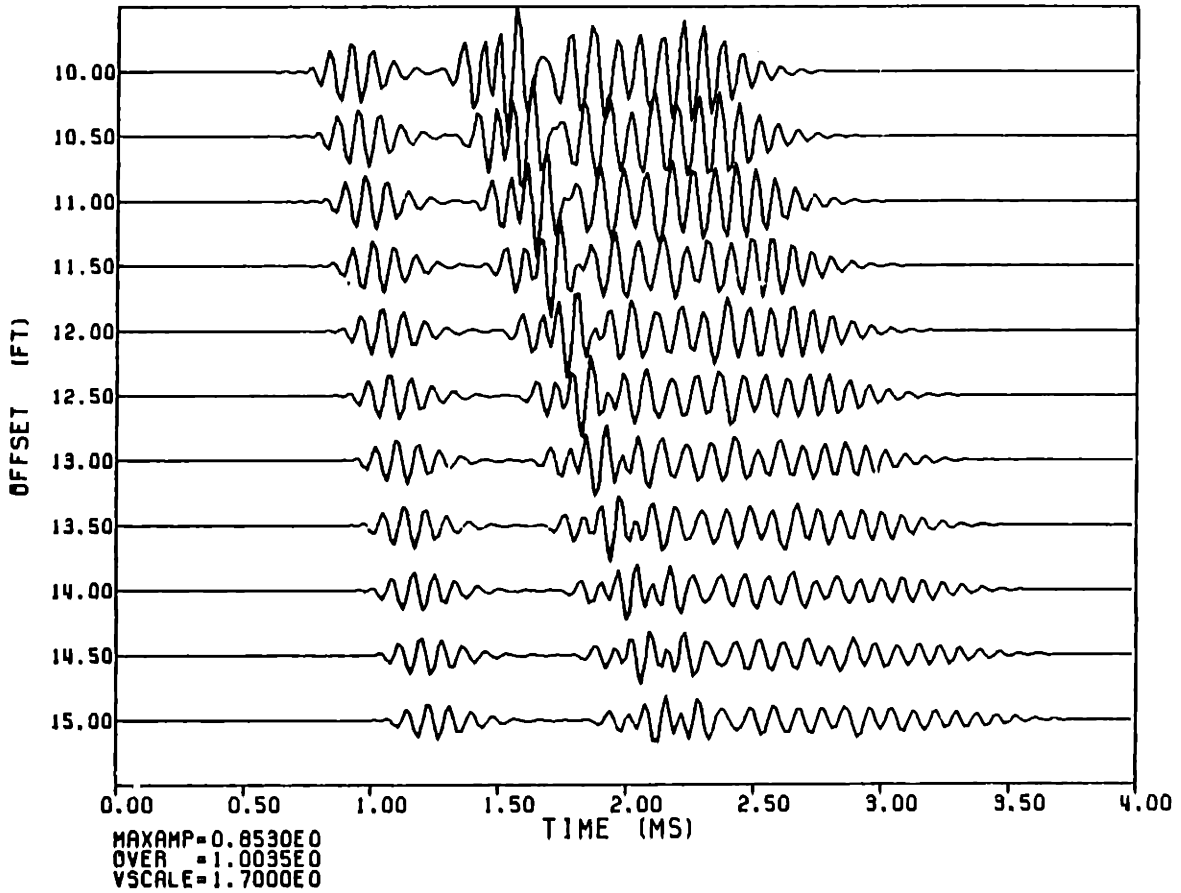

FIG. 5.18

R (FT)	VP (FT/MS)	VS (FT/MS)	RHO (GM/CC)	QP	QS
0.291600	5.5000	0.	1.2000	20.00	0.
0.333333	7.5000	3.7500	1.6000	30.00	20.00
0.	13.1200	7.0000	2.1600	60.00	60.00

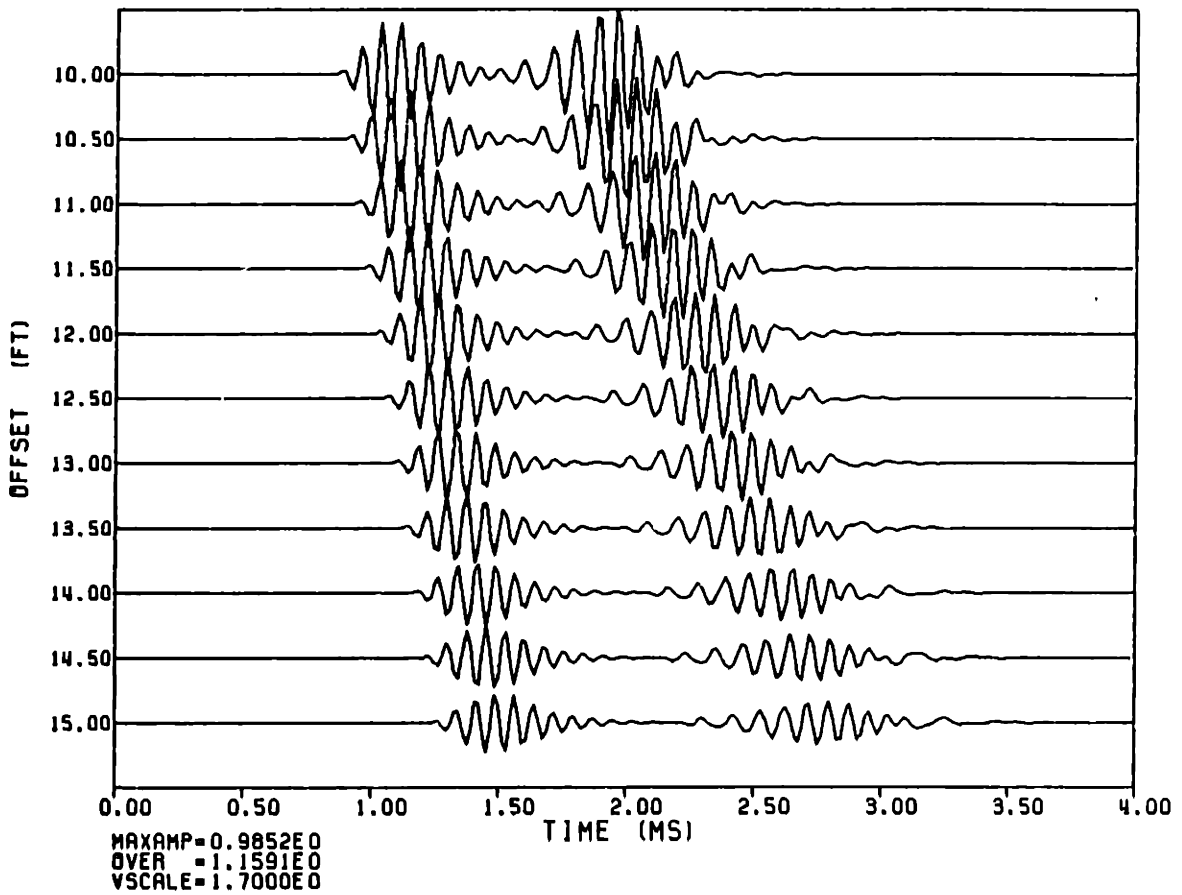

FIG. 5.19

R (FT)	VP (FT/MS)	VS (FT/MS)	RHO (GM/CC)	QP	QS
0.250000	5.5000	0.	1.2000	20.00	0.
0.333333	7.5000	3.7500	1.6000	30.00	20.00
0.	13.1200	7.0000	2.1600	60.00	60.00

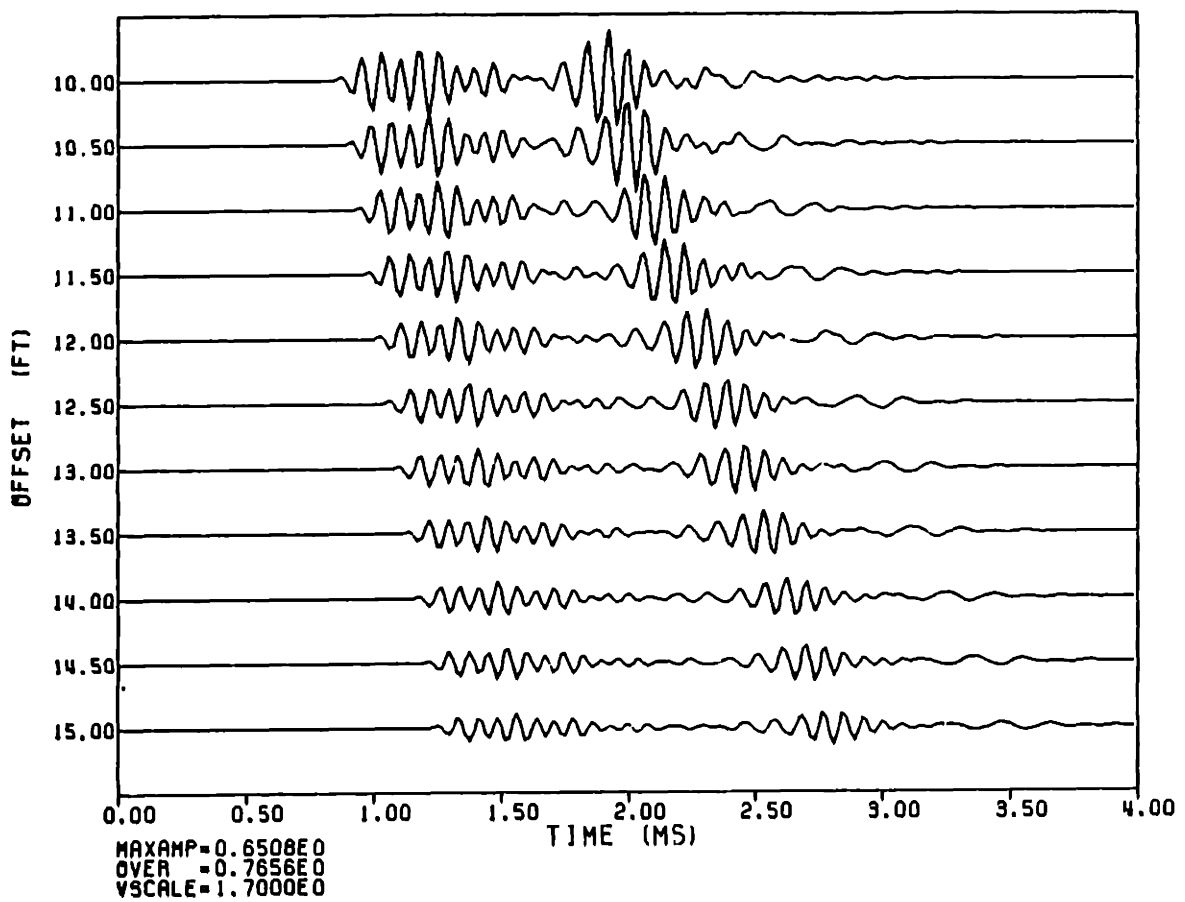

FIG. 5.20

R (FT)	VP (FT/MS)	VS (FT/MS)	RHO (GM/CC)	QP	QS
0.312500	5.5000	0.	1.2000	20.00	0.
0.333333	7.5000	4.5000	2.4000	50.00	40.00
0.	13.1200	7.0000	2.1600	60.00	60.00

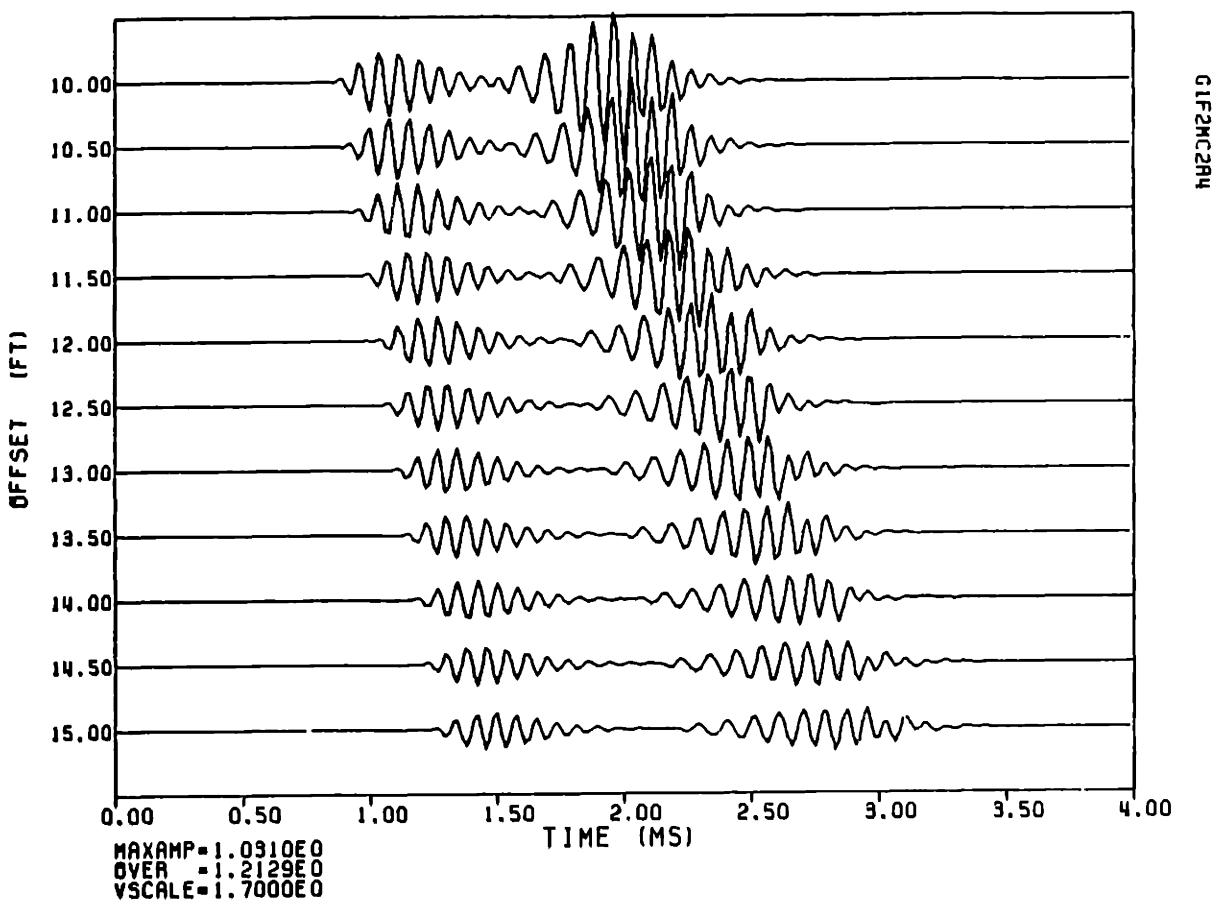

FIG. 5.21

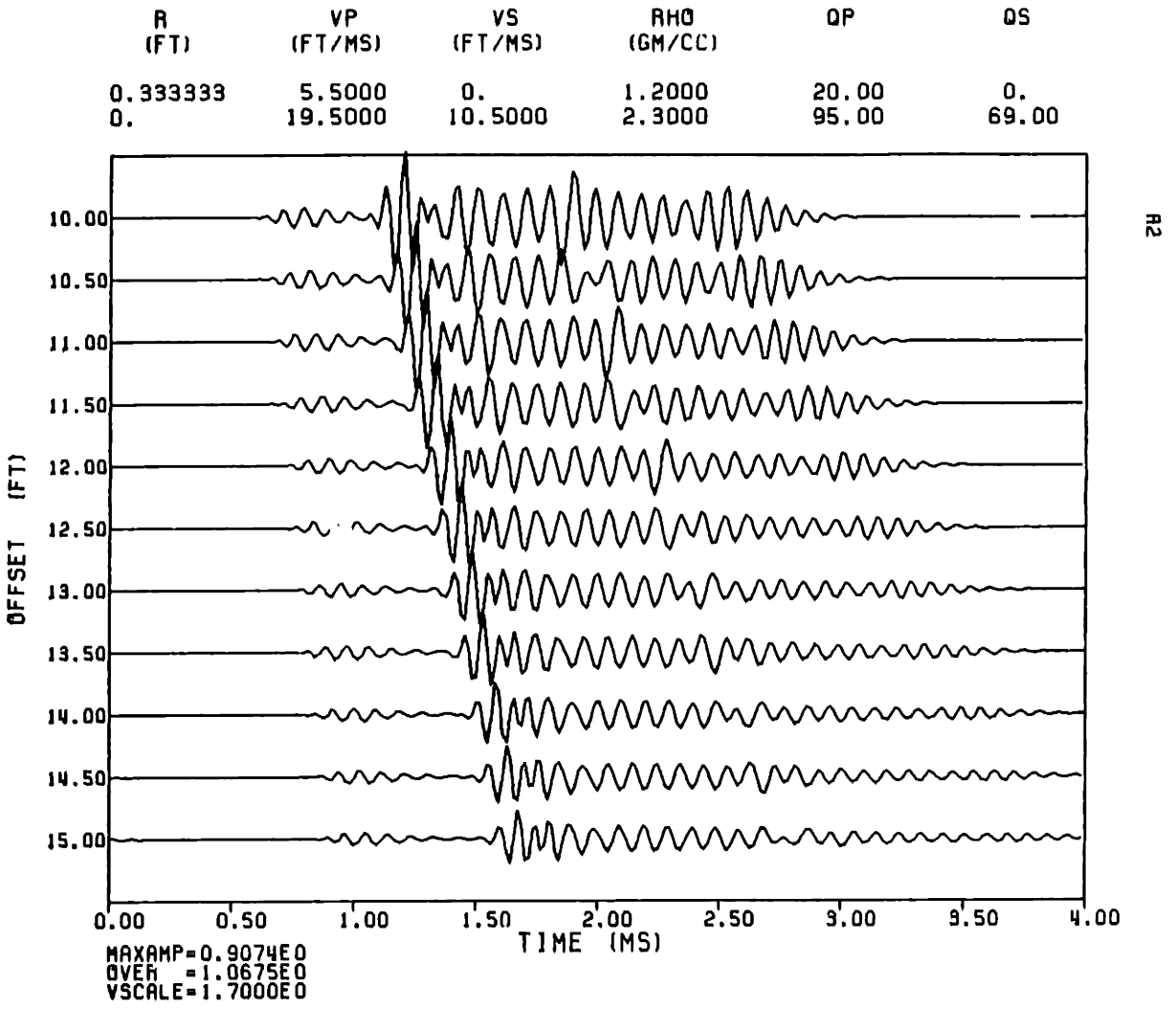
R (FT)
VP (FT/MS)
VS (FT/MS)
RHO (GM/CC)
QP
QS
0.333333 5.5000 0. 1.2000 20.00 0.
0. 19.5000 10.5000 2.3000 95.00 69.00
R2
OFFSET (FT)
10.00
10.50
11.00
11.50
12.00
12.50
13.00
13.50
14.00
14.50
15.00
0.00 0.50 1.00 1.50 2.00 2.50 3.00 3.50 4.00
TIME (MS)
MAXAMP=0.9074E0
OVER =1.0675E0
VSCALE=1.7000E0

FIG. 5.22

R (FT)	VP (FT/MS)	VS (FT/MS)	RHO (GM/CC)	QP	QS
0.250000	5.5000	0.	1.2000	20.00	0.
0.333300	7.5000	3.7500	1.6000	30.00	20.00
0.	19.5000	10.5000	2.3000	95.00	69.00

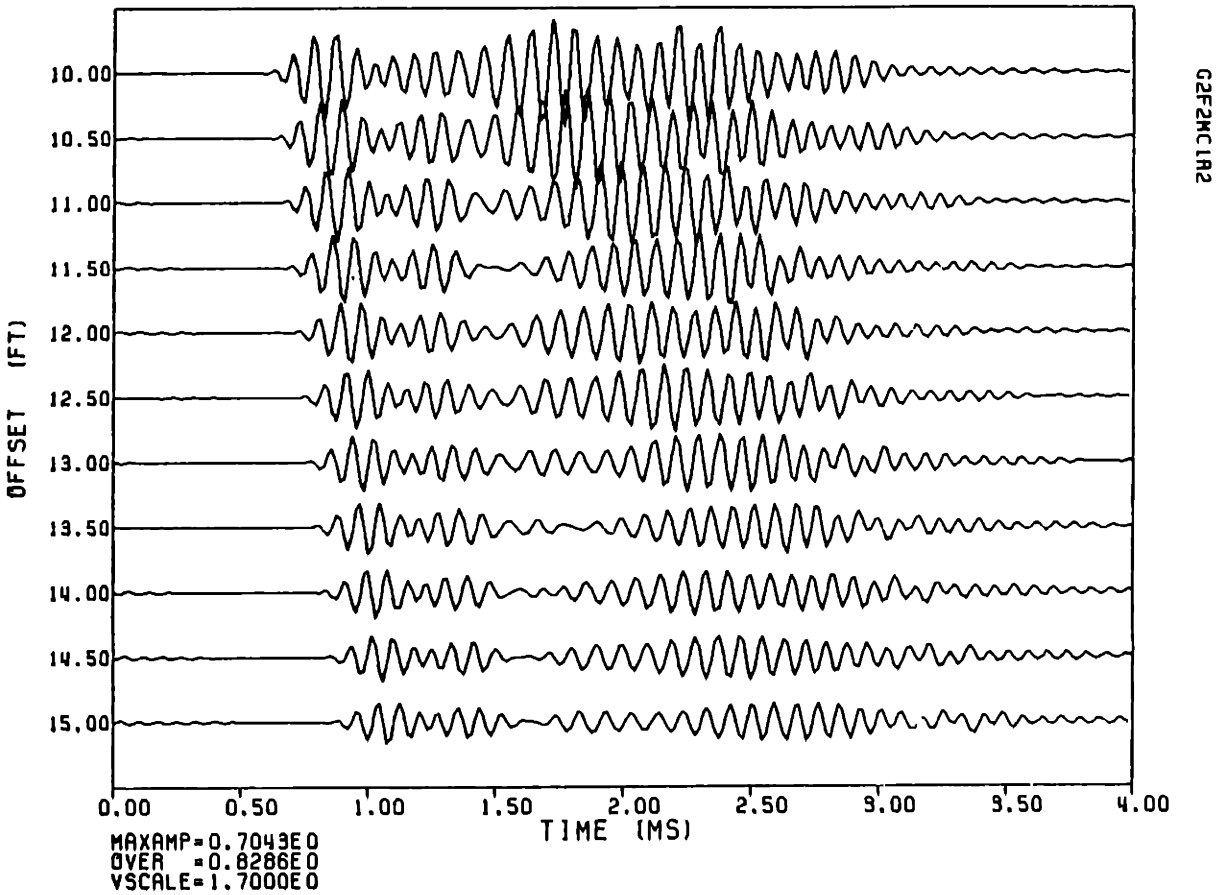

FIG. 5.23

R (FT)	VP (FT/MS)	VS (FT/MS)	RHO (GM/CC)	QP	QS
0.291600	5.5000	0.	1.2000	20.00	0.
0.333333	7.5000	3.7500	1.6000	30.00	20.00
0.	19.5000	10.5000	2.3000	95.00	69.00

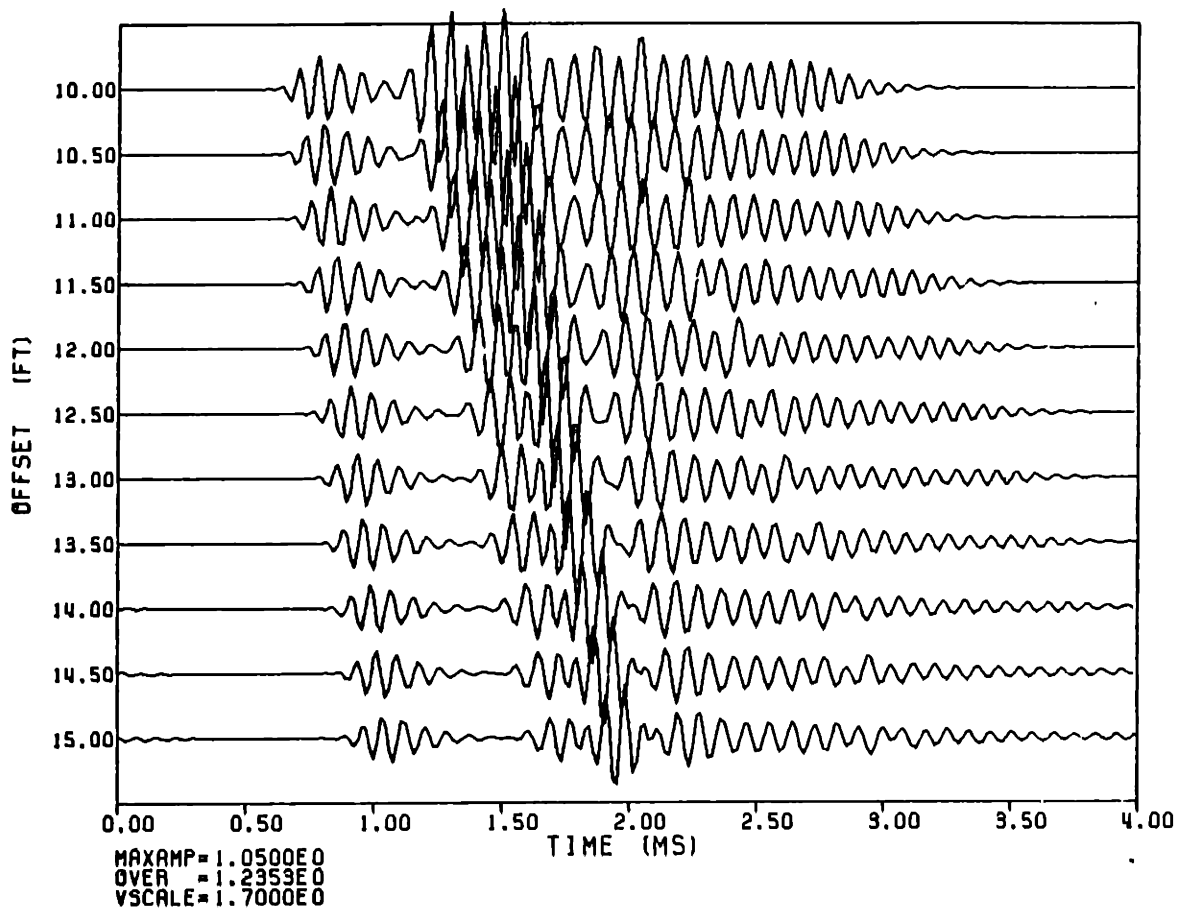

FIG. 5.24

Chapter 6

Discussion and Conclusions

The modeling technique developed in this thesis has proved to be a powerful tool for investigating complex borehole environments. A systematic investigation of a number of commonly occurring phenomena is performed through the calculation of synthetic microseismograms and dispersion curves. This leads to an understanding of the effects caused by additional radial layers (e.g. casing, invaded zone, etc.). Comparisons with field data are made whenever appropriate data are available.

The theoretical modeling is based on the Thomson-Haskell propagator matrix method. The borehole environment is treated as an arbitrary number of coaxial annuli surrounding a fluid cylinder. The layers may be either solid or fluid. This is a significant improvement over models which permit solid layers only. It allows the investigation of an important geometry, that of unbonded casing in boreholes. In addition, Q values can be specified for each type of wave in each layer. The attenuation due to each layer can vary greatly. Steel Q values are much higher than those of the other layers in a cased borehole. It is necessary to account for this fact in order to determine realistic relative amplitudes for the different

arrivals.

A variety of borehole environments have been studied. These include cased as well as open borehole geometries. Through extensive modeling we have found that:

1. In a well bonded cased hole the formation body waves are affectly only slightly by the casing and cement layers. Velocities determined are those of the formation and not of the casing. In some situations the presence of the steel and cement can make the observation of the formation arrivals more difficult. The amplitudes of these signals are affected by the relationship between the formation and cement velocities. They can be significantly reduced if the cement velocities are close to or greater than those of the formation. The layer of cement diminishes the effect of the formation on the guided wave portion of the microseismograms. In most situations the Stoneley wave is controlled by the steel and the cement but if the cement layer is extremely thin, or not present, the formation influence becomes important.

2. A fluid layer between the steel and the cement frees the pipe to ring. The thickness of the fluid layer influences the amplitude and duration of the observed casing arrival. A thick layer results in a large, ringing signal which can obscure the formation energy. The first arrival is from the casing even if the fluid layer is extremely thin. Although the formation energy may be obscured by the pipe signal, it is present in the

microseismograms. The character of the waveform will change as the formation properties change. A thin layer may not completely mask the formation signal though. It may be possible to discern the formation body wave arrivals if the amplitude of the casing arrival diminishes rapidly.

3. The thicknesses of the fluid and cement layers are more important if the fluid is located between the cement and the formation. In this case the steel and cement are bonded together but are not bonded to the formation. A large cement layer can damp out the steel ringing sufficiently to permit the observation of the formation arrivals. The casing signal is not large enough to dominate the waveform. If the fluid layer is large, the amplitudes of the formation arrivals will be reduced making them more difficult to distinguish.

If the amount of cement bonded to the steel is small it will not be sufficient to damp the ringing of the casing. In this case the steel and cement act in unison and the first arrival is from the combination of these layers. The velocity of the composite is intermediate to the velocities of the two layers. It varies with the velocities and thicknesses of the cement and steel layers. A thicker cement layer has more influence resulting in lower velocities.

4. In an open borehole with an invaded or damaged zone, or mud cake, the arrivals observed generally correspond to those of the formation. These additional layers do not necessarily limit the ability of a long spaced

tool to measure the formation properties. The formation arrivals are observed unless the thickness of the altered layer is large or the source-receiver separation is very short.

5. Although there is little effect on the measured velocities, there can be substantial changes in the amplitudes and character of the microseismograms. A mud cake or a layer which has been altered so that the velocities are lower than those in the original formation can result in greatly increased P-wave amplitudes. The focusing of energy due to the different velocity layers can more than double the P-wave amplitudes relative to those observed in an unaltered formation. The amplitudes will be lower if the velocities of the altered zone are higher than the pre-invasion velocities. This situation decreases the amount of energy directed back into the borehole.

While the model employed in this study goes beyond other layered models, there are still some simplifications. This section discusses the assumptions about the geometries and borehole environments which are inherent in the modeling.

Perhaps the most notable phenomenon not accounted for by the present model is bed boundaries. All the modeling here assumes that the borehole consists of one uniform formation. The assumption actually is that all sources and receivers on the tool are within the same formation and are not close to any bed boundaries. This is valid for thick formations

but the tool will cross a number of bed boundaries when logging thinly bedded strata.

The model used here can accommodate an arbitrary number of radial layers but the central cylinder must be a fluid. The assumption that this implies is that there is no tool in the center of the borehole. Obviously there will be a tool in any real data collecting situation. Cheng and Toksöz (1981) examined the effects of a rigid tool at the center of the borehole. They concluded that the largest effect of the presence of the tool was to decrease the thickness of the fluid annulus. This influences the excitation of the various modes causing them to behave as if the borehole had a smaller radius. Another assumption of our model is the fact that the source and receiver are both centered on the axis. Ideally this is the situation for a real tool also. Every acoustic logging tool has some means for centering it in the borehole, and particularly in cased boreholes centering the tool is reliable. The assumption of no tool then does not overly constrain the applicability of the current model.

Another important simplification of this model is one that is common in much of seismology, that of flat layers or smooth interfaces. The layers treated here are assumed to be perfect cylindrical shells. In the real borehole environment there may be borehole wall irregularities. Washouts and breakouts that can be quite large in some situations. It is necessary to identify such zones from caliper logs made before casing. Minor

irregularities are not a major problem in the cased hole geometries. The steel pipe is virtually a perfect cylindrical shell. As a consequence, the central fluid layer is also a perfect cylinder and the inner boundary of the cement is smooth. The case of an invaded or damaged zone is more difficult to model with discrete layers. The fluid invasion certainly does not stop abruptly at a specified radius. There is a gradual decrease in the amount of borehole fluid present in the formation as the radius increases. Spreading the transition over a large number of layers produces similar results though. The microseismograms were not sufficiently different from the single layer models to warrant the additional computations. In the future it may be worthwhile to look at layered models with velocity gradients. Channeling, washouts, and major borehole irregularities cannot be satisfactorily handled by the treatment developed here and are left to the finite difference and finite element methods. Partial bonding conditions also cannot be accommodated with the present model. All boundaries are considered to be welded contacts or perfect fluid-solid interfaces. In the well bonded case, the bonding is perfect. The other extreme of complete unbonding is also possible but the intermediate conditions are not.

Keeping in mind that the above limitations occur only in exceptional cases, for most applications the method developed here is a fast and efficient method for full waveform acoustic logging in radially layered boreholes. It provides a straight forward approach and a physical

understanding of the effects of casing and altered zones on wave propagation in boreholes.

References

Abramowitz, A. and Stegun, I.A., Ed., 1970, Handbook of mathematical functions: New York, Dover Publications, 1046pp.

Aki, K. and Richards, P., 1980, Quantitative Seismology Theory and Methods: v.I., San Francisco, W.H. Freeman and Co., 932pp.

Anderson, D.L., and Archambeau, C.B., 1964, The anelasticity of the earth: J. Geophys. Res., v.69., p.2071-2084.

Arditty, P.C., Arens, G., and Staron, P., 1981, EVA: A long-spacing sonic tool for evaluation of acoustic velocities and attenuations, 51st Annual International Meeting SEG, Los Angeles, CA.

Azimi, S.A., Kalinin, A.V., and Pivovarov, B.L., 1968, Impulse and transient characteristics of media with linear and quadratic absorption laws: Phys. Solid Earth, p.88-93.

Baker, L.J., 1984, The effect of the invaded zone in full waveform acoustic logging: Geophysics, v.49, p.796-809.

Bhasavanija, K., 1983, A finite difference model of an acoustic logging tool: the borehole in a horizontally layered geologic medium: Ph.D. thesis, Colorado School of Mines, Golden, CO., 149pp.

Biot, M.A., 1952, Propagation of elastic waves in a cylindrical bore containing a fluid: Jour. of Appl. Phys., v.23., p.977-1005.

Biot, M.A., 1956, Theory of propagation of elastic waves in a fluid-saturated porous solid: J. Appl. Phys., v.23, p.977-1005.

Bouchon, M. and Aki, K., 1977, Discrete wavenumber representation of seismic-source wave fields: Bull. Seism. Soc. Am., v.67, p.259-277.

Bouchon, M., 1980, Calculation of complete seismograms for an explosive source in a layered medium: Geophysics, v.45, p.197-203.

Brown, H.D., Grijalva, V.E., and Raymer, L.L., 1970, New developments in sonic wave train display and analysis in cased holes: transactions, eleventh annual logging symposium, SPWLA, paper F.

Chan, A.K. and Tsang, L., 1983, Propagation of acoustic waves in a fluid-filled borehole surrounded by a concentrically layered transversely isotropic formation: J. Acoust. Soc. Am., v.74, p.1605-1616.

Chang, S.K. and Everhart, A.H., 1983, A study of sonic logging in a cased borehole: J. Pet. Tech., v.35., p.1745-1750.

Chen, S.T, and Willen, D.E., 1984, Shear wave logging in slow formations: transactions, twenty-fifth annual logging symposium, SPWLA, paper DD.

Cheng, C.H. and Toksöz, M.N., 1981, Elastic wave propagation in a fluid-filled borehole and synthetic acoustic logs: Geophysics, v.46., p.1042-1053.

Cheng, C.H. and Toksöz, M.N., 1983, Determination of shear wave velocities in "slow" formations: twenty-fourth annual logging symposium, SPWLA, paper V.

Cheng, C.H., Tubman, K.M., and Toksöz, M.N., 1981, Propagation of seismic waves in a multilayered borehole: 51st Annual International SEG Meeting, Los Angeles, CA.

Cheng, C.H., Toksöz, M.N., and Willis, M.E., 1982, Determination of in situ attenuation from full waveform acoustic logs: J. Geophys Res., v.87., p.5477-5484.

Cheng, C.H., Toksöz, M.N., and Tubman, K.M., 1983, Determination of shear velocity in "soft" formations: 53st Annual International SEG Meeting, Las Vegas, Nevada.

Dobrin, M.B., 1976, Introduction to Geophysical Prospecting, New York, McGraw Hill.

Futterman, W.I., 1962, Dispersive body waves: J. Geophys. Res., v.67., p.5257-5291.

Grosmangin, M., Kokesh, F.P., and Majani, P., 1961, A sonic method for analyzing the quality of cementation of borehole casings: J. Pet. Tech., p. 165-171.

Haskell, N.A., 1953, The dispersion of surface waves in multilayered media: Bull. Seism. Soc. Am., v.43., p.17-34.

Kerr, R.A., 1984, Continental Drilling Heading Deeper, Science, v.224, p.1418-1420.

Kjartansson, E., 1979, Constant Q-wave propagation and attenuation: J. Geophys. Res., v.84, p.4737-4748.

Lebreton, F., Sarda, J., Troceveme, F., and Morlier, P., 1978, Logging test in porous media to evaluate the influence of their permeability on

acoustic waveforms: nineteenth annual logging symposium, SPWLA.

Liu, O.Y., 1984, Stoneley wave-derived Δt shear log: transactions, twenty-fifth annual logging symposium, SPWLA, paper ZZ.

Paillet, F. and White, J.E., 1982, Acoustic modes of propagation in the borehole and their relationship to rock properties: Geophysics, v.47., p.1215-1228.

Pardo-Casas, F., 1984, Application of the finite difference method in the study of wave propagation in a borehole: M.S. thesis, M.I.T., Cambridge, MA.

Pardue, G.H., Morris, R.L., Gollwitzer, L.H., and Moran, J.H., 1963, Cement bond log - a study of cement and casing variables: J. Pet. Tech., p.545-555.

Riddle, G.A., 1962, Acoustic wave propagation in bonded and unbonded oil well casing: S.P.E. paper number 454

Roever, W., Rosenbaum, J., and Vining, T., 1974, Acoustic waves from an impulsive source in a fluid-filled borehole: J. Acoust. Soc. Am., v.55, p.1144-1157.

Rosenbaum, J.H., 1974, Synthetic microseismograms: logging in porous formations, Geophysics, v.39., p.14-32.

Schoenberg, M., Marzetta, T., Aron, J., and Porter, R., 1981, Space-time dependence of acoustic waves in a borehole: J. Acoust. Soc. Am., v.70., p.1496-1507.

Staal, J.J., and Robinson, J.D., 1977, Permeability profiles from acoustic logging: S.P.E. paper no. 6821, 52nd Annual Fall Tech. Conf. and Exh. S.P.E. of AIME, Denver, CO.

Thomson, W.T., 1950, Transmission of elastic waves through a stratified solid: J. Appl. Physics, v.21., p.89-93.

Tubman, K.M.,Cheng, C.H., and Toksöz, M.N., 1982, Effects of Casing on Full Waveform Acoustic Logs: 52nd Annual International SEG Meeting, Dallas, TX.

Tubman, K.M.,Cheng, C.H., and Toksöz, M.N., 1983, Depth of Investigation of Downhole Acoustic Logging Tools in Altered Formations, EOS, v.64., p.268.

Tubman, K.M.,Cheng, C.H., and Toksöz, M.N., 1984a, Synthetic full waveform acoustic logs in cased boreholes: Geophysics, v.49., p.1051-1059.

Tubman, K.M.,Cheng, C.H., and Toksöz, M.N., 1984b, Determination of formation properties in cased boreholes using full waveform acoustic logs: transactions, twenty-fifth annual logging symposium, SPWLA, paper CC.

Tsang, L. and Rader, D., 1979, Numerical evaluation of transient acoustic waveform due to a point source in a fluid-filled borehole: Geophysics, v.44., p.1706-1720.

Walker, T., 1968, A full-wave display of acoustic signal in cased holes: J.Pet. Tech., p.811-824.

White, J.E., 1983, Underground Sound: Elsevier, New York, 253pp.

White, J.E. and Zechman, R.E., 1968, Computed response of an acoustic logging tool: Geophysics, v.33., p.302-310.

White, J.E., and Tongtaow, C., 1981, Cylindrical waves in transversely isotropic media: J. Acoust. Soc. Am., v.70, p.1147-1155.

Whittier, J.S. and Jones, J.P., 1967, Axially symmetric wave propagation in a two-layered cylinder: Int. J. Solids Structures, v.3., p.657-675.

Willis, M.E., 1983, Seismic velocity and attenuation from full waveform acoustic logs: Ph.D. thesis, M.I.T., Cambridge, MA., 357pp.

Winbow, G.A., 1980, How to separate compressional and shear arrivals in a sonic log: 50th Annual International Meeting SEG, Dallas, TX.

Zhang, J. and Cheng, C.H., 1984, Numerical studies of body amplitudes in full waveform acoustic logs: M.I.T. Full Waveform Acoustic Logging Annual Report, p.75-102.

Appendix A

Boundary Calculations

This appendix gives the details of the calculations necessary to relate stresses and displacements at each type of interface encountered. Each combination of fluid and solid layers is treated separately. The results can then be combined to relate stresses and displacements across an arbitrary number of layers with arbitrary composition (solid or fluid).

The constants defining the potentials for a particular layer n, A_n, A'_n, B_n and B'_n, are found in terms of the constants in the next layer inward (layer $n-1$). These are in turn expressed in terms of A'_1 and possibly A_n from an inner layer. These are the constants that determine the potentials for the first layer. The relationships between these terms are expressed using two sets of constants: a_i and c_i. This set of constants has no particular physical meaning. They are used only to keep the derived expressions manageable. The results of each of the following sections can be used as the starting point for another section if further calculations are required.

A.1 Fluid-Solid Boundary

Let layer n be the fluid layer and layer $n+1$ the solid. The boundary is then at r_n. The boundary conditions are continuity of radial displacement and stress and zero axial stress. The axial displacement can be discontinuous.

$$u_n(r_n) = u_{n+1}(r_n) \tag{A.1a}$$

$$\sigma_n(r_n) = \sigma_{n+1}(r_n) \tag{A.1b}$$

$$\tau_n(r_n) = \tau_{n+1}(r_n) = 0 \tag{A.1c}$$

In the fluid layer there are two constant terms, A_n and A'_n. It is assumed that these are both expressed in terms of A'_1. Shortly, it will be clear that this is always the case. The solid has four constants: A_{n+1}, A'_{n+1}, B_{n+1}, and B'_{n+1}. There are three equations, then, and five constants to be determined. A'_{n+1}, B_{n+1}, and B'_{n+1} are found in terms of A_{n+1} and A'_1.

The equation for continuity of normal stress (equation A.1a) can be written explicitly as:

$$\mathbf{D}_{n+1_{11}}A_{n+1}+\mathbf{D}_{n+1_{12}}A'_{n+1}+\mathbf{D}_{n+1_{13}}B_{n+1}+\mathbf{D}_{n+1_{14}}B'_{n+1} = \mathbf{D}_{n_{11}}A_n+\mathbf{D}_{n_{12}}A'_n \tag{A.2}$$

where, A_n and A'_n are both in terms of A'_1:

$$A_n = a_0 A'_1$$

$$A'_n = a_1 A'_1$$

a_i are constants. Substituting into equation (A.2) yields:

$$D_{n+1_{11}}A_{n+1}+D_{n+1_{12}}A'_{n+1}+D_{n+1_{13}}B_{n+1}+D_{n+1_{14}}B'_{n+1}=(D_{n_{11}}a_0+D_{n_{12}}a_1)A'_1 \quad \textbf{(A.3)}$$

In a similar manner, the continuity of normal stress (equation A.1b) can be written:

$$D_{n+1_{31}}A_{n+1}+D_{n+1_{32}}A'_{n+1}+D_{n+1_{33}}B_{n+1}+D_{n+1_{34}}B'_{n+1}=(D_{n_{11}}a_0+D_{n_{12}}a_1)A'_1 \quad (A.4)$$

and zero tangential stress at the boundary (equation A.1c) can be written as:

$$D_{n+1_{41}}A_{n+1}+D_{n+1_{42}}A'_{n+1}+D_{n+1_{43}}B_{n+1}+D_{n+1_{44}}B'_{n+1}=0 \quad (A.5)$$

A set of constants c_i is defined to simplify notation. Let:

$$c_0=D_{n_{11}}a_0+D_{n_{12}}a_1$$

$$c_1=D_{n_{31}}a_0+D_{n_{32}}a_1$$

A'_{n+1} can be eliminated from equations (A.3) and (A.5). This yields:

$$c_2A_{n+1}+c_3B_{n+1}+c_4B'_{n+1}=c_0A'_1 \quad (A.6)$$

where:

$$c_2=D_{n+1_{11}}-\frac{D_{n+1_{12}}D_{n+1_{41}}}{D_{n+1_{42}}}$$

$$c_3=D_{n+1_{13}}-\frac{D_{n+1_{12}}D_{n+1_{43}}}{D_{n+1_{42}}}$$

$$c_4=D_{n+1_{14}}-\frac{D_{n+1_{12}}D_{n+1_{44}}}{D_{n+1_{42}}}$$

Similarly, A'_{n+1} can also be eliminated from equations (A.4) and (A.5) to give:

$$c_5 A_{n+1} + c_6 B_{n+1} + c_7 B'_{n+1} = c_1 A'_1 \qquad \text{(A.7)}$$

where:

$$c_5 = D_{n+1_{31}} - \frac{D_{n+1_{32}} D_{n+1_{41}}}{D_{n+1_{42}}}$$

$$c_6 = D_{n+1_{33}} - \frac{D_{n+1_{32}} D_{n+1_{43}}}{D_{n+1_{42}}}$$

$$c_7 = D_{n+1_{34}} - \frac{D_{n+1_{32}} D_{n+1_{44}}}{D_{n+1_{42}}}$$

B_{n+1} can now be eliminated from (A.6) and (A.7) to give and expression for B'_{n+1} in terms of A_{n+1} and A'_1:

$$B'_{n+1} = c_8 A_{n+1} + c_9 A'_1 \qquad \text{(A.8)}$$

where:

$$c_8 = \frac{\frac{c_3 c_5}{c_6} - c_2}{c_4 - \frac{c_3 c_7}{c_6}}$$

$$c_9 = \frac{c_0 - \frac{c_3 c_1}{c_6}}{c_4 - \frac{c_3 c_7}{c_6}}$$

Substituting equation (A.8) into equation (A.7):

$$c_5 A_{n+1} + c_6 B_{n+1} + c_7 (c_8 A_{n+1} + c_9 A'_{n+1}) = c_1 A'_1$$

Solving for B_{n+1} yields:

$$B_{n+1} = c_{10} A_{n+1} + c_{11} A'_{n+1} \qquad \text{(A.9)}$$

where:

$$c_{10} = \frac{-c_5 - c_7 c_8}{c_6}$$

$$c_{11} = \frac{c_1 - c_7 c_9}{c_6}$$

Substituting equation (A.8) and equation (A.9) into equation (A.6) yields:

$$D_{n+1_{41}} A_{n+1} + D_{n+1_{42}} + D_{n+1_{43}} (c_{10} A_{n+1} + c_{11} A'_1) + D_{n+1_{44}} (c_8 A_{n+1} + c_9 A'_1) = 0$$

Which can be solved to find and expression for A'_{n+1} in terms of A_{n+1} and A'_1:

$$A'_{n+1} = c_{12} A_{n+1} + c_{13} A'_1 \qquad \text{(A.10)}$$

where:

$$c_{12} = \frac{-D_{n+1_{41}} - D_{n+1_{43}} c_{10} - D_{n+1_{44}} c_8}{D_{n+1_{42}}}$$

$$c_{13} = \frac{-D_{n+1_{43}} c_{11} - D_{n+1_{44}} c_9}{D_{n+1_{42}}}$$

Equations (A.10), (A.9), and (A.8) then give A'_{n+1}, B_{n+1}, and B'_{n+1} in terms of A'_1 and A_{n+1}.

A.2 Solid-Fluid Boundary

The solid, layer n, has constants A_n, A'_n, B_n, and B'_n, all expressed in terms of A'_1 and A_n (or A from some inner solid layer). The fluid, layer $n+1$, has constants A_{n+1} and A'_{n+1}. The boundary conditions are the same as in the previous case of a solid-fluid boundary. A_n and A'_n are

determined in terms of A'_1. The continuity of radial displacement is written as:

$$D_{n+1_{11}} A_{n+1} + D_{n+1_{12}} A'_{n+1} = c_{16} A_n + c_{17} A'_1 \qquad (A.11)$$

where:

$$c_{16} = D_{n_{11}} c_{14} + D_{n_{12}} c_{12} + D_{n_{13}} c_{10} + D_{n_{14}} c_8$$

$$c_{17} = D_{n_{11}} c_{15} + D_{n_{12}} c_{13} + D_{n_{13}} c_{11} + D_{n_{14}} c_9$$

The continuity of radial stress gives:

$$D_{n+1_{31}} A_{n+1} + D_{n+1_{32}} A'_{n+1} = c_{18} A_n + c_{19} A'_1 \qquad (A.12)$$

where:

$$c_{18} = D_{n_{31}} c_{14} + D_{n_{32}} c_{12} + D_{n_{33}} c_{10} + D_{n_{34}} c_8$$

$$c_{19} = D_{n_{31}} c_{15} + D_{n_{32}} c_{13} + D_{n_{33}} c_{11} + D_{n_{34}} c_9$$

The condition that the axial stress must vanish at the interface is written explicitly as:

$$0 = c_{20} A_n + c_{21} A'_1 \qquad (A.13)$$

where:

$$c_{20} = D_{n_{41}} c_{14} + D_{n_{42}} c_{12} + D_{n_{33}} c_{10} + D_{n_{34}} c_8$$

$$c_{21} = D_{n_{41}} c_{15} + D_{n_{42}} c_{13} + D_{n_{43}} c_{11} + D_{n_{44}} c_9$$

A_n is eliminated from equations (A.11) and (A.13). The result is:

$$D_{n+1_{11}} A_{n+1} + D_{n+1_{12}} A'_{n+1} = c_{22} A'_1 \qquad (A.14)$$

where:

$$c_{22} = c_{17} - \frac{c_{16}c_{21}}{c_{20}}$$

Similarly eliminating A_n from equations (A.12) and (A.13) yields:

$$D_{n+1_{31}} A_{n+1} + D_{n+1_{32}} A'_{n+1} = c_{23} A'_1 \qquad \text{(A.15)}$$

where:

$$c_{23} = c_{19} - \frac{c_{18}c_{21}}{c_{20}}$$

A'_{n+1} is then eliminated from equations (A.14) and (A.15). The result is:

$$A_{n+1} = a_0 A'_1 \qquad \text{(A.16)}$$

where:

$$a_0 = \frac{c_{17} - \frac{c_{16}c_{21}}{c_{20}} - \left(c_{19} - \frac{c_{18}c_{21}}{c_{20}}\right)\left(\frac{D_{n+1_{12}}}{D_{n+1_{32}}}\right)}{D_{n+1_{11}} - \frac{D_{n+1_{12}} D_{n+1_{31}}}{D_{n+1_{32}}}}$$

Substituting equation (A.16) into equation (A.14) yields:

$$A'_{n+1} = a_1 A'_1 \qquad \text{(A.17)}$$

where:

$$a_1 = \frac{c_{22} - D_{n+1_{11}} a_0}{D_{n+1_{12}}}$$

If this fluid layer is the outermost fluid layer, (layer f), the displacements

and stresses are now related across all the layers. Otherwise, the results of this solid-fluid case can serve as input for the fluid-solid boundary conditions if the next layer $n+2$ is a solid. (Recall that the constants a_0 and a_1 were used earlier in the case of a fluid-solid boundary.)

A.3 Solid-Solid Boundary

In the inner solid n, there are four constants A_n, A'_n, B_n, and B'_n, all of which are expressed in terms of A_n and A'_1. The outer solid has constants A_{n+1}, A'_{n+1}, B_{n+1}, and B'_{n+1}. The boundary conditions at r_n are the continuity of radial and axial displacements and stresses:

$$u_n(r_n) = u_{n+1}(r_n) \tag{A.18a}$$

$$v_n(r_n) = v_{n+1}(r_n) \tag{A.18b}$$

$$\sigma_n(r_n) = \sigma_{n+1}(r_n) \tag{A.18c}$$

$$\tau_n(r_n) = \tau_{n+1}(r_n) \tag{A.18d}$$

A_{n+1}, A'_{n+1}, B_{n+1}, and B'_{n+1} will be found in terms of A'_1 and A_n.

If there are several solid layers together in a group, this section is used repeatedly, determining all constants in terms of A'_1 and A_i, where i is the innermost layer of the group. All four components of the displacement-stress vector are continuous across r_n, the interface between the two solid layers n and $n+1$. Thus:

$$\mathbf{u}_n(r_n) = \mathbf{u}_{n+1}(r_n)$$

or

$$\mathbf{D}_n(r_n)\mathbf{a}_n = \mathbf{D}_{n+1}(r_n)\mathbf{a}_{n+1}$$

Rearranging:

$$\mathbf{a}_{n+1} = \mathbf{D}_{n+1}^{-1}(r_n)\mathbf{D}_n(r_n)\mathbf{a}_n \tag{A.19}$$

$\mathbf{a}_n$ is known in terms of A'_1 and A_n, (or A from some inner solid layer) . Equation (A.19) can thus be written:

$$\begin{pmatrix} A_{n+1} \\ A'_{n+1} \\ B_{n+1} \\ B'_{n+1} \end{pmatrix} = \mathbf{D}_{n+1}^{-1}(r_n)\mathbf{D}_n(r_n) \begin{pmatrix} c_{14}A_n + c_{15}A'_1 \\ c_{12}A_n + c_{13}A'_1 \\ c_{10}A_n + c_{11}A'_1 \\ c_8A_n + c_9A'_1 \end{pmatrix} \tag{A.20}$$

Equation (A.20) gives A_{n+1}, A'_{n+1}, B_{n+1}, and B'_{n+1} in terms of A_n and A'_1. The results can be put into the form:

$$A_{n+1} = c_{14}A_n + c_{15}A'_1$$

$$A'_{n+1} = c_{12}A_n + c_{13}A'_1$$

$$B_{n+1} = c_{10}A_n + c_{11}A'_1$$

$$B'_{n+1} = c_8A_n + c_9A'_1$$

where the constants c_i do *not* have the same values as in equation (A.20). They are new values determined by the matrix multiplication. The reason for using the same terms is that if the next layer (n+2) is also solid, these new values are substituted directly into equation (A.20) to continue through all solid layers.

A.4 Fluid-Fluid Boundary

The inner fluid, layer n, has constants A_n and A'_n, both in terms of A'_1. The outer fluid has constants A_{n+1} and A'_{n+1}. The boundary conditions are the continuity of radial displacement and stress:

$$u_n(r_n) = u_{n+1}(r_n) \tag{A.21a}$$

$$\sigma_n(r_n) = \sigma_{n+1}(r_n) \tag{A.21b}$$

The inner fluid has constants A_n and A'_n which are both known in terms of A'_1. The outer fluid has constants A_{n+1} and A'_{n+1}.

The continuity of radial displacement (equation A.21a) can be written explicitly as:

$$A'_1(\alpha_0 D_{n_{11}} + \alpha_1 D_{n_{12}}) = D_{n+1_{11}} A_{n+1} + D_{n+1_{32}} A'_{n+1} \tag{A.22}$$

The continuity of radial stress (equation A.21b) is:

$$A'_1(\alpha_0 D_{n_{31}} + \alpha_1 D_{n_{32}}) = D_{n+1_{31}} A_{n+1} + D_{n+1_{32}} A'_{n+1} \tag{A.23}$$

A'_{n+1} is eliminated from equations (A.22) and (A.23) to yield:

$$A_{n+1} = \alpha'_0 A'_1 \tag{A.24}$$

where

$$a'_0 = \frac{a_0 D_{n_{11}} + a_1 D_{n_{12}} - \frac{D_{n+1_{12}}}{D_{n+1_{32}}}(a_0 D_{n_{31}} + a_1 D_{n_{32}})}{D_{n+1_{11}} - \frac{D_{n+1_{12}} D_{n+1_{31}}}{D_{n+1_{32}}}} \qquad \textbf{(A.25)}$$

A'_{n+1} is determined by substituting equation (A.24) into equation (A.22). The result is:

$$A'_{n+1} = a'_1 A'_1 \qquad \text{(A.26)}$$

where:

$$a'_1 = \frac{a_0 D_{n_{11}} + a_1 D_{n_{12}} - a'_0 D_{n+1_{11}}}{D_{n+1_{12}}} \qquad \text{(A.27)}$$

a'_0 and a'_1 replace a_0 and a_1 if further calculations are required.

Appendix B

Numerical Considerations

Good numerical accuracy is essential for the calculations performed in this thesis. Microseismograms and other calculations must have as little numerical noise as possible to facilitate interpretation and analysis. This appendix describes the precautions taken to insure and confirm the reliability of the results.

Bessel functions I_0 and I_1 can be calculated over the entire range of of arguments using recurrence relations (Abramowitz and Stegun, 1970). This provides fast and accurate results with a straightforward method. In order to determine the maximum order at which to begin the recurrence, a relationship is found between the magnitude of the argument and the order at which the magnitude of the Bessel function falls below a certain level (Zemanek, personal communication). This level is set to be the desired accuracy of the function. For the sake of speed, asymptotic expansions are used for large arguments.

In general, K_0 and K_1 are much more difficult to determine accurately than are I_0 and I_1. No single method can provide satisfactory results over

the entire range of arguments encountered. The ascending series representation (Abramowitz and Stegun, 1970) is used to find K_0 for arguments with magnitude less than 5. Above this level, asymptotic expansions are used. K_1 is determined from the Wronskian. This is a more efficient and more accurate method than going through another series calculation. Once I_0, I_1, and K_0 are known there are only 3 multiplications and 1 addition required to use the Wronskian rather than the larger amount of calculation necessary for a series to converge (which will depend on the argument). As a check of accuracy of the calculated values, results are compared for a number of techniques. Methods used for comparison include: comparisons with tables, relations between solutions, limiting forms for small arguments, ascending series, Wronskians, integral representations, and recurrence relations. On the real axis, results were also compared with polynomial approximations. Double precision calculations were also performed for comparison with the single precision results.

Limits on the recurrence relations and series expansions are set so as to provide a minimum accuracy of 5 digits for the Bessel functions. The actual accuracy depends on which function is calculated as well as its argument.

Another important factor in the generation of the $\omega-k$ spectrum is the convergence criterion. This controls the maximum wavenumber (k) used

in the calculations for a given frequency. It is necessary for the spectrum to be extended to values of k high enough to include the energy for all waves. The actual criterion is a comparison of the present spectrum value with the average of all previous values for a particular frequency. The calculations are ended when the most recent spectrum value is less than 1 percent of the average. The use of the average in the comparison prevents a single large peak in the spectrum from causing a premature end of the calculations. Observation of the spectrum provides a check on the proper behavior of the convergence scheme. It is obvious if a peak in the spectrum comes to an end because an insufficient number of wavenumber points were calculated.

Both temporal and spatial wraparound must be addressed because the calculations sample in both frequency and wavenumber. The frequency sampling rate is determined so that all expected arrivals are within the resulting time window. In exceptional cases, some temporal wraparound may occur but in no case is it allowed to overlap any other arrival. Similarly, the wavenumber spacing is chosen so that the first arrival from an imaginary source arrives after the end of the time window. The value for Δk is determined using source-receiver separations that are longer than those routinely used in the analysis so it is more strict than is necessary. The addition of the imaginary frequency component, ω_i, also aides in minimizing wraparound by introducing additional attenuation. This effect is later removed from the resulting time series. While minor

temporal wraparound does not hinder the analysis, no amount of spatial wraparound is allowed. As a final check, a number of tests were performed with various wavenumber sampling rates. Any difference in the waveform would indicate insufficient sampling. The above procedures confirmed that both the frequency and wavenumber sampling prevented wraparound problems.

A final point that was examined as a source of numerical error is the matrix inversion performed in relating stresses and displacements across the layers (see equation 2.8a). The matrix inversion is performed using the Gauss-Jordan method utilizing pivoting for more reliable results. Checks on the accuracy of the inversion were done by performing the calculations using double precision. The changes in the final solution as a result of the extra precision were observed in the fifth decimal place. It was therefore decided that the extra computational expense necessary to perform a double-precision matrix inversion was not warranted. In fact, the use of double precision was never found to be sufficiently beneficial to justify the roughly four fold increase in computation time.

The techniques and results employed in thesis were carefully examined for possible sources of error. All major problems were evaluated and treated so as to minimize numerical inaccuracies. Accuracy checks and comparisons indicate the calculated results are reliable and stable.